POLITECNICO DI MILANO

Department of Energy

Doctoral Program in Radiation Science and Technology

XXIV Cycle

Modelling of Fission Gas Swelling and Release in Oxide Nuclear Fuel and Application to the TRANSURANUS Code

Doctoral Dissertation of:

Giovanni Pastore

Matr. n. 738743

Tutor:

Prof. Lelio Luzzi

Supervisors:

Dr. Paul Van Uffelen

Prof. Lelio Luzzi

The Chair of the Doctoral Program:

Prof. Carlo Enrico Bottani

March 2012

To my parents in gratitude

Acknowledgements

It is a pleasure to thank the many people who made this PhD thesis possible.

I am profoundly indebted to my Supervisor, Prof. Lelio Luzzi, for believing in me, for guiding me during the PhD, for the opportunities that I received from him, for his teaching, advice and constant support. To him, I owe my deepest gratefulness and respect.

I would like to express my gratitude to my Supervisor, Dr. Paul Van Uffelen, for the scientific and personal support, fruitful discussions, guidance and encouragement during my research period at the JRC/ITU and further. With my heartfelt thanks and highest esteem.

I wish to truly thank Prof. Klaus Lassmann, for the invaluable guidance and advice on numerical issues and fundamental concepts of fuel rod modelling, the Fortran 95 programming language, and the Transuranus code. To him goes my gratitude and admiration.

I am grateful to the professors of the Department of Energy, Nuclear Engineering Division (CeSNEF) of the Politecnico di Milano, for their teaching during my university studies and PhD.

I would like to thank all the people of the Nuclear Power Plants Group, for what I learned from them, and for the pleasant and stimulating working environment at the Politecnico di Milano. In particular, I am grateful to Prof. Marco Ricotti, for the support received over the years. I wish to thank Prof. Antonio Cammi, for the interesting talks and kindness. I am thankful to all my PhD colleagues, for the fruitful collaboration and the nice time spent together.

JRC/ITU is gratefully acknowledged, for the enriching experience and the support. I wish to thank the people of the Materials Research Unit, for the favourable welcome, stimulating and friendly working environment, scientific support and instructive debates. In particular, I am thankful to Dr. Arndt Schubert, for the fruitful and interesting discussions, and to Dr. Valentino Di Marcello, for the collaboration, comments, and good company. A special thank is due to Dr. Jacques van de Laar, for the technical suggestions, and the exquisite kindness and helpfulness.

Many thanks to Dr. Paul Blair (Westinghouse), for the valuable comments on the work, and to Dr. Glyn Rossiter (NNL), for the useful information.

This thesis is dedicated to my father, Carlo, and to my mother, Renza, for all that I learned and received from them all along my life. To mom and dad goes my eternal gratitude and love.

Contents

List of acronyms

AGR	Advanced Gas-cooled Reactor
ANL	Argonne National Laboratory
BNFL	British Nuclear Fuels Limited
BOL	Beginning-Of-Life
BWR	Boiling Water Reactor
CEA	Commissariat à l'Énergie Atomique
CEN	Centre d'Étude de l'énergie Nucléaire
CPL	Conditioning Power Level
EOL	End-Of-Life
EPRI	Electric Power Research Institute
FGR	Fission Gas Release
FP	Fission Product
FUMEX	FUel Modelling at EXtended burn-up
HBS	High Burn-up Structure
IAEA	International Atomic Energy Agency
IFPE	International Fuel Performance Experiments
INEEL	Idaho National Engineering and Environmental Laboratory
ITU	Institute for Transuranium Elements
JRC	Joint Research Centre
LOCA	Loss-Of-Coolant Accident
LWR	Light Water Reactor
MOX	Mixed OXide
NEA	Nuclear Energy Agency
PCCI	Pellet-Cladding Chemical Interaction
PCI	Pellet-Cladding Interaction
PCMI	Pellet-Cladding Mechanical Interaction
PIE	Post-Irradiation Examinations
PNNL	Pacific Northwest National Laboratory
PWR	Pressurized Water Reactor
OD	Outer Diameter
OECD	Organisation for Economic Co-operation and Development
ORNL	Oak Ridge National Laboratory
PIE	Post Irradiation Examinations
PSI	Paul Scherrer Institut
R&D	Research & Development
RIA	Reactivity-Initiated Accident
RTL	Ramp Terminal Level

SCC	Stress Corrosion Cracking
SCK	Studiecentrum voor Kernenergie
SEM	Scanning Electron Microscopy
TEM	Transmission Electron Microscopy

List of symbols

The following list includes the symbols that are of most extensive use in the present work. The other symbols are defined in the text.

A_c	Cross-sectional area of the coolant channel [m^2]
A_{gb}	Projected area of grain-boundary bubbles [m^3]
b	Irradiation-induced resolution parameter [s^{-1}]
B	Model parameter [m]
bu	Burn-up [at%]
c	Specific heat [$J \cdot kg^{-1} \cdot K^{-1}$]
C_b	Concentration of intra-granular gas residing in bubbles [$(at.) \cdot m^{-3}$]
C_{gb}	Concentration of gas at the grain boundaries [$(at.) \cdot m^{-2}$]
C_s	Concentration of intra-granular gas existing as single atoms [$(at.) \cdot m^{-3}$]
C_{SB}	Stefan-Boltzmann constant [$W \cdot m^{-2} \cdot K^{-4}$]
C_t	Concentration of intra-granular gas (single atoms + bubbles) [$(at.) \cdot m^{-3}$]
D_{eff}	Effective intra-granular gas diffusion coefficient [$m^2 \cdot s^{-1}$]
d_{gap}	Radial gap width [m]
D_s	Single gas atom diffusion coefficient in grains [$m^2 \cdot s^{-1}$]
D_v	Vacancy diffusion coefficient in grain boundaries [$m^2 \cdot s^{-1}$]
e	Emissivity [-]
E	Young's modulus [Pa]
F	Fission rate density [$(fiss.) \cdot m^{-3} \cdot s^{-1}$]
F_c	Fraction of grain boundary surface covered by bubbles (fractional coverage) [/]
$F_{c,sat}$	Fractional coverage at grain boundary saturation [/]
$f(r)$	Radial power density distribution function [-]
g	Trapping parameter [s^{-1}]
$h_{cl,c}$	Heat transfer coefficient between the cladding and the coolant [$W \cdot m^{-2} \cdot K^{-1}$]
h_{film}	Heat transfer coefficient in the cladding-coolant convection film [$W \cdot m^{-2} \cdot K^{-1}$]
h_{gap}	Gap conductance [$W \cdot m^{-2} \cdot K^{-1}$]
h_{rad}	Radiative component of the gap conductance [$W \cdot m^{-2} \cdot K^{-1}$]
h_{con}	Contact pressure contribution to the gap conductance [$W \cdot m^{-2} \cdot K^{-1}$]
h_g	Conductive component of the gap conductance [$W \cdot m^{-2} \cdot K^{-1}$]
H	Meyer hardness [Pa]
k	Boltzmann constant [$J \cdot K^{-1}$]
l_f	Length of a fission fragment track [m]
l_{gas}	Gas extrapolation length [m]
m	Number of fission gas atoms contained in each intra-granular bubble [(at.)]
n_{fgr}	Number of fission gas atoms released into the fuel rod free volume [(at.)]
n_g	Number of fission gas atoms per grain-boundary bubble [(at.)]

N_{gb}	Number density of grain-boundary bubbles [(bub.)·m^{-2}]
$N_{gb,0}$	Initial number density of grain-boundary bubbles [(bub.)·m^{-2}]
N_{ig}	Number density of intra-granular bubbles [(bub.)·m^{-3}]
n_v	Number of vacancies per grain-boundary bubble [(vac.)]
p	Gas pressure in grain-boundary bubbles [Pa]
p_{cool}	Coolant pressure [Pa]
p_{con}	Fuel-cladding contact pressure [Pa]
p_{eq}	Mechanical equilibrium pressure of the gas in grain-boundary bubbles [Pa]
q'	Linear heat rate [W·m^{-1}]
q''	Heat flux [W·m^{-2}]
$q''_{cl,c}$	Heat flux from the cladding to the coolant [W·m^{-2}]
q'''	Power density [W·m^{-3}]
q'''_c	Power density in the coolant [W·m^{-3}]
q'''_{cl}	Heat generation in the cladding [W·m^{-3}]
$\bar{q}'''_{cl}$	Average power density in the cladding [W·m^{-3}]
$\bar{q}'''_f$	Average power density in the fuel [W·m^{-3}]
q_s	Specific power [W·g^{-1}]
r	Radial co-ordinate [m]
R	Radial co-ordinate in the fuel rod deformed geometry [m]
$r_{cl,i}$	Inner cladding radius [m]
$r_{cl,o}$	Outer cladding radius [m]
$r_{f,i}$	Inner fuel radius [m]
$r_{f,o}$	Outer fuel radius [m]
R_{gb}	Radius of curvature of the grain-boundary bubbles [m]
r_{gr}	Grain radius [m]
R_{ig}	Radius of intra-granular bubbles [m]
S	Model parameter [-]
t	Time [s]
T	Temperature [K]
T_c	Bulk coolant temperature [K]
$T_{cl,i}$	Temperature at the inner surface of the cladding [K]
$T_{cl,o}$	Temperature at the outer surface of the cladding [K]
$T_{f,o}$	Temperature at the outer surface of the fuel [K]
V	Volume of fuel [m^3]
V_{gb}	Volume of grain-boundary bubbles [m^3]
w	Coolant velocity [m·s^{-1}]
Y_{fg}	Yield of fission gas atoms [/]
z	Axial co-ordinate [m]
Z_0	Radius of influence of a fission fragment track [m]
α	Coefficient of linear thermal expansion [K^{-1}]
β	Fission gas generation rate [(at.)·m^{-3}·s^{-1}]
γ	UO_2/gas specific surface energy [J·m^{-2}]

δ_{gb}	Thickness of the diffusion layer in grain boundaries [m]
$\Delta\overline{R}$	Arithmetic mean roughness [m]
Δt	Time step length [s]
ΔT_{gap}	Temperature drop in the gap [K]
$\Delta V/V$	Fractional variation in fuel volume [/]
$(\Delta V/V)_{ig}$	Volumetric intra-granular fission gas swelling [/]
$(\Delta V/V)_{gas}$	Volumetric fission gas swelling [/]
$(\Delta V/V)_{gb}$	Volumetric grain-boundary fission gas swelling [/]
ε	Strain [/]
ε^{el}	Elastic strain [/]
ε^{ex}	Sum of the non-elastic strains [/]
ε^{gas}	Strain due to fission gas swelling [/]
ε_r	Radial strain [/]
ε_θ	Circumferential strain [/]
ε_z	Axial strain [/]
$\varepsilon^c{}_{eff}$	Effective creep strain [/]
ε^p	Plastic strain [/]
$\varepsilon^p{}_{eff}$	Effective plastic strain [/]
θ	Circumferential co-ordinate [m]
Θ	Semi-dihedral angle of the grain-boundary bubbles [°]
λ	Thermal conductivity [$W \cdot m^{-1} \cdot K^{-1}$]
$\overline{\lambda}$	Average thermal conductivity [$W \cdot m^{-1} \cdot K^{-1}$]
$\overline{\lambda}_{fc}$	Mean fuel-cladding thermal conductivity [$W \cdot m^{-1} \cdot K^{-1}$]
λ_{gas}	Thermal conductivity of the plenum gas mixture [$W \cdot m^{-1} \cdot K^{-1}$]
ν	Poisson's ratio [-]
ξ	Molar concentration [$mol \cdot m^{-3}$]
ρ	Density [$kg \cdot m^{-3}$]
ρ_f	Density of the fuel [$kg \cdot m^{-3}$]
ρ_{ig}	Density of the gas residing in intra-granular bubbles [$kg \cdot m^{-3}$]
σ_{eff}	Effective (Von Mises) stress [Pa]
σ_h	Hydrostatic stress [Pa]
σ_r	Radial stress [Pa]
σ_z	Axial stress [Pa]
σ_θ	Circumferential stress [Pa]
σ^{dev}	Deviatoric stress [Pa]
σ^{th}	Thermal stress [Pa]
ϕ	Weighting factor used in the thermal analysis [-]
$\varphi(\Theta)$	Geometric factor relating the volume of a lenticular bubble to that of a sphere [-]
ω	Van der Waals' volume of a fission gas atom [$m^3 \cdot (at.)^{-1}$]
Ω_{gb}	Vacancy volume in grain-boundary bubbles [m^3]
Ω_{ig}	Volume per gas atom in intra-granular bubbles [m^3]

List of figures

List of tables

Introduction

The context of the present work is the domain of research oriented toward the computational thermo-mechanical analysis of the nuclear fuel rods (fuel rod modelling). The emphasis is on the analysis of pellet-in-cladding type uranium dioxide (UO_2) fuel for light water reactors (LWRs), which constitute the majority of nuclear power reactors operated presently. The work was carried out in the frame of a collaboration between the Politecnico di Milano and the Institute for Transuranium Elements (European Commission, Joint Research Centre, Karlsruhe).

LWRs employ fuel in the form of rods comprised of ceramic fuel pellets (generally UO_2) piled-up in a zirconium-alloy cladding tube. Besides providing the heat generation and transfer to the coolant, the fuel rod is the first and the second barrier (i.e., the fuel pellets and the surrounding cladding tube, respectively) to the release of the radioactive fission products to the environment, and therefore plays a primary safety role. During irradiation in the reactor, several intricate and mutually dependent phenomena take place in the fuel rod, which continuously alter the thermal, mechanical, and chemical properties of the materials. Owing to these phenomena, both the fuel pellets and the cladding undergo various dimensional, micro-structural and chemical changes and interact with each other in thermal, mechanical and chemical manners. Fuel swelling due to fission gas and solid fission products, fuel irradiation-induced and thermal creep, fuel restructuring, fission gas and volatile fission product release, pellet cracking and hour-glassing, cladding corrosion, cladding irradiation-induced phase changes and precipitate behaviour, cladding growth, cladding irradiation-induced and thermal creep are essential aspects of the fuel rod behaviour (Olander, 1976, 2001, 2009; Konings et al., 2010; Van Uffelen et al., 2010).
The aim of fuel rod modelling is to predict the thermo-mechanical behaviour and lifetime of the nuclear fuel rods. For this purpose, the phenomena taking place in the fuel rods during irradiation are to be described. The strong interrelationship between these phenomena, as well as the non-linearity of many processes involved, calls for the development of computer codes analysing the general fuel rod behaviour. As a complement to experiments in the nuclear reactors – which require tremendous resources – the fuel rod analysis codes are presently used by industries, research centres, universities and safety authorities, in support of fuel characterization, design and licensing (Aybar and Ortego, 2005; Calvin and Nowak, 2010). In this framework, the TRANSURANUS code (Lassmann, 1988, 1992), developed at the Institute for Transuranium Elements, is the most widely adopted fuel rod analysis code in the European Union. The progress of fuel rod modelling is supported by many International Projects. In particular, the present work was carried out within the FUMEX-III (FUel Modelling at EXtended burn-up) co-ordinated research project of the IAEA (Killeen et al., 2009)[1].

[1] http://infcis.iaea.org

The structure of the fuel rod analysis codes was reviewed by Lassmann (1980). Because of the time and spatial discretization of the problem, and the non-linearities that characterize the simulated processes, the number of calls of a local model may easily reach the order of 10^6 or 10^7 during the analysis of a detailed fuel rod irradiation history. Therefore, the models implemented in the fuel rod analysis codes must be characterized by a level of complexity that is consistent with stringent computational cost requirements and the uncertainties inherent in fuel rod modelling, and by an appropriate predictive capability for the purpose of the fuel rod thermo-mechanical behaviour and structural integrity assessments.
Among the various issues involved in fuel rod modelling, the complex behaviour of the fission gases xenon and krypton offers challenges to code developers for the proper treatment of the relevant processes. Olander (1976) introduces his Chapter 13 on Swelling Due to Fission Gases by saying:

Among the myriad phenomena that occur simultaneously in a nuclear fuel element under irradiation, none has so frustrated the designer, so challenged the experimentalist, or so intrigued the theorist as the behaviour of the fission products xenon and krypton.

Although written in 1976 this statement is still valid, and even after more than 35 years of research, fission gas behaviour is still a subject of controversial discussions. Nevertheless, this area needs to be covered in fuel rod modelling because the processes of fission gas generation, diffusion, retention and release have strong implications on the thermo-mechanical behaviour of the fuel rods. On the one hand, the fission gases generated in the fuel tend to precipitate into bubbles resulting in fuel swelling, which may give rise to enhanced pellet-cladding mechanical interaction (PCMI). On the other hand, the inter-connection of the gas bubbles developing at the grain boundaries leads to fission gas release (FGR) to the free volume of the fuel rod, which causes pressure build-up and thermal conductivity degradation of the rod filling gas. The inherently coupled kinetics of the fission gas swelling and release calls for the development of physics-based, integrated models of these phenomena to be employed in fuel rod modelling (Aybar and Ortego, 2005; Calvin and Nowak, 2010). As of today, however, empirical or semi-empirical approaches are widely adopted in the fuel rod analysis codes. These models are inexpensive to use but unfit for providing insight into the underlying mechanisms, and cannot be applied beyond their range of calibration. More flexible physics-based model are necessary for describing a wider range of irradiation conditions (e.g., power ramps or high burn-up), as required by the industry. A further modelling issue concerns the role of the compressive hydrostatic stress in the fuel, acting to constrain the growth of the gas bubbles and significantly affecting both the fission gas swelling and release. This effect may be particularly marked under the conditions of strong PCMI, when high compressive hydrostatic stress may develop in the fuel due to cladding restraint (Zimmermann, 1978; Kogai et al., 1988; Mogensen et al., 1993; Kashibe and Une, 1997). According to the models of fission gas swelling and FGR presently adopted in the fuel rod analysis codes, however, the hydrostatic stress is often neglected, or considered as constant and uniform, or approximated by the external pressure of the fuel pellet (Van Uffelen et al., 2004).

The introduction fission gas swelling and release models that consistently take into account the role of the hydrostatic stress is of high importance in view of the current tendency to extend the flexibility of use (load-following) and the discharge burn-up of the nuclear fuel, which can involve the occurrence of strong PCMI (OECD/NEA, 2004). On the other hand, this aspect represents a challenging issue in view of the application to the fuel rod analysis codes, relating to the entailed necessity of numerically treating a mutual and non-linear dependence between the swelling strain and the stress.

The present work aims at providing a contribution to the modelling of fission gas swelling and release in the fuel rod analysis codes, with specific application to the TRANSURANUS code. In particular, the goals of the work include (i) the development of a physics-based, integrated model of fission gas swelling and release in UO_2 fuel during irradiation, properly considering the intrinsic coupling as well as the dependence of both phenomena on the hydrostatic stress, (ii) the demonstration of the applicability of the model to the fuel rod analysis codes (hence, to fuel design and licensing) by effective implementation in the TRANSURANUS code, and

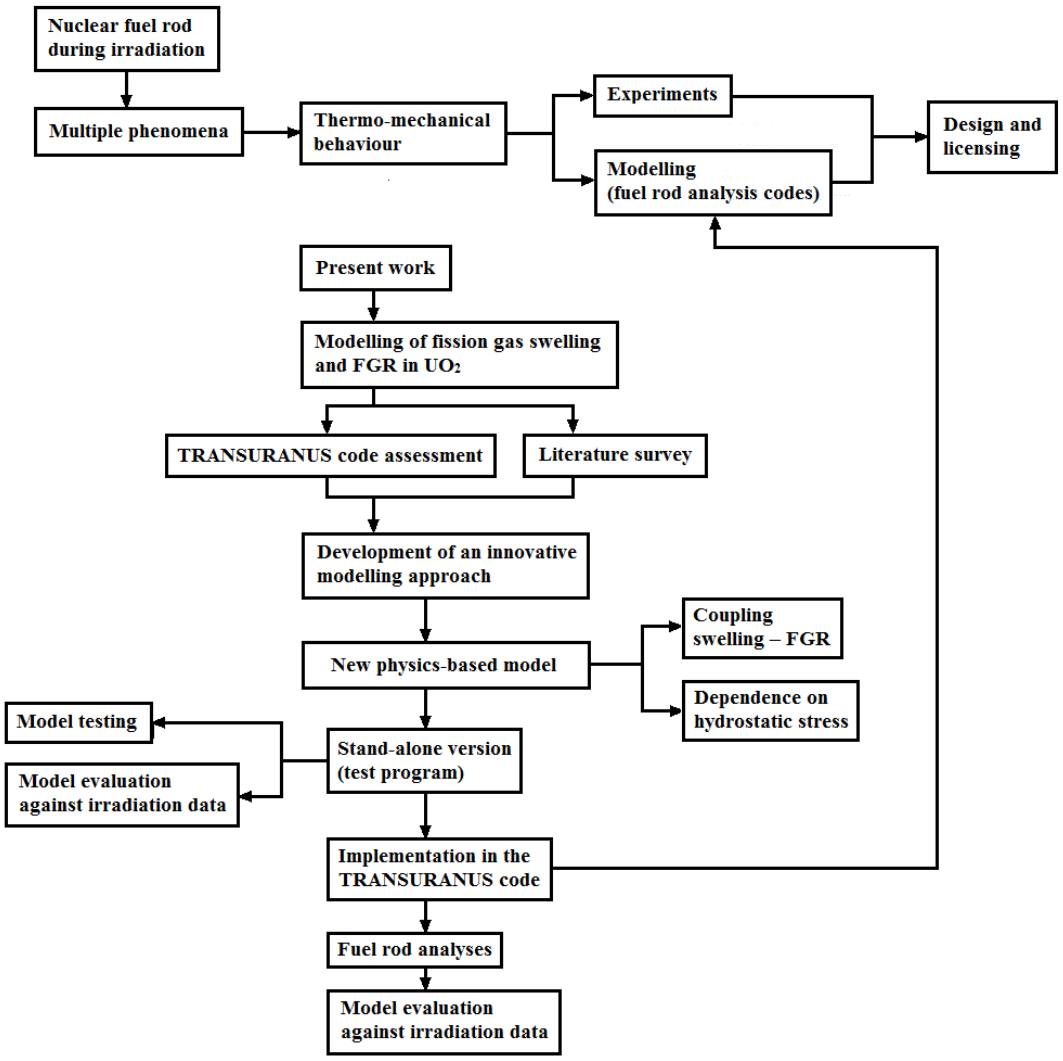

Fig. 1. Context and main stages of the present work.

(iii) the employment in fuel rod analyses and verification of the model against irradiation data. The work therefore comprises (1) a development aspect, concerning the study of the basic mechanisms of fission gas swelling and release and their appropriate representation in a model, and (2) an application aspect, concerning the implementation of the model in the TRANSURANUS code and the employment in fuel rod analyses. The achievement of the above goals requires the construction of an engineering modelling approach, which practically combines an appropriate physics-based treatment and the simplicity that is a prerequisite for the effective application to the fuel rod analysis codes.

Figure 1 outlines the context and main stages of the work, which are reflected in the following structure of the present thesis:

- Chapter 1 introduces the basic concepts of fuel rod modelling. Firstly, the main features of the LWR fuel rods are described. Then, the structure of the fuel rod analysis codes and the basic equations of the thermal and mechanical analyses are overviewed.
- Chapter 2 gives the premises of the work by briefly surveying the physical processes involved in fission gas swelling and release and the fundamental characteristics of the TRANSURANUS code.
- Chapter 3 describes a new model for fission gas swelling and release in UO_2 fuel. The basic equations of the model are given, and the underlying concepts and innovative aspects of the constructed approach are discussed.
- Chapter 4 concerns the application of the new model as stand-alone version. Calculations are presented of fission gas swelling and release in either power ramped or power cycled UO_2 fuel specimens from the International Fuel Performance Experiments (IFPE) database[2]. The results are discussed, both in terms of model capabilities to represent the relevant physical processes and by assessment of the predictions against experimental data of fission gas swelling.
- Chapter 5 deals with the application of the new model to the TRANSURANUS code. The implementation issues and methods are summarized, and the employment in fuel rod analyses is discussed. Following a critical analysis of the relevant databases, an extensive set of simulations is carried out of LWR-UO_2 fuel rod irradiation experiments involving power ramps and for the most part selected as cases of priority interest in the FUMEX-III Project. The results of the calculations are presented, showing the capabilities of the model to reproduce the peculiarities of the fission gas swelling and release, as well as the obtained predictive accuracy in terms of integral fuel rod FGR by comparison with experimental data from the IFPE database.

Chapters 3, 4 and 5 cover the original and innovative contributions of the present work.

[2] http://www.oecd-nea.org/science/fuel/ifpelst.html

Chapter 1
General concepts of fuel rod modelling

Abstract. *The aim of this chapter is to contextualize the present work in the domain of research oriented toward the computational thermo-mechanical analysis of the nuclear fuel rods. The emphasis is on the analysis of pellet-in-cladding type oxide fuel for light water reactors, which represent the majority of nuclear power reactors operated presently. In Section 1.1, the light water reactor fuel rod fundamentals are outlined, and a brief overview is given of the fuel rod analysis codes. Sections 1.2 and 1.3 present the basic equations implemented in the fuel rod analysis codes, namely, those for the heat generation and transfer from the fuel pellets to the coolant and the equations for the mechanical analysis. Conclusions are drawn in Section 1.4.*

1.1 Introduction

1.1.1 The LWR fuel rod: an outline

The core of a nuclear reactor is composed of a controlled critical configuration of a fissile material (in strict sense, the fuel) which provides the material for generating the energy that is used for the production of electricity or process heat. The fissile material is contained in a matrix, normally a metallic alloy or a ceramic compound, and the combination of fissile material and matrix is commonly referred to as nuclear fuel (Konings et al., 2010). Uranium-oxide-based nuclear fuels are generally adopted in light water reactors (LWRs), which provide approximately 85% of the nuclear power generated worldwide. As shown in Fig. 1.1, the LWR fuel exists in the form of fuel rods (oxide fuel pellets + cylindrical metallic matrix) bundled in a fuel assembly. The LWR reactor core is comprised of fuel assemblies in an arrangement that satisfies basic structural, thermal-hydraulics, and neutronics requirements (Olander, 2009).

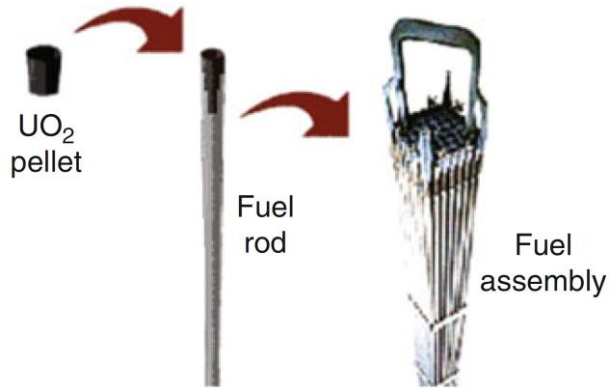

Fig. 1.1. Sketch of the LWR fuel rod and assembly – from (Calvin and Nowak, 2010).

Figure 1.2 shows a generic LWR fuel rod. The matrix consists of a ~4 m length of a zirconium-alloy (e.g., Zircaloy) cladding tube with an OD of about 0.9-1.1 cm for pressurized water reactor (PWR) fuel rods and about 1.2-1.4 cm OD for boiling water reactor (BWR) rods. The cladding tube is filled with a ~3 m stack of fuel pellets. The fuel is a polycrystalline sintered of either uranium dioxide (UO_2) with uranium enrichments up to 5%, or mixed oxide (MOX), i.e., a mixture of UO_2 and plutonium dioxide (PuO_2). A gap of about 80-100 μm under cold conditions (160-200 μm diametrically) is present between the pellets and the cladding. The gap is needed to facilitate the loading of the pellets, but also to anticipate for the swelling of the fuel pellets during irradiation (Section 1.3). The pellets are kept in place by a metallic spring that is mounted on the top of the pellet stack. The free volume around the spring (the plenum) serves as buffer volume for the fission gas that is released during the irradiation to avoid over-pressurization of the cladding. The fuel rods are pressurized with helium (about 2-2.5 MPa in PWRs and 0.3 MPa in BWRs), to assure a good thermal conductance of the gap between the pellets and the cladding, and then end-capped. Besides providing the heat generation and transfer to the coolant, the fuel rod is the first and the second barrier (i.e., the fuel pellets and the surrounding cladding tube, respectively) to the release of the radioactive fission products to the environment, and therefore plays a primary safety role.
During irradiation in the reactor, several intricate and mutually dependent phenomena take place in the fuel rod, which continuously alter the thermal, mechanical, and chemical properties of the materials. Owing to these phenomena, both the fuel pellets and the cladding undergo various dimensional, micro-structural and chemical changes and interact with each

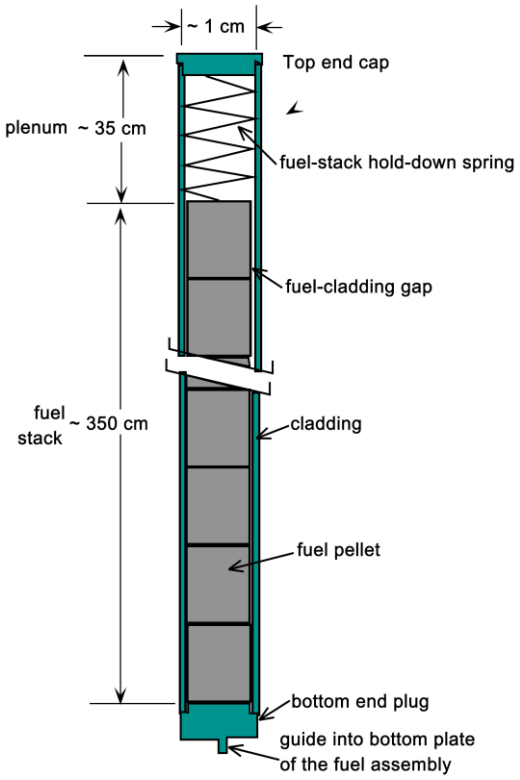

Fig. 1.2. Schematic of a generic LWR fuel rod – from (Olander, 2009).

other in thermal, mechanical and chemical manners. Fuel pellet swelling due to fission gas and solid fission products, fuel irradiation-induced and thermal creep, fuel restructuring, fission gas and volatile fission product release, pellet cracking and hour-glassing, cladding corrosion, cladding irradiation-induced phase changes and precipitate behaviour, cladding growth, cladding irradiation-induced and thermal creep are essential aspects of the fuel rod behaviour (Olander, 1976, 2001, 2009; Konings et al., 2010; Van Uffelen et al., 2010). Moreover, when the fuel-cladding gap is closed, fuel deformation affects the deformation of the cladding. The pellet-cladding mechanical interaction (PCMI) and the pellet-cladding chemical interaction (PCCI) have strong implications on the LWR fuel rod performance and received much attention in the last three decades.

To assure the safe and economic operation of the nuclear fuel rods in all the reactor operating conditions, there is a need for fuel characterization and optimization through an integrated theoretical, experimental, and computational approach. For the purpose of computational fuel modelling, increasingly complex and efficient fuel rod analysis codes are developed.

1.1.2 Fuel rod analysis codes

The aim of fuel rod modelling is to predict the thermo-mechanical behaviour and lifetime of the nuclear fuel rods. For this purpose, the phenomena taking place in the fuel rods during irradiation in the reactor (Sub-section 1.1.1) are to be described. The strong interrelationship between these phenomena, as well as the non-linearity of many processes involved, calls for the development of computer codes analysing the general fuel rod behaviour.

As a complement to experiments in the nuclear reactors and post-irradiation examinations (PIE) – which require tremendous resources (cost, time, people) – the fuel rod analysis codes (also referred to as fuel performance codes) are presently used in support of fuel characterization and design, for R&D purposes, and to verify the compliance with the safety criteria (Aybar and Ortego, 2005). In this framework, the fuel rod analysis codes are adopted by industries, research centres, universities, regulatory and licensing authorities. Here is list (by no means exhaustive) of some of the most widely used fuel rod analysis codes: COMETHE (Belgonucleaire, Belgium), COPERNIC (AREVA NP, Germany), ENIGMA (British Energy, BNFL, UK), FALCON (EPRI, USA), FRAPCON (PNNL, USA), FRAPTRAN (PNNL, USA), LIFE (ANL, USA), MACROS (SCK•CEN, Belgium), ORIGEN (ORNL, USA), PARFUME (INEEL, USA), SPHERE (PSI, Switzerland), TOUTATIS (CEA, France), and TRANSURANUS (ITU, Germany).

In general, two groups of fuel rod analysis codes can be identified (Lassmann, 1988):

1. codes describing the behaviour of a whole fuel rod, and
2. codes analysing local details.

Although the capabilities for modelling all pellets individually exist in principle, the resulting fine spatial discretization would result in high computational costs that, in view of the uncertainties involved, would be not justified by the value of the added detail. For the

assessment of the overall fuel rod behaviour, reasonable accuracy can be obtained by smearing the fuel column and representing it as a continuous body (Lassmann, 1988). In most cases, the overall behaviour of a fuel rod is obtained by quasi two-dimensional modelling, which is sometimes referred to as 1½-dimensional (1½-D) modelling. This means that the axisymmetric behaviour of a whole fuel rod is represented by a stack of one-dimensional (radial) calculations coupled axially by the coolant energy equation, a common internal fuel rod gas pressure and, in some models, by a one-dimensional model for the axial friction forces. In the next sections of this chapter, reference will be made to 1½-D modelling. Specific problems due to non-axisymmetric conditions or axial effects, particularly end effects (e.g., local pellet-cladding interaction effects) are treated in multi-dimensional calculations, in most cases based on finite element techniques (Matthews, 1978; Marchal et al., 2009; Jiang et al., 2011). Of course, the physical phenomena to be modelled are the same for both groups of fuel rod analysis codes, although the degree of sophistication differs largely not only between these groups, but also within each group. The fuel rod analysis codes belonging to the first group are sometimes referred to as *integral* codes. Among them, the most widely used tool in the European Union is the TRANSURANUS code (Lassmann, 1988, 1992, 2001), which was developed at the Institute for Transuranium Elements (JRC/ITU, Karlsruhe, Germany) and is the code of reference of the present work.

Most of the key phenomena taking place in a fuel rod are dominated by the local temperature (e.g., thermal strain, thermal creep, fission gas diffusion and release, fission gas swelling), and consequently the first task in modelling the fuel rod behaviour is the calculation of the temperature distributions. However, the temperature is governed by the width and thermal conductance of the fuel-cladding gap, which themselves are controlled by deformations of the fuel and cladding, and by fission gas release (FGR). Obviously, the thermal analysis (i.e., the calculation of the temperature distribution from the centreline of the pellets to the coolant) and the mechanical analysis (i.e., the calculation of the stresses and strains of pellets and cladding, the change in the fuel-cladding gap width, and the PCMI) are interdependent and need to be consistently determined.

The structure of the fuel rod analysis codes was reviewed by Lassmann (1980). The geometry, materials, coolant pressure and coolant temperature, and the power history of a fuel rod must be given as input quantities. The geometrical representation of the fuel rod used in 1½-D modelling is shown in Fig. 1.3. The fuel and the cladding are divided into a number of axial regions and radial intervals. Each elementary volume considered in the analysis consists of a cylindrical ring, as shown on the right of Fig. 1.3. The fuel rod analysis is carried out in a discrete time mode with the consequence that the logical structure is initially constituted by a comprehensive time loop. Inside this loop, the actual fuel rod analysis is carried out locally. The interactions of physical phenomena referred to above, especially thermo-mechanical interactions, only admit purely incremental or iterative solutions so that, in the most extensive case, the analysis is again surrounded by an iteration loop. The computation procedure is broken down into a number of individual components in which self-contained problems are solved, such as thermal or mechanical analysis. It is advisable to distinguish between simple

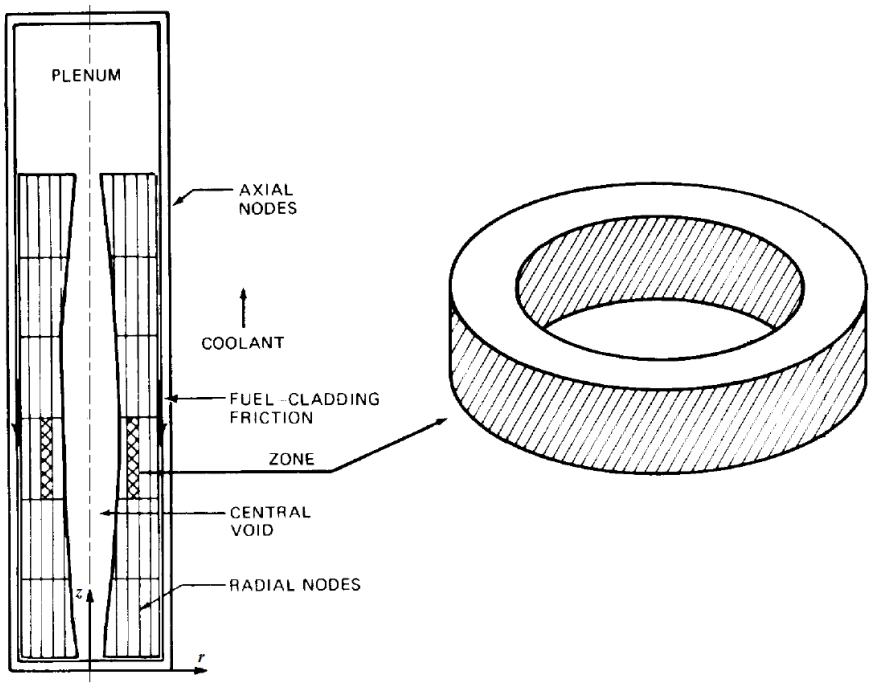

Fig. 1.3. Discretization of a fuel rod into radial and axial zones used in 1½-D modelling – from (Olander, 1976).

material parameters, such as the modulus of elasticity or the linear thermal expansion coefficient, and more complex material behaviour, such as swelling or fission gas release. Simple quantities may be made available in a materials database in various forms. To describe the complex material behaviour, physical models must be developed. For each individual model, it is necessary to develop specific test programs. Besides, special programs are necessary for handling the data case, i.e., for compiling and verifying input data (pre-processor), and evaluating the results (post-processor). Pre-processor, post-processor and the actual computer program make up the program system, the basic structure of which is shown in Fig. 1.4. Issues are involved in either kind of discretization (i.e., the spatial and the time discretizations) and in the convergence of the iteration procedure.

In 1½-D modelling, the spatial discretization of the computational domain involves a number of nodes of the order of 10^2-10^3, and a number of time steps of the order of 10^3 can be required for the analysis of a detailed irradiation history. Moreover, as discussed above, the analysis in general requires an iteration process at each time step. It follows that the number of calls of a local model may easily reach the order of 10^6 or 10^7. Therefore, the models to be adopted in fuel rod analysis codes must be constructed in view of stringent computational cost requirements.

As of today, simplified, empirical correlations are largely used in the fuel rod analysis codes to describe the complex material behaviour. Treating the complex phenomena with empirical correlations results in inability to extrapolate outside the range of parameters and irradiation conditions covered in the data set from which the correlations were drawn. In a continuous process of development and improvement, many codes are replacing empirical models with more flexible physics-based models (Calvin and Nowak, 2010; Karahan and Kazimi, 2011).

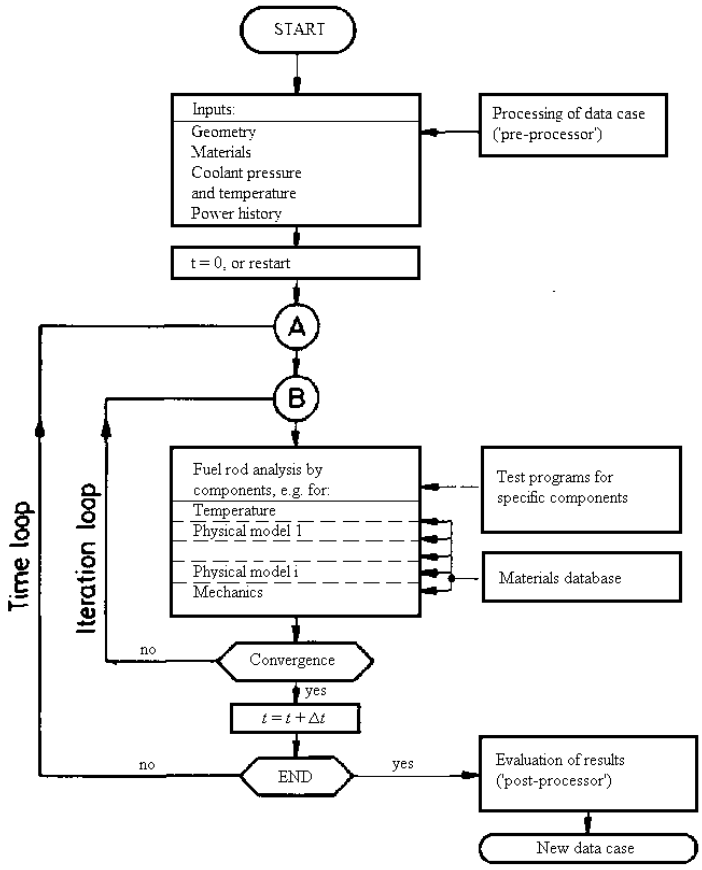

Fig. 1.4. Basic structure of a fuel rod analysis code (Lassmann, 1980). (t, Δt; time and time step, respectively).

The progress of fuel rod modelling is supported by many International Projects, such as the International Fuel Performance Experiments (IFPE) database (Sartori et al., 2010), co-sponsored by the OECD/NEA and the IAEA, and the FUMEX-III (FUel Modelling at EXtended burn-up) co-ordinated research project of the IAEA (Killen et al., 2009).

1.2 Thermal analysis

The objective of this section is to describe how the radial temperature distribution in a nuclear fuel rod is calculated in a fuel rod analysis code. The scope is limited to a description of the most important physical phenomena, along with the basic equations and the main assumptions[3]. Detailed numerical aspects as well as mathematical derivations are provided in (Olander, 1976; Lassmann, 1987; Bailly et al., 1999; Lassmann and Van Uffelen, 2004).
A cylindrical co-ordinate system is considered. In respect to the thermal analysis, a key quantity is the local power density, q''' [W·m^{-3}], that is, the produced energy per unit volume and time. It is usually assumed that q''' depends only on the radius and the time. Then, the relationship between q''' and the linear heat rate, q' [W·m^{-1}], at a generic axial location reads

[3] In Sections 1.2, 1.3 and 2.1, close reference is often made to (Van Uffelen et al., 2010).

$$q' = \int_{r_{fi}}^{r_{clo}} q'''(r)\,2\pi r dr = \int_{r_{fi}}^{r_{fo}} \bar{q}_f'''\, f(r)\,2\pi r dr + \int_{r_{cli}}^{r_{clo}} \bar{q}_{cl}'''\,2\pi r dr, \tag{1.1}$$

where r [m] is the radial co-ordinate, $r_{f,i}|r_{cl,i}$ [m] is the inner fuel|cladding radius, $r_{f,o}|r_{cl,o}$ [m] is the outer fuel|cladding radius, $\bar{q}_f'''$ and $\bar{q}_{cl}'''$ [W·m^{-3}] are the average power density in fuel and cladding, respectively, and *f(r)* [-] is a radial distribution (form) function obtained from the neutronics calculations. Generally, the linear heat rate, q', is a prescribed quantity and is a function of the axial co-ordinate, z [m], and the time, t [s]. For some phenomena (e.g., cladding irradiation-induced creep), the neutron flux is also needed, which can be prescribed as well, but may also be calculated from the local power density.

1.2.1 Axial heat transfer in the coolant

The fuel rod analysis codes use one-dimensional (axial) fluid dynamic equations for the calculation of the heat transfer in the coolant, which serves two purposes. Firstly, the axial coolant temperature in the channel provides the (Dirichlet) boundary condition for the radial temperature distribution in the fuel rod. It results from the combined solution of the mass, momentum, and energy balance equations. The simplified equation used in the fuel performance codes reads

$$c\rho\frac{\partial T}{\partial t} + c\rho w\frac{\partial T}{\partial z} = q''_{cl,c}\frac{2\pi r_{cl,o}}{A_c} + q_c''', \tag{1.2}$$

where c [J·kg^{-1}·K^{-1}], ρ [kg·m^{-3}] and w [m·s^{-1}] represent the coolant specific heat, density and velocity, respectively, T [K] the temperature, $q''_{cl,c}$ [W·m^{-2}] the heat flux from the cladding to the coolant, A_c [m^2] the channel cross-sectional area, and q_c''' [W·m^{-3}] the local power density in the coolant. The boundary condition is of convective type:

$$q''_{cl,c} = -\lambda\left.\frac{\partial T}{\partial r}\right|_{r=r_{cl,o}} = h_{cl,c}\left[T(r=r_{cl,o}) - T_c\right], \tag{1.3}$$

where λ [W·m^{-1}·K^{-1}] is the thermal conductivity, $h_{cl,c}$ [W·m^{-2}·K^{-1}] the heat transfer coefficient between cladding and coolant, and T_c [K] the (bulk) coolant temperature. For steady-state conditions,

$$c\rho w\frac{dT}{dz} = \frac{q'}{A_c} + q_c''', \tag{1.4}$$

the heat flux from the cladding to the coolant is known and is given by

$$q''_{cl,c} = \frac{q'}{2\pi\, r_{cl,o}}. \tag{1.5}$$

The coolant mass flow rate, inlet temperature and pressure are prescribed.
The second objective of the heat transfer calculation in the coolant is the derivation of the radial temperature drop between the coolant and the cladding, $T_{cl,o}$–T_c, resulting from convection:

$$q'' = h_{film}\left(T_{cl,o} - T_c\right) = \frac{q'''_c}{2\pi\, r_{cl,o}}, \tag{1.6}$$

where h_{film} [W·m^{-2}·K^{-1}] is the heat transfer coefficient in the cladding-coolant convection film, and $T_{cl,o}$ [K] the outer cladding temperature. The heat transfer coefficient in the film depends on the type of convection (forced or natural) and the type of coolant (gas, liquid, liquid metal). In the subcooled regime of a PWR, the Dittus–Boelter correlation is largely applied for calculating h_{film}, whereas in the saturated regime of a BWR the Jens–Lottes correlation is used.

1.2.2 Heat transport in the cladding

The heat transport in the cladding occurs through conduction:

$$\frac{1}{r}\frac{\partial}{\partial r}\left(r\lambda\frac{\partial T}{\partial r}\right) + q'''_{cl} = 0, \tag{1.7}$$

where q'''_{cl} [W·m^{-3}] is the heat generation in the cladding (gamma-heating, as well as the exothermic cladding oxidation process). In order to allow for the presence of an outside oxide layer, the total equivalent cladding conductivity can be obtained by applying the formula for serial thermal resistances.

1.2.3 Heat transport from the cladding to the fuel

The temperature drop in the fuel-cladding gap, ΔT_{gap} [K], is calculated as (Lassmann and Hohlefeld, 1987)

$$\Delta T_{gap} = \frac{q''}{h_{gap}}, \tag{1.8}$$

where q'' [W·m^{-2}] is the heat flux and h_{gap} [W·m^{-2}·K^{-1}] the heat transfer coefficient between the fuel and the cladding (gap conductance). The heat transfer by convection can be neglected. In general, h_{gap} depends on

- Gap width or contact pressure between the fuel and the cladding.
- Gas pressure and composition.
- Surface characteristics of the cladding and the fuel.

The gap conductance may be therefore calculated as resulting from three parallel conduction routes:

$$h_{gap} = h_{rad} + h_{con} + h_{gas}\,. \tag{1.9}$$

The radiative component is given by

$$h_{rad} = \left(\frac{C_{SB}}{1/e_f + 1/e_{cl} - 1} \right) \frac{T_{f,o}^4 - T_{cl,i}^4}{T_{f,o} - T_{cl,i}}, \tag{1.10}$$

where C_{SB} [W·m^{-2}·K^{-4}] is the Stefan-Boltzmann constant, e_f|e_{cl} [-] the fuel|cladding emissivity, $T_{f,o}$ [K] the temperature at the outer surface of the fuel, and $T_{cl,i}$ [K] the temperature at the inner surface of the cladding. The component h_{con} reproduces the improvement in heat transfer due to fuel-cladding contact pressure, and is given by

$$h_{con} = \varsigma_1 \overline{\lambda}_{fc} \overline{\Delta R} \left(\frac{p_{con}}{\overline{\Delta R}^2 H} \right)^{\varsigma_2}, \tag{1.11}$$

where $\overline{\lambda}_{fc}$ [W·m^{-1}·K^{-1}] is the mean fuel-cladding thermal conductivity, $\overline{\Delta R}$ [m] the mean value of the arithmetic mean roughness, p_{con} [Pa] the contact pressure, H [Pa] the Meyer hardness of the softer material, and ς_1 and ς_2 are model parameters. The heat transfer by conduction in the plenum gas mixture is often evaluated based on the model of Ross and Stoute (1962),

$$h_{gas} = \frac{\lambda_{gas}}{\overline{\Delta R} + d_{gap} + l_{gas}}, \tag{1.12}$$

where d_{gap} [m] is the radial gap width. The thermal conductivity of a multi-component gas is only composition-dependent and may be calculated as

$$\lambda_{gas} = \sum_{\substack{k=1 \\ j \neq k}}^{n} \left[\lambda_j \Big/ \left(1 + \sum_{\substack{k=1 \\ j \neq k}}^{n} \phi_{jk} \frac{\xi_k}{\xi_j} \right) \right], \tag{1.13}$$

with λ [W·m^{-1}·K^{-1}], ξ [mol·m^{-3}] and ϕ [-] being thermal conductivities, molar concentrations and weighting factors, respectively. The gas extrapolation length (sometimes called temperature jump distance), l_{gas} [m], allows for the imperfect heat transport across the solid–gas interface, which is material and gas pressure-dependent. Detailed formulations are discussed in (Lassmann and Hohlefeld, 1987).

As a result of fission gas release from the fuel pellets, the thermal conductivity of the plenum gas changes. In fact, the released fission gases (xenon, krypton) have a much lower thermal

conductivity than the helium-filling gas. For example, the thermal conductivity decreases by about a factor of 2 when the FGR reaches about 27% (Van Uffelen et al., 2010). At the same time, the pressure in the free volume of the fuel rod increases. This latter effect on the thermal conductivity is, however, small and can be neglected on the basis of the known data for helium (Tsederberg et al., 1971).
It is important to note that, despite detailed formulations for the gap conductance, the gap width, d_{gap}, is unavoidably affected by uncertainties, both pertaining to the input data and the mechanical analysis (e.g., pellet cracking and swelling, see Section 1.3).

1.2.4 Heat transport in the fuel

The heat produced by the slowing down of the fission fragments in the fuel pellets is removed through conduction in the pellets:

$$c\rho\frac{\partial T}{\partial t}=\frac{1}{r}\frac{\partial}{\partial r}\left(\lambda r\frac{\partial T}{\partial r}\right)+q''' . \tag{1.14}$$

The boundary conditions are:

Inner boundary: $\dfrac{\partial T(r=r_{f,i})}{\partial r}=0$ (radial symmetry)

Outer boundary: $\Delta T_{gap}=\dfrac{q''}{h_{gap}}$ (pellet surface temperature is known)

The temperature distribution in the pellets is therefore affected by two terms: the heat source and the fuel thermal conductivity. At beginning-of-life (BOL), the heat production in LWRs is subject to a slight (typically around 10%) depression. During the irradiation of the fuel, epithermal neutrons are captured preferentially near to the surface of the fuel by ^{238}U. This leads to an enrichment of ^{239}Pu at the outer periphery of the fuel. At end-of-life (EOL), the power density distribution is a steep function of the radius. This effect needs therefore to be considered and a specific model for the radial power density like TUBRNP (Lassmann et al., 2011) is a prerequisite for temperature analyses at high burn-up.
The thermal conductivity of the fuel depends on many parameters, including the temperature, the density (porosity), the stoichiometry, impurities, and burn-up. A review of the thermal conductivity (as well as of the other properties) of different fuel materials is given in (Van Uffelen et al., 2010).

1.2.5 The structure of the thermal analysis

The structure of the thermal analysis in a fuel performance code can be summarized as follows. The thermal conductivity, density, and specific heat are organized in a materials database, whereas the power density, q''', the gap conductance, h_{gap}, and the convective heat transfer coefficient between cladding and coolant, h_{film}, are formulated in a model. The heat conduction

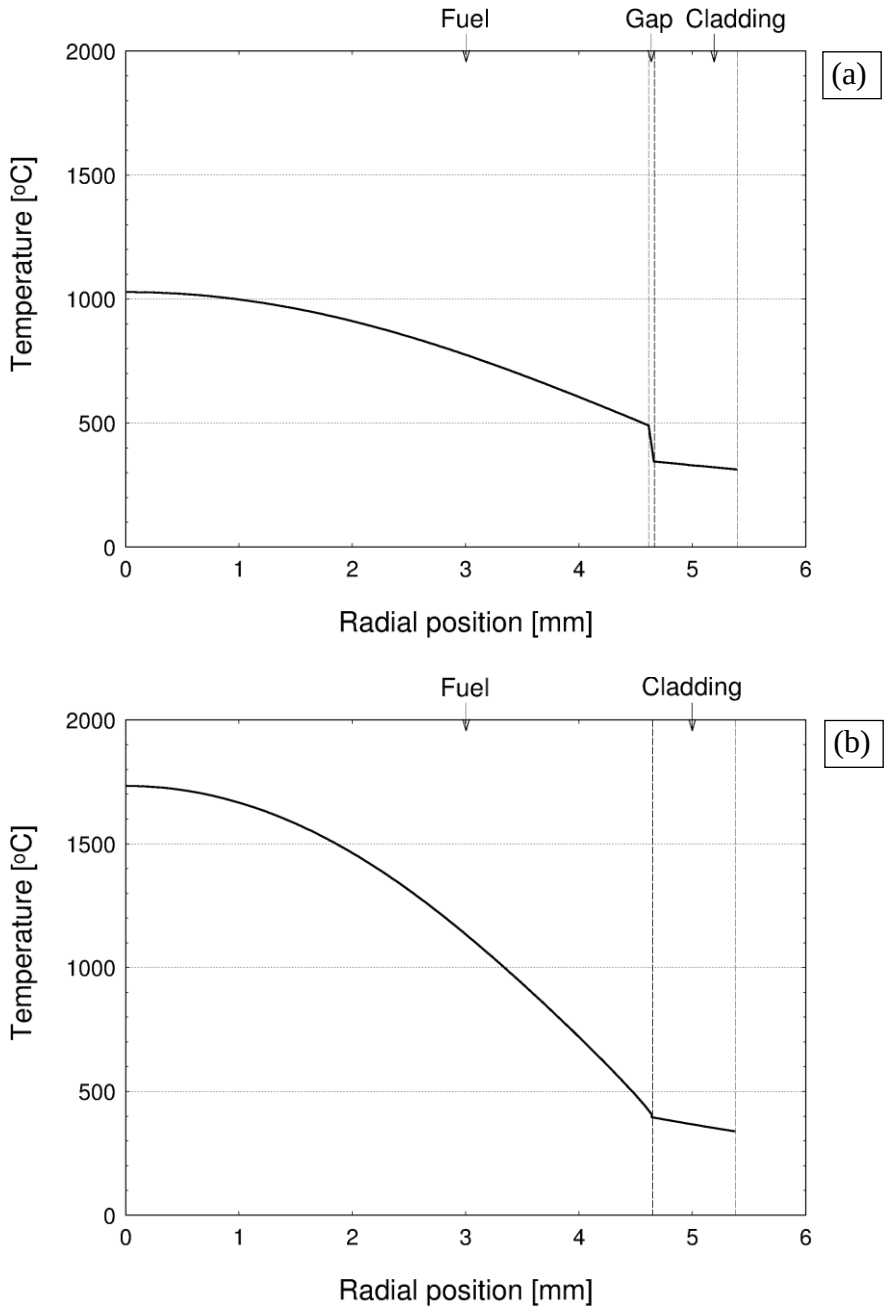

Fig 1.5. Radial temperature distribution at the mid-plane of a PWR rod (PK1-1 rod, Super-Ramp Project) calculated by means of the TRANSURANUS code. (a) BOL, q' = 22.8 kW·m^{-1}, (b) power ramp top, q' = 41.5 kW·m^{-1}.

equation in the pellets and the convection problem in the coolant are solved by a numerical algorithm. For example, the TRANSURANUS code makes use of the Newton-Raphson technique for solving the non-linear heat conduction problem (Lassmann, 1987).

The temperature distribution in a PWR rod calculated by means of the TRANSURANUS code is shown in Fig. 1.5. The figure refers to the analysis of a case from the Super-Ramp Project (Djurle, 1984), which comprehends ramp tests of LWR fuel rods after base-irradiation to moderate burn-ups. In particular, the PK1-1 rod is considered, which experienced a burn-up of about 35.4 GWd·(tM)$^{-1}$ during the base-irradiation (for details, see Chapter 5).

1.3 Mechanical analysis

The mechanical analysis consists of the calculation of stresses, strains and the corresponding displacements. Given the close coupling between the thermal and the mechanical analyses, they should be in principle performed simultaneously. In practice, however, all fuel performance codes solve them separately but provide coupling through an iterative scheme. This important numerical aspect will not be dealt with here. A general discussion on this issue is found in (Lassmann, 1980; Lassmann and Hohlefeld, 1987, Lassmann, 1992). The following sub-sections summarize how stresses and strains are calculated in both the ceramic pellets and the metallic cladding, while underlining the main assumptions and limitations[3].

1.3.1 Basic assumptions and equations

A cylindrical co-ordinate system is considered. The basic assumptions generally made in the fuel rod analysis codes are the following:

(1) The system is axisymmetric, i.e., variables do not vary along the circumferential co-ordinate.

(2) The axial strain is constant across the radius (plane strain condition).

(3) Dynamic forces are in general not treated, and the time dependence inherent in the analysis (creep) is handled incrementally.

(4) The small displacement theory is adopted.

(5) The elastic constants are isotropic and constant within the considered cylindrical ring.

(6) The total strain can be written as the sum of elastic and non-elastic components.

The first two assumptions reduce the problem to one dimension. The third and fourth assumptions indicate that the stresses are related through a local equilibrium condition for the radial force in the following form:

$$\frac{\partial \sigma_r}{\partial R} = \frac{\sigma_\theta - \sigma_r}{R}, \tag{1.15}$$

where σ_r and σ_θ represent the radial and circumferential stress, respectively, and R is the radial co-ordinate in the deformed geometry. Since the fuel stack and the cladding are treated as a continuous, uncracked medium, no discontinuities are allowed in the displacements. This is translated by the compatibility relations for the strains,

$$\begin{aligned} \varepsilon_r &= \frac{du}{dR} \\ \varepsilon_\theta &= \frac{u}{R} \\ \varepsilon_z &= C_3 \end{aligned} \quad , \tag{1.16}$$

where u represents the radial displacement, ε_r, ε_θ and ε_z [/] are the radial, circumferential and axial strain, respectively, and C_3 [-] is a constant. Based on the fifth assumption, the constitutive equations read

$$\underline{\varepsilon}^{tot} = \underline{\varepsilon}^{el} + \sum \underline{\varepsilon}^{ex}, \tag{1.17}$$

where *tot* refers to the total, *el* to the elastic and *ex* to the non-elastic strains, and

$$\underline{\varepsilon} = \begin{Bmatrix} \varepsilon_r \\ \varepsilon_\theta \\ \varepsilon_z \end{Bmatrix} \tag{1.18}$$

The combination of Eqs. 1.15-1.18 leads to the classical *semianalytical* solution of the mechanical problem. A complete derivation of the semianalytical solution of the mechanical problem adopted in the TRANSURANUS code is given in Appendix A.

1.3.2 Calculation of the elastic strains

The elastic strains for an isotropic material are reversible and given by

$$\begin{aligned} \varepsilon_r^{el} &= \frac{1}{E}\left[\sigma_r - \nu\left(\sigma_\theta + \sigma_z\right)\right] \\ \varepsilon_\theta^{el} &= \frac{1}{E}\left[\sigma_\theta - \nu\left(\sigma_r + \sigma_z\right)\right], \\ \varepsilon_z^{el} &= \frac{1}{E}\left[\sigma_z - \nu\left(\sigma_r + \sigma_\theta\right)\right] \end{aligned} \tag{1.19}$$

where E [Pa] is the Young's modulus, and ν [-] is the Poisson's ratio.

1.3.3 Calculation of the non-elastic strains: thermal strain

The non-elastic strains consist of various contributions. First of all, temperature differences result in the thermal strain, which is assumed to be isotropic and reversible:

$$\varepsilon_i^{th} = \alpha\left(T - T_0\right) \qquad i = r, \theta, z \tag{1.20}$$

The thermal expansion coefficient, α [K^{-1}], depends on the material and the temperature. The larger thermal expansion of the fuel compared to that of the cladding explains why thermal expansion is one of the largest contributions to the gap closing in a nuclear fuel rod at BOL.

1.3.4 Calculation of the non-elastic strains: swelling

The second contribution to the non-elastic strain comes from swelling, and is also assumed to be isotropic. The swelling of the fuel may be described as the composition of four contributions:

$$\varepsilon_{fuel}^{sw} = \frac{1}{3}\left[\left(\frac{\Delta V}{V}\right)_{solid} + \left(\frac{\Delta V}{V}\right)_{gas} + \left(\frac{\Delta V}{V}\right)_{dens} + \left(\frac{\Delta V}{V}\right)_{hp}\right], \tag{1.21}$$

where $\Delta V/V$ [/] is the fractional variation in fuel volume, *sol* refers to solid fission products (FPs), *gas* to fission gas, *dens* to densification, and *hp* to hot pressing.

The first term, $(\Delta V/V)_{solid}$, is attributed to the fuel swelling due to solid FPs build-up (solid swelling), and is linearly dependent on the burn-up, fission product yield, and partial volume of the species. The solid swelling rate is of the order of 0.032% per GWd·(tM)$^{-1}$ (Olander, 1976; Spino et al., 2005) and is described in the fuel rod analysis codes as a function of the burn-up by means of empirical correlations (e.g., MATPRO, 1979; Lassmann et al., 2011).

The second term, $(\Delta V/V)_{gas}$, is attributed to the fuel swelling due to fission gas bubbles (fission gas swelling), which form as a consequence of the low solubility of the fission gases in the fuel. Theoretically speaking, evaluating the fission gas swelling requires a model describing the kinetics of fission gas bubbles, and closely related with the FGR model. In most fuel rod analysis codes, however, empirical correlations are used for the fission gas swelling as a function of the temperature and burn-up (e.g., Lassmann et al., 2011). Providing a contribution towards a physics-based modelling of the fission gas swelling and its coupling with the FGR in the fuel rod analysis codes is the main subject of the present work.

During the initial stages of the irradiation (burn-up < 10 GWd·(tM)$^{-1}$), the fuel density increases as some fabrication porosity disappears as a result of the impact of the fission fragments on the (small) pores. In general, fuel densification depends on the temperature, burn-up, fission rate as well as on a combination of the initial density, the pore size distribution, and the grain size. The ideal situation is thus to adopt a fundamental model for densification, such as those proposed by Assmann and Stehle (1978) and Suk et al. (1992). However, values for the parameters involved are not always well known. Therefore, empirical correlations are used in many codes for the fraction of the original porosity that anneals out as a function of the local burn-up, the temperature and the grain size (e.g., Jackson et al., 1989), or as a function of the burn-up only (e.g., Lassmann et al., 2011).

Under the influence of high temperatures, stress levels, and defect production rates during irradiation, a fraction of the fabrication porosity disappears. This fourth contribution to fuel swelling is referred to as hot pressing and is similar to creep.

The isotropic swelling strain in the cladding is due to void (and possibly helium bubble) formation, and is not dealt with here for brevity.

1.3.5 Calculation of the non-elastic strains: plasticity and creep

The third contribution to the non-elastic strain is visco-plastic in nature. It consists of instantaneous plastic strain when the yield stress is exceeded and of time-dependent creep. For the fuel and the cladding, a simple isotropic plastic flow model can be applied.
In a multiaxial state of stress, a method of relating the onset of plastic strain to the results of a uniaxial test is required. Furthermore, when plastic strain takes place, one needs to determine (1) how much plastic strain occurred and (2) how it is distributed among the individual components of strain. For the first requirement a so-called yield-function is needed. This may be one-dimensional such as the Von Mises criterion (Suzuki, 2000; Cunningham et al., 2001):

$$\sigma_{eff} = \frac{1}{\sqrt{2}}\left[(\sigma_r - \sigma_\theta)^2 + (\sigma_r - \sigma_z)^2 + (\sigma_\theta - \sigma_z)^2\right]^{1/2}, \tag{1.22}$$

so that yielding only occurs when the effective or equivalent (Von Mises) stress, σ_{eff} [Pa], exceeds the yield stress determined from a uniaxial tensile test. Also, the anisotropic factors according to Hill's methodology were introduced (Lassmann and Van Uffelen, 2004). Finally, a multidimensional yield surface (Garcia et al., 2002) was proposed. In order to allow for work hardening, one generally assumes that the yield stress changes with the total permanent strain. The plastic strain is therefore computed incrementally.
In order to answer the second question, each increment of effective plastic strain, ε^p_{eff} [/], is related to the individual plastic strain components, ε^p_i [/], by a flow rule:

$$\Delta\varepsilon_i^p = \Delta\varepsilon_{eff}^p \frac{\partial\sigma_{eff}}{\partial\sigma_i} \qquad i = r,\theta,z\,. \tag{1.23}$$

When using the above definition of the effective stress, Eq. 1.22, one obtains the Prandtl-Reuss flow rule:

$$\Delta\varepsilon_i^p = \frac{3\Delta\varepsilon_{eff}^p}{2\sigma_{eff}}\sigma_i^{dev} \qquad i = r,\theta,z\,, \tag{1.24}$$

indicating that the plastic strain increment is proportional to the deviatoric stress, $\sigma_i^{dev} = \sigma_i - \sigma_h$, where σ_h [Pa] is the hydrostatic stress, defined as the average normal stress:

$$\sigma_h = \frac{\sigma_r + \sigma_\theta + \sigma_z}{3}\,. \tag{1.25}$$

For the time-dependent creep one needs strain rate equations, although the total creep strain is also computed incrementally (i.e., multiplying the strain rate by the time step length). For primary creep, typically an empirical expression is applied:

$$\dot{\varepsilon}^{c}_{eff} = \chi_1 (\sigma_{eff})^{\chi_2} t^{\chi_3}, \tag{1.26}$$

where $\dot{\varepsilon}^{c}_{eff}$ [/] is the effective creep strain rate, and χ_1, χ_2 χ_3 are constants.

For the secondary or steady-state creep, there are three parallel processes. The vacancy diffusion or Nabarro–Herring creep and the dislocation climb are dominating at high temperature and high stresses, respectively:

$$\dot{\varepsilon}^{c}_{eff} = \frac{\chi_4 \, q''' \sigma_{eff}}{r_{gr}^2} exp\left(-\frac{E_d}{kT}\right), \qquad \text{vacancy diffusion} \tag{1.27}$$

$$\dot{\varepsilon}^{c}_{eff} = \chi_5 \, q''' \sigma_{eff}^{4.5} exp\left(-\frac{E'_d}{kT}\right), \qquad \text{dislocation climb} \tag{1.28}$$

where r_{gr} [m] is the grain radius, E_d and E'_d [J] are activation energies, and χ_4, χ_5 are constants. The third process is irradiation-induced creep, dominating at low temperatures and assumed to be proportional to the effective stress and the local fission rate density or power density.

1.3.6 Calculation of the non-elastic strains: pellet-fragment relocation

The fourth and last non-elastic strain component stems from the relocation of the pellet fragments following pellet cracking. Pellet cracking already occurs at reactor start-up due to the differential thermal expansion since the hot pellet centre expands more than the cold periphery. In order to assess the linear heat rate at which cracking in a cylindrical pellet occurs, the maximum thermal stress, σ^{th}_{max} [Pa], in an uncracked pellet submitted to a parabolic temperature gradient,

$$\sigma^{th}_{max} = -\frac{\alpha E q'}{8\pi(1-\nu)\lambda}, \tag{1.29}$$

must be compared with the (uniaxial) fracture stress, which is approximately 130 MPa for UO_2. When using the Young's modulus E = 200 GPa, the Poisson's ratio ν = 0.31, the thermal diffusivity $\alpha = 10^{-5}$ K^{-1}, and an average thermal conductivity $\overline{\lambda}$ = 3 $W \cdot m^{-1} \cdot K^{-1}$, radial cracks are predicted to be initiated in the pellet periphery at a linear heat rate, q', of the order of 5 $kW \cdot m^{-1}$. The number of cracks is dependent on the linear hear rate. Oguma (1983) proposed a linear model for the number of radial cracks that is illustrated in Fig. 1.6. In addition to radial cracks, also axial and (especially under power ramp conditions) circumferential cracks are formed (Fig. 1.7). Owing to the larger thermal expansion of the pellet fragments in comparison with that of a monolithic cylinder and due to vibration-induced motion, the fragments move outward (relocation).

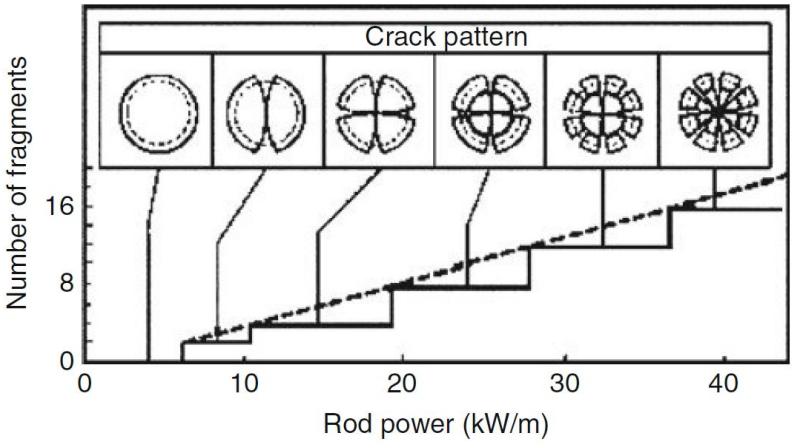

Fig. 1.6. Calculated crack pattern from thermoelastic stress (Oguma, 1983).

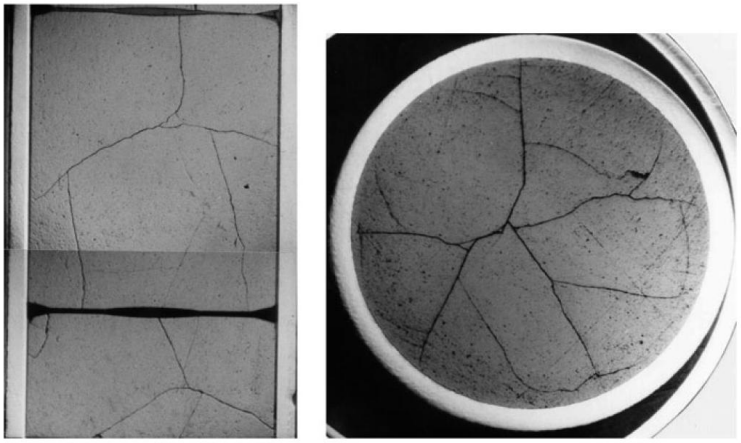

Fig. 1.7. Illustration of cracks in axial (left) and horizontal (right) cross sections of irradiated fuel pellets – from (Van Uffelen et al., 2010).

Pellet-fragment relocation has a remarkable impact on the thermal behaviour of the fuel rod, as shown in Fig. 1.8. It reduces the fuel-cladding gap size, thereby reducing the temperature levels in the fuel at beginning-of-life. This constitutes the largest contribution to the gap closing (approximately 30–50%, depending on q') but is also the one that is subject to the largest uncertainty, because of the stochastic nature of the cracking process. The contribution from pellet-fragment relocation is generally accounted for in the circumferential strain component as a (linear) function of the linear heat rate.

The effect of pellet-fragment relocation on the mechanical behaviour is also of primary importance since it reduces the overall stress in the pellets and may even change the sign of the stress in central part of the pellet from compression (in a cylinder) to traction (in fragments) (Van Uffelen et al., 2010). To allow for the cracks exactly would require the exact location and size of every crack and to solve a three-dimensional stress-strain problem in each block.

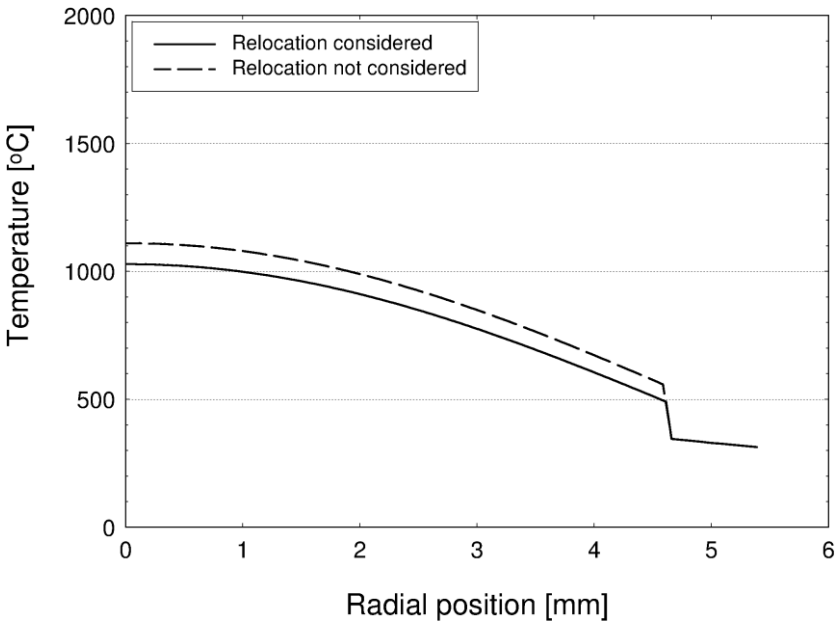

Fig. 1.8. Radial temperature distribution at the mid-plane of a PWR rod (PK1-1 rod, Super-Ramp Project) at BOL, calculated by means of the TRANSURANUS code. The comparison is presented between the calculations with (full line) and without (dashed line) taking pellet-fragment relocation into account.

Instead, either the material constants (Suzuki, 2000; Lassmann et al., 2011) or the constitutive equations are modified. An example of the former approach is that of Jankus and Weeks (1972), who proposed a reduction of the elastic constants:

$$E' = \left(\frac{2}{3}\right)^{N_{cr}} E\,, \tag{1.30}$$

$$\nu' = \left(\frac{1}{2}\right)^{N_{cr}} \nu\,, \tag{1.31}$$

where E' is the Young's modulus in presence of cracks, ν' the Poisson's ratio in presence of cracks, and N_{cr} the number of cracks. This means that an equivalent continuous and homogeneous solid body with directionally dependent (anisotropic) properties is considered. As the fuel-cladding gap closes during irradiation, the contact pressure can press the fragments inward, thereby reducing the relocated radius to a minimum value. Some codes also allow for the restoration of the elastic constants as the relocation is partially reversed (Suzuki, 2000). In order to modify the constitutive equations, a plane stress condition was proposed (Garcia et al., 2002), that is, the circumferential stress is set equal to the fill gas pressure once the radial crack appears. Both approaches, however, do not allow for crack healing.

1.3.7 Radial boundary conditions

In general, continuity of the radial stress and displacement at each radial zone is imposed, and the radial stress at the outer cladding surface is determined by the coolant pressure, p_{cool}, i.e., $\sigma_r(r_{cl,o}) = - p_{cool}$. The boundary conditions in the rod depend on the configuration. When pellet-cladding mechanical interaction is not established, the radial stress at the pellet periphery is determined by the fill gas pressure in the fuel rod, p_{gas}, i.e., $\sigma_r(r_{f,o}) = - p_{gas}$. For the boundary condition in the pellet centre, two possibilities exist. In hollow pellets, the radial stress at the pellet centre equals the fill gas pressure as well, i.e., $\sigma_r(r_{f,o}) = - p_{gas}$, whereas in the event of full cylindrical pellets the radial and circumferential stresses are equal in the pellet centre. When the fuel and cladding are in contact, the boundary condition at the pellet surface is determined by the contact pressure, i.e., $\sigma_r(r_{f,o}) = \sigma_r(r_{cl,i}) = - p_{con}$. The other radial boundary conditions remain unchanged.

1.3.8 Axial boundary conditions

The plane strain assumption entails that the axial strain is constant in the plane perpendicular to the axial axis. The axial strain is therefore determined by an axial force balance equation including the fill gas pressure, the plenum spring pressure, the fuel column weight, and the friction forces. In the case of a radial contact between fuel and cladding, both bodies may stick to each other, but some sliding may be possible in specific conditions (sticking or static vs. sliding friction). Part of the fuel rod may be "trapped", which means that rather high axial forces may act on cladding and fuel. One advantage of two-dimensional and three-dimensional finite element models is that such effects are automatically included in the analysis through the use of specific gap elements.

The stress distributions for the Super-Ramp PK1-1 rod calculated by means of the TRANSURANUS code are shown in Fig. 1.9 and Fig. 1.10 (fuel and cladding, respectively). It can be noted that high compressive hydrostatic stress (Eq. 1.25) develops at the power ramp top, when strong PCMI takes place. It is expected that high compressive hydrostatic stress due to cladding restraint during power ramps considerably affects the kinetics of both the fission gas swelling and release by compression of the grain-boundary fission gas bubbles (Kogai et al., 1988; Kashibe and Une, 1997; Koo et al., 2000). On the other hand, the swelling itself plays an important role in determining the degree of PCMI and consequently the fuel stress state. The proper modelling of this complex stress-dependent behaviour of the fission gas swelling and release for application to the fuel rod analysis codes is a primary goal of the present work. It can be also noted that a considerable tensile circumferential stress takes place in the cladding following a power ramp (Fig. 1.10-b), which may lead to cladding failure due to Pellet-Cladding Interaction/Stress Corrosion Cracking (PCI/SCC) (Roberts, 1981; Frost, 1994; Bailly et al., 1999; Suzuki et al., 2004).

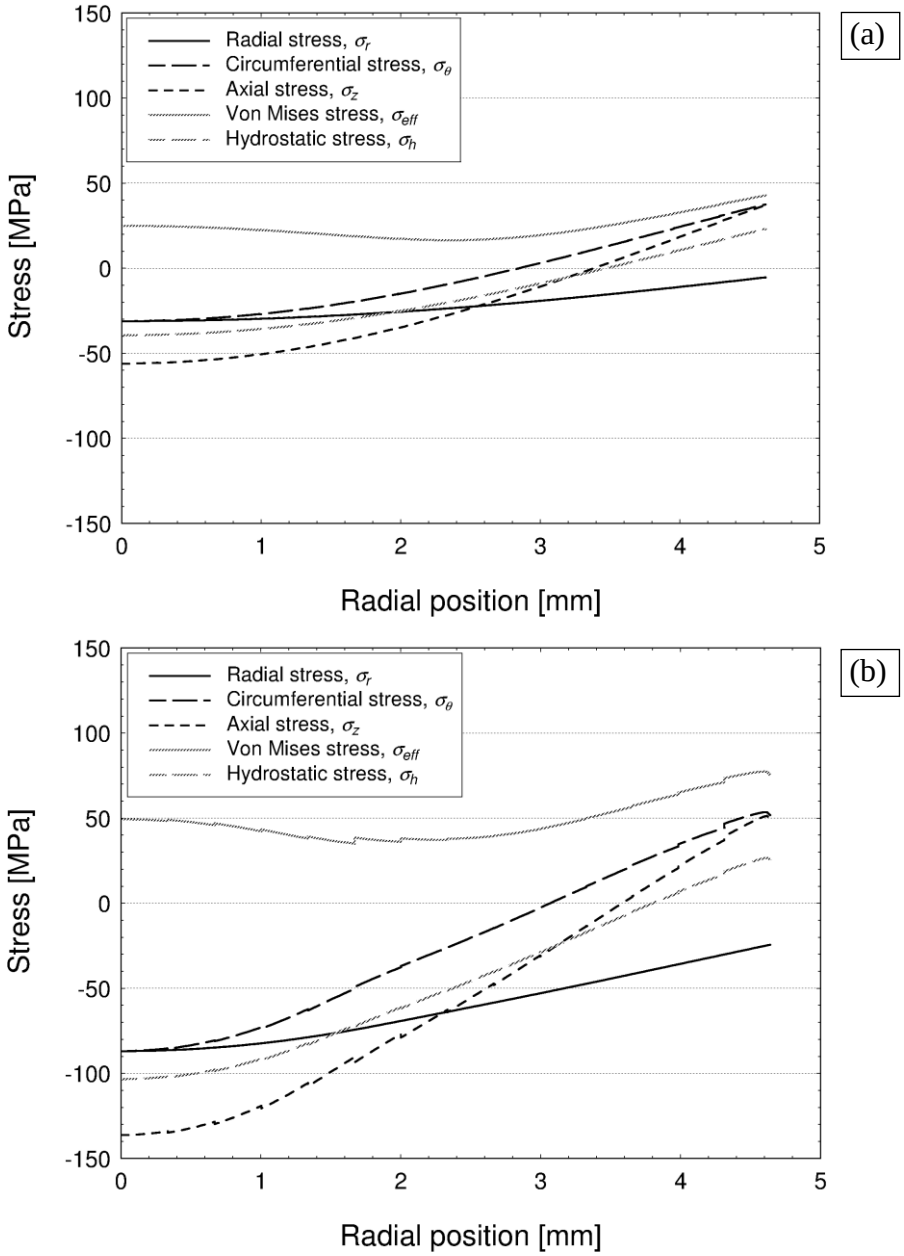

Fig 1.9. Radial stress distribution in the fuel at the mid-plane of a PWR rod (PK1-1 rod, Super-Ramp Project) calculated by means of the TRANSURANUS code. (a) BOL, $q' = 22.8$ kW·m^{-1}, (b) power ramp top, $q' = 41.5$ kW·m^{-1}.

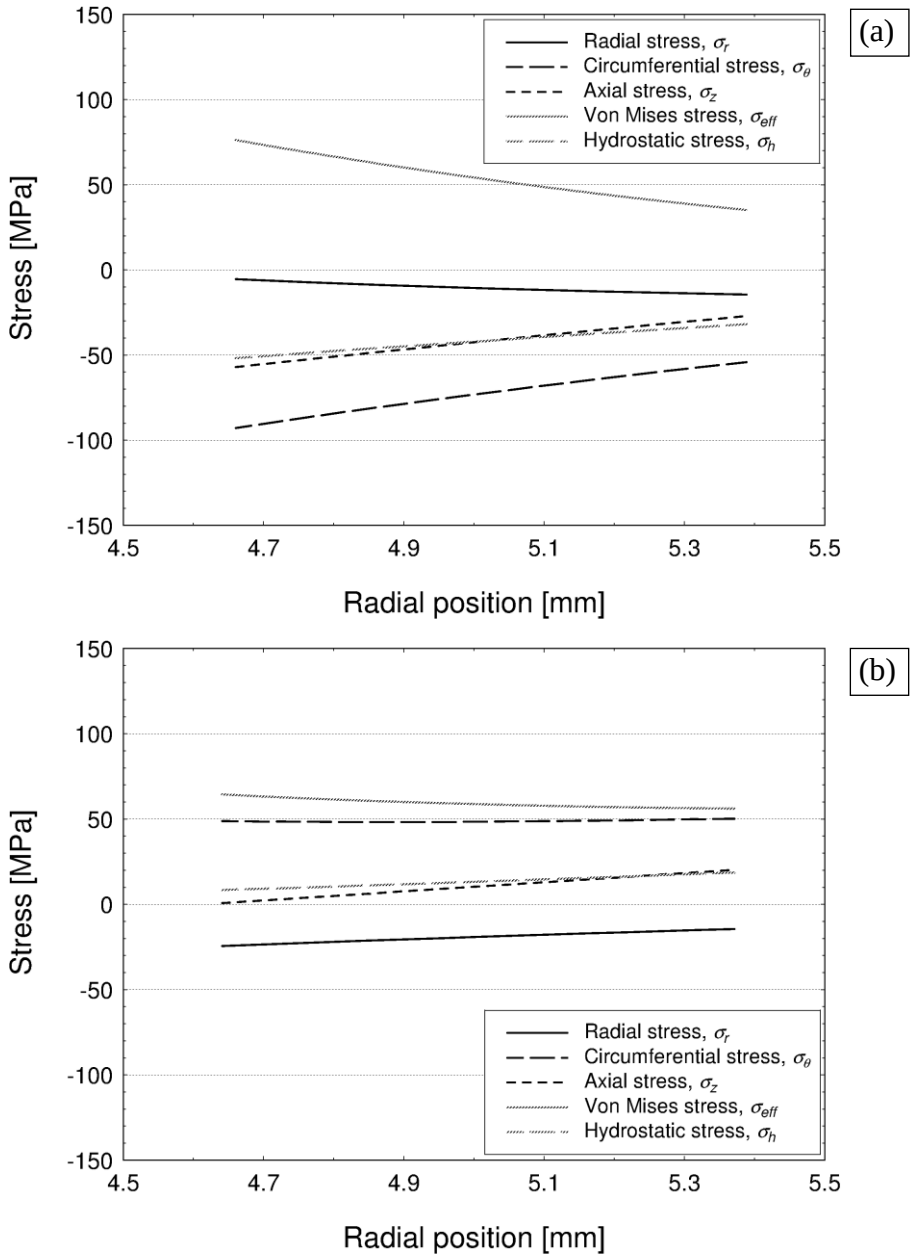

Fig 1.10. Radial stress distribution in the cladding at the mid-plane of a PWR rod (PK1-1 rod, Super-Ramp Project) calculated by means of the TRANSURANUS code. (a) BOL, $q' = 22.8$ kW·m^{-1}, (b) power ramp top, $q' = 41.5$ kW·m^{-1}.

1.4 Concluding remarks

After several decades of research on fuel rod modelling, the fuel rod analysis codes are nowadays standard tools for regulatory and safety authorities, fuel designers and researchers. In this chapter, the fundamental aspects of fuel rod computational analysis were presented. Concerning the predictive capability of the fuel rod analysis codes at the present time, the FUMEX-II co-ordinated research project of the IAEA (Killeen et al. 2007, IAEA 2011) revealed that in general under normal operating conditions:

- The temperatures can be predicted with a relative error of the order to 10%.
- The cladding elongation as well as the cladding diametrical deformation are predicted with a relative error of about 30% (although based on less data).
- the ratio of the predicted to the measured values of FGR is generally within a factor of 2, although significant room for improvement exists, especially as concerns the simulation of power ramps and PCMI conditions.

Most difficulties stem from:

- Uncertainties associated to the input values (fabrication and irradiation parameters).
- The stochastic nature of pellet cracking and its consequences on the thermal analysis (uncertainty on the gap width, especially at BOL), as well as on the mechanical analysis (validity of the compatibility and constitutive equations).
- A lack of direct measurements (e.g., stresses or parameters such as diffusion coefficients and resolution rate coefficients) or large scatter in the experimental data.
- A limited set of experimental data available in the open literature for new materials that are being introduced for reaching higher discharge burn-up (e.g., new cladding material properties).

Moreover, not many codes exhibit good mechanical modelling capabilities, and the results that were obtained were limited. In particular, fuel swelling is a difficult area for many codes (IAEA, 2011).

Models to be applied to the fuel rod analysis codes must combine an appropriate predictive capability and a level of complexity that is consistent with the stringent computational cost requirements and the uncertainties inherent in fuel rod modelling. Developing an approach to the physics-based modelling of fission gas swelling and release that allows this balance is a challenge, which is faced in the present work.

Chapter 2
Background of the work

Abstract. *The subject of the present work comprises the development and the application to the TRANSURANUS code of a new model of fission gas swelling and release in UO_2 fuel. Both the development and application aspects of the work are introduced in this chapter, by presenting the physical scope and computer framework. Then, the rationale and objectives of the work are discussed. In Section 2.1, the basic physical mechanisms involved in fission gas swelling and release are summarized. In Section 2.2, the main features of the TRANSURANUS fuel rod analysis code are overviewed. The work objectives are outlined in Section 2.3.*

2.1 Basic mechanisms of fission gas swelling and release

The processes of fission gas generation, diffusion, retention and release have a strong impact on the thermo-mechanical behaviour of the nuclear fuel rods. On the one hand, the fission gases generated in the fuel tend to precipitate into bubbles, resulting in (i) fuel swelling, which may give rise to enhanced pellet-cladding mechanical interaction (PCMI), and (ii) degradation of the fuel thermal conductivity, possibly leading to overheating of the fuel and local melting. On the other hand, fission gas release (FGR) to the free volume of the fuel rod causes pressure build-up and thermal conductivity degradation of the rod filling gas. Consequently, the fuel temperature increases, which in turn may lead to higher FGR (*thermal feedback*) until the rod fails due to cladding ballooning and cladding burst.

The effects of fission gas swelling and release as potential design-limiting factors for the nuclear fuel rods can be particularly marked at high burn-up and during power ramps (Kashibe et al., 1993; Mogensen et al., 1985). In fact, the FGR increases with increasing burn-up and following the power and temperature rise during a power ramp, possibly affecting the integrity of the cladding through increased internal pressure. Moreover, at high burn-up or during power ramps, when PCMI takes place and consequently the fuel deformation affects the deformation of the cladding, the fission gas swelling can give an important contribution to cladding strain and possibly to cladding failure (OECD/NEA, 2004). In reference to the analyses of Arimescu (2004), fission gas swelling accounted for as much as half of the permanent cladding diametral strain in PWR fuel rods subjected to power ramps to peak power levels of 39.5, 42 and 44 $kW \cdot m^{-1}$.

In view of the above implications on the thermo-mechanical behaviour of the fuel rods, the treatment of the fission gas swelling and release needs to be covered in fuel rod modelling. The basic mechanisms involved in fission gas swelling and release in UO_2 fuel during irradiation,

which represent the physical scope of the present work, are summarized briefly in the following sub-sections[3].

2.1.1 Fission gas generation

The yield of the fission products from thermal fission of ^{235}U according to the mass number (A) is reported in Fig. 2.1. The stable xenon (A=131-136) and krypton (A=83-86) isotopes, generally referred to as fission gases, are close to the peaks in the distribution and consequently comprise a significant proportion of the fission products. On average, each fission event produces about 0.3 atoms of Xe and Kr. Due to their extremely low solubility, the fission gases tend either to precipitate into bubbles or to be released from the fuel.

2.1.2 Recoil and knockout

In general, a fission event entails (among others) two fission fragments that transfer their kinetic energy to the fuel lattice. A fission fragment, close enough to a free surface (< 6-7 μm), can escape from the fuel due to its high kinetic energy (60-100 MeV). This is called recoil release. When fission fragments make elastic collisions with the nuclei of lattice atoms, a collision cascade appears. The interaction of a fission fragment, a collision cascade, or a fission track with a stationary gas atom near the surface can also cause the latter to be ejected if it happens within a distance close enough to the surface. This process is called release by knockout. Recoil and knockout can only be observed at temperatures below 1000°C, when thermally activated processes (see the following sub-sections) do not dominate. They are almost temperature-independent and therefore called athermal release mechanisms. Recoil and knockout generally contribute less than 1% to the release of the generated gas (Wise, 1985; Lewis, 1987).

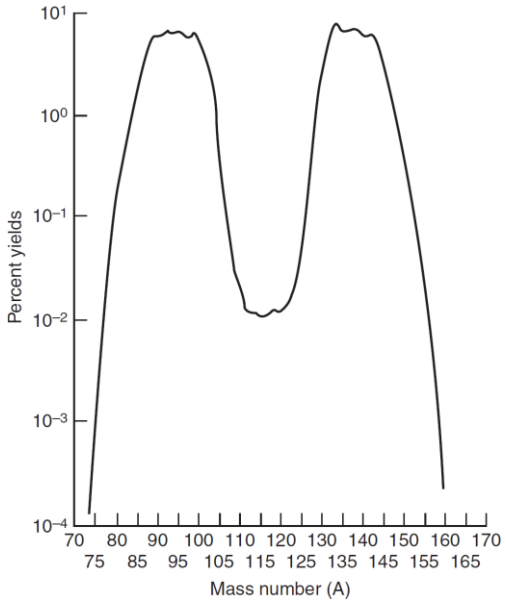

Fig. 2.1. Yield of fission products from thermal fission of ^{235}U according to mass number.

2.1.3 Intra-granular diffusion

The first step for significant release from the fuel is fission gas transport from within the grains to the grain boundaries by intra-granular diffusion of gas atoms through the crystal lattice. Mechanisms for the transport of single Xe and Kr atoms through the fuel were studied by Grimes and Catlow (1991) by considering low-energy migration pathways between solution sites as well as the stability of gas atoms at the solution sites within a defective UO_2 lattice. They postulated a cation vacancy-controlled migration pathway for Xe atoms, for which the mechanism of diffusion involves the association of a cation vacancy to the trap sites. Uranium vacancies as the slower moving species are rate-controlling for most diffusion-related processes in UO_2.

Despite the considerable effort in determining the lattice diffusion coefficient of fission gases in UO_2 (e.g., Matzke, 1980; Turnbull et al., 1982, 1988; Govers et al., 2008), strong variation still exists in the available data. The lattice diffusion coefficient is influenced by the temperature, deviations from stoichiometry and additives (e.g., Cr, Nb), phase changes and therefore also indirectly by the burn-up. Also the fission fragments are supposed to contribute to the diffusion process, which is referred to as irradiation-enhanced diffusion. This is due to the interaction of the fission fragments and the associated irradiation damage cascades with the fission gas atoms in the lattice, resulting in displacement of the gas atoms. Indeed, there is a constant process of slowing down of fission fragments in the fuel causing fission spikes or tracks to be formed. The fission tracks have a length in the order of 6-7 microns, wherein about 15000 Frenkel pairs are produced instantaneously (Matzke, 1980). Only 5000 pairs remain after direct annihilation. The width of the permanently disturbed zone is of approximately 7 nm. Significant temperature increases along the axis occur causing large stress gradients leading, for instance, to a separation of vacancies from interstitials and hence a largely temperature-independent, irradiation-enhanced diffusion, as well as irradiation-induced resolution of inert gas atoms from intra-granular bubbles or even complete bubble destruction. Irradiation-induced diffusion dominates at temperatures below 1000°C, indicatively, and is temperature-independent. For temperatures between 1000°C and 1400°C, vacancies controlling the gas atom diffusion are generally assumed to be created both thermally and by the damage cascades related to fission fragments. Above 1400°C, purely thermal (intrinsic) diffusion is considered, that is, diffusion by thermally created vacancies predominates. These three temperature regimes are reflected in the three components of the single gas atom diffusion coefficient proposed by Turnbull et al. (1982, 1988) and often applied in the fuel rod analysis codes (for details, see Section 3.2).

2.1.4 Trapping

In nuclear fuels, either natural (e.g., impurities, dislocation lines, and closed pores) or irradiation-induced imperfections in the solid (e.g., intra-granular fission gas bubbles, vacancy clusters in fission tracks, and solid fission product precipitates) depress the amount of fission gas available for diffusion by temporarily or permanently trapping the migrating atoms.

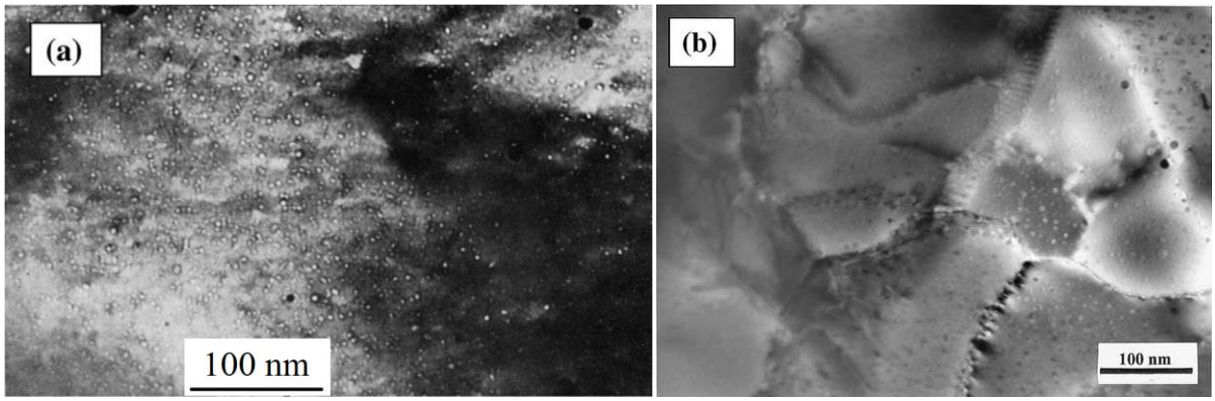

Fig. 2.2. TEM images of intra-granular gas bubbles – from (Olander and Wongsawaeng, 2006).

Experiments show that for burn-ups characteristic of power reactors, gas atom trapping due to intra-granular fission gas bubbles is predominant. Transmission electron microscopy (TEM) images of intra-granular bubbles in irradiated UO_2 are shown in Fig. 2.2. Experimental observations reveal a population of nanometre-size bubbles within the grains that stabilizes early during irradiation to a bubble size of a few nanometres and bubble densities of ~10^{23}-10^{24} (bub.)·m^{-3} (Cornell et al., 1969; Cornell, 1971; Baker, 1977a, 1977b). The fission gas swelling induced by intra-granular bubbles is generally less important than the swelling due to grain-boundary bubbles, at least for burn-ups below about 45 GWd·$(tM)^{-1}$ (White and Tucker, 1983; Mogensen et al., 1985; Kashibe et al., 1993).

2.1.5 Irradiation-induced resolution

A fraction of the gas atoms trapped into the intra-granular bubbles can be re-dissolved in the lattice through the interaction of the fission fragments with the bubbles. Irradiation-induced resolution of fission gas atoms from bubbles takes place by one of two mechanisms (Olander and Wongsawaeng, 2006). The heterogeneous mechanism occurs by complete destruction of small bubbles by fission fragments passing through or nearby them. The homogeneous mechanism occurs by removal of single fission gas atoms by scattering collisions with fission fragments or uranium recoils whose paths intersect the bubbles. The irradiation-induced resolution process favours intra-granular diffusion of fission gas by countering the effect of trapping into intra-granular bubbles. For (larger) grain-boundary bubbles, irradiation-induced resolution is supposed to be less effective (Rest, 2003; Spino et al., 2005).

2.1.6 Intra-granular bubble motion

The motion of intra-granular bubbles provides an additional mechanism with respect to single gas atom diffusion in order to describe fission gas transport to the grain boundaries. Bubble motion was experimentally observed in UO_2 during post-irradiation annealing experiments (Gulden, 1967; Baker, 1977b), and may significantly contribute to the gas transport to the grain boundaries during power transients and at high temperature (Matthews and Wood, 1979).

It is known that diffusion models commonly adopted in the fuel rod analysis codes and based on single gas atom diffusion have a tendency to under-predict the rate of gas transport to the grain boundaries during irradiation at high temperature (Lassmann and Benk, 2000). This tendency may be ascribed to the neglected contribution of bubble motion to gas diffusion. An approach to the modelling of intra-granular gas diffusion, including an estimation of the effect of bubble motion, is presented in Appendix B.

2.1.7 Grain growth

Grain growth is observed in LWR fuel under irradiation, that is, large grains grow at the expense of smaller ones. Grain growth affects fission gas release in two ways. Firstly, due to the low solubility of the fission gas, the moving grain boundary does not redeposit any gas in the newly formed crystal behind, thus acting as a filter and contributing to the collection of gas at the grain boundaries (*grain boundary sweeping*). Secondly, the average diffusion distance for the fission gas increases as the grain grows, thus tending to reduce the rate of gas transport to the grain boundaries.

2.1.8 Grain-boundary diffusion

It is generally accepted that diffusion in crystalline solids proceeds more rapidly along grain boundaries than through the lattice. This is due to the atomic jump frequency in these planar defects, which is about a million times greater than the jump frequency of regular lattice atoms in stoichiometric materials at 0.6 times the absolute melting temperature (Van Uffelen et al., 2010). Nevertheless, release of fission gas from irradiated UO_2 is mainly assisted by growth and eventual inter-connection of grain-boundary bubbles (Sub-section 2.1.9). Hence, grain boundary diffusion is only considered to contribute to the inflow of fission gas atoms in the grain-boundary bubbles, rather than to the long-range transport along grain boundaries to the fuel exterior (Olander and Van Uffelen, 2001).

2.1.9 Grain-boundary bubble development

The kinetics of both the fission gas swelling and release is determined by the development of the grain-boundary bubbles. Observations of lightly irradiated fuel reveal large numbers of small, discrete, lenticular bubbles on the grain boundaries. As irradiation proceeds, the size of the bubbles increases due to the inflow of gas atoms and vacancies, and their number density decreases as a consequence of coalescence. The (μm-size) grain-boundary bubbles act to retain the fission gases on the grain boundaries, thereby contributing to swelling (grain-boundary swelling). At high exposures and temperatures, the growing bubbles inter-connect leading to the formation of continuous pathways (tunnel network), through which the gas can be released to the fuel rod free volume. The release of gas from the fuel assisted by inter-connection of grain-boundary bubbles is sometimes called thermal FGR (and referred to simply as FGR in this thesis).

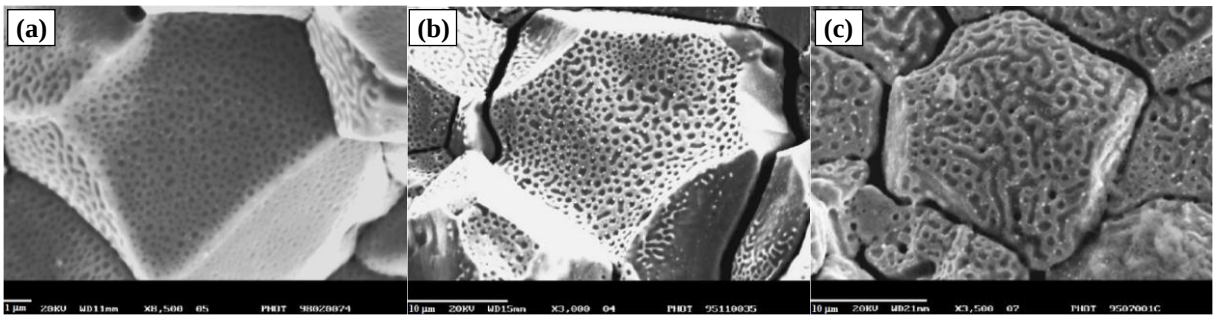

Fig. 2.3. SEM images of grain-boundary gas bubbles in UO_2 fuel at different irradiation times and conditions. (a) Early stage of bubble development, (b) intermediate stage of bubble development, (c) advanced bubble development – from (White, 2004).

The compressive hydrostatic stress in the fuel was proven to significantly affect both the fission gas swelling and release by inhibiting the growth of the grain-boundary bubbles. This effect may be particularly marked under PCMI conditions, when high compressive hydrostatic stress may develop in the fuel due to cladding restraint (Turnbull and Tucker, 1974; Zimmermann, 1978; Kogai et al., 1988; Walker et al., 1988, Mogensen et al., 1993; Kashibe and Une, 1997). In Fig. 2.3, scanning electron microscopy (SEM) images of grain-boundary bubbles in UO_2 fuel at different irradiation times and conditions are presented. Figure 2.3-a shows an example of the very early stages of bubble development, with high bubble density and low bubble size. Figure 2.3-b shows the results of extensive bubble coalescence as an increased bubble size and a reduced bubble density. Figure 2.3-c shows an advanced stage of bubble development, involving the presence of large bubbles and a high degree of inter-connection.
As emerging from the above scenario, the grain-boundary swelling and the FGR are inherently coupled phenomena, since they both ensue from the development of the grain-boundary fission gas bubbles.

2.2 The TRANSURANUS code

The prerequisite for the application of a physical model to fuel design and licensing is the effective incorporation in a fuel rod analysis code, which provides the framework for the analysis of the overall (integral) fuel rod behaviour (Section 1.1). The TRANSURANUS fuel rod analysis code constitutes the computer framework of application of the present work. In particular, reference is made to the v1m1j11 version of the code (Lassmann et al., 2011).
Developed at the Institute for Transuranium Elements (JRC/ITU, Karlsruhe, Germany), the TRANSURANUS code is designed to perform the analysis of a whole nuclear fuel rod based on quasi two-dimensional modelling – that is, the axisymmetric behaviour of the fuel rod is described by axially coupling a stack of one-dimensional radial calculations (Section 1.1). The code is written in the FORTRAN 95 programming language (Metcalf et al., 2004), and is featured by a flexible mathematical-numerical structure into which physical models can be incorporated. The fuel rods found in the majority of power reactors can be analysed for a wide

range of different situations, as given in experiments, under normal, off-normal and accident conditions. Also, the code incorporates a comprehensive data bank for various fuel, cladding, and coolant materials. The time scale of the problems to be treated may range from milliseconds to years, thanks to the use of advanced numerical solution techniques, which are very fast and stable[4]. The TRANSURANUS code is applied for the design as well as for the licensing of the nuclear fuel, and is used by research centres, universities, industrial partners and nuclear safety authorities.
The basic equations of the thermal and mechanical analyses in the TRANSURANUS code are those presented in Sections 1.2 and 1.3, and in Appendix A. In Sub-section 2.2.1, an outline is given of the structure of the code. Details can be found in (Lassmann et al., 2011).

2.2.1 Structure of the code

According to the geometrical representation exploited by the TRANSURANUS code, the fuel rod is divided into discrete axial positions and radial zones. At every time step, the analysis is firstly carried out for each axial position, and axial coupling is subsequently performed (see also Section 1.1). Given the above approach, the structure of the problem is defined by:

- The analysis of the whole fuel rod at different times.
- The axial coupling for a specific time.
- The analysis at the single axial positions for a specific time.

The structure of the TRANSURANUS code reflects the above theoretical structure, the code being designed through the following three levels:

- The first level is the main driver of the code, in which the time integration is organised. The current time, $t_{n+1} = t_n + \Delta t$, is determined, where t_n is the previous time and Δt is the minimum time step given by stability or accuracy criteria.
- The second level controls the axial loop over all the axial positions, i.e., the axial coupling and its convergence.
- The third level controls the analysis at the single axial positions for a specific time, i.e., at this level the thermal and mechanical analyses are performed, for which all physical models are needed.

A simplified schematization of the third level is given in Fig. 2.4, which is limited to the main TRANSURANUS subprograms for the thermal analysis, the mechanical analysis, and the calculation of the fission gas swelling and release. Distinction is made between explicit and implicit models. For an explicit model, the increment during the time step depends only on results of the previous time, t_n. This numerical technique is adequate for slowly varying physical

[4] The computational time required for the analysis of a typical LWR fuel rod irradiation history by means of the TRANSURANUS code is of the order of few minutes.

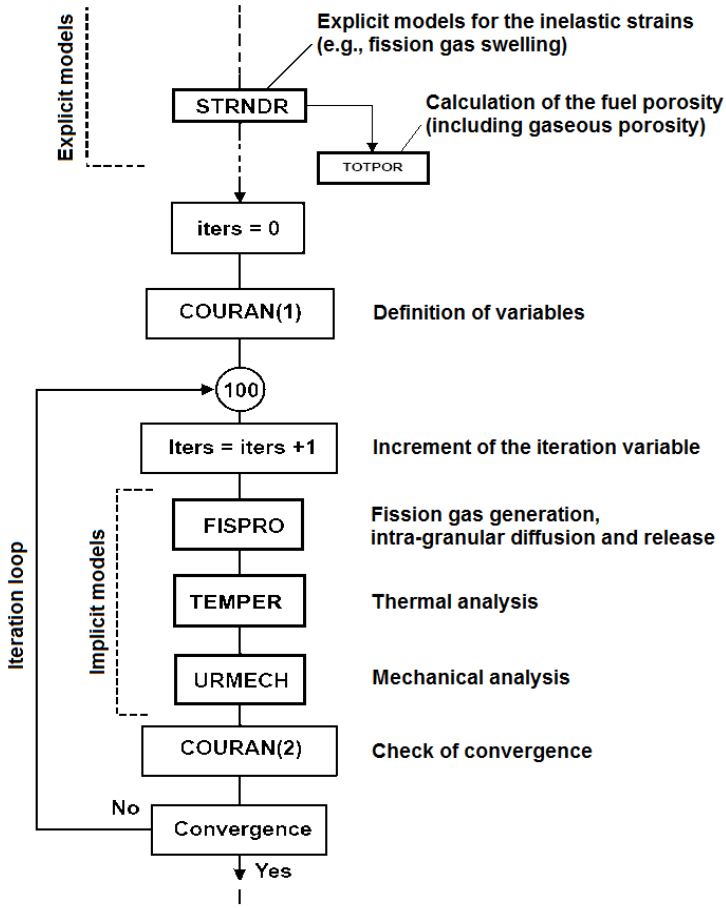

Fig. 2.4. Basic structure of the analysis at a single fuel rod axial position in the TRANSURANUS code. The scheme includes the main subprograms for the thermal analysis, the mechanical analysis, and the calculation of the fission gas swelling and release (Lassmann et al., 2011).

phenomena. For implicit (or mixed explicit-implicit) models, the increment depends on the results at the current time, t_{n+1}, and it is in almost all cases highly non linear. Special procedures for obtaining convergence (iteration schemes) are necessary.

A basic theoretical concept of the computational mechanics in the TRANSURANUS code is that all volume changes due to the various phenomena (e.g., swelling) are expressed via strains. The strains are calculated by means of physical models. Given the strains, the stresses are calculated by means of the equations of the mechanical analysis (Appendix A). This concept represents a common feature of the fuel rod analysis codes (Olander, 1976).

Numerical convergence of the whole thermo-mechanical analysis is obtained through an iteration procedure (Fig. 2.4). It is known that the volume changes related to certain phenomena (e.g., fission gas swelling) are in turn dependent on the stress. The implementation of models for these phenomena that consider the (generally non-linear) physical dependence on the stress involves difficulties concerning the numerical convergence of the fuel rod calculations.

2.2.2 Standard models of fission gas swelling and release

In the current version of the TRANSURANUS code, the fission gas swelling and release are described by two distinct models. The standard model for the swelling of UO_2 fuel (Lassmann et al., 2011) is based on the MATPRO swelling model FSWELL (MATPRO, 1979). In particular, the correlation for the volumetric fission gas swelling reads

$$\Delta\left(\frac{\Delta V}{V}\right)_{gas} = a(T)\,exp\left(-c\cdot bu\right)\Delta bu\,, \tag{2.1}$$

where $\Delta(\Delta V/V)_{gas}$ [/] is the increment of volumetric fission gas swelling during a time step, bu [at%] the burn-up, Δbu the burn-up increment during the time step, and a, c [(at%)$^{-1}$] are empirical parameters.

The condition $\Delta(\Delta V/V)_{gas} = 0$ is applied in the TRANSURANUS code when contact pressure takes place between the fuel and the cladding. That is, a total inhibition of the fission gas swelling is considered under PCMI conditions (e.g., during a power ramp or at high burn-up), when high compressive hydrostatic stress may arise in the fuel due to cladding restraint. However, this simplified approach do not allow for the significant swelling that (although partially inhibited by the compressive hydrostatic stress) can occur during a power ramp (Arimescu, 2004; Cheon et al., 2004) and at high burn-up (Spino et al., 2005).

The standard model for FGR in UO_2 fuel (Lassmann et al. 2011) basically consists of two parts:

1. Solution of the equation describing the intra-granular diffusion of the fission gas.
2. Modelling of the inter-connection condition of the grain-boundary gas bubbles.

As concerns the first part, the diffusion equation describing the time evolution of the concentration of gas generated uniformly at a rate β [(at.)·m^{-3}·s^{-1}] within a spherical grain is

$$\frac{\partial C_t}{\partial t} = D_{eff}\,\frac{1}{r^2}\frac{\partial}{\partial r}\left(r^2\,\frac{\partial C_t}{\partial r}\right) + \beta\,, \tag{2.2}$$

where C_t [(at.)·m^{-3}] is the concentration of intra-granular gas, t [s] the time, r [m] the radial co-ordinate in the spherical grain, and D_{eff} [m^2·s^{-1}] the effective diffusion coefficient of fission gas atoms in presence of intra-granular bubbles (see also Section 3.2). Efficient algorithms are implemented in the TRANSURANUS code for the numerical solution of Eq. 2.2 (Elton and Lassmann, 1987; Lassmann and Benk, 2000), allowing the rate of gas transport to the grain boundaries to be calculated. The standard TRANSURANUS option for the effective diffusion coefficient is the correlation of Matzke (1980):

$$D_{eff} = 5\cdot 10^{-8}\,exp\left(-\frac{40262}{T}\right), \tag{2.3}$$

where T [K] is the temperature.

As concerns the second part of the FGR model, the inter-connection condition of the gas bubbles at the grain boundaries is represented by a concept of grain boundary saturation. It is assumed that, when the concentration of gas at the grain boundaries, C_{gb} [(at.)·m^{-2}], exceeds a specific (empirical) threshold value, all the gas that further reaches the grain boundaries is released to the fuel rod free volume. As standard TRANSURANUS option, the threshold concentration of gas at the grain boundaries is

$$C_{gb,th} = 6.022 \cdot 10^{19} \text{ (at.)} \cdot \text{m}^{-2}. \quad (2.4)$$

In addition to the standard option, an alternative treatment is available in the TRANSURANUS code, which is specific for the simulation of power ramps. In fact, enhancement of FGR is expected during rapid power changes due to pellet micro-cracking that means new paths for the release of fission gas (burst release). To allow for this effect, a model was developed, which considers a complete release of the gas inventory at the grain boundaries when empirical conditions defining the power ramp are fulfilled (Van Uffelen et al. 2008, Lassmann et al., 2011). This burst release model is based on that of Koo et al. (1999) and provided improvements in the simulation of FGR for power ramp-tested fuel rods (Van Uffelen et al. 2008, Schubert et al., 2011).
Finally, empirical models are included in the TRANSURANUS code for taking into account the athermal release mechanisms and the grain boundary sweeping effect (Section 2.1), which are not described here for brevity. Details can be found in (Lassmann et al. 2011).

2.2.3 Previous assessments

During the preliminary stages of the present work, the predictive capability of the TRANSURANUS code was assessed, in order to identify the main issues in view of code developments (Pastore et al., 2009a, 2009b). In particular, simulations were carried out of irradiation experiments of LWR-UO_2 fuel rods, power ramp-tested after base-irradiation to moderate burn-up. The results were compared with experimental data from the International Fuel Performance Experiments (IFPE) database (Sartori et al., 2010). The capabilities of the TRANSURANUS code to analyse the fission gas behaviour (swelling and release) were investigated. From these studies, the following main conclusions were drawn:

- The predictions in terms of FGR at the end-of-life suffer from a moderate but systematic under-estimation of the experimental data.
- Introducing more sophisticated models, properly taking into account the effect of the hydrostatic stress on both the fission gas swelling and the FGR, is necessary for the purpose of properly simulating these phenomena under PCMI conditions.
- In general, incorporating in the code a physics-based model of fission gas swelling and release, taking into account the intrinsic coupling between these phenomena, is advisable.

Open issues are therefore involved in the modelling of fission gas swelling and release in the TRANSURANUS code. More in general, this area currently represents a main subject of the research on fuel rod modelling, and a primary topic of International Projects supporting the development of fuel rod analysis codes, such as the Coordinated Research Project FUMEX-III (FUel Modelling at EXtended burn-up) of the IAEA (Killeen et al., 2009).

2.3 Main objectives of the work

The present work aims at providing a contribution to the modelling of fission gas swelling and release in the fuel rod analysis codes, with specific application to the TRANSURANUS code. In particular, the goals of the work include:

1. The development of a physics-based, integrated model of fission gas swelling and release in UO_2 fuel oriented to the application to fuel rod analysis codes, which incorporates a consistent description of the dependence of both phenomena on the hydrostatic stress.
2. The demonstration of the applicability of the developed model to the fuel rod analysis codes (hence, to fuel design and licensing) by implementation in the TRANSURANUS code and meeting of the basic requirements, in terms of numerical convergence and computational times.
3. The employment in fuel rod analyses and verification of the new model through assessment of the results against irradiation data.

The achievement of the above goals requires the construction of a modelling approach, which combines an appropriate physics-based treatment and the simplicity that is a prerequisite for the effective application to the fuel rod analysis codes. The stress-dependence represents a challenging issue in view of the implementation of the new model in the TRANSURANUS code, relating to the implied necessity of numerically treating a mutual and non-linear dependence between stresses and strains (Sub-section 2.2.1). For the verification of the model, reference will be made to fuel irradiation data from the IFPE database (Sartori et al., 2010).

Chapter 3
A new model of fission gas swelling and release

Abstract. *A new model is presented for the calculation of both the fission gas swelling and release in UO_2 fuel during irradiation. The emphasis is on the modelling of the grain-boundary gas bubble development, which involves the basic issues in demonstrating the applicability of a physics-based, integrated and stress-dependent treatment of the fission gas swelling and release to the fuel rod analysis codes. The model incorporates the fundamental physical processes of gas diffusion and precipitation in grains, growth and coalescence of the grain-boundary bubbles, and gas release from the grain boundaries to the fuel rod free volume. Following an engineering approach, representations of the processes from the literature are revisited and combined in a treatment, characterized by a level of simplicity that allows effective application to the fuel rod analysis codes. The chapter is organized as follows. In Section 3.1, the general modelling approach is introduced. In Section 3.2, a simple treatment of the intra-granular gas diffusion and swelling is described, which is preliminary and being further developed (Appendix B). In Section 3.3, the treatment of the gas behaviour at the grain boundaries is discussed, which comprises the original contributions related to the model development aspect of the present work. Conclusions are drawn in Section 3.4.*

3.1 Introduction

The fundamental physical processes, which control the kinetics of fission gas swelling and release in irradiated UO_2 fuel and were discussed in some detail in Section 2.1, may be summarized as follows. Fission gas atoms generated in the fuel grains partly precipitate into intra-granular bubbles, leading to intra-granular swelling (Mogensen et al., 1985; Kashibe et al., 1993). At the same time, a fraction of the gas atoms diffuse towards the grain boundaries through repeated trapping in and irradiation-induced resolution from intra-granular bubbles (Speight, 1969; Olander, 1976; Matzke, 1980; White and Tucker, 1983; Lösönen, 2000; Olander and Wongsawaeng, 2006). Although a part of the gas atoms that reach the grain boundaries are dissolved back to the grain interior by irradiation (Manley, 1968; Van Uffelen, 2002; Rest, 2003; Kim, 2004), the majority of the grain-boundary gas precipitates and diffuses into grain-boundary bubbles acting to increase the bubble internal pressure and generally maintaining bubbles in a non-equilibrium state (White, 2004). Grain-boundary bubbles grow with inflow of gas atoms from within the grains, and with accompanying absorption of vacancies from the grain boundaries driven by the bubble over-pressure (Speight and Beere, 1975; White, 2004), thereby contributing to gas retention and swelling. Bubble growth and the associated mechanisms of bubble coalescence and inter-connection

eventually lead to the formation of a tunnel network through which a fraction of the gas reaching the grain boundaries is released to the fuel rod free volume (Turnbull, 1974; Turnbull and Tucker, 1974; Tucker and White, 1979; White and Tucker, 1983; Mogensen et al., 1985). The inherently coupled kinetics of fission gas swelling and release calls for the development of physics-based, integrated models of these phenomena to be employed in fuel rod modelling (Aybar and Ortego, 2005; Calvin and Nowak, 2010). As of today, however, empirical or semi-empirical approaches are widely adopted in the fuel rod analysis codes. The model presented in this thesis incorporates the above processes in order to evaluate the fission gas swelling and release on a physical basis. The model is kept as simple as possible in view of (i) the efficient application to the fuel rod analysis codes and the related stringent computational cost requirements (Section 1.1), (ii) the uncertainties pertaining to fuel rod analysis (Lassmann, 1980), and (iii) the uncertainties associated to some of the model parameters like the gas atom diffusion coefficient (at least a factor of 10) (White and Tucker, 1983; Matzke, 1980; White, 1994). The model is comprised of two modules, which describe the gas behaviour within the grains and at the grain boundaries, respectively. The main assumptions and equations of the model are discussed in the following sections.

3.2 Intra-granular gas behaviour

The first step in fission gas swelling and release consists of the mutually dependent processes of gas diffusion within the fuel grains (intra-granular diffusion) and development of the intra-granular bubble population (Section 2.1). Modelling of these two processes allows estimating the arrival rate of gas at the grain boundaries and the fission gas swelling induced by intra-granular bubbles (intra-granular swelling), the former providing the source term for the grain-boundary gas behaviour model. In the fuel rod analysis codes, the intra-granular gas diffusion is generally treated assuming the fuel grains to be spherical and making use of an effective diffusion coefficient allowing for the effect of the intra-granular bubbles, which was firstly introduced by Speight (1969). The calculation of the effective diffusion coefficient is often based on empirical correlations, rather than on physics-based modelling of the intra-granular bubble development. Also, the intra-granular swelling contribution is usually not distinguished from the contribution due to grain-boundary bubbles, and calculated empirically. The above approach to the modelling of the intra-granular gas behaviour is adopted, for instance, in the TRANSURANUS code (Section 2.2).

The model developed in this work includes an intra-granular module, which is intended as a first step towards the physics-based description of the intra-granular bubble development and the related effects on fission gas swelling and diffusion. The proposed treatment allows to estimate in a simple way the characteristics of the intra-granular bubbles and the related impact on the effective diffusion coefficient, as well as the intra-granular swelling. However, the basic issues in demonstrating the applicability of an integrated and stress-dependent model of fission gas swelling and release to the fuel rod analysis codes concern the modelling of the gas behaviour at the grain boundaries. It is therefore underlined that a detailed description of

the development of the intra-granular bubble population is beyond the scope of the present work, and the proposed treatment is to be considered as preliminary. Further developments are underway concerning the modelling of the intra-granular gas behaviour (Van Uffelen et al., 2011), as reported in Appendix B. The treatment of the intra-granular gas behaviour, as applied in the present work, is outlined in Sub-sections 3.2.1 and 3.2.2.

3.2.1 Intra-granular fission gas diffusion

The models for intra-granular diffusion of fission gas adopted in the fuel rod analysis codes almost invariably rely on the formulation of Speight for the problem of diffusion of gas atoms in presence of gas bubbles (Speight 1969). The formulation of Speight is based on the assumptions that (i) single gas atoms diffuse through the crystal lattice with a single atom diffusion coefficient, D_s [$m^2 \cdot s^{-1}$], (ii) gas bubbles are immobile, (iii) gas atoms are absorbed into bubbles at a rate g [s^{-1}] (trapping parameter), (iv) gas atoms are knocked back from bubbles into the lattice at a rate b [s^{-1}] (irradiation-induced resolution parameter), and (v) trapping and irradiation-induced resolution are in equilibrium (quasi-stationary approach), giving

$$\frac{C_s}{C_b} = \frac{b}{g}, \tag{3.1}$$

where C_s [(at.)$\cdot m^{-3}$] is the concentration of intra-granular gas existing as single atoms, and C_b [(at.)$\cdot m^{-3}$] is the concentration of intra-granular gas residing in bubbles. In this respect, the ratio $b/(b+g)$ may be considered as the fraction of intra-granular gas that exists as single atoms and is therefore available for diffusion.
Under the above assumptions, the intra-granular diffusion in presence of bubbles may be evaluated by solving a single diffusion equation, instead of a diffusion equation for the single gas atoms coupled with an equation for the gas balance in the bubbles. The diffusion equation reads in one-dimensional spherical geometry

$$\frac{\partial C_t}{\partial t} = D_{eff} \frac{1}{r^2} \frac{\partial}{\partial r} \left(r^2 \frac{\partial C_t}{\partial r} \right) + \beta, \tag{3.2}$$

where C_t [(at.)$\cdot m^{-3}$] is the total concentration of intra-granular gas (as single atoms + in bubbles), t [s] the time, D_{eff} [$m^2 \cdot s^{-1}$] the effective diffusion coefficient, and r [m] the radial co-ordinate in the spherical grain. The gas generation rate, β [(at.)$\cdot m^{-3} \cdot s^{-1}$], is given by $Y_{fg}F$, where Y_{fg} [(at.)$\cdot$(fiss.)$^{-1}$] is the yield of fission gas atoms and F [(fiss.)$\cdot m^{-3} \cdot s^{-1}$] the fission rate density. Eq. 3.2 is formally identical to the equation solved by Booth (1957) for the case of diffusion of single gas atoms in absence of bubbles, where the single atom diffusion coefficient is replaced by the effective diffusion coefficient (Speight, 1969)

$$D_{eff} = \frac{b}{b+g} D_s. \tag{3.3}$$

Considering the effects of trapping in and irradiation-induced resolution from intra-granular bubbles, the *apparent* diffusion rate of gas atoms under irradiation is therefore described by a lower (effective) diffusion coefficient, since only a fraction $b/(b+g)$ of the gas – namely, the fraction existing as single atoms – contributes to diffusion, while the remaining fraction $g/(b+g)$ is trapped into immobile bubbles. Adopting Eqs. 3.2 and 3.3 implies considering the parameters g, b and D_s as spatially independent within a grain (Speight, 1969; Wood and Matthews, 1980). Also, when adopting the quasi-stationary approach (Eq. 3.1), one assumes that equilibrium between trapping and resolution occurs on a shorter time scale than that of variation of the parameters g and b. This assumption is graver for rapidly changing power or temperature conditions.

The effective diffusion coefficient is often considered as a parameter in the fuel rod analysis codes (e.g., Lassmann et al., 2001). In order to obtain a more physical treatment, the effective diffusion coefficient may be calculated from the single atom diffusion coefficient, D_s, by means of Eq. 3.3. In this case, modelling is needed of the intra-granular bubble population, whose characteristics determine the magnitudes of the parameters g and b. As resulting from transmission electron microscopy (TEM) examinations of irradiated UO_2, the salient characteristics of the intra-granular bubble population are the high concentration (~10^{23}-10^{24} (bub.)·m^{-3}) and the small, nearly-uniform size of the bubbles (typically ~ 2 nm diameter). In the present work, a preliminary approach to the modelling of the intra-granular bubble development is attempted, by adopting the following simplifying assumptions:

- Intra-granular bubbles are spherical, homogeneously distributed and of equal size (Ham, 1958; Cornell, 1971; Turnbull, 1971; White and Tucker, 1983; Lösönen, 2002; Massih and Forsberg, 2008).
- The gas residing in the intra-granular bubbles is equally distributed in the bubbles.
- The number density of the intra-granular bubbles, N_{ig}, remains constant throughout irradiation at an initially nucleated level. A value $N_{ig} = 7 \cdot 10^{23}$ (bub.)·m^{-3}, typical for irradiated UO_2 (Olander and Wongsawaeng, 2006), is adopted. Considering a fixed number density of bubbles is consistent with the model of Speight (1969). Nevertheless, this assumption may be questioned, since dependence of the bubble number density on both burn-up and temperature was experimentally observed (Baker, 1977a; Mogensen et al, 1985; Kashibe et al., 1993). However, the bubble number density is approximately constant for temperatures up to about 1600°C (Cornell et al., 1969; Cornell, 1971), pertaining to LWR fuel under normal operating conditions.
- The volume occupied by each gas atom inside the intra-granular bubbles, Ω_{ig}, is constant and equal to $3 \cdot 10^{-29}$ m^3, which corresponds to a constant gas density of ~$7 \cdot 10^3$ kg·m^{-3} and is appropriate for bubble radii ranging from 0.5 to 2 nm (Olander and Wongsawaeng, 2006). The assumption of constant gas density follows from the observation that the intra-granular bubbles are small enough that the surface-tension stress keeps the gas density near that of solid xenon (Lösönen, 2000; Olander and Wongsawaeng, 2006).

Under the above assumptions, the radius of a bubble containing *m* fission gas atoms is given by

$$R_{ig} = Bm^{1/3}, \tag{3.4}$$

where $B = (3\Omega_{ig}/4\pi)^{1/3} = 2 \cdot 10^{-10}$ m. The number of fission gas atoms contained in each bubble, *m*, is calculated as

$$m = \frac{C_b}{N_{ig}}, \tag{3.5}$$

where, considering that $C_t = C_s + C_b$ and adopting the quasi-stationary approach (Eq. 3.1), C_b is given by

$$C_b = \frac{g}{g+b} C_t . \tag{3.6}$$

In order to evaluate the effective diffusion coefficient consistently with the above treatment of the intra-granular bubbles, analytical descriptions are needed of the three parameters appearing in the right-hand side of Eq. 3.3. In the present model, the three-term formulation for the single atom diffusion coefficient, D_s, proposed by Turnbull et al. (1982, 1988) and used by many authors (e.g., White and Tucker, 1983; Bernard et al., 2002; Lösönen, 2000) is adopted:

$$D_s = D_1 + D_2 + D_3, \tag{3.7}$$

where D_1 represents high temperature intrinsic diffusion by means of thermally activated vacancies, and D_2 and D_3 represent the effect of irradiation enhancement. The first two terms are calculated as

$$D_1 = 7.6 \cdot 10^{-10} \, exp\left(-\frac{4.86 \cdot 10^{-19}}{kT} \right), \tag{3.8}$$

$$D_2 = 3.22 \cdot 10^{-16} \sqrt{q_s} \, exp\left(-\frac{1.90 \cdot 10^{-19}}{kT} \right), \tag{3.9}$$

where k [J·K^{-1}] is the Boltzmann constant, T [K] the temperature, and q_s [W·g^{-1}] the specific power. The purely rating dependent term, D_3, is not taken into account, since it has no visible effect on the diffusion of stable gas atoms (White, 1994, Lösönen, 2002). Applying $q_s = 30$ W·g^{-1} produces the single atom diffusion coefficient as a function of the temperature presented in Fig. 3.1, where experimental data from Matzke (1980) and White (1994) are also shown. It can be noticed that the uncertainties related to the experimental data are extremely high, which unavoidably limits the accuracy of fission gas behaviour calculations. This may justify the adoption of simple models of fission gas swelling and release in the fuel rod analysis codes.

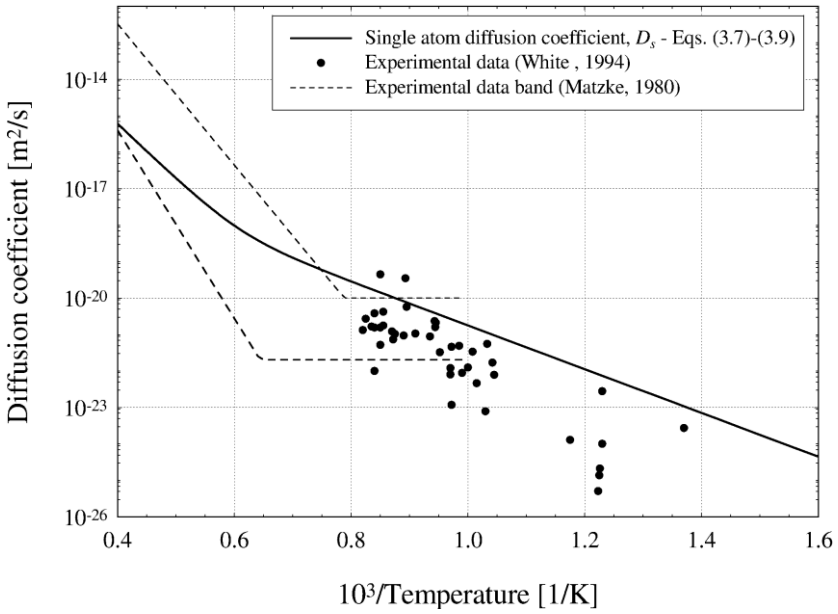

Fig. 3.1. Single atom diffusion coefficient according to Turnbull et al. (1982, 1988) (q_s = 30 W·g^{-1}) and experimental data from White (1994) and Matzke (1980).

The following expressions are adopted for the trapping and the irradiation-induced resolution parameters (Ham, 1958; White and Tucker, 1983):

$$g = 4\pi D_s R_{ig} N_{ig} , \tag{3.10}$$

$$b = 3.03 F \pi l_f \left(R_{ig} + Z_0\right)^2 , \tag{3.11}$$

where l_f [m] is the length of a fission fragment track and Z_0 [m] the radius of influence of a fission fragment track. The values l_f =6·10^{-6} m and Z_0=10^{-9} m (White and Tucker 1983) are used in the new model, while the calculation of N_b and R_b is performed as described above.

Figure 3.2 shows an analytical study of the effective diffusion coefficient, D_{eff}, as a function of the temperature, obtained by introducing Eqs. 3.7-3.11 in Eq. 3.3. Only for the purpose of this analytical study, typical LWR values are used for the specific power and fission rate density. Moreover, an empirical correlation proposed by White and Tucker (1983) and based on the experimental data of Baker (1977a) is used for the intra-granular bubble radius, which reads R_{ig} = 5·10^{-10}[1+106exp(1.2·10^{-19}/(kT))]. The study is therefore aimed at giving a qualitative account of the effect of the intra-granular bubbles on gas atom diffusion, rather than at accurately assessing the effective diffusion coefficient as calculated by the model (that depends on the specific irradiation conditions to which the model is applied). For this purpose, the single atom diffusion coefficient, D_s (Eqs. 3.7-3.9) and the fraction of gas existing as single atoms, $b/(b+g)$, are also shown. With increasing temperature, D_{eff} (full grey line) is increasingly attenuated compared to D_s. The attenuation corresponds to the decrease of

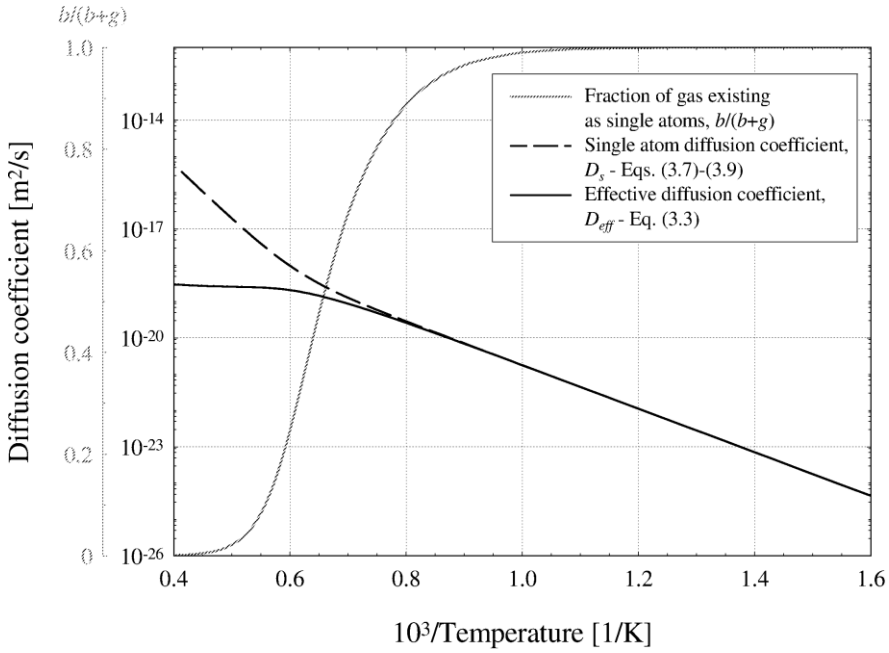

Fig. 3.2. Single atom diffusion coefficient according to Turnbull et al. (1982, 1988) compared with the effective diffusion coefficient. The calculated fraction of gas existing as single atoms is also shown. Values adopted for the parameters: q_s = 30 W·g^{-1}, $F = 10^{19}$ (fiss.)·m^{-3}·s^{-1}, $R_{ig} = 5\cdot10^{-10}[1+106\exp(1.2\cdot10^{-19}/(kT))]$ (White and Tucker, 1983).

the fraction of gas that exist as single atoms and is therefore available for diffusion, which is due to enhancement of the trapping effect with increasing temperature.

The formulation of Speight for the effective diffusion coefficient, which is adopted here, has a tendency to under-predict the rate of gas transport to the grain boundaries during irradiation at high temperature (Lassmann and Benk, 2000). Under these conditions, a considerable fraction of the intra-granular gas is trapped into bubbles (Fig. 3.2), and bubble motion (not considered in the formulation of Speight) may significantly contribute to intra-granular gas diffusion (see also Section 2.1). The model presented in Appendix B (Van Uffelen et al., 2011), which is a development of the preliminary treatment of the intra-granular gas behaviour described in this section, comprises an extension of the formulation of Speight, including an estimation of the contribution of bubble motion to fission gas diffusion.

3.2.2 Intra-granular fission gas swelling

The simple treatment of the intra-granular bubble development described in Sub-section 3.2.1 allows to estimate, in a preliminary way, the intra-granular contribution to the swelling. Under the assumptions discussed in Sub-section 3.2.1, the volumetric intra-granular fission gas swelling, normalized to the unit volume of fuel, is given by

$$\left(\frac{\Delta V}{V}\right)_{ig} = N_{ig}\left(\frac{4}{3}\pi R_{ig}^3\right). \tag{3.12}$$

3.2.3 Calculation sequence

The following calculation sequence is adopted in applying the intra-granular module at each computational time step:

(i) The trapping and irradiation-induced resolution parameters are estimated by means of Eqs. 3.10 and 3.11, using the intra-granular bubble radius calculated at the previous time step. At the first time step, an initial bubble radius R_{ig} = 0.5 nm (lower limit) is adopted (e.g., Govers et al., 2008).

(ii) The effective diffusion coefficient is calculated by means of Eq. 3.3.

(iii) The variation of the intra-granular gas concentration during the time step is calculated by numerical solution of Eq. 3.2, thus allowing calculation of both the intra-granular and grain-boundary gas concentrations at the current time step.

(iv) The concentration of intra-granular gas residing in bubbles is calculated by means of Eq. 3.6.

(v) The number of gas atoms contained in each bubble is calculated by means of Eq. 3.5.

(vi) The bubble radius is calculated by means of Eq. 3.4.

(vii) The intra-granular fission gas swelling is calculated by means of Eq. 3.12.

3.3 Grain-boundary gas behaviour

The intra-granular diffusion of fission gas determines the arrival rate of gas at the grain boundaries, thus driving the development of the grain-boundary bubble population. The development of the grain-boundary bubbles in turn determines the kinetics of both the grain-boundary contribution to the swelling and the FGR (Section 2.1). The fission gas swelling induced by grain-boundary bubbles (grain-boundary swelling) is generally more important than the intra-granular swelling, at least for burn-ups below about 45 GWd·(tM)$^{-1}$ (White and Tucker, 1983; Mogensen et al., 1985; Kashibe et al., 1993).

The grain-boundary module of the new model consists of a conveniently simple description of the fundamental processes governing the development of the grain-boundary bubble population, allowing the physics-based and integrated calculation of the fission gas swelling and release, as inherently coupled phenomena. The dependence of the processes on the compressive hydrostatic stress in the fuel, acting to constrain bubble growth and consequently affecting both the swelling and the FGR (Turnbull and Tucker, 1974; Zimmermann, 1978; Kogai et al., 1988; Walker et al., 1988, Mogensen et al., 1993; Kashibe and Une, 1997), is consistently considered. Properly taking into account the role of the hydrostatic stress in fission gas swelling and release is of particular importance for the analysis of the fuel rod behaviour at extended burn-up or during power ramps (when high compressive hydrostatic stress may develop in the fuel due to strong PCMI) and of the related, safety-relevant issues in terms of fuel rod structural integrity (OECD/NEA, 2004). Nevertheless, introducing the stress-dependence of the swelling in a model to be applied to the fuel rod analysis codes represents a major challenge from the viewpoint of the numerical stability of the fuel rod calculations.

3.3.1 Main assumptions

In order to simplify the problem, the developed model involves the following main assumptions:

- The grain-boundary gas bubbles are considered to reside at the interfaces between two grains (grain faces). Peculiarities related to the presence of grain edges (where three grains meet) are neglected (e.g., Kogai, 1997; Massih and Forsberg, 2008).
- An initial concentration of grain-boundary bubbles (nucleation centres), $N_{gb,0}$ [(bub.)·m^{-2}], is given, and no further nucleation is considered during the irradiation. This corresponds to the assumption that the geometric size of the initial population leads to absorption of any newly nucleated bubble, giving the effect that the nucleation is a one-off process (White, 2004). The choice of $N_{gb,0}$ is not too critical since the concentration of bubbles falls very quickly once bubble growth and coalescence commence (White, 2004). In the present model, a value $N_{gb,0} = 4 \cdot 10^{13}$ (bub.)·m^{-2} is adopted, in line with Cheon et al. (2004) and consistently with experimental observations pointing out bubble number densities between $1 \cdot 10^{13}$ (bub.)·m^{-2} and $5 \cdot 10^{13}$ (bub.)·m^{-2} (White, 2004).
- The absorption rate of gas at the grain-boundary bubbles equals the rate of gas transport to the grain boundaries. This corresponds to the hypothesis of instantaneous absorption at the bubbles of the gas atoms reaching the grain boundaries. A more accurate description could be obtained by solution of the full time-dependent diffusion equation, but numerical solutions indicate this to be an unnecessary refinement (White, 2004). The validity of this approximation follows from the large difference between the lattice and grain boundary diffusivities of gas atoms (a factor of 10^2-10^6 in the temperature range from 1000°C to 1700°C (Olander and Van Uffelen, 2001)).
- The gas on the grain boundaries is equally distributed in the grain-boundary bubbles.
- The gas residing in the grain-boundary bubbles obeys the Van der Waals' equation of state.
- All the grain-boundary bubbles have, at any instant, equal size and equal lenticular shape of circular projection. A uniform, average bubble size is therefore considered at any instant (mean-field approximation, e.g., Veshchunov, 2008).
- The flux of gas atoms dissolved from the grain boundaries back to the grain interior by irradiation is neglected (Rest, 2003; Spino et al., 2005).
- The athermal (recoil and knock-out) release mechanisms (Section 2.1), which contribute less than 1% to the release of the generated gas (Wise, 1985; Lewis, 1987), are not considered.

The new model describes the grain-boundary bubble growth, coalescence and inter-connection in order to estimate the kinetics of the bubble size and number density, allowing for their time dependence and interrelation. For this purpose, the development of the grain-boundary bubbles may be conveniently considered as resulting from the following processes:

1. The growth of bubbles through the collection of fission gas atoms and vacancies.
2. The mutual interaction between bubbles through coalescence leading to larger but fewer bubbles.
3. The release of fission gas from the grain boundaries to the fuel rod free volume.

The modelling of these processes is discussed in Sub-sections 3.3.2, 3.3.3 and 3.3.4.

3.3.2 Bubble growth

Mechanical equilibrium requires that the pressure of the gas in the bubble is balanced by the surface tension force and the hydrostatic stress. The mechanical equilibrium pressure, p_{eq} [Pa], of the gas in a lenticular bubble of circular projection is given by

$$p_{eq} = \frac{2\gamma}{R_{gb}} - \sigma_h , \tag{3.13}$$

where γ [J·m^{-2}] is the UO_2/gas specific surface energy, R_{gb} [m] the bubble radius of curvature, and σ_h [Pa] the hydrostatic stress (considered to be negative if the solid medium is under compression). Although the assumption that the grain-boundary bubbles are always in mechanical equilibrium has been largely adopted in fission gas behaviour models (e.g., Koo et al., 2000; Massih and Forsberg, 2008; Veshchunov, 2008), in general the grain-boundary gas bubbles exist in a non-equilibrium state and tend to restore equilibrium by absorption or emission of vacancies. The model of Speight and Beere (1975) describes the growth (or shrinkage) of the grain-boundary bubbles as proceeding by absorption (or emission) of vacancies in grain boundaries, induced by the difference between the pressure of the gas in the bubble, p [Pa], and the mechanical equilibrium pressure. The vacancy absorption/emission rate at a bubble is given by

$$\frac{dn_v}{dt} = \frac{2\pi D_v \delta_{gb}}{kTS}\left(p - p_{eq}\right), \tag{3.14}$$

where n_v [(vac.)] is the number of vacancies in the bubble, D_v [m^2·s^{-1}] the vacancy diffusion coefficient in grain boundaries, δ_{gb} [m] the thickness of the diffusion layer in grain boundaries, and S [-] is calculated as (White, 2004)

$$S = -\frac{1}{4}\left[\left(3 - F_c\right)\cdot\left(1 - F_c\right) + 2\,ln\left(F_c\right)\right], \tag{3.15}$$

with F_c (/) being the fraction of grain boundaries covered by bubbles (fractional coverage). The following expression is used in the developed model for the vacancy diffusion coefficient in grain boundaries (Reynolds and Burton, 1969; Kogai, 1997):

$$D_v = 6.9 \cdot 10^{-4} \, exp\left(-\frac{5.35 \cdot 10^{-19}}{kT} \right), \tag{3.16}$$

and a value $\delta_{gb} = 5 \cdot 10^{-10}$ m is used in line with Kogai (1997).
For describing the thermodynamic state of the grain-boundary bubbles, the Van der Waals' equation of state is adopted[5]:

$$p\left(V_{gb} - n_g \omega\right) = n_g kT, \tag{3.17}$$

where n_g [(at.)] is the number of fission gas atoms per bubble, k [J·K^{-1}] the Boltzmann constant, T [K] the temperature, V_{gb} [m^3] the bubble volume, and ω [m^3·(at.)$^{-1}$] the Van der Waals' volume of a fission gas atom. Given that each bubble consists of vacancies and gas atoms, the volume of a bubble comprising n_g fission gas atoms and n_v vacancies is given by

$$V_{gb} = n_g \omega + n_v \Omega_{gb}, \tag{3.18}$$

where Ω_{gb} [m^3] is the atomic (vacancy) volume in the bubble. A value $\Omega_{gb} = 4.09 \cdot 10^{-29}$ m^3 is adopted in the model (Kogai, 1997). Combination of Eqs. 3.17 and 3.18 gives for the pressure of the gas in the bubble

$$p = \frac{kT}{\Omega_{gb}} \frac{n_g}{n_v}, \tag{3.19}$$

The above approach was proposed earlier by White (2004) and allows to calculate the bubble growth rate from the rate of inflow of gas atoms along with the rate of absorption (emission) of vacancies in the bubble. The combined effects of gas atom inflow and vacancy absorption (emission) are interactive, since the addition of fission gas atoms gives rise to a change in the bubble pressure via Eq. 3.19, which immediately affects the propensity of the bubble to absorb (or emit) vacancies through Eq. 3.14. Also, the hydrostatic stress, σ_h, affects the mechanical equilibrium pressure (Eq. 3.13) and hence the bubble growth rate through Eq. 3.14.
Given the volume, V_{gb}, of a lenticular bubble of circular projection, the bubble radius of curvature is calculated as

$$R_{gb} = \left(\frac{3V_{gb}}{4\pi\varphi(\Theta)} \right)^{1/3}. \tag{3.20}$$

where Θ is the semi-dihedral angle of the bubble.

[5] For gases such as Xe and Kr, which are of interest here, the correction for the pressure in the Van der Waals' equation of state is relatively small and can be neglected (e.g., Olander, 1976; Massih and Forsberg, 2008). This simplification was introduced in Eq. (3.17).

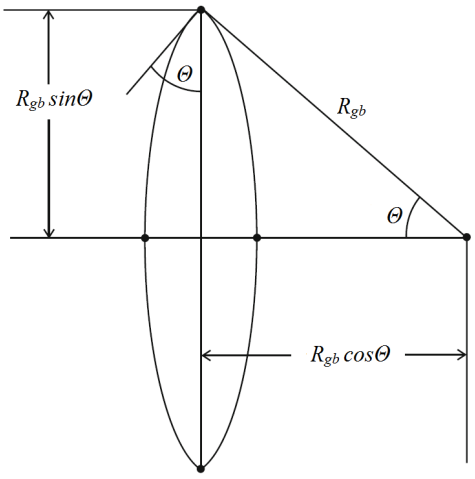

Fig. 3.3. Schematic representation (cross-sectional view) of a lenticular grain-boundary bubble with radius of curvature R_{gb}.

The geometric factor, $\varphi(\Theta)$, relating the volume of a lenticular-shape bubble to that of a sphere, is given by

$$\varphi(\Theta) = 1 - 1.5\cos\Theta + 0.5(\cos\Theta)^3 . \tag{3.21}$$

The conventionally accepted value for Θ is 50°. Figure 3.3 shows a schematic of a grain-boundary bubble as represented in the model. The projected area of the bubble, A_{gb} [m^2], is given by

$$A_{gb} = \pi(\sin\Theta)^2 R_{gb}^2 , \tag{3.22}$$

and the fractional coverage, F_c [/], is given by

$$F_c = A_{gb} N_{gb} , \tag{3.23}$$

where N_{gb} [(bub.)·m^{-2}] is the number density of grain-boundary bubbles. In view of the experimental observations showing that N_{gb} markedly varies throughout the irradiation (Section 2.1), a variable bubble number density model is introduced. The time evolution of the bubble number density is evaluated on a physical basis, by describing the underlying processes of bubble coalescence and FGR, as discussed in the following sub-sections.

3.3.3 Bubble coalescence

In the coalescence process, grain-boundary bubbles intersect and merge into larger but fewer bubbles. Bubble growth brings about mechanical interference between bubbles and coalescence, and consequent progressive reduction in the bubble number density and increase in the average bubble size (Section 2.1). Given that each bubble consists of vacancies and gas atoms, the coalescence event must preserve the volume of the interacting bubbles. In line with

White (2004), the coalescence rate may be considered as related to the rate of increase of the bubble projected area, A_{gb}, resulting from bubble growth. In this respect, an increase in the bubble area by an amount ∂A_{gb} leads to interaction of the bubble with $4N_{gb}\partial A_{gb}$ surrounding bubbles. It is easy to demonstrate that this is correct for circular bubbles of the same size in a regular square lattice. Considering each bubble in turn, the total rate of loss of bubbles by coalescence following an increase in the bubble projected area, A_{gb}, due to bubble growth is given by (White, 2004)

$$\frac{dN_{gb}}{dt} = -2N_{gb}^2\left(\frac{\partial A_{gb}}{\partial t}\right)_g, \tag{3.24}$$

where the factor of 4 is reduced to 2 to avoid counting each interaction twice, and $(\partial A_{gb}/\partial t)_g$ denotes the variation of the bubble area owing solely to bubble growth. Under the assumption of White that the newly coalesced bubble retains the same area of the two individual parent bubbles (White, 2004), the coalescence event has no impact on the average bubble area. Hence, in the model of White the total rate of increase in the average bubble area is given by $dA_{gb}/dt = (\partial A_{gb}/\partial t)_g$, and Eq. 3.24 gives the relationship between the total rate of loss of bubbles and the total rate of increase in bubble area.

Veshchunov (2008) modified the model of White by introducing the variation of the average bubble area associated with the coalescence mechanism. Veshchunov assumed the bubbles to be always in mechanics equilibrium, and that the surrounding solid medium is stress-free ($\sigma_h = 0$). Moreover, he assumed that the gas in the bubbles obeys the perfect gas law. It can be demonstrated that, under these assumptions, the area of a newly coalesced bubble that retains the gas content of the two parent bubbles equals the summation of the areas of the parent bubbles. Hence, according to the approach of Veshchunov, the total bubble area (summation of the areas of all the bubbles) or, equivalently, the total bubble area per unit grain boundary area (fractional coverage, Eq. 3.23) is conserved through coalescence. Given that the bubble number density, N_{gb}, decreases through coalescence, the conservation of the fractional coverage, $N_{gb}A_{gb}$, implies a variation of the average bubble area, A_{gb}, due to coalescence. As a result, the total rate of increase in the average bubble area may be expressed as

$$\frac{dA_{gb}}{dt} = \left(\frac{\partial A_{gb}}{\partial t}\right)_g + \left(\frac{\partial A_{gb}}{\partial t}\right)_c, \tag{3.25}$$

where $(\partial A_{gb}/\partial t)_c$ denotes the variation of the average bubble area owing solely to coalescence. The variation of the fractional coverage is due solely to bubble growth and may be expressed as

$$\frac{d\left(N_{gb}A_{gb}\right)}{dt} = N_{gb}\left(\frac{\partial A_{gb}}{\partial t}\right)_g, \tag{3.26}$$

where

$$\frac{d\left(N_{gb}A_{gb}\right)}{dt} = N_{gb}\frac{dA_{gb}}{dt} + A_{gb}\frac{dN_{gb}}{dt}. \tag{3.27}$$

Superposition of Eqs. 3.25, 3.26 and 3.27 yields

$$\left(\frac{\partial A_{gb}}{\partial t}\right)_c = -\frac{A_{gb}}{N_{gb}}\frac{dN_{gb}}{dt}, \tag{3.28}$$

Combining Eqs. 3.24, 3.25 and 3.28, one obtains for the total rate of loss of bubbles by coalescence according to the model of Veshchunov (2008)

$$\frac{dN_{gb}}{dt} = -\frac{2N_{gb}^2}{1+2N_{gb}A_{gb}}\frac{dA_{gb}}{dt} \tag{3.29}$$

In the present work, the model of Veshchunov is revisited by removing – consistently with the assumptions discussed in Sub-section 3.3.1 – the hypotheses of bubbles in mechanical equilibrium, stress-free solid, and perfect gas. It is considered that the newly coalesced bubble retains the gas atom and vacancy content of the two parent bubbles, which entails that the volume of the newly coalesced bubble equals the sum of the volumes of the parent bubbles. Hence, according to the new model, the total bubble volume (summation of the volumes of all the bubbles) or, equivalently, the total bubble volume per unit grain boundary area is conserved through coalescence. Given that the bubble number density, N_{gb}, decreases through coalescence, the conservation of the total bubble volume per unit grain boundary area, $N_{gb}V_{gb}$, implies a variation of the average bubble volume, V_{gb}, due to coalescence. Then, the total rate of increase in the average bubble volume may be expressed as

$$\frac{dV_{gb}}{dt} = \left(\frac{\partial V_{gb}}{\partial t}\right)_g + \left(\frac{\partial V_{gb}}{\partial t}\right)_c, \tag{3.30}$$

where $(\partial V_{gb}/\partial t)_g$ denotes the variation of the bubble volume owing solely to bubble growth, and $(\partial V_{gb}/\partial t)_c$ the variation of the average bubble volume owing solely to coalescence.
The variation of the total bubble volume per unit grain boundary area is due solely to bubble growth and may be expressed as

$$\frac{d\left(N_{gb}V_{gb}\right)}{dt} = N_{gb}\left(\frac{\partial V_{gb}}{\partial t}\right)_g, \tag{3.31}$$

where

$$\frac{d\left(N_{gb}V_{gb}\right)}{dt} = N_{gb}\frac{dV_{gb}}{dt} + V_{gb}\frac{dN_{gb}}{dt}. \tag{3.32}$$

Superposition of Eqs. 3.30, 3.31 and 3.32 yields

$$\left(\frac{\partial V_{gb}}{\partial t}\right)_c = -\frac{V_{gb}}{N_{gb}}\frac{dN_{gb}}{dt}, \tag{3.33}$$

Given that $V_{gb} \sim A_{gb}^{3/2}$, the validity of Eq. 3.30 implies the validity of Eq. 3.25, and Eq. 3.33 can be written in terms of average bubble area as

$$\left(\frac{\partial A_{gb}}{\partial t}\right)_c = -\frac{2}{3}\frac{A_{gb}}{N_{gb}}\frac{dN_{gb}}{dt}, \tag{3.34}$$

Combining Eqs. 3.24, 3.25 and 3.34, one obtains for the total rate of loss of bubbles by coalescence according to the new model

$$\frac{dN_{gb}}{dt} = -\frac{6N_{gb}^2}{3+4N_{gb}A_{gb}}\frac{dA_{gb}}{dt} \tag{3.35}$$

3.3.4 Fission gas release

The release of fission gas from the grain boundaries following inter-connection of grain-boundary bubbles (Section 2.1) is usually modelled based on a principle of grain boundary saturation. Models adopted in the fuel rod analysis codes often consider an empirical saturation concentration of gas at the grain boundaries (e.g., Bernard et al., 2002; Lassmann et al., 2011), i.e., when the concentration of gas at the grain boundaries exceeds a threshold value, all the gas that further reaches the grain boundaries is assumed to be released to the fuel rod free volume. This treatment does not consider, however, the dependence of the grain-boundary bubble growth and subsequent inter-connection on the temperature and the hydrostatic stress through the equation of state of the gas. This can be allowed for in a physics-based model that directly describes the grain-boundary bubble development.

In the new model, rather than considering a saturation concentration of gas at the grain boundaries, a saturation fraction of grain boundary surface covered by bubbles (saturation coverage) is introduced. It is considered that once the fractional coverage attains the saturation value, $F_{c,sat}$, the bubble number density and projected area obey the saturation coverage condition (Veshchunov, 2008)

$$F_c = N_{gb}A_{gb} = F_{c,sat}\,. \tag{3.36}$$

This implies that a fraction of the gas reaching the grain boundaries is transferred to the fuel exterior to compensate for bubble growth. More precisely, it is considered that any further bubble growth is balanced by loss (venting) of bubbles through gas release in order to maintain the saturation coverage condition, that is, $dF_c/dt = 0$. It follows that the rate of variation of the

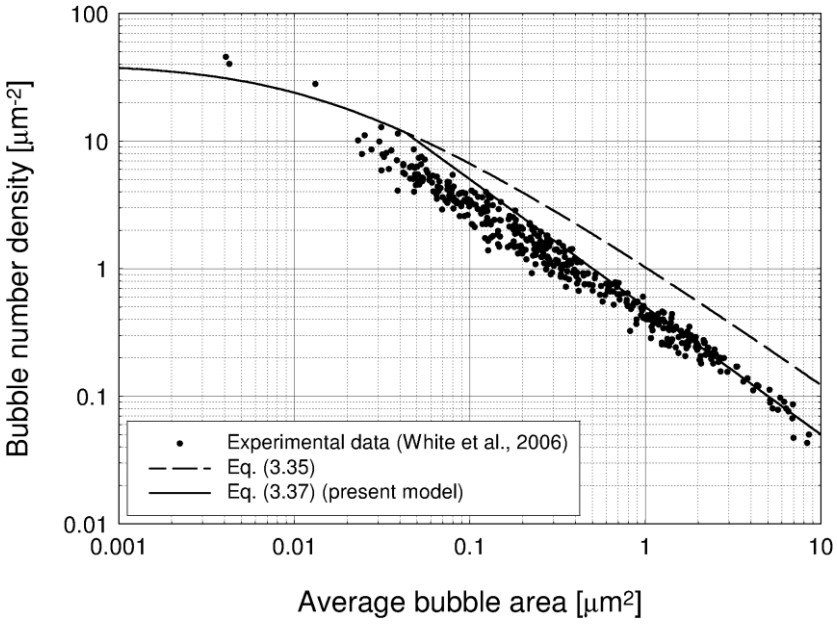

Fig. 3.4. Variation of the bubble number density with the bubble projected area according to the developed model. Eq. 3.37 is compared with experimental data (White et al., 2006). Eq. 3.35 is also shown. An initial bubble number density $N_{gb,0} = 4 \cdot 10^{13}$ (bub.)·m^{-2} is considered.

bubble number density is governed by coalescence (Sub-section 3.3.3) for $F_c < F_{c,sat}$, and by gas release after attainment of the saturation coverage, and is described by

$$\begin{aligned} \frac{dN_{gb}}{dt} &= -\frac{6N_{gb}^2}{3+4N_{gb}A_{gb}}\frac{dA_{gb}}{dt} && \text{if } N_{gb}A_{gb} < F_{c,sat} \\ \frac{dN_{gb}}{dt} &= -\frac{N_{gb}}{A_{gb}}\frac{dA_{gb}}{dt} && \text{if } N_{gb}A_{gb} = F_{c,sat} \end{aligned} \quad . \tag{3.37}$$

The adopted value for $F_{c,sat}$ is 0.5 (e.g., Koo et al., 2000; White, 2004; Veshchunov, 2008). Eq. 3.37 allows to evaluate the observed reduction in the number density of grain-boundary bubbles in UO_2 throughout irradiation (White, 2004). Figure 3.4 compares Eq. 3.37 with the experimental data of bubble number density and corresponding average bubble projected area from (White et al., 2006). The bifurcation between the dashed line (Eq. 3.35) and the full line (Eq. 3.37) corresponds to the attainment of the saturation coverage. The developed variable bubble number density model (Eq. 3.37) appears to reasonably conform to the data.

According to the above discussed description, and considering that each bubble contains n_g fission gas atoms, the FGR is calculated by means of

$$\begin{aligned} \frac{dn_{fgr}}{dt} &= 0 && \text{if } N_{gb}A_{gb} < F_{c,sat} \\ \frac{dn_{fgr}}{dt} &= n_g\frac{N_{gb}}{A_{gb}}\frac{dA_{gb}}{dt} && \text{if } N_{gb}A_{gb} = F_{c,sat} \end{aligned} \quad , \tag{3.38}$$

where n_{fgr} is the number of gas atoms released to the fuel rod free volume. This simple approach allows reproducing the incubation behaviour (Vitanza et al., 1978) and the dependence of the FGR on the hydrostatic stress (Kogai et al., 1988; Walker et al., 1988; Mogensen et al., 1993), as well as the coupling between the fission gas swelling and release, on a physical basis.

3.3.5 Grain-boundary swelling

The equations presented in the previous sub-sections allow to calculate the evolution of the number density and the size of the grain-boundary bubbles, as well as the amount of fission gas released to the fuel rod free volume. Since a uniform population of bubbles is considered (Sub-section 3.3.1), the volumetric grain-boundary fission gas swelling, normalized to the unit volume of fuel, is calculated as

$$\left(\frac{\Delta V}{V}\right)_{gb} = \frac{1}{2}\frac{N_{gb}}{(1/3)r_{gr}}\left(\frac{4}{3}\pi R_{gb}^3 \varphi(\Theta)\right), \tag{3.39}$$

where r_{gr} [m] is the radius of the spherical fuel grains, $(1/3)r_{gr}$ is the grain volume to surface ratio, and the factor 1/2 is introduced because a grain-boundary bubble is shared by two neighbouring grains.

3.3.6 Calculation sequence

The following calculation sequence is adopted in applying the grain-boundary module at each computational time step:

(i) The inflow of gas atoms in the grain-boundary bubbles is calculated as the arrival rate of gas at the grain boundaries provided by the intra-granular module (Sub-section 3.2.1). At the first time step, an initial bubble radius R_{gb} = 10 nm is used.

(ii) The bubble growth rate is calculated on the basis of the Speight and Beere model by solving incrementally Eq. 3.14, giving the time evolution of the temperature and hydrostatic stress-dependent bubble size.

(iii) The decrease of bubble number density through coalescence/FGR, as well as the FGR rate, are calculated by solving incrementally Eqs. 3.37 and 3.38, using the new projected area after the effect of bubble growth.

(iv) The grain-boundary fission gas swelling is calculated by means of Eq. 3.39.

The (total) volumetric fission gas swelling, $(\Delta V/V)_{gas}$, is calculated as the summation of the intra-granular swelling and the grain-boundary swelling:

$$\left(\frac{\Delta V}{V}\right)_{gas} = \left(\frac{\Delta V}{V}\right)_{ig} + \left(\frac{\Delta V}{V}\right)_{gb}. \tag{3.40}$$

Table 3.1.
Values adopted for the model parameters.

Symbol	Definition	Value / expression
D_s	Gas atom diffusion coefficient in grains	$D_1+D_2+D_3$ ($m^2 \cdot s^{-1}$) $D_1=7.6 \cdot 10^{-10} \cdot exp(-4.86 \cdot 10^{-19}/kT)$ $D_2=3.22 \cdot 10^{-16} \cdot q_s^{1/2} \cdot exp(-1.90 \cdot 10^{-19}/kT)$ D_3 not considered T: temperature (K) q_s: specific power ($W \cdot g^{-1}$)
D_v	Vacancy diffusion coefficient in grain boundaries	$6.9 \cdot 10^{-4} \cdot exp(-5.35 \cdot 10^{-19}/kT)$ $m^2 \cdot s^{-1}$
$F_{c,sat}$	Fractional coverage at grain boundary saturation	0.5
k	Boltzmann constant	$1.38 \cdot 10^{-23}$ $J \cdot K^{-1}$
l_f	Length of a fission fragment track	$6 \cdot 10^{-6}$ m
$N_{gb,0}$	Initial number density of grain-boundary bubbles	$4 \cdot 10^{13}$ (bub.)$\cdot m^{-2}$
N_{ig}	Number density of intra-granular bubbles	$7 \cdot 10^{23}$ (bub.)$\cdot m^{-3}$
Z_0	Radius of influence of a fission fragment track	10^{-9} m
γ	UO_2/gas specific surface energy	1 $J \cdot m^{-2}$
δ_{gb}	Thickness of the diffusion layer in grain boundaries	$5 \cdot 10^{-10}$ m
Θ	Semi-dihedral angle of grain-boundary bubbles	50°
ω	Van der Waals' volume of a fission gas atom	$8.5 \cdot 10^{-29}$ $m^3 \cdot (at.)^{-1}$
Ω_{gb}	Vacancy volume in grain-boundary bubbles	$4.09 \cdot 10^{-29}$ m^3
Ω_{ig}	Volume per gas atom in intra-granular bubbles	$3 \cdot 10^{-29}$ m^3

Given the isotropic nature of the swelling, the strains due to fission gas swelling (Section 1.3) are calculated as (Lassmann et al., 2011)

$$\varepsilon_{r,\theta,z}^{gas} = \frac{1}{3}\left(\frac{\Delta V}{V}\right)_{gas} . \tag{3.41}$$

The values adopted for the model parameters are summarized in Table 3.1.

3.4 Concluding remarks

A model was developed for the analysis of the fission gas swelling and release in UO_2 fuel during irradiation as inherently coupled phenomena, which represents a pragmatic compromise between the strength of a physics-based description and the simplicity required for application to the fuel rod analysis codes. The model is based on concepts presented earlier by Speight, Beere, White, Tucker, Veshchunov, which are revisited and combined in a practical treatment, aimed to grasp the fundamental peculiarities of the fission gas behaviour. In particular, a simple approach is adopted to describe the development of the intra-granular bubbles, which determine the intra-granular contribution to the swelling and affect the diffusion of gas to the grain boundaries. This treatment of the intra-granular gas behaviour is preliminary and being further developed (Appendix B). The main and most innovative part of the model describes the development of the grain-boundary bubbles, which determines the

kinetics of both the grain-boundary contribution to the swelling and the fission gas release. In particular, the mutually dependent processes of grain-boundary bubble growth, coalescence and inter-connection are described. In outline:

- The Speight and Beere model is adopted for describing the growth of the grain-boundary bubbles, and its dependence on the hydrostatic stress in the fuel. The latter aspect is of particular importance for the analysis of the fuel rod behaviour at extended burn-up or during power ramps and of the related, safety-relevant issues.
- Bubble coalescence is described by means of a revisited model of White.
- Bubble inter-connection and the subsequent gas release from the grain boundaries are modelled by adopting a concept of fractional coverage saturation.

The model is intended to provide a contribution to the development of the fuel rod analysis codes for application in both research and industrial frameworks, since it offers the advantages of a physics-based treatment in terms of flexibility in comparison with widely used semi-empirical models of fission gas behaviour. To this purpose, testing, implementation in a fuel rod analysis code, and evaluation of the model were carried out, as discussed in the next chapters.

Chapter 4
Model application as stand-alone version

Abstract. *In this chapter, calculations performed using the stand-alone version of the new model of fission gas swelling and release are presented. In particular, the model was applied to the analysis of either power ramped or power cycled UO_2 fuel specimens. Despite its simplicity, the model was proven to reproduce the main peculiarities of the fission gas behaviour, consistently with the observations reported in the literature. The comparison of the results with an extensive dataset of fission gas swelling measurements is presented as a first step of verification. The predictive accuracy for different irradiation conditions is reasonable, without applying any fitting to the model parameters. The chapter is organized as follows. In Section 4.1, the stand-alone version of the model is briefly described. In Section 4.2, the experimental database is presented, which is adopted for the model evaluation. In Section 4.3, details are given about the set-up of the calculations. In Section 4.4, the results are discussed, both in terms of model capabilities to represent the relevant processes and assessment of the predictions against experimental data from the IFPE database. Conclusions are drawn in Section 4.5.*

4.1 Introduction

As mentioned in Section 1.1, specific test programs are to be developed for the physical models before implementation in a fuel rod analysis code. A test program (or stand-alone model version) is generally designed to perform a zero-dimensional ('point') analysis. Moreover, the input parameters of the model (e.g., specific power, temperature, stress) are defined by the user. Differently, when implemented in a fuel rod analysis code, the model is called for every node of the computational domain, and it is integrated in a consistent fuel rod analysis. In this respect, the construction of a test program may be considered as an intermediate step of the work of development and application of a new model, lying between the definition of the mathematical formulation of the model and its implementation in a fuel rod analysis code. The importance of this intermediate step is twofold:

- It allows to assess the model capabilities to represent the relevant processes and to evaluate the quantities of interest, decoupled from the multiple interrelations with the other aspects of the thermo-mechanical analysis.
- It allows to address the basic numerical issues, decoupled from those related to the incorporation of the model in a pre-existing, complex numerical framework.

In this work, a test program was developed for the new model of fission gas swelling and release in UO_2 fuel described in Chapter 3. The program receives the fuel fabrication data (porosity

and grain size) and the time-dependent specific power, temperature and hydrostatic stress as input. Linear interpolation is performed of the time-dependent quantities within the user-defined time steps. The program consists of Fortran 95 subroutines designed to consistently calculate the fuel density, power density, fission gas generation rate, fission gas concentrations within the grains, at the grain boundaries and released to the fuel rod free volume, and the fission gas swelling. The 'point' analysis is surrounded by a time loop, and a simple time step control was developed and implemented in order to assure adequate numerical accuracy.
Besides representing the first step towards the incorporation of the model in a fuel rod analysis code, the stand-alone version of the model allowed to investigate the model capabilities for the simulation of real irradiation histories and to perform a first verification of the predictions against experimental data from the IFPE database, as discussed in the next sections.

4.2 Experimental database

The experiments of the AGR/Halden Ramp Test Programme (White et al., 2006) involved the power ramp test of Advanced Gas-cooled Reactor (AGR) UO_2 fuel rods in the Halden Reactor, after base-irradiation in the Hinkley Point, Torness and Halden Reactors up to burn-ups of around 21 GWd·(tM)$^{-1}$. Extensive post-irradiation examinations (PIE) of the irradiated fuel by scanning electron microscopy (SEM) were performed to measure the fission gas swelling due to grain-boundary gas bubbles. The results of the study were made available through the IFPE database (Sartori et al., 2010). Some details of the different irradiation tests and SEM examinations, on which the experimental data of grain-boundary swelling considered in the present work are referred to, are given in Table 4.1. The fuel rods were subject to either power ramps or power cycling. The schematic of the ramp tests is presented in Fig. 4.1 and the times and powers of each stage are summarized in Table 4.2. The ramp test consists of a conditioning time, τ_1, and a subsequent power ramp, followed by a holding time (if any) at the ramp terminal power level, τ_{2b}, and reactor scram. The ramps denoted as slow are those in which the power increasing time, τ_{2a}, is of the order of 45 min and the fast ramps are those for

Table 4.1.
Details of considered irradiation tests and PIE/SEM examinations from the AGR/Halden Ramp Test Programme.

Rod identifier	Burn-up [GWd·(tM)$^{-1}$]	Ramp type	Peak rating [kW·m^{-1}]	Holding time	SEM zones	Boundaries measured
4000	20.7	Fast	40	30.0 min	5	48
4004	20.5	Fast	40	2.38 min	6	44
4005	20.8	Fast	40	2.0 min	5	39
4064	20.1	Slow	43	–	5	63
4065	9.3	Slow	41.8	–	5	43
4159	20.2	Cycles	18-26	115·4 h	5	56
4160	20.1	Cycled	18-26	115·4 h	6	45
4162	12.6	Slow	40	–	4	47
4163	12.6	Fast	40	2.0 min	5	37
					46	422

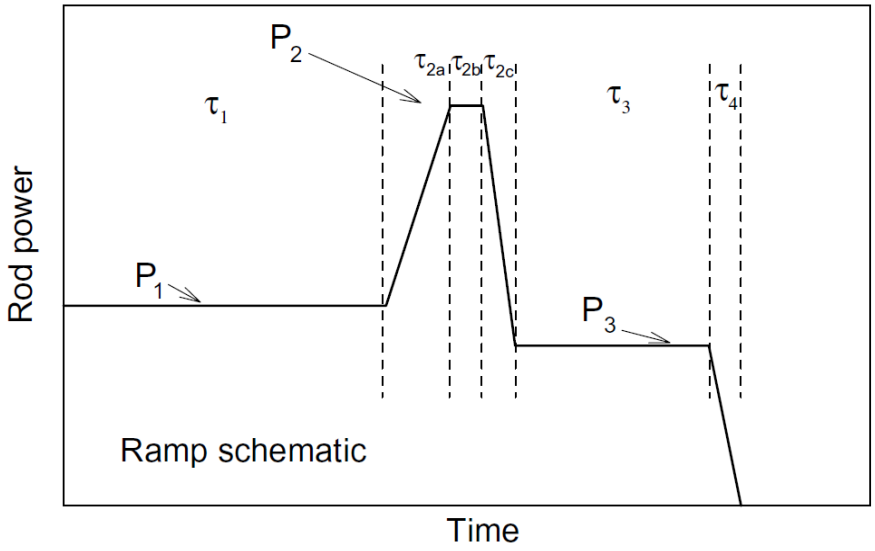

Fig. 4.1. Schematic of a generic ramp test of the AGR/Halden Ramp Test Programme – from (White et al., 2006). The parameters for each case are reported in Table 4.2.

which τ_{2a} lies within the range 1-2 min. The two power-cycled fuel rods were subjected to 115 four-hour cycles, the details of which are summarized in Table 4.3. For each irradiation test, the PIE/SEM examinations were performed at different zones of the fuel specimen, allowing the construction of an extensive database of grain-boundary swelling measurements. Moreover, the specific power, temperature, and hydrostatic stress for each SEM zone were evaluated by means of the ENIGMA code (White et al., 2006), thus providing the basis for reconstruction

Table 4.2
Details of power ramps in the irradiation tests of the AGR/Halden Ramp Test Programme.

Rod identifier	Power 1 [kW·m^{-1}]	τ_1	τ_{2a} [min]	Power 2 [kW·m^{-1}]	τ_{2b} [min]	τ_{2c} [s]	Power 3 [kW·m^{-1}]	τ_3 [min]	τ_4
4000	14.0	12d	1.52	40.0	30.0	100	14.0	99.0	SCRAM
4004	14.0	12d	1.97	40.0	2.38	90	14.0	99.0	SCRAM
4005	14.0	12d	1.32	40.0	2.0	–	SCRAM	–	–
4064	20.0	15wk	47.0	43.0	0.0	–	SCRAM	–	–
4065	19.3	3wk	47.0	41.8	0.0	–	SCRAM	–	–
4162	18.0	3wk	45.0	40	0.0	40	18.0	6	–
4163	18.0	3wk	2.0	40.0	2.0	80	SCRAM	–	–

Table 4.3
Details of power cycles in the irradiation tests of the AGR/Halden Ramp Test Programme.

Rod identifier	Power 1 [kW·m^{-1}]	Time 1	Ramp up	Power up [kW·m^{-1}]	Ramp down	Power down [kW·m^{-1}]	De-conditioning [kW·m^{-1}]	Last phase
4159 and 4160	18.0	7d	30 min	26.0 for 1h	30 min	18.0 for 2h	18.0 for 2d	Shut-down
			115 – 4h cycles					

Table 4.4.
Summary of the post-irradiation experimental data of grain-boundary swelling considered in the present work.

SEM zone	$(\Delta V/V)_{gb}$ [%]	SEM zone	$(\Delta V/V)_{gb}$ [%]	SEM zone	$(\Delta V/V)_{gb}$ [%]
4000-A	0.97±0.35	4064-A	1.07±0.58	4160-A	2.61±0.57
4000-B	0.68±0.12	4064-B	0.86±0.32	4160-B	2.30±0.56
4000-C	0.53±0.10	4064-C	0.63±0.22	4160-C	2.60±0.36
4000-D	0.46±0.10	4064-D	0.74±0.19	4160-D	1.64±0.20
4000-F	0.17±0.4	4064-E	0.59±0.26	4160-E	1.22±0.21
				4160-F	0.74±0.09
4004-A	0.62±0.13	4065-A	1.25±0.43	4162-A	0.70±0.26
4004-B	0.70±0.26	4065-B	1.35±0.30	4162-B	0.46±0.17
4004-C	0.44±0.11	4065-C	0.97±0.26	4162-C	0.43±0.18
4004-D	0.56±0.15	4065-D	0.79±0.15	4162-D	0.43±0.22
4004-E	0.27±0.07	4065-E	0.21		
4004-F	0.16				
4005-A	0.94±0.16	4159-A	1.85±0.22	4163-A	0.60±0.20
4005-B	0.57±0.20	4159-B	1.67±0.26	4163-B	0.59±0.18
4005-C	0.42±0.12	4159-C	1.37±0.16	4163-C	0.35±0.10
4005-D	0.54±0.15	4159-D	1.06±0.15	4163-D	0.40±0.06
4005-E	0.27±0.02	4159-E	0.91±0.28	4163-E	0.26±0.13

of the experiments and verification of fission gas swelling models. In Table 4.4, a summary of the post-irradiation experimental data of volumetric grain-boundary swelling, $(\Delta V/V)_{gb}$, for each SEM zone is given. All the available grain-boundary swelling data are reported, except for that related to the SEM zone 4160-G, which was not used in the present work in view of the lack of information on the fuel grain size during the ramp test (White et al., 2006).

4.3 Set-up of calculations

Simulations of the ramp tests from the AGR/Halden Ramp Test Programme were performed by means of the stand-alone version of the new model of fission gas swelling and release. 46 SEM zones (Table 4.4) were analysed. The calculations were carried out coherently with the fuel fabrication data and the details of the irradiation histories provided in (White et al., 2006). Moreover, the following assumptions were made in order to assess the initial conditions for the analysis of the ramp tests:

- All the fission gas generated during the base-irradiation is considered to be retained inside the fuel grains at the beginning of the calculation. This hypothesis is consistent with the observation that, in all of the cases studied, the base-irradiation resulted in negligible fission gas release and microstructural changes (White et al., 2006).
- The fuel grain size is assumed to remain constant at the final (measured) value throughout the ramp test. Grain growth calculations based on the model of Ainscough et al. (1973) showed that the predicted grain growth is lower than or comparable to the experimental scatter for the grain size measurements (White et al., 2006) in all the analysed cases.

4.4 Results and discussion

4.4.1 Model capabilities

The results of the calculations are firstly presented for the exemplifying case of the SEM zone 4000-A. The fuel specimen was characterized by a burn-up of 20.7 GWd·(tM)$^{-1}$ and was subject to a fast ramp followed by a holding time at the ramp terminal power level of 30 min duration (Table 4.1). The time-dependent input quantities (specific power, temperature and hydrostatic stress) are presented in Fig. 4.2. The specific power was maintained at about 13 W·g^{-1} during the

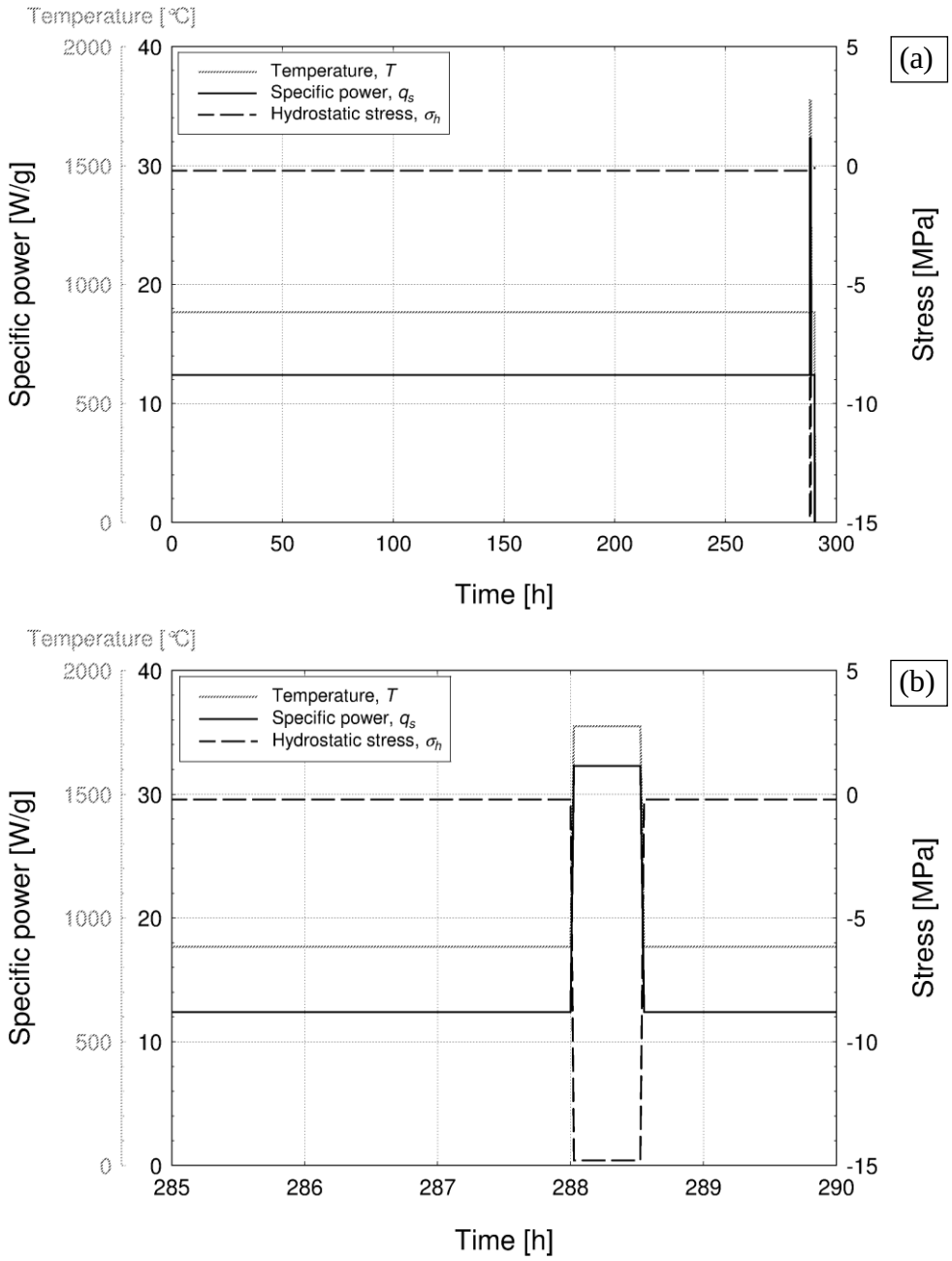

Fig. 4.2. Temperature, specific power, and hydrostatic stress as a function of the time for the SEM zone 4000-A. (a) Entire ramp test, (b) zoom on the ramp.

conditioning time, and raised up to about 32 $W \cdot g^{-1}$ during the power ramp[6]. The fuel temperature and the compressive hydrostatic stress reached values of about 1775°C and 15 MPa, respectively, at the top of the ramp.

The output of the stand-alone model version is shown in Fig. 4.3 in terms of intra-granular bubble radius and volumetric intra-granular swelling as a function of the time. A slight increase

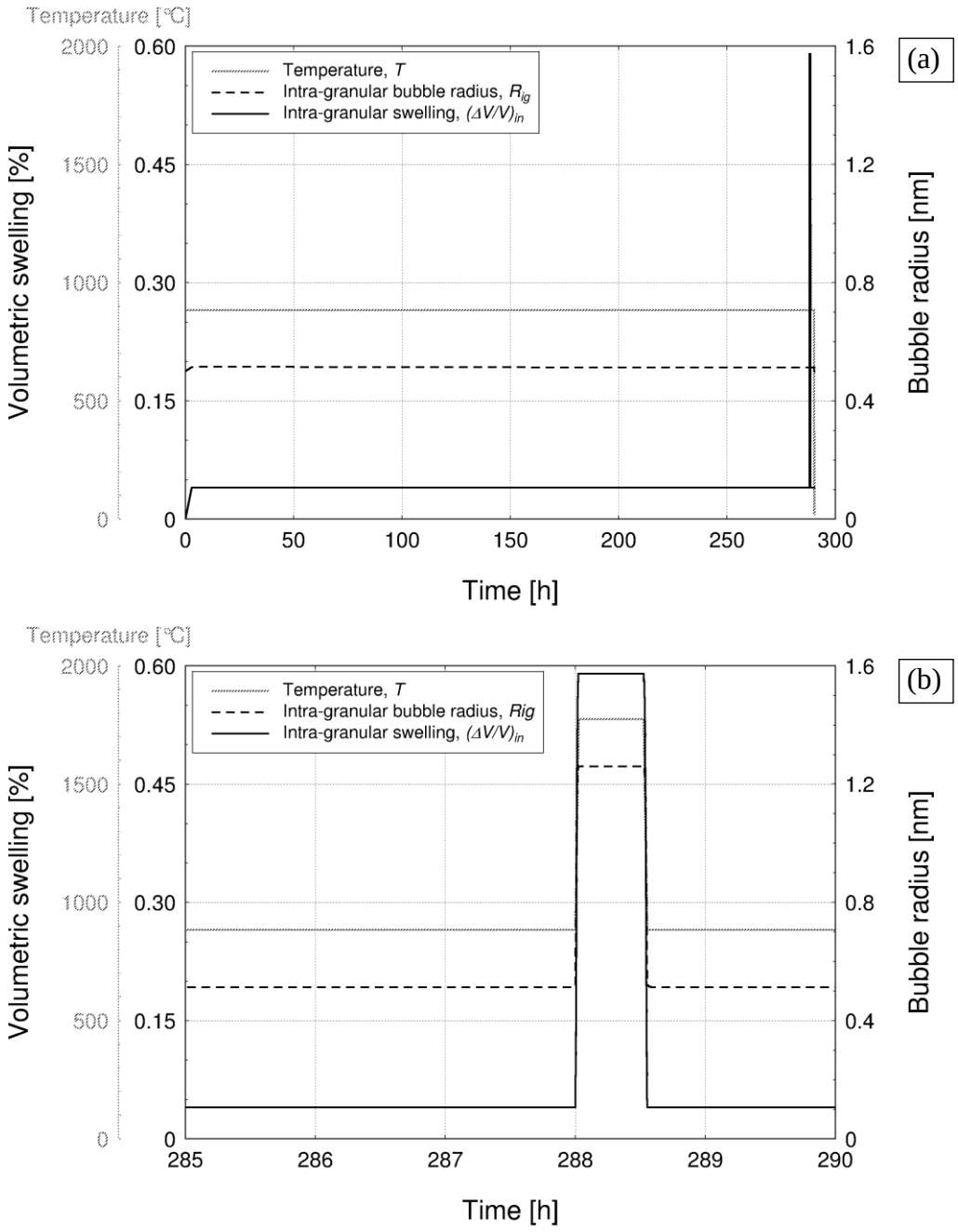

Fig. 4.3. Calculated intra-granular bubble radius and intra-granular swelling as a function of the time for the SEM zone 4000-A. The temperature is also shown. (a) Entire ramp test, (b) zoom on the ramp.

[6] The specific power is a prescribed quantity for the 'point' analyses presented in this chapter, while the linear heat rate is generally prescribed for fuel rod analyses.

of the intra-granular bubble radius is observed during the conditioning time. This behaviour is ascribed to the moderate temperature (about 880°C) and the associated slight trapping effect of the gas atoms in the bubbles (Section 3.2). Following the temperature rise during the ramp, the intra-granular bubbles rapidly grow, and the intra-granular swelling correspondingly increases.
The results in terms of grain-boundary bubble radius of curvature and volumetric grain-boundary swelling as a function of the time are shown in Fig. 4.4. The grain-boundary bubbles grow throughout the irradiation by diffusional inflow of gas atoms and vacancies. Also, bubble growth

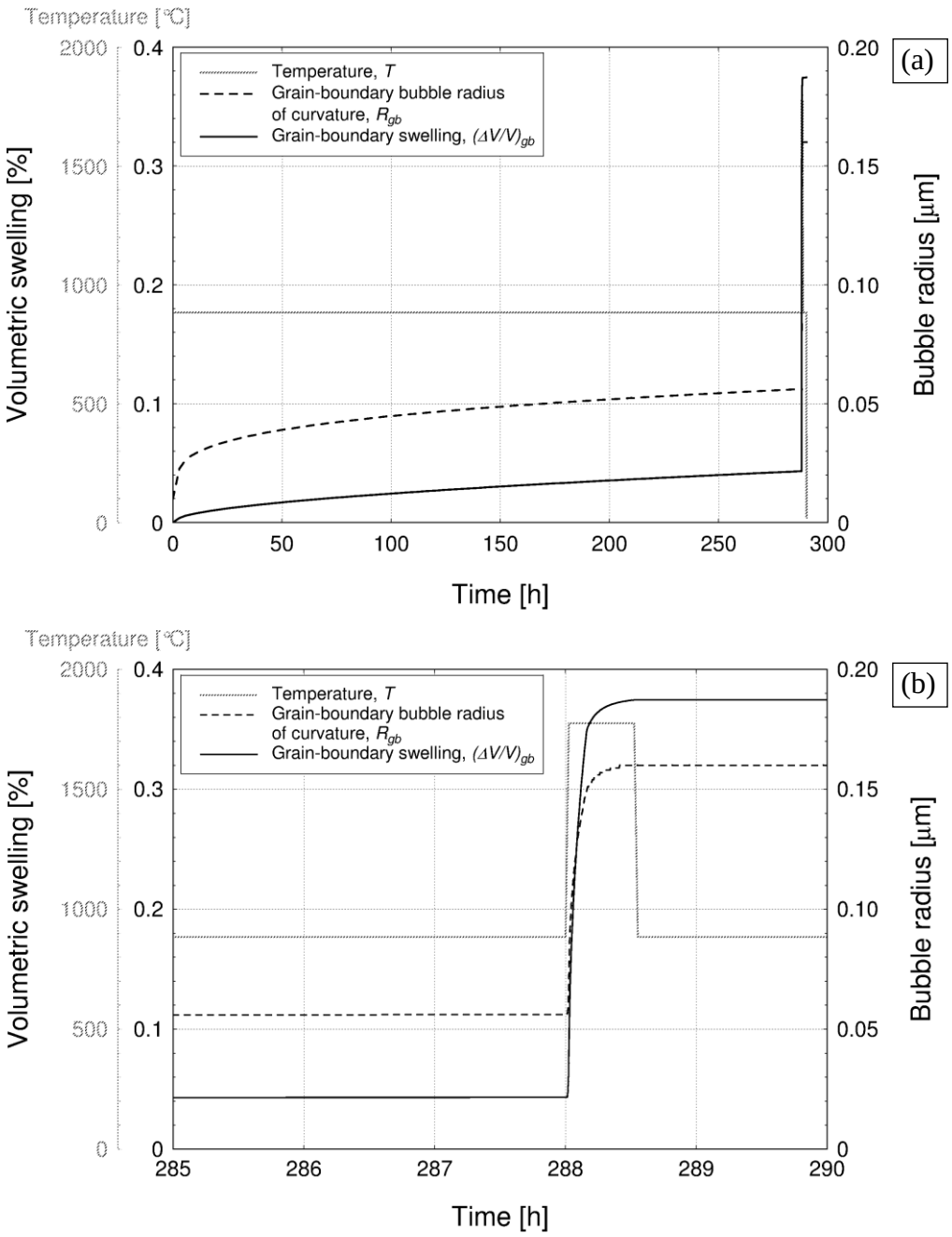

Fig. 4.4. Calculated grain-boundary bubble radius of curvature and grain-boundary swelling as a function of the time for the SEM zone 4000-A. The temperature is also shown. (a) Entire ramp test, (b) zoom on the ramp.

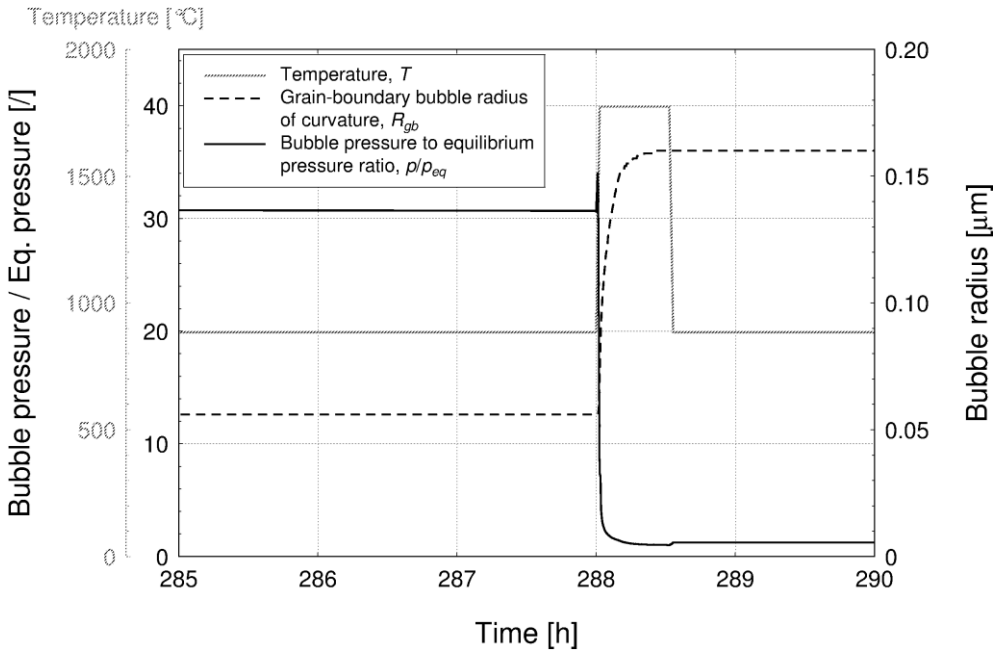

Fig. 4.5. Calculated grain-boundary bubble radius of curvature and ratio of the gas pressure in the bubble to the mechanical equilibrium pressure as a function of the time for the SEM zone 4000-A. The temperature is also shown. Zoom on the ramp is displayed.

brings about bubble coalescence and the related increase in the bubble radius (Section 3.3). During the ramp, the bubble growth rate increases as a consequence of the temperature rise, and the grain-boundary swelling correspondingly accelerates. To give more details about the model capabilities to simulate the growth kinetics of the grain-boundary bubbles, Fig. 4.5 shows the ratio of the gas pressure in the grain-boundary bubbles (bubble pressure) to the mechanical equilibrium pressure as a function of the time (full black line). During the conditioning time at moderate temperature, the bubble over-pressure is high ($p/p_{eq} \approx 30$) due to the low vacancy mobility and consequent low vacancy absorption rate at the bubbles. Subsequent excursion to higher temperatures during the power ramp brings about (i) a further increase of the bubble over-pressure, which drives the absorption of vacancies at the bubbles, and (ii) an enhanced mobility of vacancies and gas atoms (Section 3.3). Both these effects favour the bubble growth during the ramp and the subsequent holding time at high temperature. Following the ramp, the rapid vacancy absorption acts to decrease the bubble over-pressure, thus progressively decreasing the bubble growth rate. However, the ratio of the bubble pressure to the equilibrium pressure remains > 1 (over-pressurized bubbles) even at high temperature. The finding that the grain-boundary bubbles are generally over-pressurized in irradiated UO_2 fuel is consistent with the results reported in (White, 2004).

Owing to significant bubble growth during the ramp and the subsequent holding time, the fractional coverage increases to the saturation value of 0.5 (saturation coverage). In accordance with the concept of grain boundary saturation included in the model, a constant

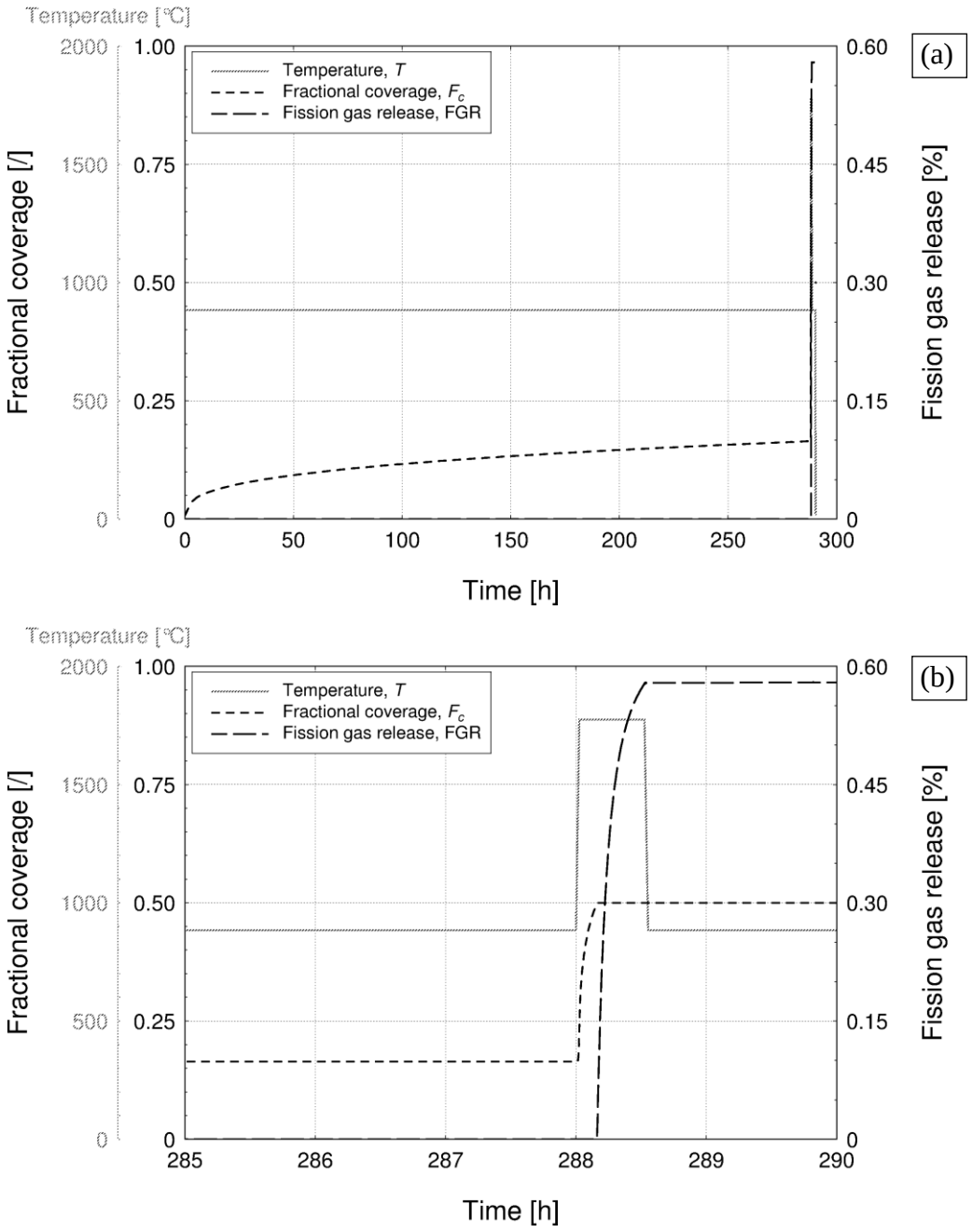

Fig. 4.6. Calculated fractional coverage and fission gas release (defined as the ratio of the released to the generated gas) as a function of the time for the SEM zone 4000-A. The temperature is also shown. (a) Entire ramp test, (b) zoom on the ramp.

fractional coverage condition is maintained after attainment of the saturation coverage, compensating for bubble growth by FGR from the grain boundaries (Section 3.3). This behaviour is shown in Fig. 4.6. FGR starts at the attainment of the saturation coverage and rapidly increases as the bubbles grow. Hence, the model reproduces the experimentally observed incubation behaviour of the FGR (Vitanza et al., 1978), on a physical basis.

Figure 4.7 displays the evolution of the radius of curvature (dashed black line) and the number density (full black line) of the grain-boundary bubbles. The number density progressively decreases throughout the irradiation by coalescence and (once FGR commences) by gas venting from the grain boundaries (Section 3.3). The decrease of the bubble number density accelerates during the power ramp, when rapid bubble growth brings

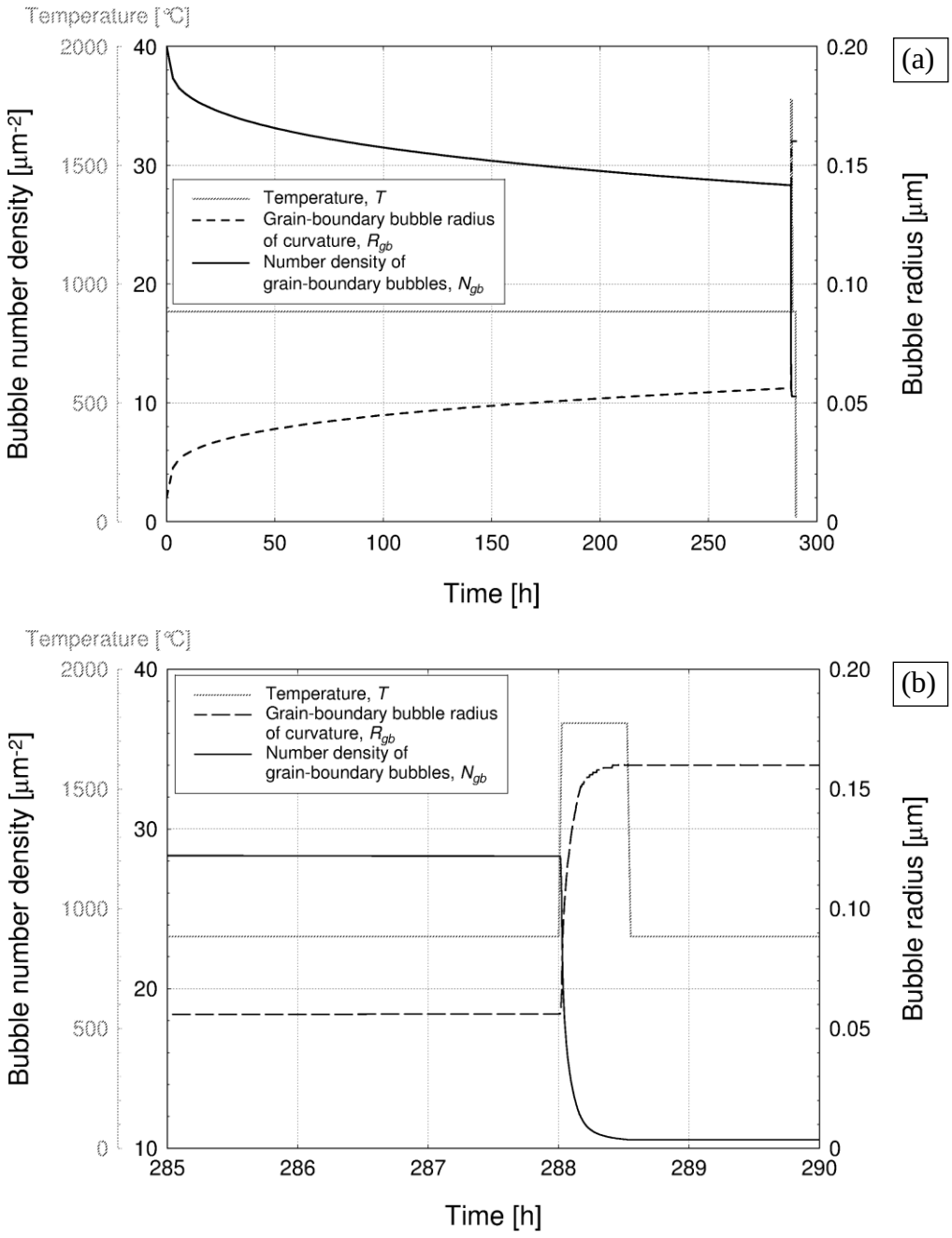

Fig. 4.7. Calculated grain-boundary bubble radius of curvature and number density as a function of the time for the SEM zone 4000-A. The temperature is also shown. (a) Entire ramp test, (b) zoom on the ramp.

about strong coalescence and subsequent onset of the FGR. The simple but physics-based representation of bubble coalescence and FGR included in the model therefore allows to reproduce the experimentally observed decrease of the number density of the grain-boundary bubbles as the irradiation proceeds (White, 2004).

The calculated grain-boundary swelling and FGR for the SEM zone 4000-A are shown together in Fig. 4.8 (black lines). It can be noted that the coupling between swelling and FGR is consistently reproduced by the model, since the swelling rate is reduced by loss of gas from the grain boundaries as FGR takes place. The comparison with the results obtained by neglecting the stress-dependence (grey lines in Fig. 4.8) points out the role of the hydrostatic stress in affecting the fission gas swelling and release by inhibiting the growth of the grain-boundary bubbles. Both the swelling and the FGR are reduced by the compressive stress. Also, the stress delays the FGR by slowing down the bubble growth and consequently retarding the attainment of the saturation coverage. The effect of the hydrostatic stress is relevant during the power ramp, when (i) the stress is higher due to the onset of pellet-cladding mechanical interaction, and (ii) the bubble radius is larger, meaning that the surface tension force – that competes with the hydrostatic stress in affecting the bubble growth rate (Section 3.3) – is lower. The results are therefore in qualitative agreement with the experimental observations pointing out the above effects of the hydrostatic stress on the fission gas swelling and release (Zimmermann, 1978; Kogai et al., 1988; Walker et al., 1988, Mogensen et al., 1993; Kashibe and Une, 1997).

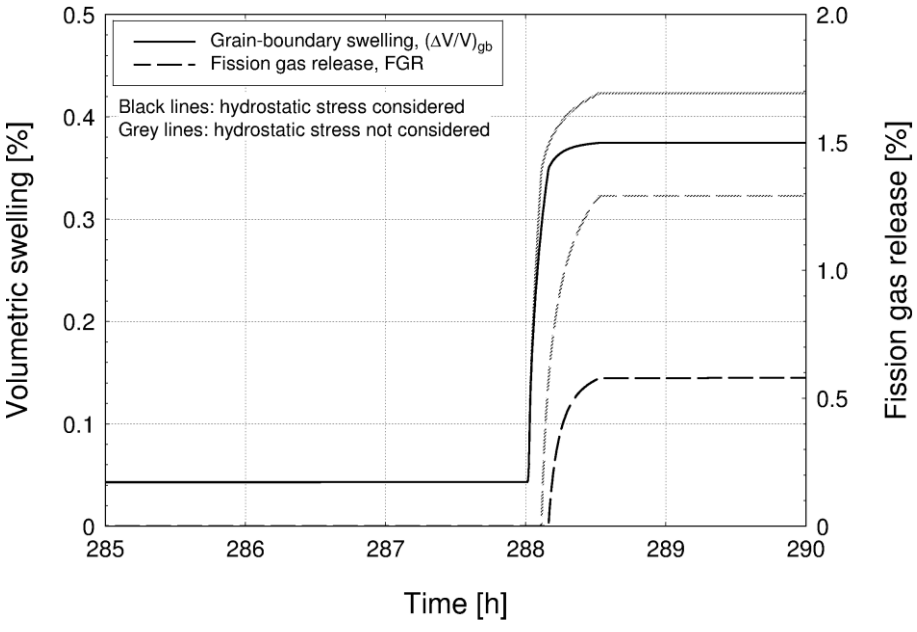

Fig. 4.8. Calculated grain-boundary swelling and fission gas release (defined as the ratio of the released to the generated gas) as a function of the time for the SEM zone 4000-A. The grey lines correspond to the results obtained by neglecting the stress-dependence in the model. Zoom on the ramp is displayed.

The time-dependent input quantities are presented in Fig. 4.9 for the SEM zone 4000-F, which belongs to the same fuel rod as the SEM zone 4000-A but lies in a colder (more peripheral) region of the fuel pellet. The temperature was maintained at about 780°C during the conditioning time, and raised to 1460°C during the power ramp. The compressive hydrostatic stress reached a value of about 3 MPa at the top of the ramp.
The output of the stand-alone model version is shown in Fig. 4.10 in terms of grain-boundary bubble radius of curvature and volumetric grain-boundary swelling as a function of the time.

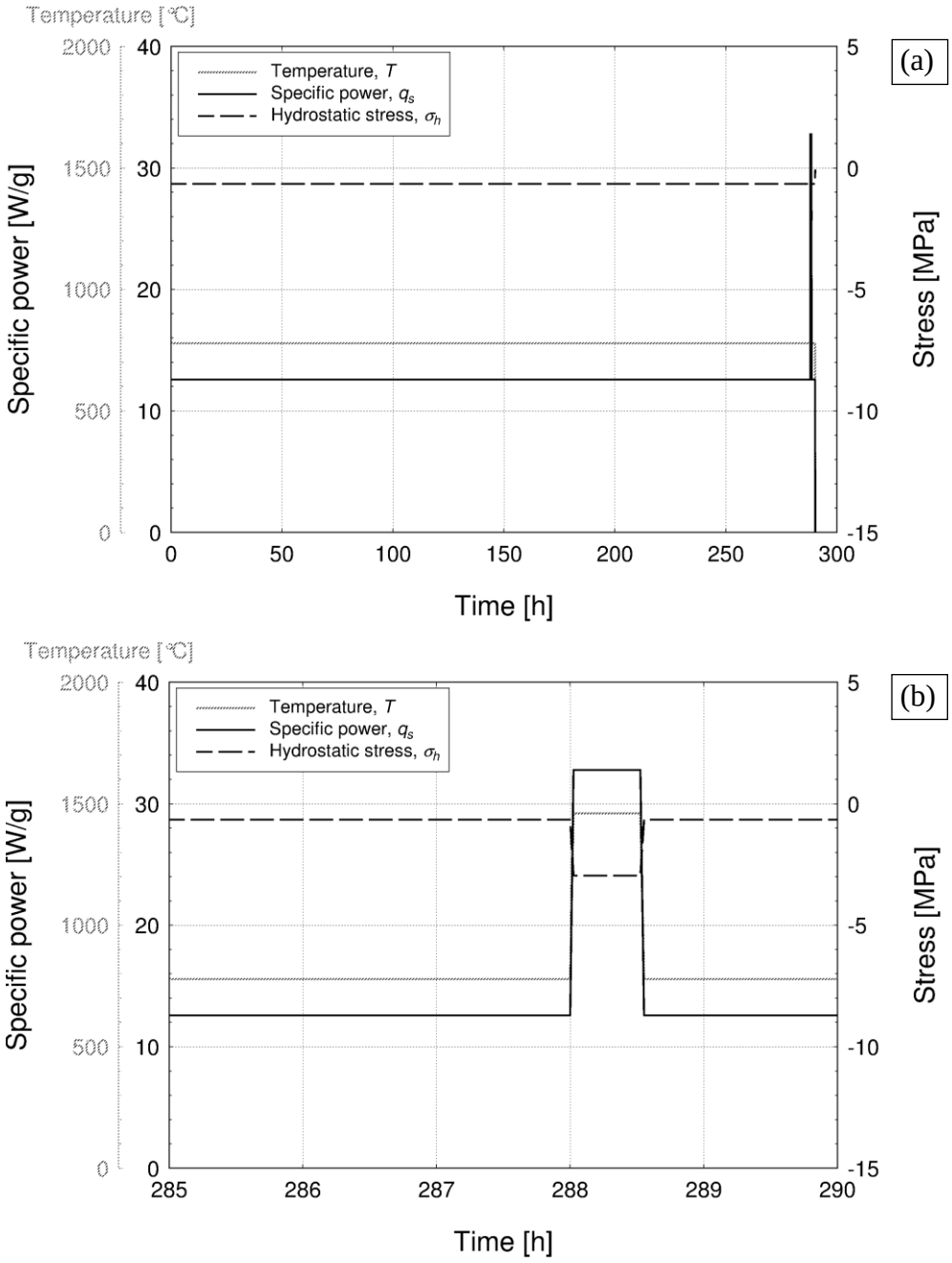

Fig. 4.9. Temperature, specific power, and hydrostatic stress as a function of the time for the SEM zone 4000-F. (a) Entire ramp test, (b) zoom on the ramp.

Due to the lower temperature, the bubble radius and the swelling are lower compared to the SEM zone 4000-A. Also, the bubble over-pressure (Fig. 4.11) is generally higher compared to the SEM zone 4000-A, due to the lower vacancy mobility at lower temperature.
FGR does not occur in this case, since the fractional coverage does not reach the saturation value owing to the reduced bubble growth. When applied to fuel rod analyses, it is therefore expected that the model predicts lower grain-boundary swelling and FGR with increasing distance from the pellet centre, reflecting the spatial dependence of the temperature in the fuel and consistently with the experimental observations (White et al., 2006).

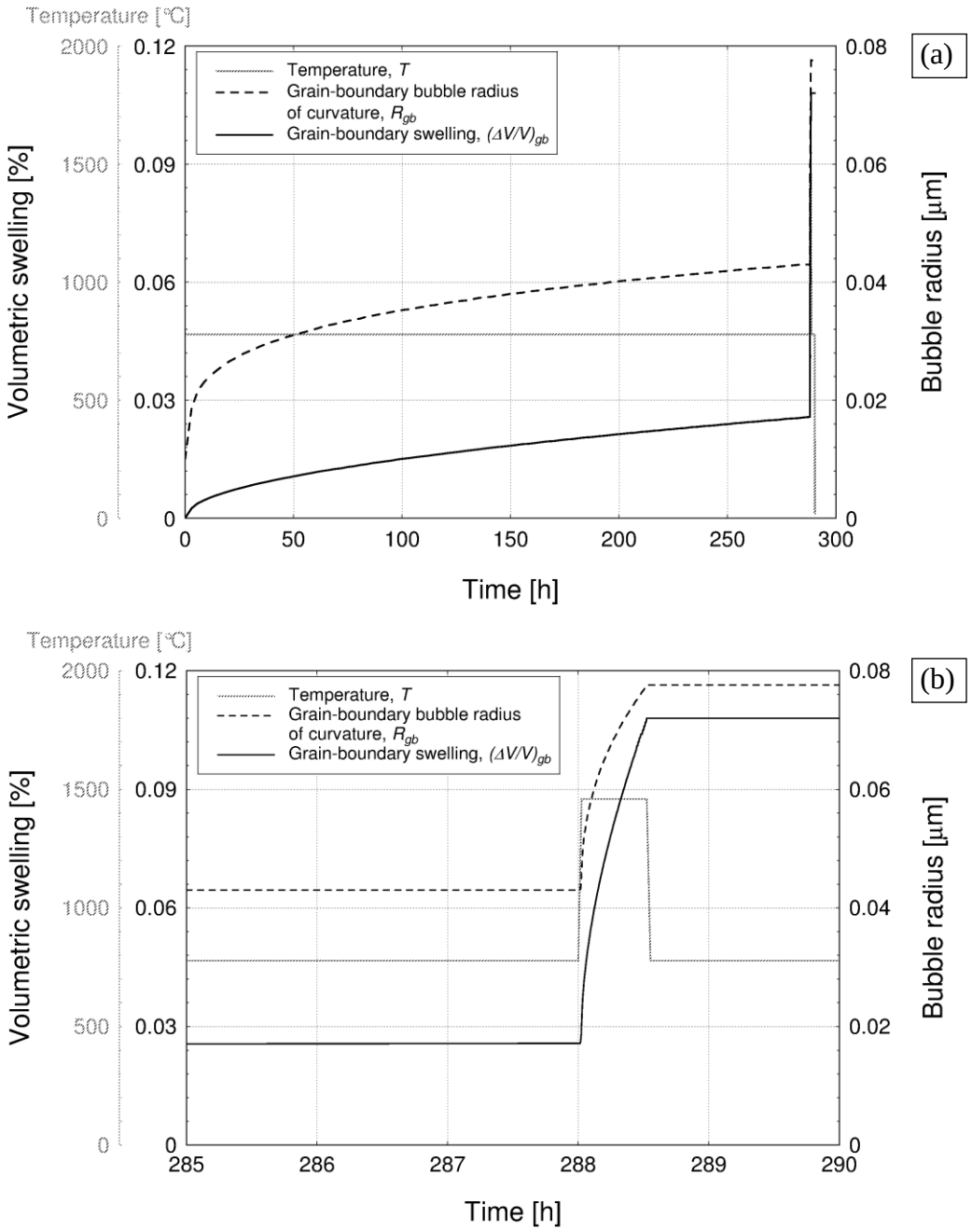

Fig. 4.10. Calculated grain-boundary bubble radius of curvature and grain-boundary swelling as a function of the time for the SEM zone 4000-F. The temperature is also shown (a) Entire ramp test, (b) zoom on the ramp.

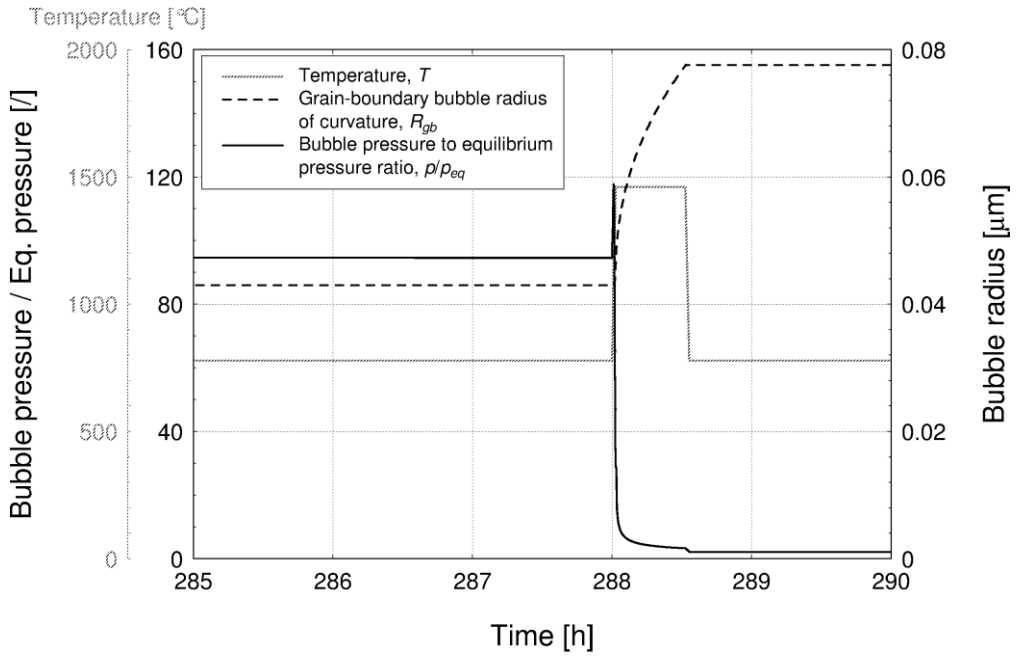

Fig. 4.11. Calculated grain-boundary bubble radius of curvature and ratio of the gas pressure in the bubble to the mechanical equilibrium pressure as a function of the time for the SEM zone 4000-F. The temperature is also shown. Zoom on the ramp is displayed.

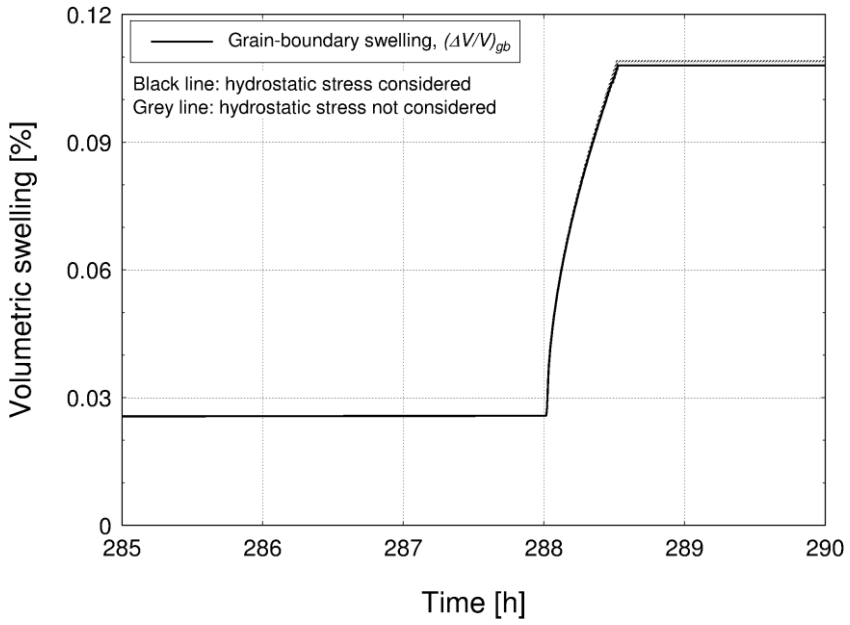

Fig. 4.12. Calculated grain-boundary swelling as a function of the time for the SEM zone 4000-F. The grey line corresponds to the swelling obtained by neglecting the stress-dependence in the model. Zoom on the ramp is displayed.

Figure 4.12 shows the grain-boundary swelling for the SEM zone 4000-F, calculated both considering (black line) and neglecting (grey line) the hydrostatic stress. The dependence of the calculated swelling on the stress is almost negligible in this case, as a consequence of the

low stress and the small bubble radius (that is, the surface tension force is dominant in comparison with the hydrostatic stress).

The time-dependent input quantities are presented in Fig. 4.13 for the SEM zone 4064-A. The fuel specimen was characterized by a burn-up of 20.1 GWd·(tM)$^{-1}$ and was subject to a slow ramp followed by reactor scram (Tables 4.1 and 4.2). The specific power was maintained at about 16 W·g^{-1} during the conditioning time, and raised up to about 35 W·g^{-1} during the power

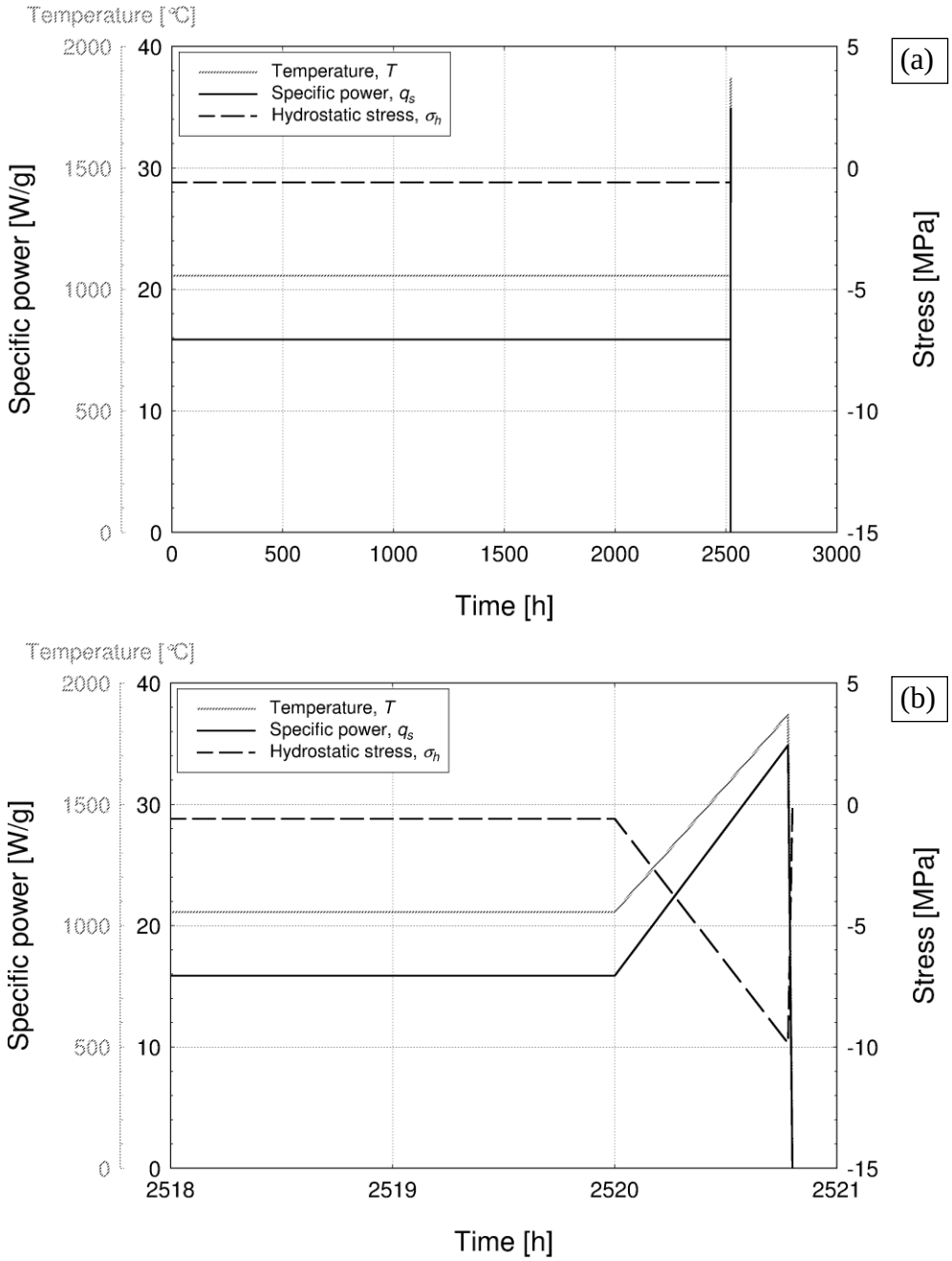

Fig. 4.13. Temperature, specific power, and hydrostatic stress as a function of the time for the SEM zone 4064-A. The temperature is also shown. (a) Entire ramp test, (b) zoom on the ramp.

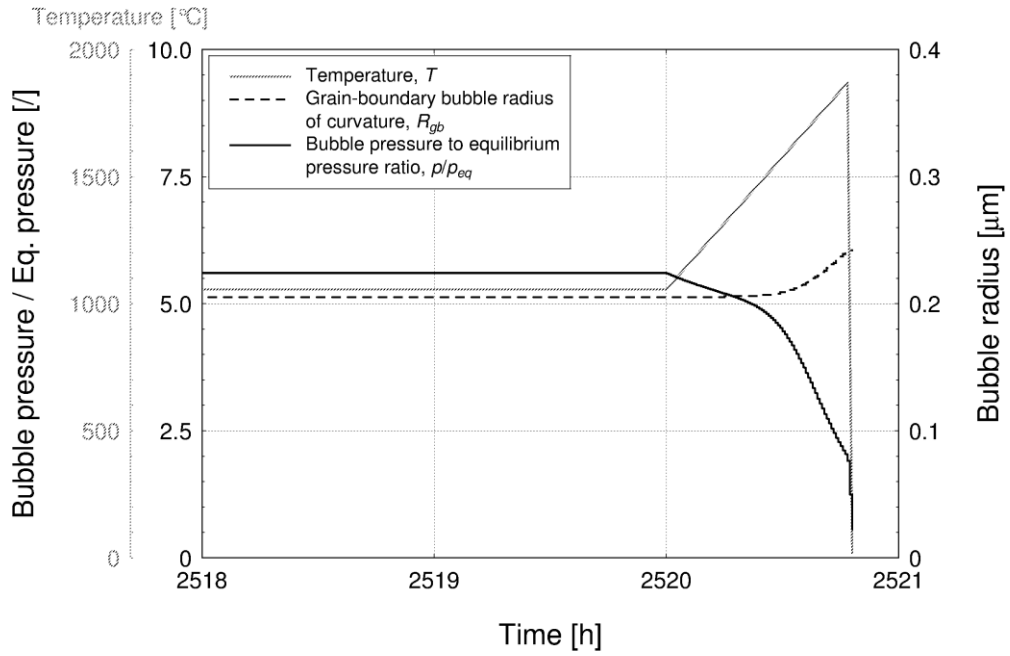

Fig. 4.14. Calculated grain-boundary bubble radius of curvature and ratio of the gas pressure in the bubble to the mechanical equilibrium pressure as a function of the time for the SEM zone 4064-A. The temperature is also shown. Zoom on the ramp is displayed.

ramp. The fuel temperature and the compressive hydrostatic stress reached values of about 1870°C and 10 MPa, respectively, at the top of the ramp.

Figure 4.14 shows the calculated radius of curvature of the grain-boundary bubbles as a function of the time, along with the ratio of the bubble pressure to the mechanical equilibrium pressure. The results confirm the dependence of the grain-boundary bubble growth rate on the temperature, and the general over-pressurization of the grain-boundary bubbles.

Figure 4.15 reports the calculated grain-boundary swelling and FGR as a function of the time. Figure 4.15-a confirms that the model consistently couples the swelling and the FGR, since the swelling rate decreases due to loss of gas from the grain boundaries when FGR commences. The capability of the model to reproduce the incubation behaviour of the FGR can also be appreciated. Figure 4.15-b shows the expected rapid increase of both the swelling and the FGR following the temperature rise during the power ramp.

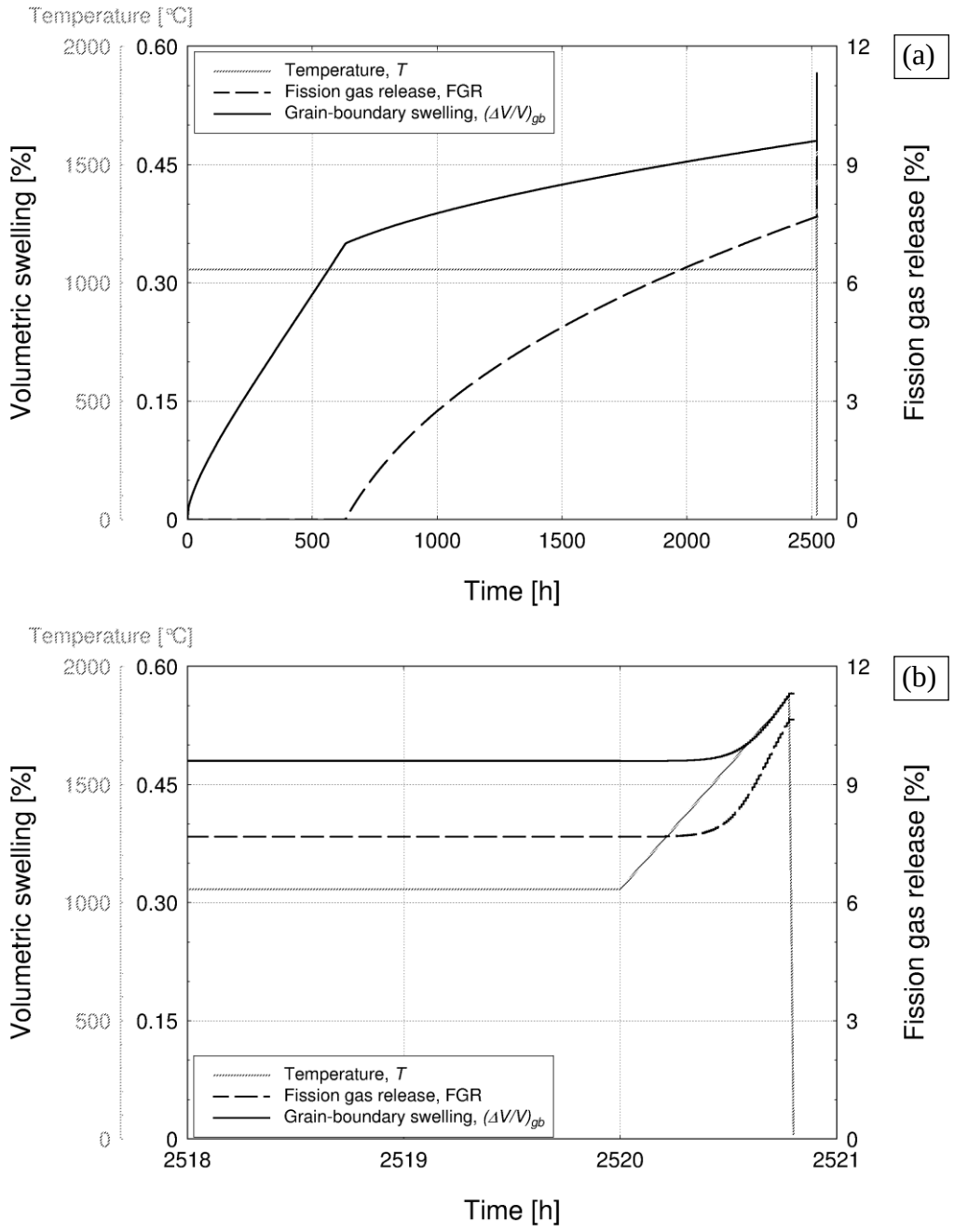

Fig. 4.15. Calculated grain-boundary swelling and fission gas release (defined as the ratio of the released to the generated gas) as a function of the time for the SEM zone 4064-A. (a) Entire ramp test, (b) zoom on the ramp.

As an example of power cycle case, the calculation results are presented for the SEM zone 4159-A. The fuel specimen was characterized by a burn-up of 20.2 GWd·(tM)$^{-1}$, and was subject to 114 power cycles of 4 h duration (Tables 4.1 and 4.3). The time-dependent input quantities (specific power, temperature and hydrostatic stress) are presented in Fig. 4.16. The specific power was about 14 W·g^{-1} at the start of each cycle, and about 21 W·g^{-1} at the top of each cycle. The temperature ranged from 980°C (start) to 1360°C (top), and the compressive hydrostatic stress from 0.3-0.5 MPa (start) to 0.5-35 MPa (top), approximately.

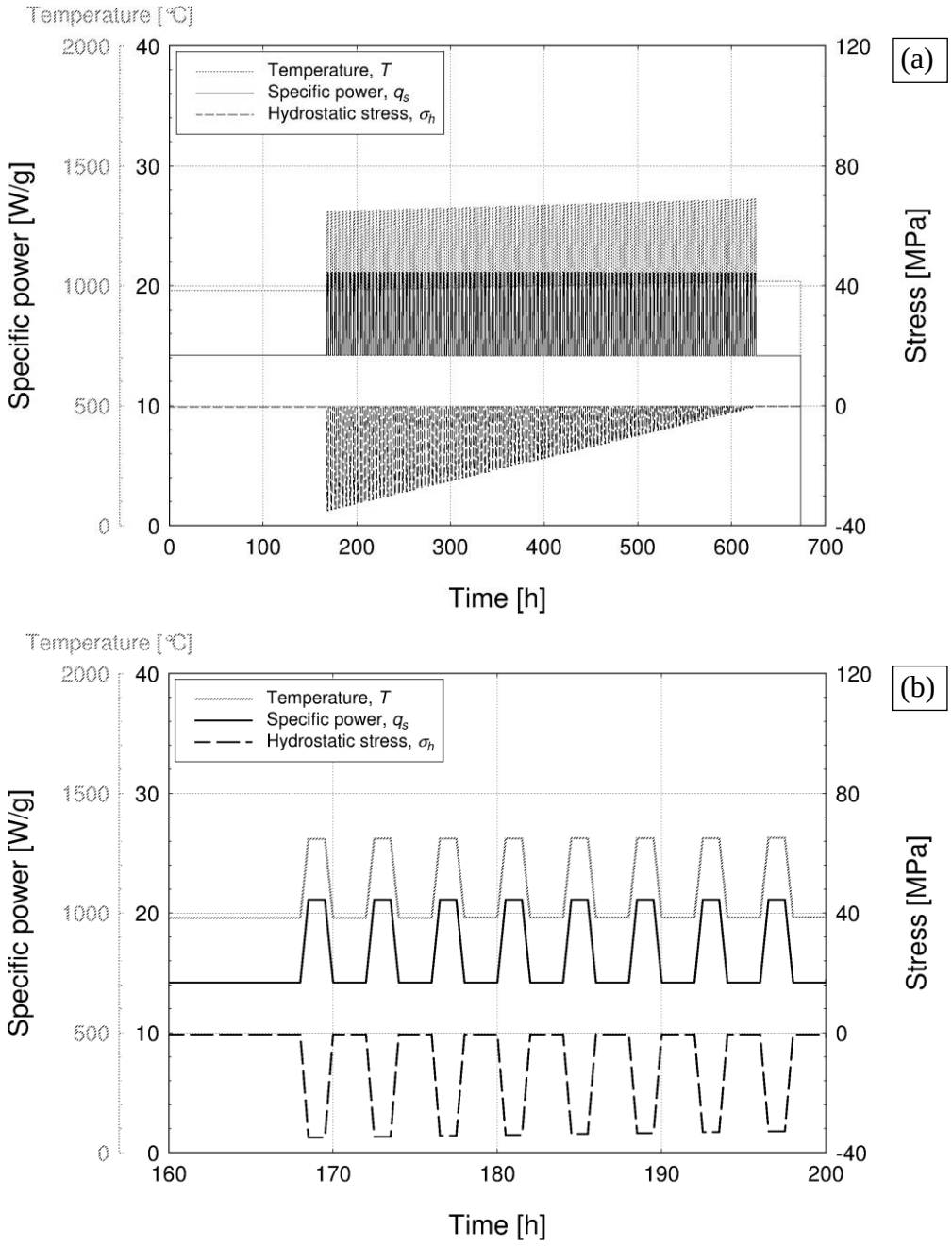

Fig. 4.16. Temperature, specific power, and hydrostatic stress as a function of the time for the SEM zone 4159-A. The temperature is also shown. (a) Entire cycling test, (b) zoom on the first cycles.

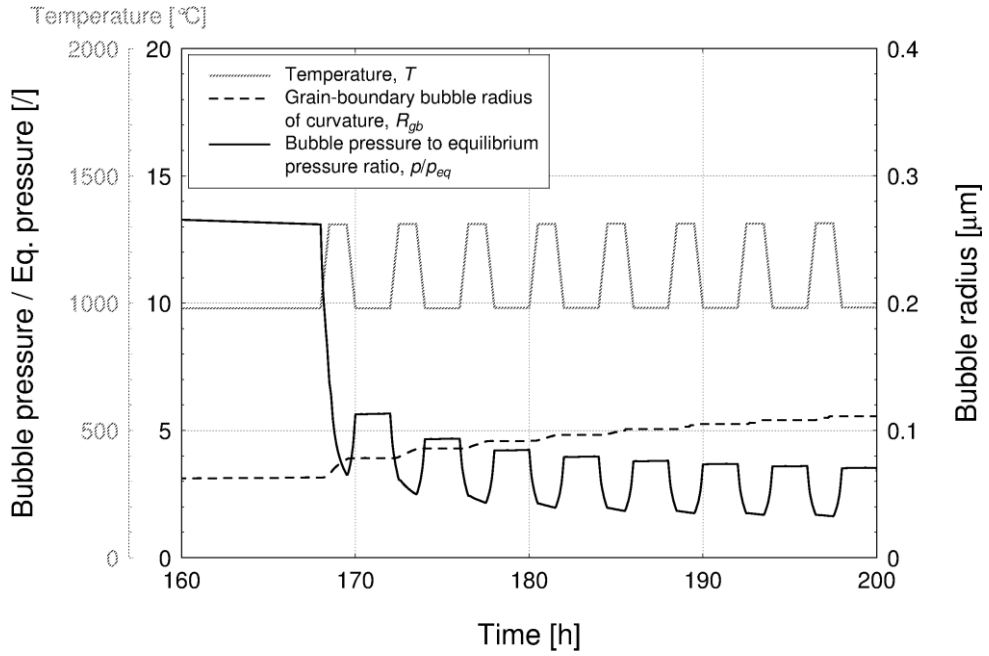

Fig. 4.17. Calculated grain-boundary bubble radius of curvature and ratio of the gas pressure in the bubble to the mechanical equilibrium pressure as a function of the time for the SEM zone 4159-A. The temperature is also shown. Zoom on the first cycles is displayed.

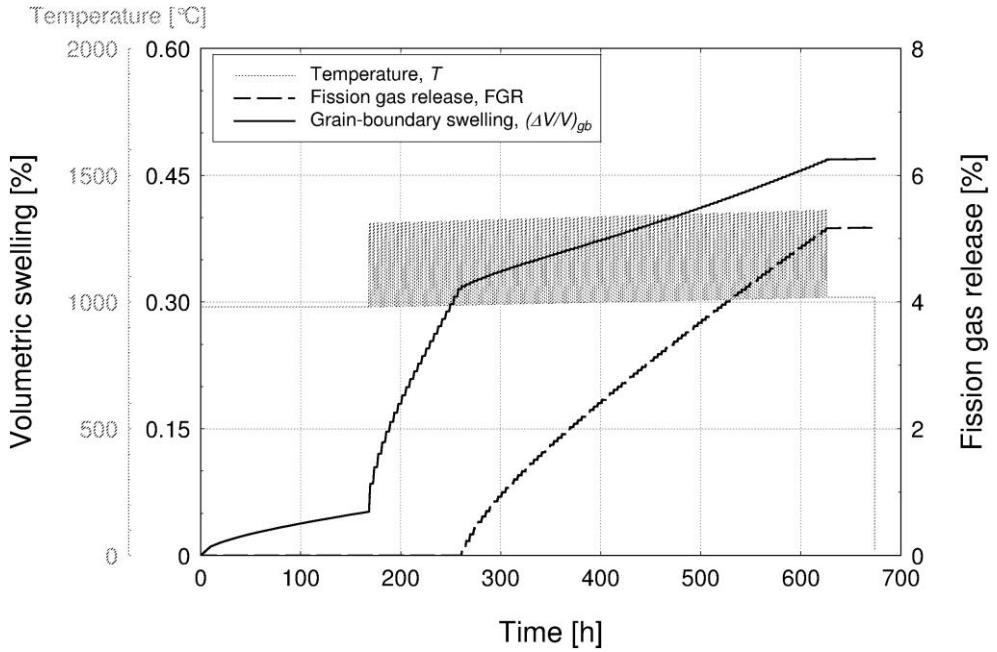

Fig. 4.18. Calculated grain-boundary swelling and fission gas release (defined as the ratio of the released to the generated gas) as a function of the time for the SEM zone 4159-A. The temperature is also shown. The entire cycling test is displayed.

Figure 4.17 displays the radius of curvature of the grain-boundary bubbles and the bubble pressure to equilibrium pressure ratio as a function the time. The temperature-dependence of the bubble radius and over-pressure on the terms discussed above is confirmed.
Figure 4.18 shows the calculated grain-boundary swelling and FGR, pointing out the temperature-dependence of and coupling between these quantities, as well as the incubation behaviour of the FGR. Therefore, the analysis of this case qualitatively confirms the model calculations as a physically sound representation of the relevant processes.

4.4.2 Assessment of the results against experimental data of grain-boundary swelling

As a first step of verification of the model, the comparison of the calculations with all the 46 post-irradiation experimental data of grain-boundary swelling considered in the present work (Table 4.4) is shown in Fig. 4.19. Even if a moderate but systematic under-estimation is observed, this first quantitative assessment points out a reasonable overall agreement, without any tuning of the model parameters. Given the different characteristics of the simulated experiments, the model appears to be applicable to various irradiation conditions. This flexibility is a fundamental advantage pertaining to physics-based models. The discrepancies are expected to be to some degree associated with errors in the specific power, temperature, and hydrostatic stress values used as input data for the present calculations. Moreover, the uncertainties pertaining to the model parameters unavoidably limit the predictive accuracy of any model of fission gas swelling and release (Section 3.1). For example, the model results in terms of both grain-boundary swelling and FGR depend on the calculated arrival rate of gas at the grain-boundaries, that is, on the intra-granular diffusion calculations (Chapter 3). In turn, the

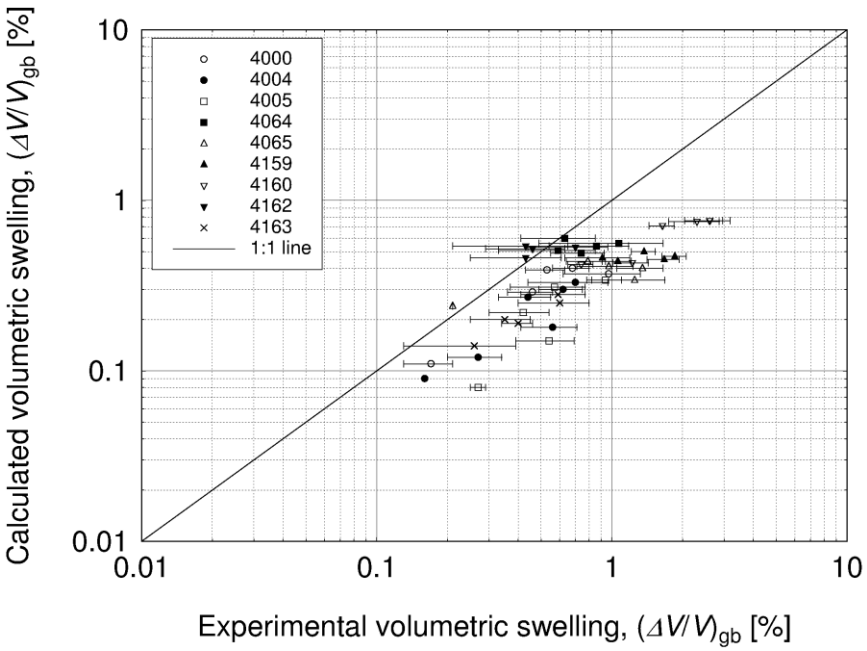

Fig. 4.19. Comparison between the calculated values of grain-boundary swelling and the experimental data. All the 46 cases analysed in the present work are considered.

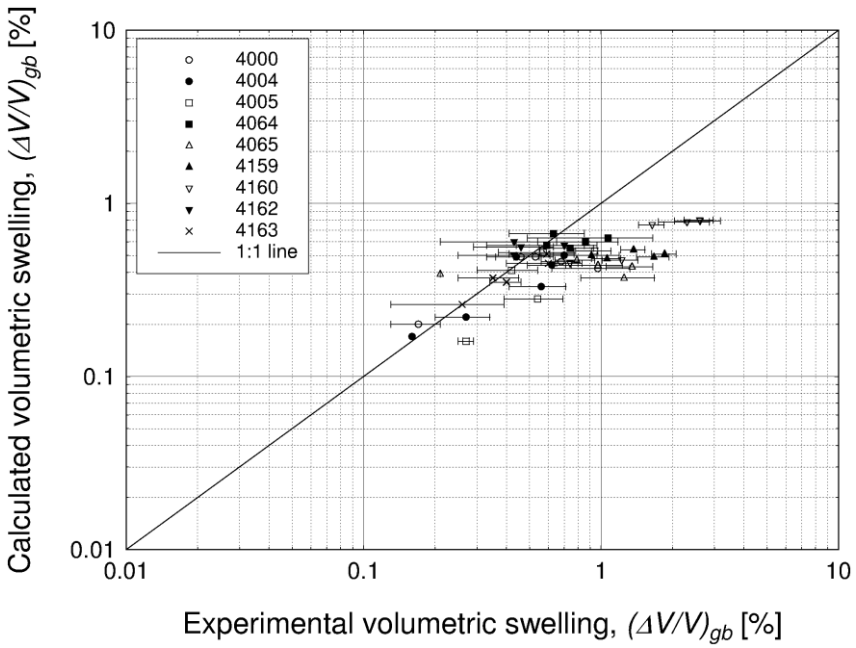

Fig. 4.20. Comparison between the calculated values of grain-boundary swelling, obtained by applying a gas atom diffusion coefficient multiplied by a factor of 5, and the experimental data. All the 46 cases analysed in the present work are considered.

accuracy of the intra-granular diffusion calculations is affected by the uncertainties associated to the model parameters, above all the gas atom diffusion coefficient, which is characterized by an uncertainty of at least a factor of 10 (Section 3.1). In order to preliminarily evaluate the predictive capability of the new model in the light of this intrinsic limitation, a sensitivity analysis was carried out taking into consideration the uncertainties pertaining to the gas atom diffusion coefficient by means of a multiplication by a factor of 5. The results in terms of grain-boundary swelling are reported in Fig. 4.20. A remarkable difference is noticed in comparison with the results presented in Sub-section 4.4.2, pointing out that the systematic under-estimation observed in Fig. 4.19 may be largely ascribed to the uncertainties pertaining to the diffusion coefficient. It is concluded that the level of detail of the physical description adopted in the model is consistent with the intrinsic uncertainties.

4.5 Concluding remarks

As a preliminary step towards the implementation in a fuel rod analysis code, the developed model of fission gas swelling and release was coded as stand-alone version and applied to the analysis of either power ramped or power cycled UO_2 fuel specimens. A qualitative study of the calculation results pointed out that the model consistently reproduces the main peculiarities of the fission gas behaviour, on a physical basis and in accordance with the observations reported in the literature. In particular, the model was proven to consistently describe:

- The development of the grain-boundary gas bubbles in terms of growth kinetics and progressive number density decrease.

- The over-pressurization of the grain-boundary bubbles.
- The coupling between the fission gas swelling and release.
- The dependence of both the fission gas swelling and release on the irradiation time (burn-up).
- The dependence of both the fission gas swelling and release on the temperature.
- The reduction of the fission gas swelling by the compressive hydrostatic stress.
- The reduction and delay of the fission gas release by the compressive hydrostatic stress.
- The incubation behaviour of the fission gas release.

A first quantitative assessment was carried out of the predictive capability of the model against a dataset of grain-boundary swelling measurements from the IFPE database. The systematic comparison of the calculation results with the experimental data, along with a sensitivity analysis on the gas atom diffusion coefficient, pointed out that:

- The average predictive accuracy is reasonable, without any fitting of the model parameters.
- The model is applicable to various irradiation conditions.
- A moderate but systematic under-estimation is observed, which may be largely ascribed to the uncertainties pertaining to the diffusion coefficient.
- The level of detail of the physical description adopted in the model is consistent with the intrinsic uncertainties.

Despite its simplicity, the model therefore appears to provide both a physically acceptable representation of the relevant processes and an effective predictive character. Moreover, due to its physical basis, the model exhibits advantages in comparison with empirical correlations, both in terms of understanding of the relevant physical details and flexibility of application. However, the implementation in a fuel rod analysis code is needed in order to demonstrate the applicability of the model to integral fuel rod analyses, and therefore to the nuclear fuel design and licensing. This is dealt with in the next chapter.

Chapter 5
Model application to the TRANSURANUS code

Abstract. *In this chapter, the implementation of the new model in the TRANSURANUS fuel rod analysis code and the results obtained through integral fuel rod analyses are discussed. After incorporation in the mathematical-numerical framework of the code, the model was evaluated for the simulation of power ramped LWR-UO_2 fuel rods. The application of the model to the TRANSURANUS code was proven to bring about a sound description of the fuel rod behaviour in terms of fission gas swelling and release, with reasonable computational times. The main innovative aspects with respect to the treatments previously adopted in the code include the physical foundation of the model and the coupling between the fission gas swelling and release. Moreover, the experimentally observed dependence of both the fission gas swelling and release on the local hydrostatic stress in the fuel is reproduced. The appropriate modelling of this peculiarity is of high importance in view of the current tendency to extend the flexibility of use (load-following) and the discharge burn-up of the nuclear fuel, which can involve the occurrence of strong PCMI and consequently of high compressive hydrostatic stress in the fuel due to cladding restraint. The comparison of the results with experimental data from the IFPE database in terms of integral fuel rod FGR is presented, pointing out a reasonable overall agreement without any tuning of the physical model parameters, along with some improvements compared to the predictions obtained using the standard models of the TRANSURANUS code. The chapter is organized as follows. In Section 5.1, the main issues and methods concerning the implementation of the model in the TRANSURANUS code are briefly overviewed. In Section 5.2, the experimental databases considered for the verification of the model are described. In Section 5.3, the results of the analyses are presented, showing the capabilities of the new model to reproduce the peculiarities of the fission gas swelling and release, as well as the obtained predictive accuracy in terms of integral fuel rod FGR. Conclusions are drawn in Section 5.4.*

5.1 Implementation of the model in the TRANSURANUS code

After being developed coherently with the goals of the work (Chapters 2 and 3) and subsequently applied as stand-alone version with encouraging results (Chapter 4), the new model of fission gas swelling and release was successfully implemented in the TRANSURANUS fuel rod analysis code. The new model was incorporated in the mathematical-numerical framework of the code as an implicit model, which provides calculation of both the fission gas swelling and release. The model was coupled with the pre-existing TRANSURANUS subprograms for the calculation of the fission gas generation rate and the solution of the intra-granular gas diffusion equation (Section 2.2). Also, the TRANSURANUS models (Lassmann et al., 2011)

were adopted for taking into account the athermal release mechanisms and the grain boundary sweeping effect (Section 2.1). Moreover, the new model was integrated with the MATPRO (1979) model for the swelling due to solid fission products (solid swelling, see Section 1.3), in order to provide a comprehensive and consistent calculation of the fuel swelling.

As a contribution to the non-elastic strains (Section 1.3), the calculated swelling affects the calculated stresses through the mechanical analysis (Appendix A). Since the gas bubbles contribute to the fuel porosity (gaseous porosity), the fission gas swelling also influences the fuel thermal conductivity and temperature. On the other hand, the FGR acts to degrade the thermal conductance of the fuel-cladding gap and to increase the fuel rod internal pressure (Lassmann et al., 2011). In turn, the whole thermo-mechanical analysis provides the input parameters for the model in terms of stresses, temperatures and source term of fission products. The local hydrostatic stress (defined by Eq. 1.25) is considered in the model calculations, while in the fission gas swelling and FGR models currently adopted in the fuel rod analysis codes, the hydrostatic stress is often neglected, or approximated as constant and uniform, or represented by the external pressure of the fuel pellet (e.g., Koo et al., 2000; Suzuki, 2000; Van Uffelen et al., 2004; Lassmann et al., 2011). The new model was therefore implemented as an interactive part of the mathematical-numerical structure of the TRANSURANUS code, providing a consistent matching between the non-linear, stress-dependent fission gas swelling and release calculations and the thermo-mechanical fuel rod analysis. Also, given that the differential equations involved in the model and governing the grain-boundary gas behaviour are solved incrementally (Section 3.3), a simple accuracy-controlling time step criterion was developed and implemented. In a preliminary approach, the following limitation was proven to assure suitable accuracy of the fission gas swelling and release calculations for all the cases analysed in the present work:

$$\Delta t \leq 3.6 \left[N_{gb} \left(\frac{\partial A_{gb}}{\partial t} \right)_g \right]^{-1} \tag{5.1}$$

where Δt [s] is the time step length, N_{gb} [(bub.)·m^{-2}] the number density of grain-boundary gas bubbles, and $(\partial A_{gb}/\partial t)_g$ [m^2·s^{-1}] the variation of the bubble area owing to bubble growth (Section 3.3). The performed calculations pointed out the obtainment of stable numerical solutions in all the considered conditions, with reasonable computational times (see also Sub-section 5.3.3), thus proving the meeting of the numerical convergence and computational cost requirements.

Adopting the new model, the TRANSURANUS code was employed for the analysis of the irradiation experiments of the Super-Ramp and Inter-Ramp Projects (Djurle 1979, 1984). The results in terms of fission gas swelling and release were critically evaluated and compared with the predictions obtained using the standard models of the code. Moreover, the model was evaluated against experimental data of integral fuel rod FGR[7], as discussed in the next sections.

[7] Integral quantities are those referred to the entire fuel rod – e.g., total amounts of fission gas generated and released in the fuel rod, inner rod pressure.

5.2 Experimental databases

The databases of the Super-Ramp and Inter-Ramp Projects refer to PWR-UO_2 and BWR-UO_2 fuel rods, respectively, power ramp-tested in the Studsvik reactor R2 after base-irradiation. During the Super-Ramp and Inter-Ramp Projects, 46 fuel rods (26 and 20, respectively) were tested, that means a total irradiation time of approximately 180 equivalent years in reactor.
The Super-Ramp rods were base-irradiated in a burn-up range of 28 to 45 GWd·(tM)$^{-1}$, while those of Inter-Ramp experienced burn-ups of 8-20 GWd·(tM)$^{-1}$. In addition to PWR and BWR standard type fuel rods, several rods with different design parameters (i.e., gap width, fuel density and grain size, ^{235}U enrichment, annular and solid pellets, gadolinium content) were tested through these two Projects. The main pre-irradiation characterization data for the different groups of rods are summarized in Tables 5.1 and 5.2. An example of base-irradiation and power ramp is shown in Fig. 5.1, and the power ramp test features for all the fuel rods considered in the present work are reported in Tables 5.3 and 5.4. The ramp test consists of a

Table 5.1.
Pre-irradiation data for the different groups of PWR fuel rods from the Super-Ramp Project.

Group	Pellet type	Average burn-up [GWd/tU]	Diametral gap width [μm]	UO_2 density [%TD]	Average grain size [μm]	Enrichment [wt% ^{235}U]
PK1	Standard	33–36	191–200	95*	6.0	3.20
PK2	Standard	41–45	145	94*	5.5	3.21
PK4	Gd_2O_3 (4.1 wt%)	33–34	167–169	94*	5.5	3.19
PK6	Large grain	34–37	145–146	95*	22.0	2.99
PW3	Standard	28–31	170	94**	10.5	8.26
PW5	Annular	32–33	162–165	95**	16.9	5.74

*Calculated from pellet density measurements. **Calculated from measurements of pellet weights and dimensions.

Table 5.2.
Pre-irradiation data for the different groups of BWR fuel rods from the Inter-Ramp Project.

Group	Pellet type	Average burn-up [GWd/tU]	Diametral gap width [μm]	UO_2 density [%TD] *	Average grain size [μm]	Enrichment [wt% ^{235}U]
LR	Standard	8.5–10.3	150	95	8.3	2.82
LS	Standard	8.2–10.4	150	95	8.3	2.82
TR	Standard	10	80	95	8.3	2.82
TS	Standard	9.8	80	95	8.3	2.82
DR	Standard	7.9	150	93	10.9	2.82
HR	Standard	16.6–19.8	150	95	8.4	3.50
HS	Standard	16.6–19.3	150	95	8.4	3.50
BR	Standard	19.9	250	95	8.4	3.50

* Design specifications.

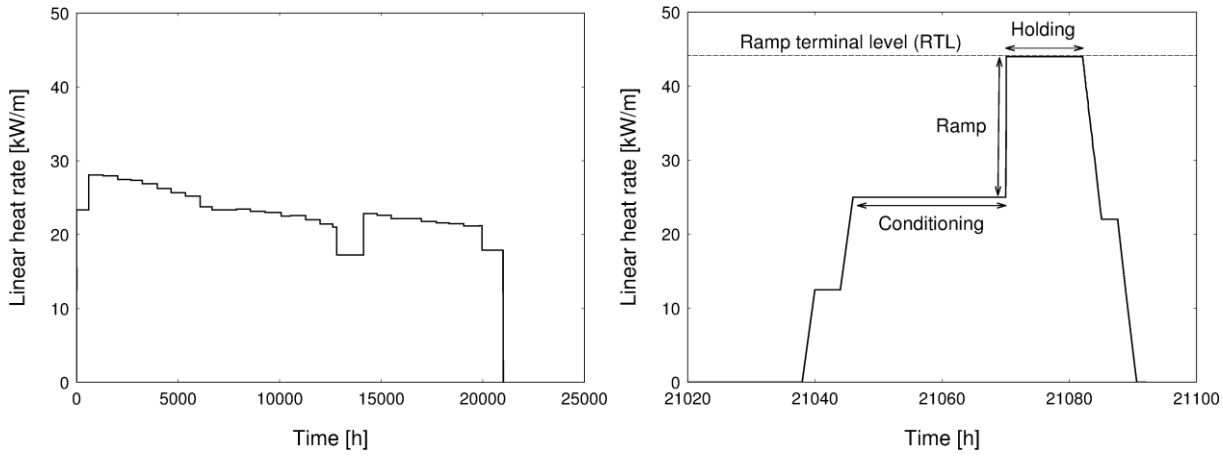

Fig. 5.1. Linear heat rate history in axial peak position for the Super-Ramp PK1-2 rod, during the base-irradiation (left-hand side) and the ramp test (right-hand side).

Table 5.3.
Features of the ramp tests in axial peak position for the Super-Ramp PWR fuel rods considered in the present work.

Rod	Conditioning power level [kW·m^{-1}]	Conditioning time [min]	Power ramp rate [kW·m^{-1}· min^{-1}]	Ramp terminal level [kW·m^{-1}]	Holding time at RTL [min]
PK1-1	25.0	1440	9.0	41.5	720
PK1-2	25.0	1440	8.0	44.0	720
PK1-3	25.0	1440	8.5	47.5	720
PK1-4	25.0	1440	9.5	47.5	720
PK2-1	25.0	1440	8.5	41.0	720
PK2-2	25.0	1440	9.5	46.0	720
PK2-3	25.0	1440	8.5	49.0	720
PK2-4	25.0	1440	8.5	44.0	1°
PK2-S	25.0	1440	8.5	44.0	720
PK4-1	25.0	1440	8.0	39.0	720
PK4-2	25.0	1440	8.5	44.5	720
PK4-3	25.5	1440	11.0	50.5	720
PK6-2	25.5	1440	9.0	40.0	720
PK6-3	25.0	1440	9.0	43.0	720
PK6-S	24.0	1440	10.0	41.0	720
PW3-2	25.5	1440	10.0	35.3	720
PW3-3	25.0	1440	10.0	37.2	720

° Intentionally interrupted.

conditioning time and a subsequent power ramp, followed by a holding time at the ramp terminal level (RTL), and reactor shut-down. With reference to an extensive experimental analysis program and to detailed records of fuel rods power histories (Djurle, 1979, 1984), wide experimental databases were constructed during the Super-Ramp and Inter-Ramp Projects,

Table 5.4.
Features of the ramp tests in axial peak position for the Inter-Ramp BWR fuel rods considered in the present work.

Rod	Conditioning power level [kW·m^{-1}]	Conditioning time [min]	Power ramp rate [kW·m^{-1}· min^{-1}]	Ramp terminal level [kW·m^{-1}]	Holding time at RTL [min]
LR1	29.8	1440	4.8	43.8	1440
LS2	31.8	1440	3.9	43.8	1440
LS3	25.0	1440	3.9	41.8	1440
TR1	30.7	1440	4.2	42.2	1440
DR1	22.9	1440	4.5	43.2	1440
HR2	23.0	1440	4.5	38.0	1440
HR4	29.0	1440	4.2	46.1	1440
HR5	29.0	1440	4.2	47.9	1440
HS1	30.3	1440	3.9	47.8	26°
HS2	24.8	1440	3.9	41.0	1440
BR1	31.1	1440	3.9	51.0	1440

° Intentionally interrupted.

which were made available through the IFPE database (Sartori et al., 2010) and constitute a useful basis for the verification of the fuel rod analysis codes. Most of the rods (namely, the PK6 and PW3 rod groups of the Super-Ramp Project and all the rods of the Inter-Ramp Project) were selected within the FUMEX-III co-ordinated research project of the IAEA (Killeen et al., 2009) as cases of priority interest for comparison and validation of different fuel rod analysis codes.

All the fuel rod irradiation experiments from the Super-Ramp and Inter-Ramp Projects were simulated in the present work by means of the TRANSURANUS code, using the new, implemented model for the calculation of the fission gas swelling and release. The available information on the fuel rod fabrication data and irradiation conditions was critically analysed and consistent input files were set up for the TRANSURANUS code. The analyses were carried out coherently with the power histories and coolant conditions from the beginning-of-life (BOL) to the end of the ramp test (end-of-life – EOL), using the design specifications and pre-irradiation characterization data of the analysed rods provided in (Djurle, 1979, 1984). An example of TRANSURANUS input file used for the fuel rod analyses presented in this chapter is reported in Appendix C. With reference to the various options available to the TRANSURANUS code for the treatment of the other relevant phenomena and material properties, a suitable setup for the test conditions of interest was established on the basis of previous assessments of the code (Luzzi, 2002; Van Uffelen et al., 2007; Di Marcello and Luzzi, 2008; Luzzi et al., 2008; Pastore et al., 2009a, 2009b), taking into account the different specificity of PWR and BWR type fuel rods.

5.3 Results and discussion

5.3.1 Model capabilities

As a first exemplifying case[8], the results of the analysis of the PK1-1 fuel rod from the Super-Ramp Project are presented. The linear heat rate (input quantity) and the calculated fuel

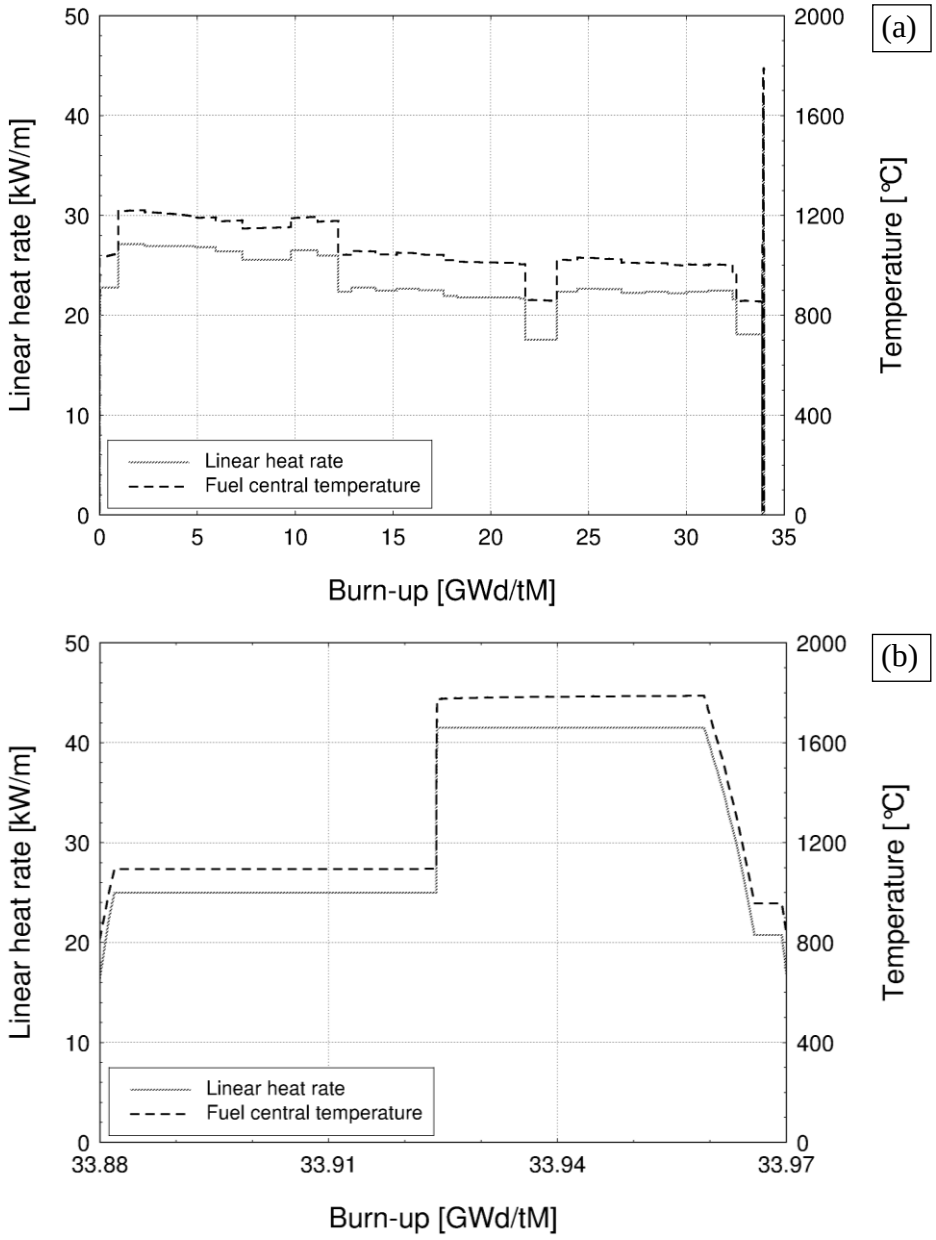

Fig. 5.2. Linear heat rate and fuel central temperature as a function of the burn-up at the mid-plane of the PK1-1 fuel rod. (a) Entire irradiation time, (b) zoom on the ramp test.

[8] Analyses were systematically performed of all the 46 fuel rods of the Super-Ramp and Inter-Ramp Projects. The exemplifying cases discussed here are representative of the general model capabilities observed for the whole set of simulations.

central temperature as a function of the burn-up are shown in Fig. 5.2. The considered axial position is the fuel rod mid-plane (peak linear heat rate and temperature position). The PK1-1 rod was characterized by a peak linear heat rate of 17.5-27.1 kW·m^{-1} during the base-irradiation, approximately, and it was raised from a conditioning power level (CPL) of 25.0 kW·m^{-1} to a RTL of 41.5 kW·m^{-1} during the ramp test (Table 5.3). At the top of the power ramp (beginning of the holding time), the calculated fuel temperature reached a value of about 1770°C at the pellet centre, and about 410°C at the pellet surface. Figure 5.3 displays the radial width of the fuel-cladding gap at the fuel rod mid-plane as a function of the burn-up.

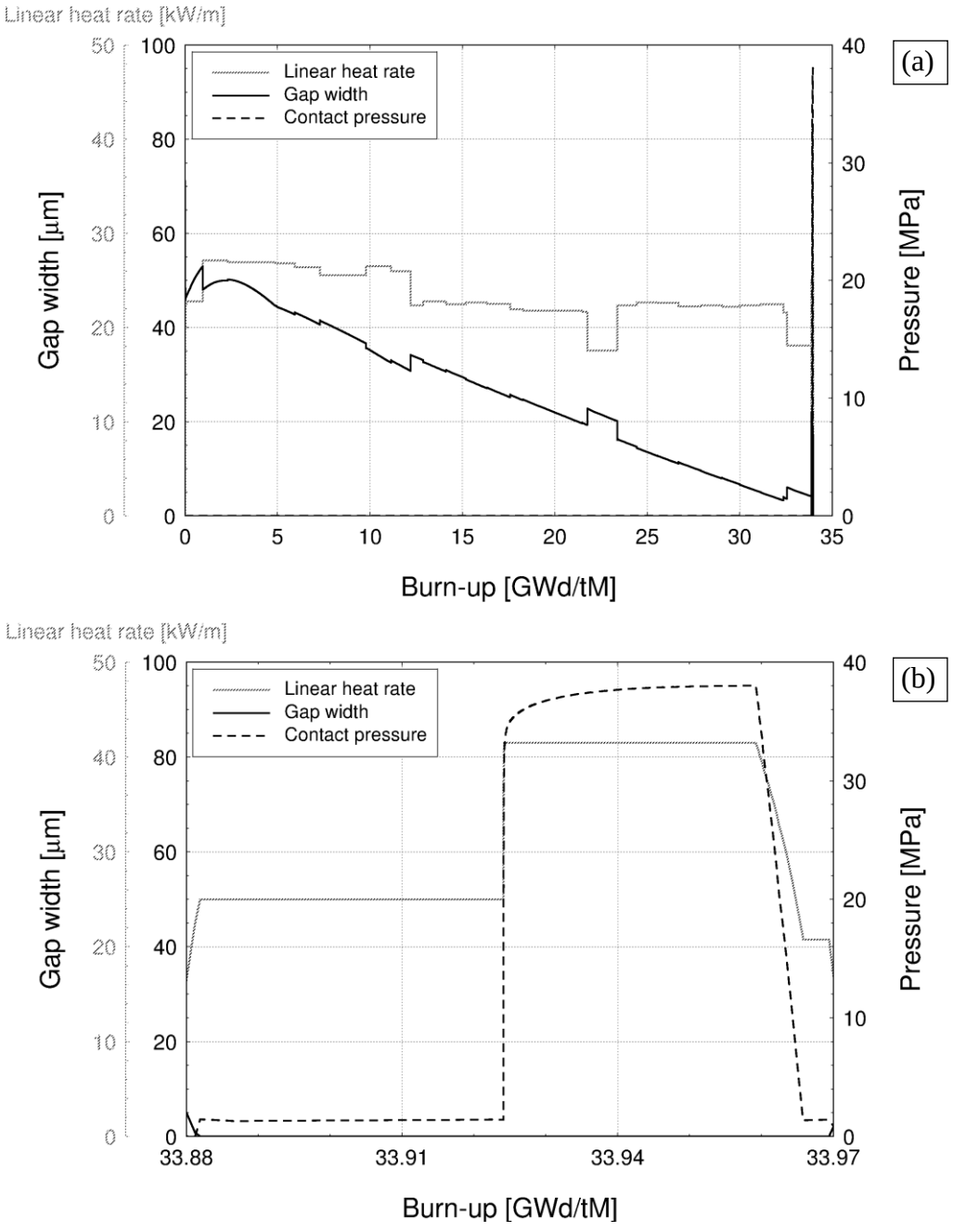

Fig. 5.3. Linear heat rate, radial gap width and fuel-cladding contact pressure as a function of the burn-up at the mid-plane of the PK1-1 fuel rod. (a) Entire irradiation time, (b) zoom on the ramp test.

Starting from the initial value of 100 μm, the gap width abruptly decreases at BOL due to pellet-fragment relocation (Section 1.3). During the early stages of the base-irradiation (burn-up < 2.3 GWd·(tM)$^{-1}$, approximately), the gap width tends to increase due to fuel densification. Subsequently, the gap width progressively reduces as a consequence of the fuel swelling and of the cladding creep-down due to the external coolant pressure. At the beginning of the conditioning time, the gap closes and pellet-cladding mechanical interaction (PCMI) occurs, leading to the onset of fuel-cladding contact pressure (Fig. 5.3). The contact pressure strongly increases during the power ramp as a consequence of the fuel swelling and the differential thermal expansion of the fuel and the cladding, and may determine high compressive hydrostatic stress in the fuel (Section 1.3).

The calculated volumetric fission gas swelling, FGR and temperature for the PK1-1 rod at a burn-up of about 10 GWd·(tM)$^{-1}$ are displayed in Fig. 5.4 as a function of the pellet radius. The considered axial position is the fuel rod mid-plane. The summation of the contributions due to intra-granular and grain-boundary gas bubbles is considered as the fission gas swelling (Section 3.3). The grain-boundary swelling, however, was proven to be the dominant contribution to the calculated fission gas swelling for all the cases analysed in the present work. The FGR is defined as the ratio of the released to the generated gas. It is worth underlining that the gas locally released/generated (hence, the local FGR) is represented in the profile shown in Fig. 5.4, which differs from the integral FGR considered further in this chapter. Figure 5.4 shows that both the calculated swelling and FGR decrease with increasing distance from the pellet centre, reflecting the spatial dependence of the temperature in the fuel. In fact, the temperature drives both the inflow of gas atoms and the vacancy absorption at the grain-boundary bubbles, thus determining the bubble growth and coalescence rate, and in

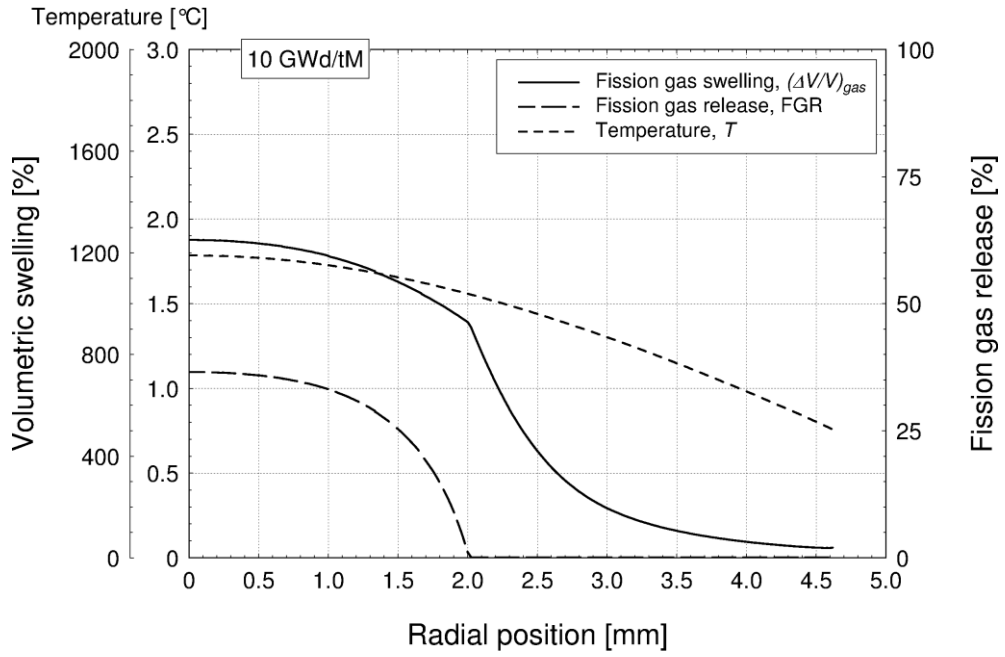

Fig. 5.4. Fission gas swelling, fission gas release and temperature as a function of the pellet radius at the mid-plane of the PK1-1 fuel rod. The figure refers to a burn-up of 10 GWd·(tM)$^{-1}$.

turn the fission gas swelling and release (Sections 3.3 and 4.4). As predicted by the model, the FGR does not occur beyond a certain distance from the pellet centre (apart from the small contribution due to the athermal release that is not perceptible in the figures). The fuel zone, which is not affected by significant FGR, lies towards the decreasing temperatures, where the condition of grain boundary saturation (Section 3.3) is not attained. It is also noticed that the swelling gradient abruptly changes at the radial position delimiting the zone where FGR takes place. In fact, the new model physically considers the swelling as dependent on the amount of gas retained on the grain boundaries, which is in turn affected by the FGR. The curves

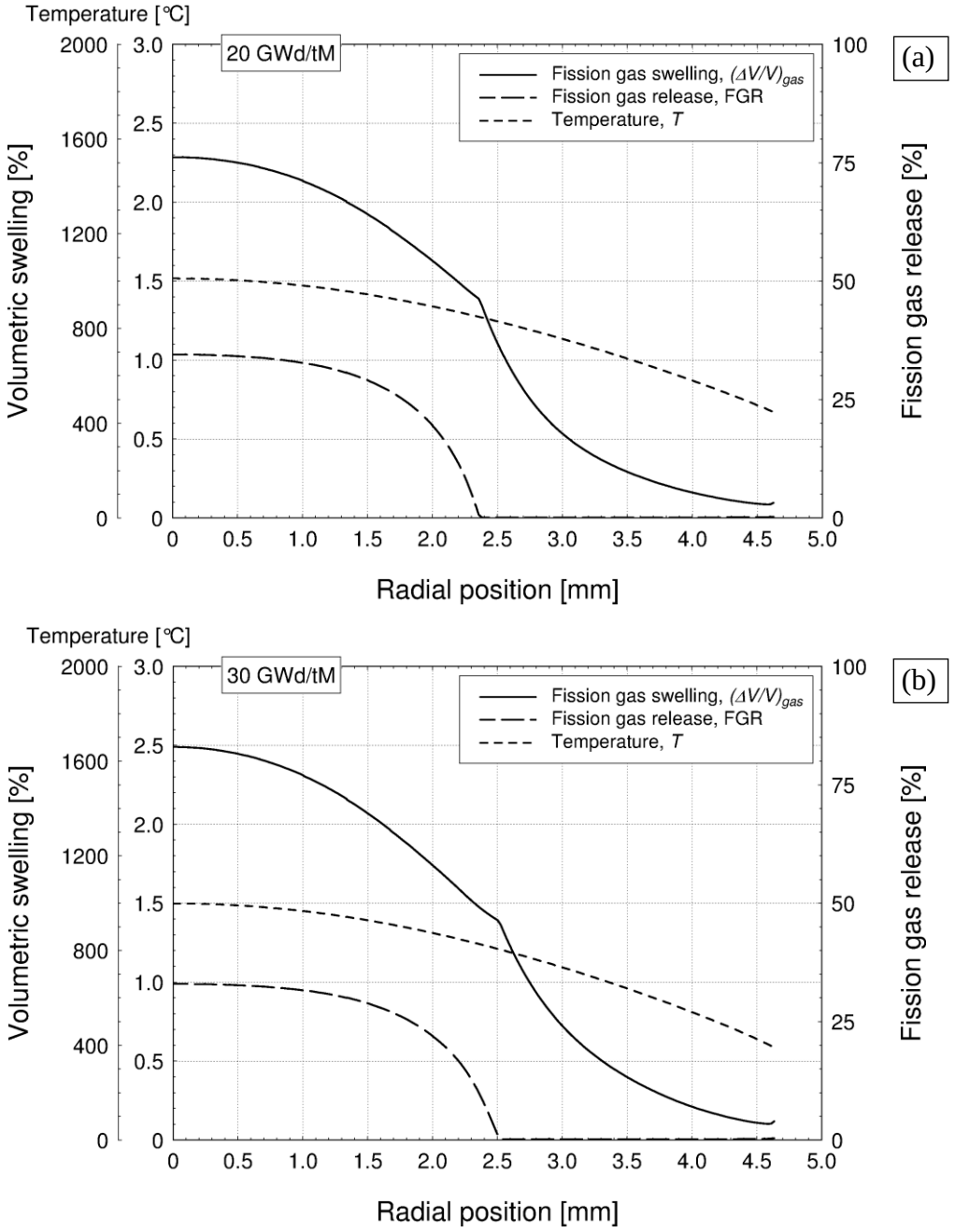

Fig. 5.5. Fission gas swelling, fission gas release and temperature as a function of the pellet radius at the mid-plane of the PK1-1 fuel rod. The graphs refer to burn-ups of (a) 20 GWd·(tM)$^{-1}$ and (b) 30 GWd·(tM)$^{-1}$.

presented in Fig. 5.4 therefore reflect the physical basis of the model and demonstrate the consistent coupling between the fission gas swelling and release. This peculiarity was previously not considered in the TRANSURANUS code (see Sub-section 5.3.3) and represents an innovative contribution of the present work.

Figure 5.5 shows the fission gas swelling, FGR and temperature radial profiles for the PK1-1 rod at burn-ups of about 20 GWd·(tM)$^{-1}$ and about 30 GWd·(tM)$^{-1}$. The dependence of the swelling and the FGR on the temperature is evident. Also, the comparison between Fig. 5.4 and Fig. 5.5 points out that the model catches the dependence of both phenomena on the burn-up. In particular, the swelling increases with burn-up due to the progressive inflow of gas atoms and vacancy absorption at the grain-boundary bubbles (see also Section 4.4). Bubble growth with burn-up is also reflected in progressive broadening of the fuel portion affected by the FGR. The physical complementarity between the fission gas swelling and release can be appreciated.

When also considering the calculated solid swelling (not shown here), the predicted rate of (radially averaged) total volumetric fuel swelling for the PK1-1 rod during the base-irradiation is of about 0.09% per GWd·(tM)$^{-1}$. This value falls within the experimental range of 0.08-0.1% per GWd·(tM)$^{-1}$ for burn-ups ≤ 40 GWd·(tM)$^{-1}$ (Assmann and Manzel, 1977; Zimmermann, 1978; Franklin et al., 1984; Spino et al., 2005), thus proving the physical acceptability and reasonable predictive accuracy of the new model in terms of swelling.

The radial profiles of fission gas swelling, hydrostatic stress and temperature for the PK1-1 rod at the top of the power ramp (beginning of the holding time, see Fig. 5.1) are shown in Fig. 5.6. It is worth pointing out that the discontinuities observed in the stress profile represent a characteristic of the TRANSURANUS code analyses and are related to the different elastic

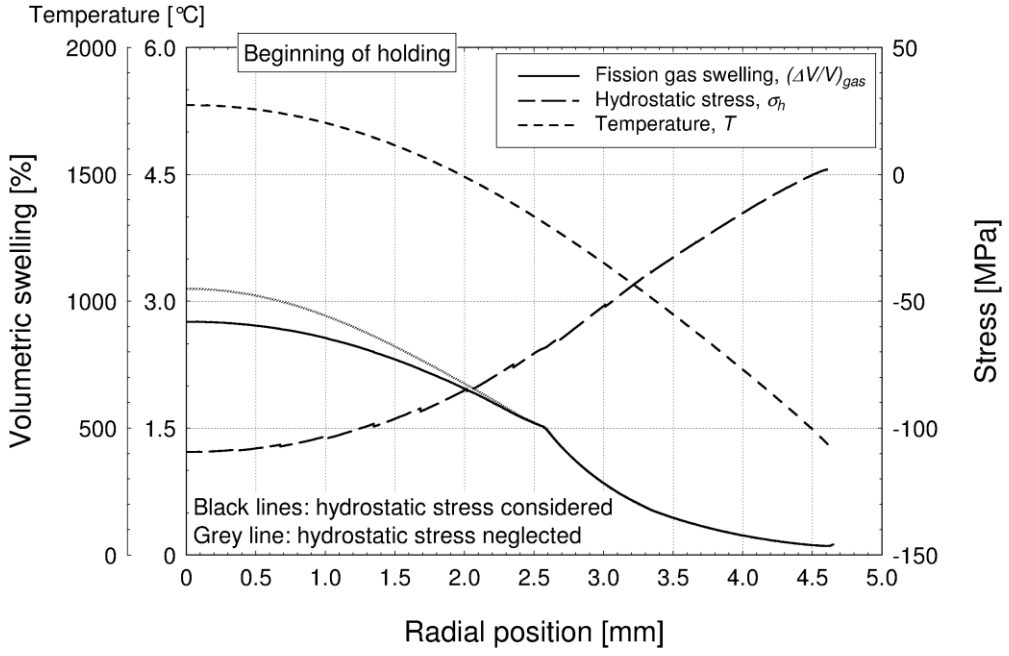

Fig. 5.6. Fission gas swelling, hydrostatic stress (considered to be negative if compressive) and temperature as a function of the pellet radius at the mid-plane of the PK1-1 fuel rod. The fission gas swelling calculated by neglecting the stress-dependence is also shown. The figure refers to the beginning of the holding time.

constants calculated at the different zones of spatial discretization. Due to strong PCMI, high compressive hydrostatic stress takes place in the central zone of the fuel pellet (about 110 MPa at the pellet centre) following the power ramp. High compressive hydrostatic stress due to cladding restraint under PCMI conditions was experimentally observed to significantly affect both the fission gas swelling and release (Zimmermann, 1978; Kogai et al., 1988; Walker et al., 1988, Mogensen et al., 1993; Kashibe and Une, 1997). In particular, the compressive stress reduces the growth rate of the grain-boundary bubbles and consequently suppresses the fission gas swelling, also delaying and reducing the FGR. An improved understanding of the fuel behaviour under PCMI conditions is of high importance in view of the current tendency to extend

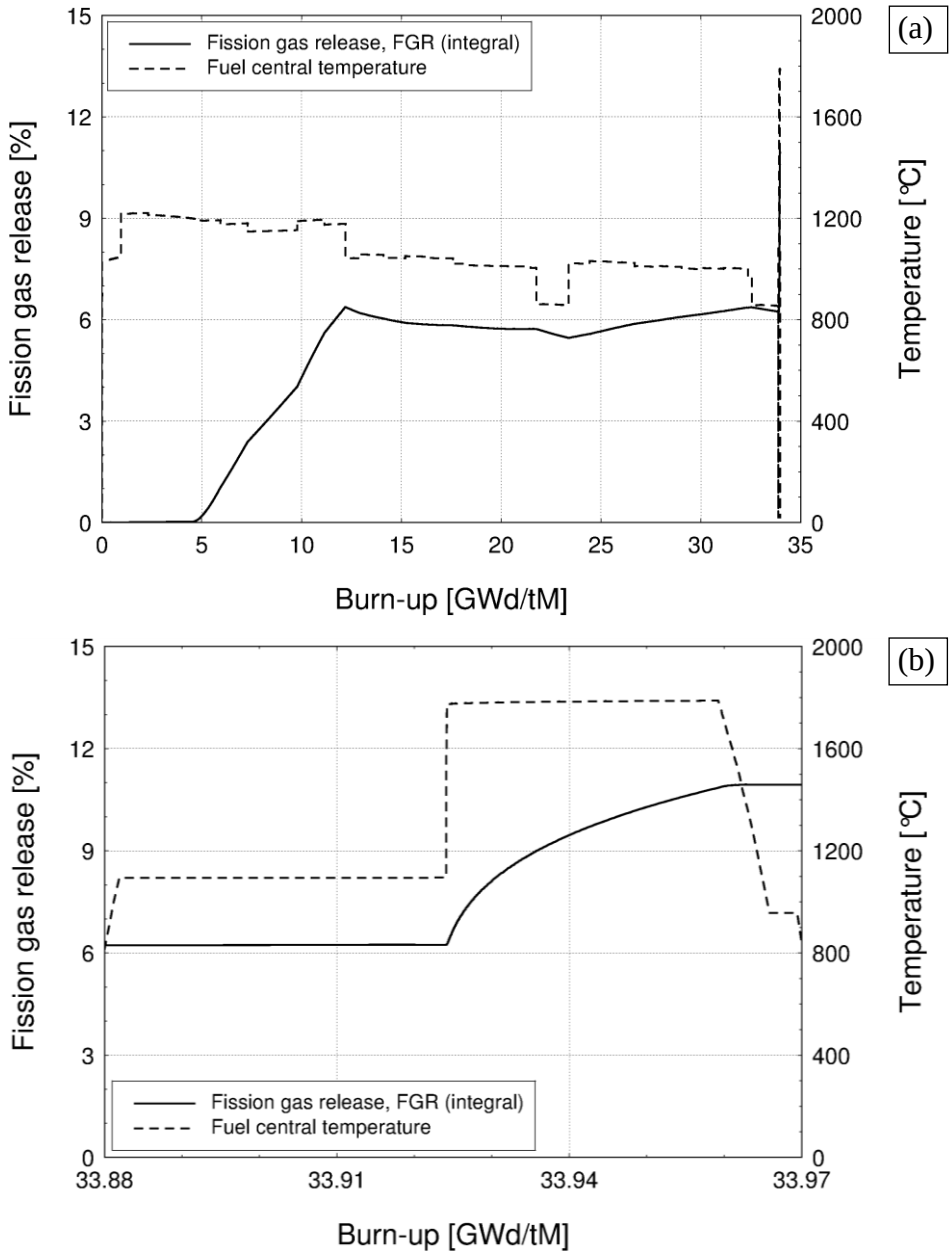

Fig. 5.7. Integral fission gas release and fuel central temperature as a function of the burn-up at the mid-plane of the PK1-1 fuel rod. (a) Entire irradiation time, (b) zoom on the ramp test.

the discharge burn-up and the flexibility of use (load-following) of the nuclear fuel. From this viewpoint, it is essential to develop models that properly take into consideration the dependence of the fission gas swelling and release on the hydrostatic stress (OECD/NEA, 2004). The grey line in Fig. 5.6 represents the swelling profile calculated by neglecting the stress-dependence in the model. The effect of the stress in suppressing the swelling, as reproduced by the new model, is noticeable.

The calculated integral fission gas release[9] and fuel central temperature as a function of the burn-up for the PK1-1 rod are presented in Fig. 5.7. The experimentally observed incubation behaviour of the FGR (Vitanza et al., 1978), and its dependence on the temperature, can be appreciated. Figure 5.8 compares the integral FGR during the ramp test as a function of the burn-up with that obtained by neglecting the stress-dependence in the model. The radially averaged hydrostatic stress in the fuel as a function of the burn-up is also displayed. It is worth emphasizing that the new model consistently takes into account the local hydrostatic stress. The radially averaged value is presented in Fig. 5.8 only as indicative of the development of a high compressive hydrostatic stress during the power ramp test, which results from PCMI and the associated fuel-cladding contact pressure (Fig. 5.3). As for the complementary phenomenon of fission gas swelling, the FGR is remarkably affected by the hydrostatic stress during the power ramp test. As the FGR proceeds by growth of the grain-boundary bubbles, inhibition of the bubble growth by the compressive stress significantly reduced the FGR (see also Section 4.4). It is also noticed that, during the stages of irradiation before the ramp, the FGR in absence of stress is slightly lower than that calculated by considering the stress. This

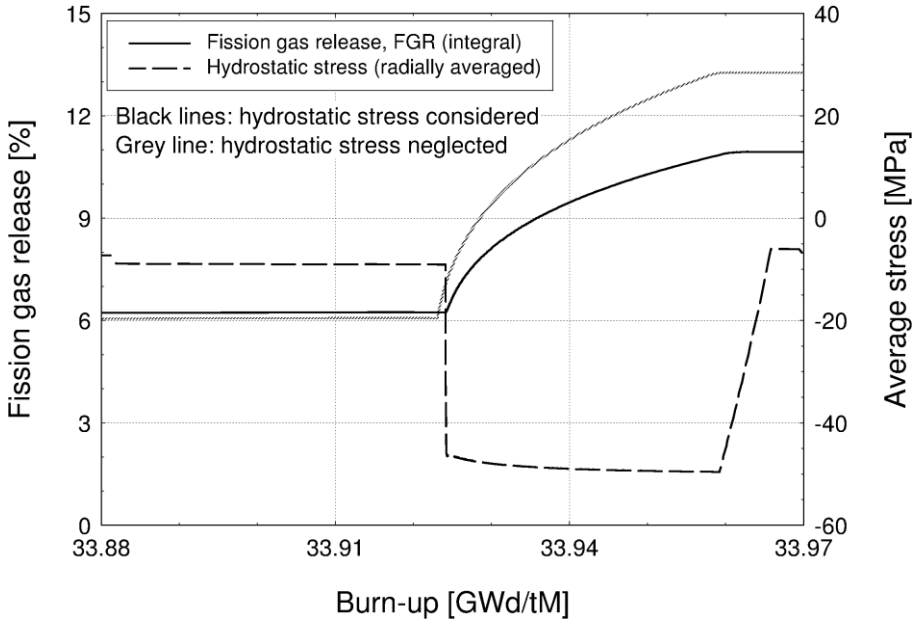

Fig. 5.8. Integral fission gas release and radially averaged hydrostatic stress (considered to be negative if compressive) in the fuel as a function of the burn-up at the mid-plane of the PK1-1 fuel rod. Both curves obtained by considering and by neglecting the hydrostatic stress are shown. Zoom on the ramp test is displayed.

[9] Ratio of the total fission gas released to the total fission gas generated in the fuel rod.

was proven to be ascribed to the higher swelling in absence of stress, that means lower fuel temperature during the base-irradiation in this case since the fuel-cladding gap is narrower, and its thermal conductance is consequently higher. Since the temperature affects the FGR by driving the inflow of gas atoms and the vacancy absorption at the bubbles (Section 3.3), the above indirect effect of the swelling on the FGR turns out to dominate in this case during the stages before the ramp.

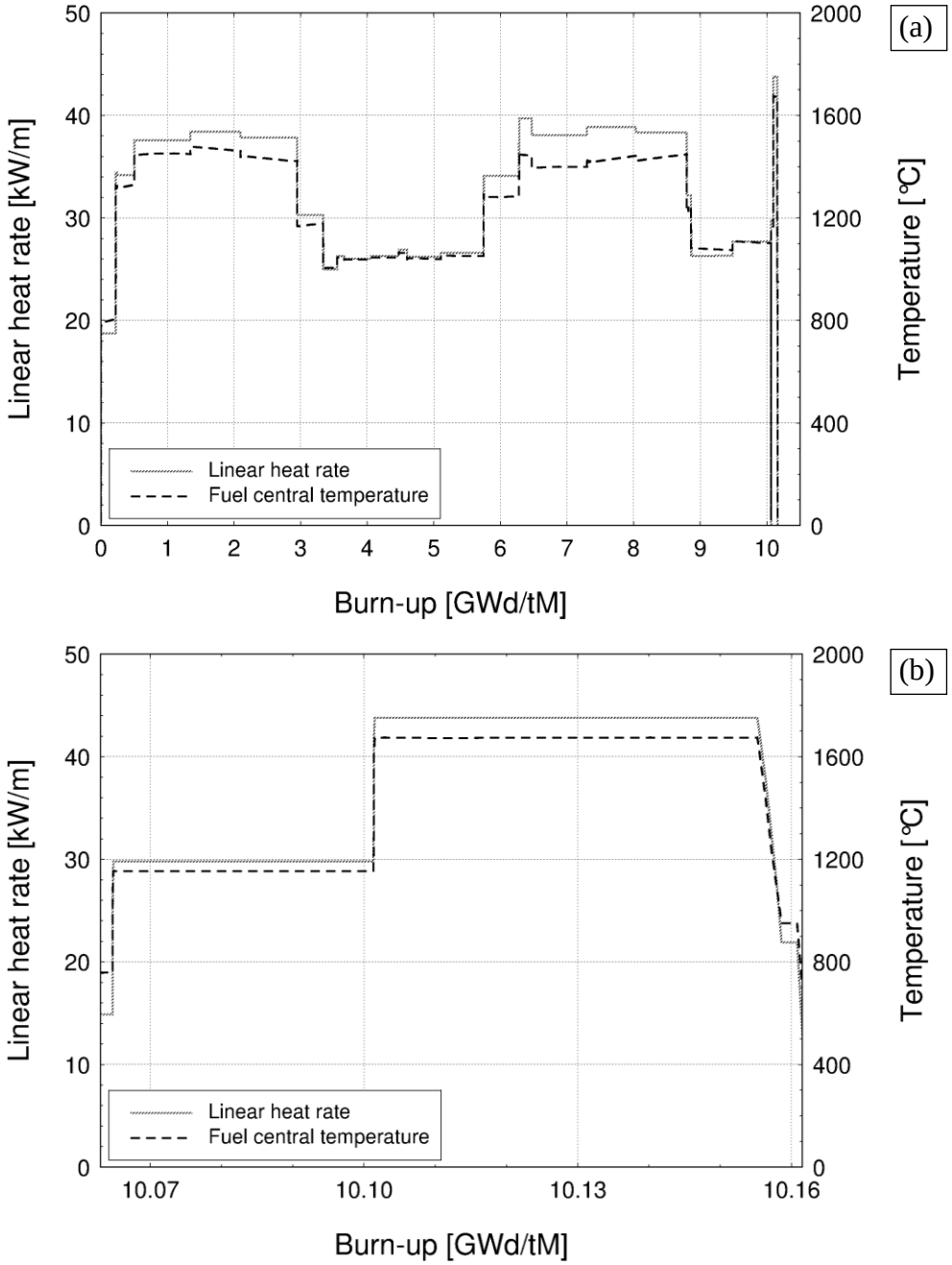

Fig. 5.9. Linear heat rate and fuel central temperature as a function of the burn-up at the mid-plane of the LR1 fuel rod. (a) Entire irradiation time, (b) zoom on the ramp test.

As a further exemplifying case, the results of the analysis of the LR1 fuel rod from the Inter-Ramp Project are presented. The linear heat rate and the calculated fuel central temperature as a function of the burn-up at the fuel rod mid-plane are shown in Fig. 5.9. The LR1 rod was characterized by a peak linear heat rate of 25.0-39.7 $kW \cdot m^{-1}$ during the base-irradiation, approximately, and it was raised from a CPL of 29.8 $kW \cdot m^{-1}$ to a RTL of 43.8 $kW \cdot m^{-1}$ during the ramp test (Table 5.4). At the beginning of the holding time, the calculated fuel temperature reached a value of about 1675°C at the pellet centre, and about 455°C at the pellet surface.

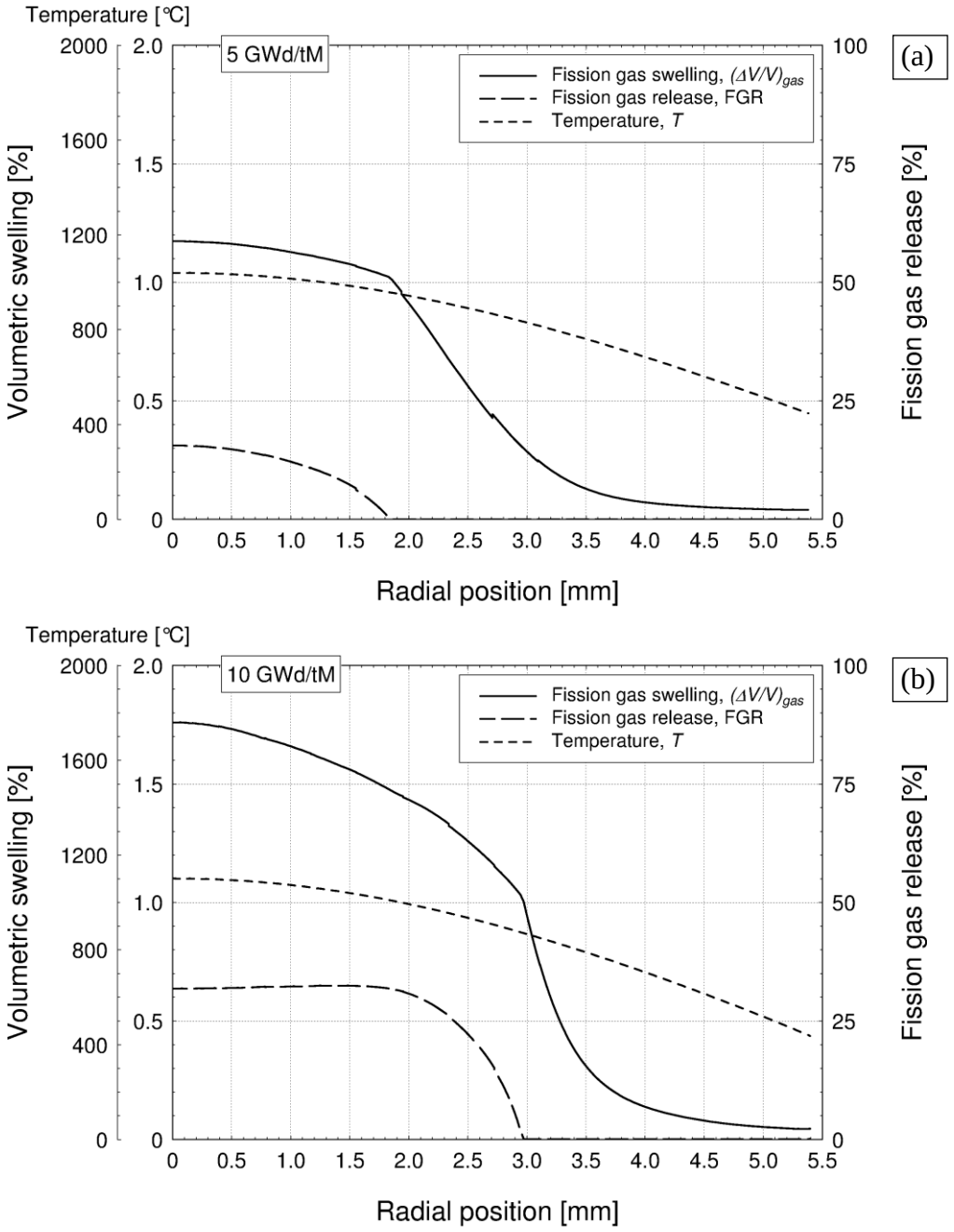

Fig. 5.10. Fission gas swelling, fission gas release and temperature as a function of the pellet radius at the mid-plane of the LR1 fuel rod. The graphs refer to burn-ups of (a) 5 $GWd \cdot (tM)^{-1}$ and (b) 10 $GWd \cdot (tM)^{-1}$.

Figure 5.10 shows the fission gas swelling, FGR and temperature radial profiles at the mid-plane of the LR1 rod, for burn-ups of about 5 GWd·(tM)$^{-1}$ and about 10 GWd·(tM)$^{-1}$. As for the previously discussed case of the PK1-1 rod, the burn-up and temperature-dependence of both swelling and FGR, as well as the consistent coupling between these phenomena, is evident.

Considering the calculated solid swelling, the predicted rate of radially averaged total fuel swelling is of about 0.11% per GWd·(tM)$^{-1}$ for the LR1 fuel rod during the base-irradiation, which is close to the experimental range of 0.08-0.1% per GWd·(tM)$^{-1}$. The reasonable predictive accuracy of the new model in terms of swelling is therefore confirmed.

The radial profiles of fission gas swelling, hydrostatic stress and temperature for the LR1 rod at the top of the power ramp (beginning of the holding time) are shown in Fig. 5.11. Also in this case, the compressive hydrostatic stress in the central zone of the pellet is high (about 60 MPa at the pellet centre), as a consequence of strong PCMI. The calculated swelling is remarkably affected by the stress, as highlighted by the comparison with the curve obtained by neglecting the stress-dependence in the model (grey line). These results confirm the capability of the model to take into account the role of the hydrostatic stress on the fission gas swelling. Since the stresses are computed starting from the calculated strains in the TRANSURANUS code (Appendix A), the stress is in turn affected by the swelling (for instance, note the rapid change of the both the swelling and the stress gradients in correspondence of a pellet radius of about 3 mm in Fig. 5.11).

The calculated integral fuel rod fission gas release and fuel central temperature as a function of the burn-up at the mid-plane of the LR1 rod are presented in Fig. 5.12. The incubation behaviour and temperature-dependence of the FGR can be appreciated. The FGR obtained by

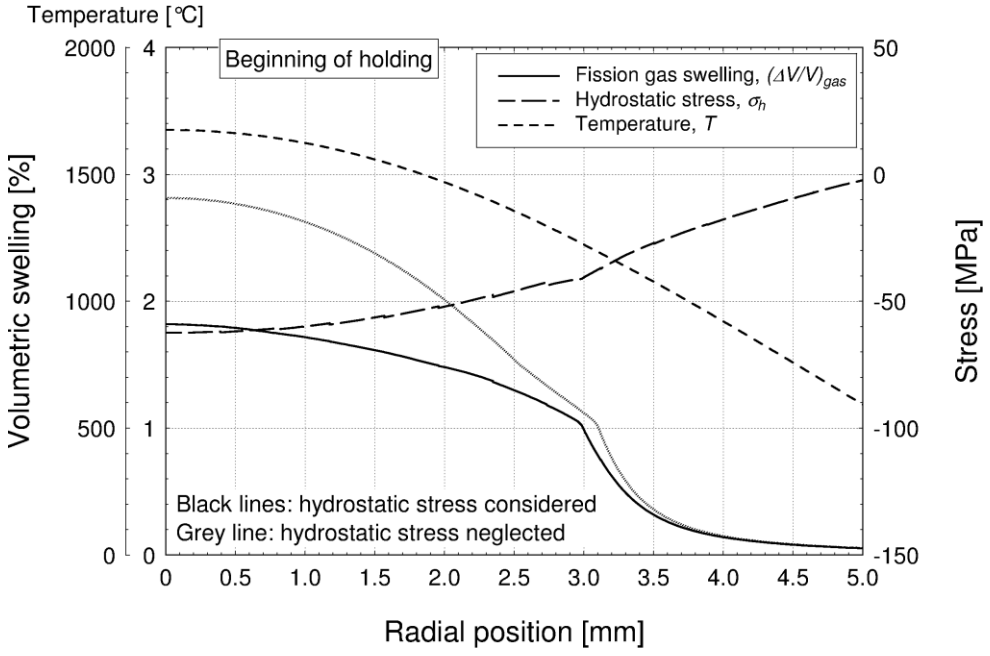

Fig. 5.11. Fission gas swelling, hydrostatic stress (considered to be negative if compressive) and temperature as a function of the pellet radius at the mid-plane of the LR1 fuel rod. The fission gas swelling calculated by neglecting the hydrostatic stress is also shown. The figure refers to the beginning of the holding time.

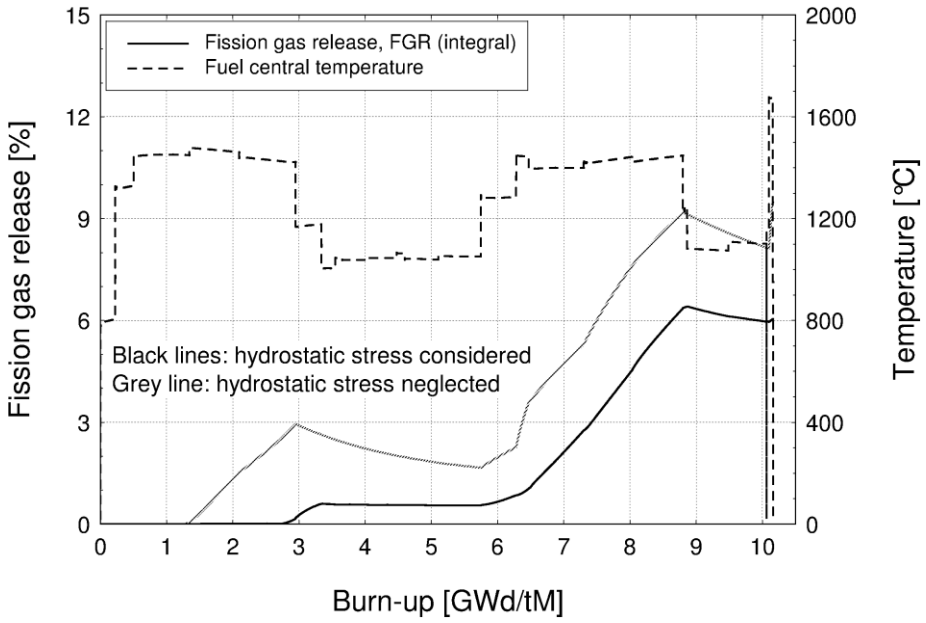

Fig. 5.12. Integral fission gas release and fuel central temperature as a function of the burn-up at the mid-plane of the LR1 fuel rod. The fission gas release calculated by neglecting the hydrostatic stress is also shown. The entire irradiation time is displayed.

neglecting the stress-dependence in the model (grey line) is also reported. The comparison points out the effect of the compressive hydrostatic stress in delaying and reducing the FGR by inhibiting the growth of the grain-boundary bubbles. It is noticed that the stress markedly affects the FGR during the whole irradiation, also in absence of PCMI. These results point out the importance of the role played by the hydrostatic stress, and the significance of developing stress-dependent models of fission gas swelling and release.

5.3.2 Assessment of the results against experimental data of integral FGR

In order to verify the new model of fission gas swelling and release implemented in the TRANSURANUS code, the results of the performed analyses were systematically compared with experimental data of integral FGR, which is a quantity of direct interest for fuel design, licensing, and for safety assessments. Since measurements of fission gas swelling are not available, a direct evaluation of the model in terms of swelling predictions is not viable through the analysis of the Super-Ramp and Inter-Ramp cases. In this work, the model was evaluated in terms of swelling predictions only as stand-alone version (Section 4.4), and a verification in these terms through integral fuel rod analyses would be useful in perspective. However, given the interrelation between the integral FGR and the other multiple aspects of the fuel rod thermo-mechanical behaviour, the results presented in this sub-section are indicative of the overall performance of the new model integrated in the TRANSURANUS code.

Experimental data of integral FGR at the EOL are available for 18 rods of the Super-Ramp Project and 11 rods of the Inter-Ramp Project. All these cases are considered here, except for the Super-Ramp rod PK4-S, because the corresponding experimental FGR is stated as

unreliable (Djurle, 1984). Being a highly non-linear process, strongly influenced by the temperature and feedback effects, accurate modelling of the FGR by means of the fuel rod analysis codes is recognised to be difficult (IAEA, 1998). Moreover, the calculated integral FGR is influenced by the uncertainties pertaining to the whole fuel rod analysis. For instance, Bernard et al. (2002) found that a 5% uncertainty on the calculated temperature could lead to a 30% uncertainty on the calculated FGR. Finally, the accuracy of the predictions is unavoidably limited by the uncertainties pertaining to the model parameters like the fission gas diffusion coefficient (Section 3.2 and Section 4.4). In view of these uncertainties, a deviation within a factor of 2 between the predicted and the experimental values of FGR is commonly regarded as satisfactory.

The comparison between the FGR results obtained by using the new model and the experimental values at the EOL for the Super-Ramp cases is presented in Fig. 5.13. The overall agreement is good. The average deviation between the predicted and the experimental values is a factor of about 1.5.

The comparison between the calculated and the experimental FGR at the EOL for the Inter-Ramp cases is presented in Fig. 5.14. On average, the predicted values deviate from the experimental ones by a factor of about 1.8. However, a significant over-prediction is observed of the FGR values lower than 10%. Indeed, it is known that the region of FGR of the order of 1% is extremely difficult to predict accurately by means of the fuel rod analysis codes (IAEA, 1998).

It is concluded that the new model of fission gas swelling and release applied to the TRANSURANUS code allows a reasonable predictive accuracy in terms of FGR, without applying any fitting to the model parameters. Also, the overall agreement appears to be consistent with the intrinsic uncertainties.

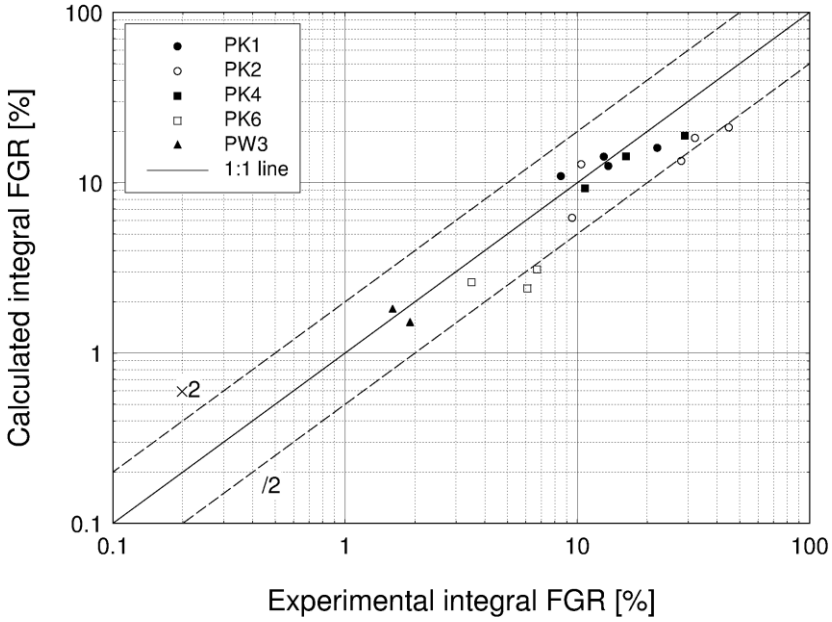

Fig. 5.13. Comparison between the calculated values of integral fission gas release at the EOL and the experimental data for the Super-Ramp cases.

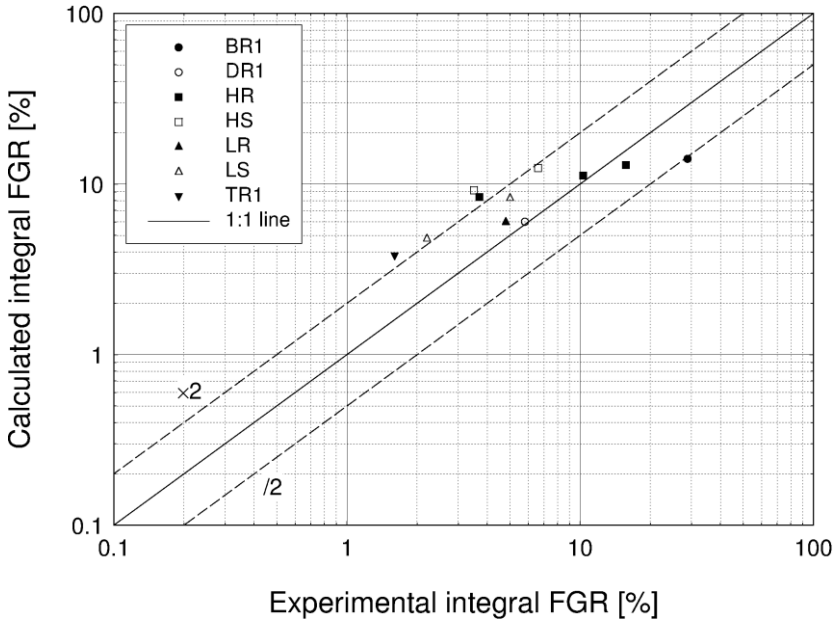

Fig. 5.14. Comparison between the calculated values of integral fission gas release at the EOL and the experimental data for the Inter-Ramp cases.

5.3.3 Comparison with the standard models of the TRANSURANUS code

In order to compare the new model with the standard models of the TRANSURANUS code in terms of capability to represent the peculiarities of the fission gas swelling and release, the representative case of the PK1-1 fuel rod is considered. Figure 5.15 shows the linear heat rate as a function of the burn-up at the rod mid-plane during the ramp test. Figure 5.16 adds the contact pressure between the fuel and the cladding, and the radially averaged hydrostatic stress in the fuel. As mentioned in Sub-section 5.3.1, the fuel-cladding gap is closed during the whole ramp test of the PK1-1 rod, and contact pressure consequently takes place. As a result of the fuel swelling and the differential thermal expansion of the fuel and the cladding, the contact pressure strongly increases during the power ramp and the subsequent holding time, causing the development of high compressive hydrostatic stress in the fuel (Fig. 5.16).
Figure 5.17 shows the radial profiles of fission gas swelling calculated by using the new model, at the significant instants highlighted in Fig. 5.15 (start of the ramp and end of the holding time). The partial inhibition of the fission gas swelling by the compressive hydrostatic stress, as taken into account by the new model, is pointed out by the comparison between the curves obtained by considering (black lines) and neglecting (grey lines) the hydrostatic stress. In particular, the swelling at the end of the holding time would be remarkably higher in absence of compressive hydrostatic stress, as evidenced by the difference between the dashed lines in Fig. 5.17. The predicted swelling is therefore considerably suppressed during the power ramp and the subsequent holding time by the high compressive hydrostatic stress that develops in the fuel as a consequence of strong PCMI. The difference between the full black line (start of the ramp) and the dashed black line (end of the holding time) in Fig. 5.17 represents the increment of fission gas swelling during the ramp and the subsequent holding time.

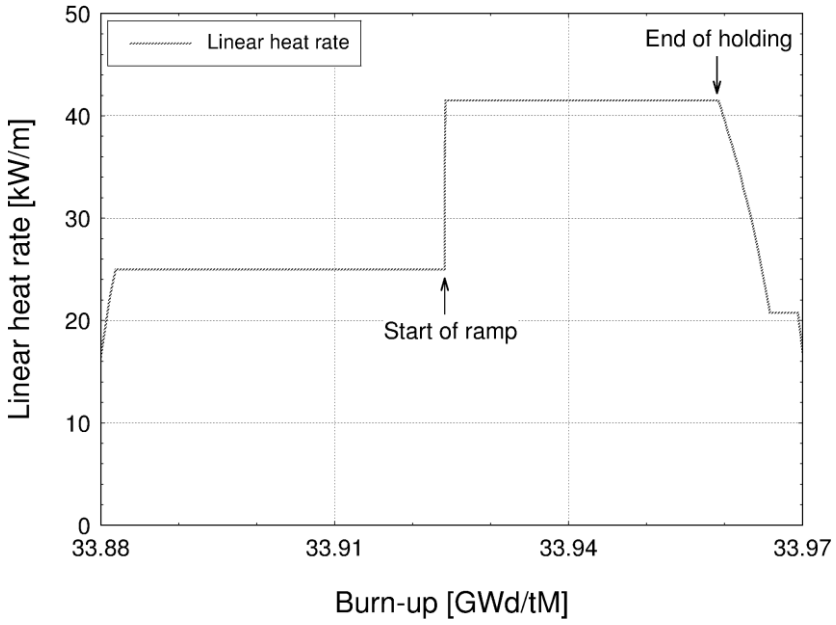

Fig. 5.15. Linear heat rate as a function of the burn-up at the mid-plane of the PK1-1 fuel rod. Zoom on the ramp test is displayed. The two significant instants considered further in this sub-section are highlighted.

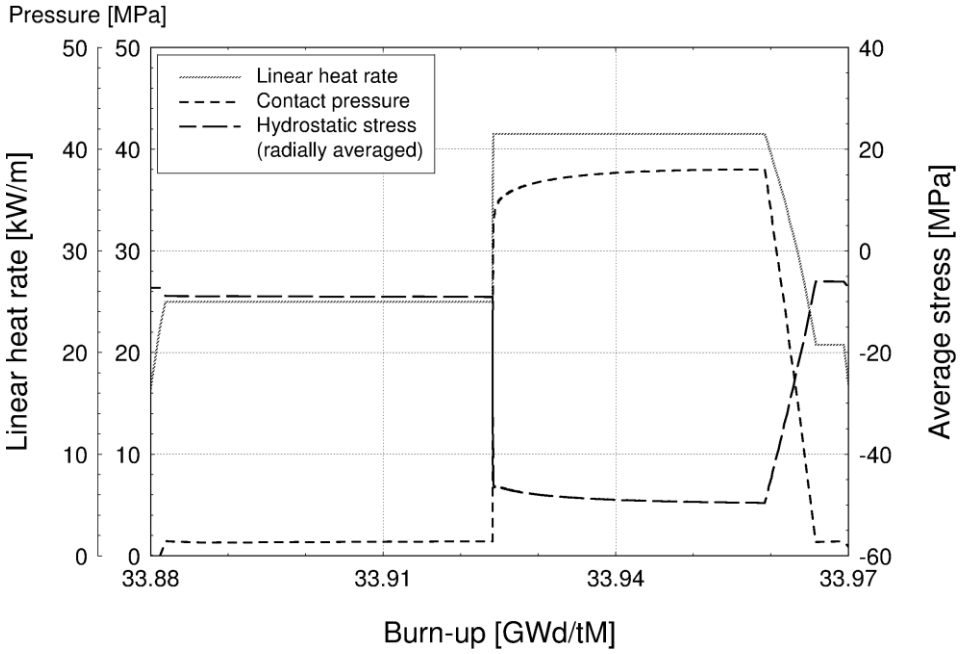

Fig. 5.16. Linear heat rate, fuel-cladding contact pressure and radially averaged hydrostatic stress (considered to be negative if compressive) in the fuel as a function of the burn-up at the mid-plane of the PK1-1 fuel rod. The figure refers to the adoption of the new model. Zoom on the ramp test is displayed.

Although partially inhibited by the compressive hydrostatic stress, the calculated fission gas swelling significantly increases during this period, as a consequence of the high power and temperature. The significance of the fission gas swelling during power ramps is confirmed by indications from the literature and has safety-relevant consequences in terms of cladding strain

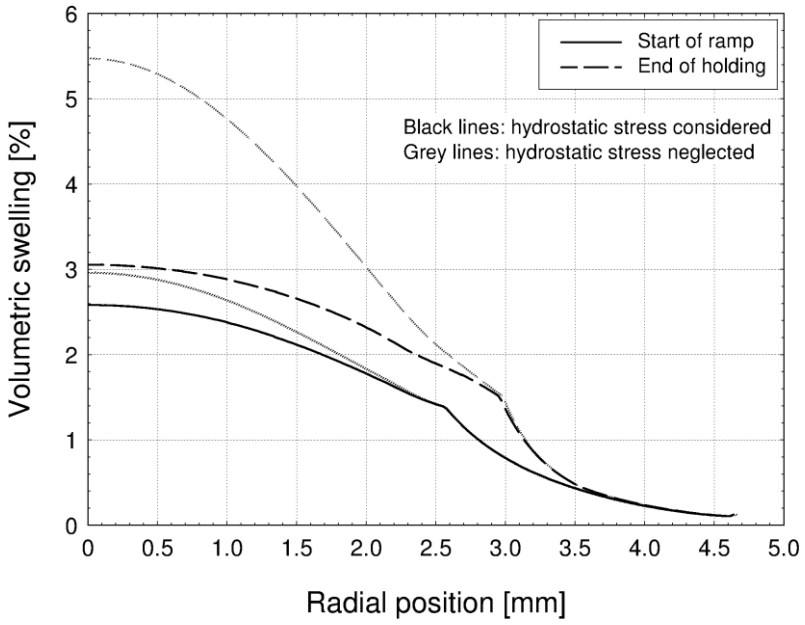

Fig. 5.17. Fission gas swelling as a function of the pellet radius at the mid-plane of the PK1-1 fuel rod. The considered instants are the start of the ramp and the end of the holding time. The figure refers to the adoption of the new model. The fission gas swelling calculated by neglecting the hydrostatic stress is also shown.

and possible cladding failure (Arimescu, 2004; Cheon et al., 2004).

Figure 5.18 compares the results obtained by adopting the new model with those obtained by using the standard models of TRANSURANUS, in terms of fission gas swelling and FGR as a function of the pellet radius at the mid-plane of the PK1-1 rod. Again, the significant instants highlighted in Fig. 5.15 (start of the ramp and end of the holding time) are considered. The quantitative differences between the results of the different models are ascribed to the different features and parameters of the standard TRANSURANUS models (Section 2.2) and the new model (Chapter 3). However, qualitative differences are also observed, which point out the innovative aspects pertaining to the modelling approach developed in the present work.

As mentioned in Section 2.2, the standard swelling model of the TRANSURANUS code does not take into account the fission gas swelling in presence of contact pressure between the fuel and the cladding (PCMI conditions). Since contact pressure is present during the whole ramp test of the PK1-1 rod (Fig. 5.16), no swelling increment is considered by the standard TRANSURANUS model between the start of ramp and the end of holding time. In fact, the swelling profiles of Fig. 5.18-a are superimposed. However, this simplified approach does not allow for the significant swelling that (although partially inhibited by the compressive hydrostatic stress) can occur during a power ramp as a result of the high power and temperature, and the related issues. As an innovative aspect of the present work, the new model introduces the dependence of the fission gas swelling on the hydrostatic stress, and consistently calculates the increment of swelling during the power ramp and the subsequent holding time (Fig. 5.17 and Fig. 5.18-b). In consideration of this capability, the new model may allow to improve the TRANSURANUS code for the analysis of the fuel behaviour under

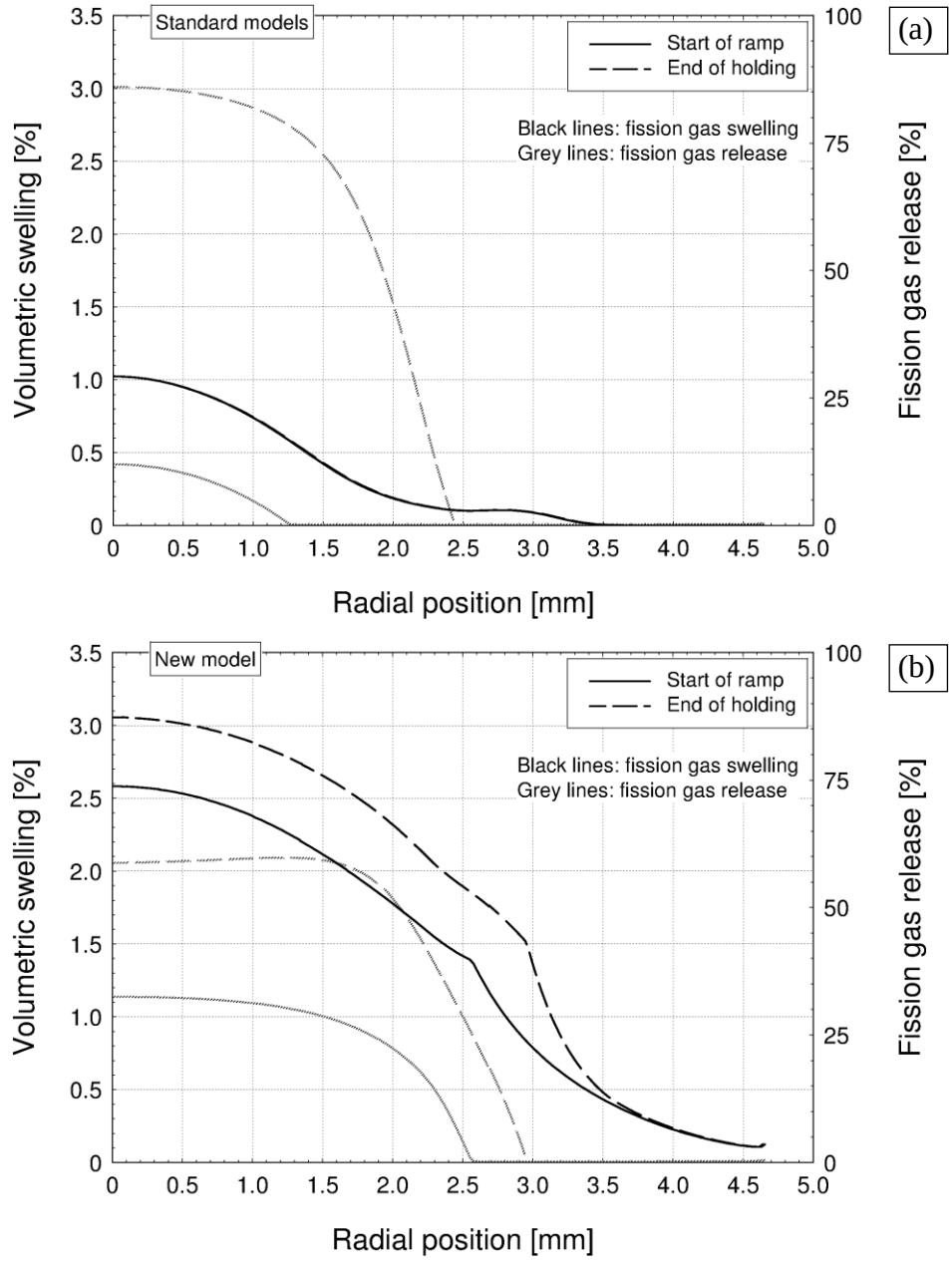

Fig. 5.18. Fission gas swelling and fission gas release as a function of the pellet radius at the mid-plane of the PK1-1 fuel rod. The considered instants are the start of the ramp and the end of the holding time. (a) Standard models of TRANSURANUS, (b) new model. In Fig. 5.18-a, the swelling curves are superimposed.

PCMI conditions, which is of high importance in view of the current tendency to extend the operating margins of the nuclear fuel rods.

As shown in Fig. 5.18, both the new model and the standard TRANSURANUS model predict a remarkable increment of FGR from the start of the ramp to the end of the holding time, brought about by the high power and temperature. However, the physical coupling between the fission gas swelling and release, as well as the dependence of the FGR on the hydrostatic stress, are not considered by the standard TRANSURANUS models, while the new model introduces these peculiarities (see also Sub-section 5.3.1).

In general, the new model of fission gas swelling and release allows a deeper insight into the relevant physical details compared to the standard TRANSURANUS models.

Figure 5.19 shows the predictions in terms of integral FGR at the EOL for the Super-Ramp and Inter-Ramp cases. The comparison is proposed between the results obtained by adopting the standard FGR model of the TRANSURANUS code and the new model of fission gas swelling and release. By using the standard model, a systematic under-estimation of the experimental data is observed, and the predicted values deviate on average from the experimental ones by a factor of about 2.1 for both the Super-Ramp and the Inter-Ramp databases. By adopting the new

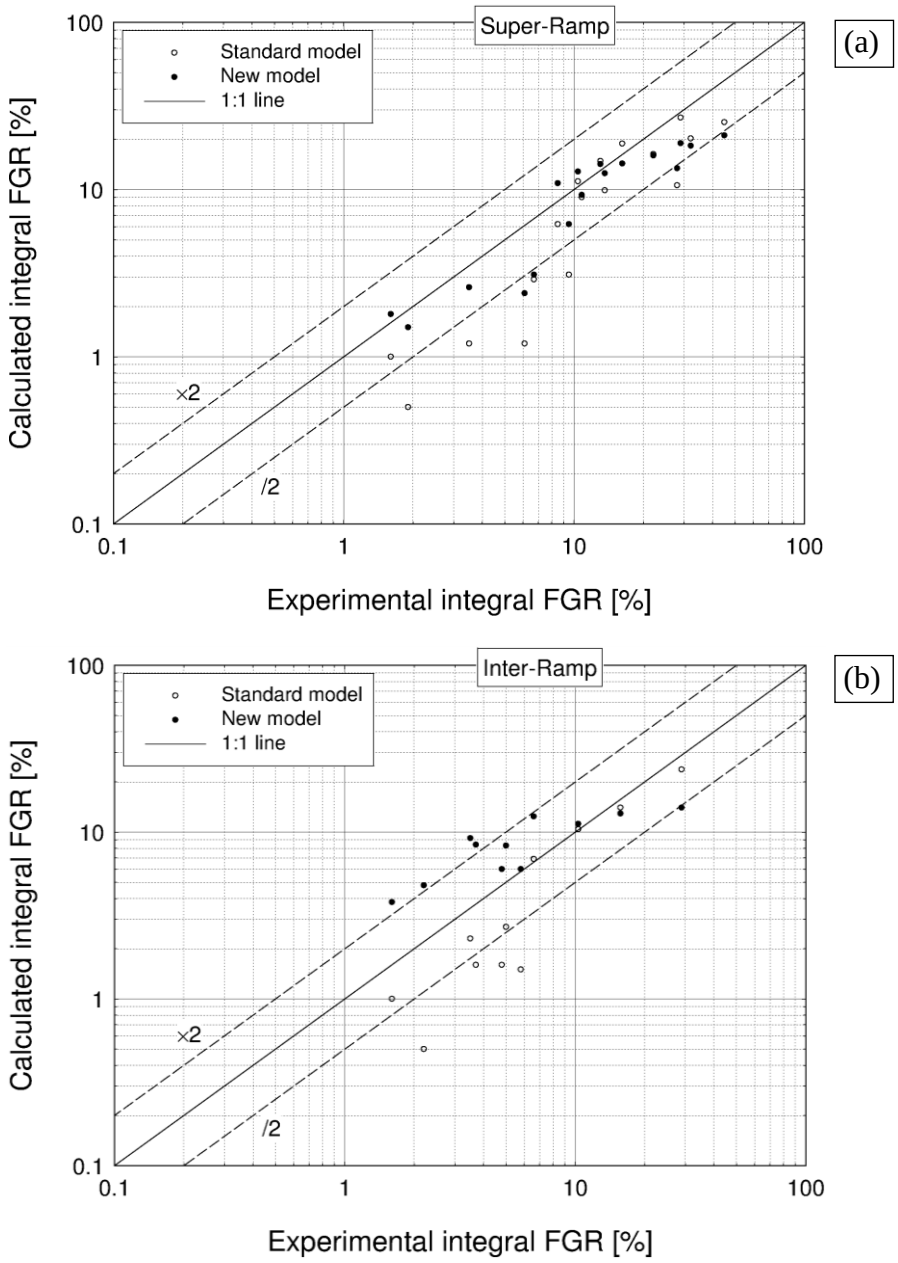

Fig. 5.19. Comparison between the calculated values of integral fission gas release at the EOL and the experimental data for (a) the Super-Ramp cases and (b) the Inter-Ramp cases. Both the results obtained by adopting the new model and the standard model of TRANSURANUS are reported.

model, the average deviation is of a factor of about 1.5 for the Super-Ramp cases, and about 1.8 for the Inter-Ramp cases (Sub-section 5.3.2). Also, the systematic under-estimation that occurs when the standard model is used appears to be overcome. Hence, the results indicate that the new model may allow to improve the predictive accuracy of the TRANSURANUS code in terms of FGR.

For the analyses performed in the present work, when adopting the new model the computational time increased by a factor of about 3-7 (depending on the considered case) compared to that obtained when using the standard models of the TRANSURANUS code. Anyhow, when the new model is adopted, the computational times are reasonable and of the order of few minutes in all the considered cases (see footnote 4, p.33).

5.4 Concluding remarks

The applicability of the new model of fission gas swelling and release to the fuel rod analysis codes was demonstrated by successful implementation in the TRANSURANUS code. During the implementation, consistent matching was provided between the non-linear, stress-dependent model calculations and the thermo-mechanical fuel rod analysis. Numerical stability and reasonable computational times were obtained. The new model, applied to the TRANSURANUS code, was evaluated through the simulation of power ramped LWR-UO_2 fuel rods from the Super-Ramp and Inter-Ramp Projects of the IFPE database. With reference to the study of the calculation results, the following main conclusions are drawn:

- The model catches the dependence of both the fission gas swelling and release on the burn-up and the temperature.
- The physical coupling between the fission gas swelling and release is consistently described.
- The role of the compressive hydrostatic stress in suppressing the fission gas swelling and in delaying and reducing the FGR is reproduced, in accordance with the observations reported in the literature. This aspect represented a major challenge of the present work from the viewpoint of the numerical stability of the fuel rod calculations.
- The predictions in terms of integral fuel rod FGR are in reasonable agreement with the experimental data, without any tuning of the model parameters.

The comparison with the results obtained by using the standard models of the TRANSURANUS code indicated that the implementation of the new model represents a significant innovation. The character of the present work as a progress in the development of the TRANSURANUS code is threefold:

- The physical foundation of the code was enhanced by replacing a semi-empirical description with a physics-based and integrated treatment of the fission gas swelling and release.

- A stress-dependent description of the fission gas swelling and release was introduced in the code. This feature is of particular importance for the proper simulation of the fuel behaviour under PCMI conditions.
- The predictive capability of the code in terms of integral FGR turns out to be improved for the considered irradiation experiments, as emerges from the assessment of the results against the experimental data.

In view of future developments, the new model provides a framework to integrate further physical details. Specifically, for the purpose of the improved simulation of power ramps, the burst release effect due to pellet micro-cracking during rapid power changes (for which a model is presently available in the TRANSURANUS code, see Section 2.2) may be considered. The incorporation of such effect in the new model would lead to a complete transient fission gas behaviour model in the TRANSURANUS code that could deal with design basis accident conditions such as LOCA and RIA. In view of the stochastic nature of pellet micro-cracking, however, only semi-empirical approaches to the modelling of the burst release effect were proposed (e.g., Koo et al., 1999), and this aspect is beyond the scope of the present work. Finally, for the accurate analysis of high burn-up fuel, the peculiarities of the fission gas behaviour in the high burn-up structure (HBS) are to be modelled (Blair et al., 2006). Given the moderate burn-ups considered (see Section 4.2 and Section 5.2), however, this issue is not of relevance for the analyses carried out in the present work, and is beyond the scope of this thesis. In perspective, integrating in the new model suitable treatments of the burst release effect and of the fission gas behaviour in the HBS, as well as a physics-based description of the athermal release mechanisms, represents an interesting development of the present work.

Conclusions

In the context of fuel rod modelling, the analysis of the coupled phenomena of fission gas swelling and release represents a challenging issue in view of the complexity of the underlying physical processes. In this work, a new model of fission gas swelling and release in UO_2 fuel during irradiation was developed and applied to the TRANSURANUS code, presently used in the European Union by nuclear safety authorities, industry, research centres and universities. The main outcomes of the work, which was carried out within the FUMEX-III co-ordinated research project of the IAEA, may be summarized as follows:

- The new model practically combines a physics-based description and the level of simplicity that is a prerequisite for the effective implementation in the fuel rod analysis codes.
- By application as stand-alone version, the model was firstly proven to reproduce the main peculiarities of the fission gas behaviour, on a physical basis and in accordance with the observations reported in the literature. Despite its simplicity, the model consistently describes the intrinsic coupling between the fission gas swelling and release, the incubation behaviour of the FGR, and the dependence of both the fission gas swelling and release on the compressive hydrostatic stress in the fuel.
- As resulting from the analysis of either power ramped or power cycled UO_2 fuel specimens using the stand-alone version of the model, and from a first assessment of the predictions against experimental data, the predictive accuracy in terms of grain-boundary swelling is reasonable, without tuning of the model parameters.
- The new model of fission gas swelling and release was consistently implemented in the TRANSURANUS code. Matching was provided between the non-linear, stress-dependent model calculations and the thermo-mechanical fuel rod analysis. Stability of the numerical solutions and reasonable computational times were obtained.
- Adopting the new model, the TRANSURANUS code was employed for an extensive set of simulations of LWR-UO_2 fuel rods irradiation experiments involving power ramps. The main peculiarities of the phenomena are confirmed to be reproduced consistently with the experimental observations.
- The assessment of the results of the fuel rod analyses against experimental data of integral fuel rod FGR pointed out a reasonable overall agreement, without any fitting of the model parameters.
- The successful application to the TRANSURANUS code indicated that (i) the model can be employed in integral fuel rod analyses (hence, in the nuclear fuel design and licensing), and (ii) the model may be of interest for implementation in other fuel rod analysis codes.

- The comparison with the capabilities of the standard models of the TRANSURANUS code indicated that the implementation of the new model represents a significant progress in the code development. The innovative aspects are mainly related to (i) the advantages of a physics-based and integrated treatment in terms of flexibility of application and understanding of the underlying mechanisms, compared to the previously adopted empirical and semi-empirical models, and (ii) the consistent evaluation of the dependence of both the fission gas swelling and release on the hydrostatic stress. Being of high importance in order to properly analyse the fuel rod behaviour under PCMI conditions and the related, safety-relevant issues, the latter aspect is topical in view of the tendency to extend the operating margins of the nuclear fuel rods.
- The current results are promising in view of future applications of the model, implemented in the TRANSURANUS code, in both research and industrial frameworks.

In perspective, a more extensive verification of the model, both in terms of comparison with experimental data and numerical stability of the fuel rod calculations, is envisaged. Also, some modelling aspects can be refined, and new features can be introduced. In particular, developments are underway concerning the modelling of the intra-granular gas behaviour, as reported in Appendix B. Moreover, given the physical foundation of the model, it may be modified according to the specificity of different fuel types (e.g., MOX). Finally, integrating further physical details (e.g., burst release, high burn-up effects, athermal release mechanisms) represents an interesting development in view of improving the predictive capability and extending the range of applicability of the new model.

To summarize, the general features of the model developed in the present work, in terms of physical foundation and computational efficiency, constitute a framework that allows the application to fuel rod modelling of the physics-based, integrated and stress-dependent treatment of the fission gas swelling and release. The underlying approach is generally applicable and can be reproduced in order to develop increasingly complex and advanced models with the above fundamental capabilities to be implemented in the fuel rod analysis codes. Therefore, in addition to some specific modelling aspects, the basic engineering approach constitutes, in essence, the most significant and innovative contribution of the work.

References

Ainscough J.B., Oldfield B.W., Ware J.O. (1973). Isothermal grain growth kinetics in sintered UO_2 pellets, Journal of Nuclear Materials, vol. 49, pp. 117-128.

Arimescu, V.I. (2004). Fuel Swelling Importance in PCI Mechanistic Modelling, Proceedings of the International Seminar on Pellet-Clad Interaction in Water Reactor Fuels, Aix-en-Provence, France, March 9-11, 2004.

Assmann H., Manzel R. (1977). The matrix swelling rate of UO2, Journal of Nuclear Materials, vol. 68, pp. 360-364.

Assmann H., Stehle H. (1978). Thermal and in-reactor densification of UO_2: mechanisms and experimental results, Nuclear Engineering and Design, vol. 48, pp. 49-67.

Aybar H.S., Ortego P. (2005). A review of nuclear fuel performance codes, Progress in Nuclear Energy, vol. 46, no. 2, pp. 127-141.

Bailly H., Ménessier D., Prunier C. (1999). The nuclear fuel of pressurized water reactors and fast reactors, Lavoisier Publishing.

Baker C. (1977a). The fission gas bubble distribution in uranium dioxide from high temperature irradiated SGHWR fuel pins, Journal of Nuclear Materials, vol. 66, pp. 283-291.

Baker C. (1977b). The migration of intragranular fission gas bubbles in irradiated uranium dioxide, Journal of Nuclear Materials, vol. 71, pp. 117-123

Bentejac F., Hourdequin N. (2004). TOUTATIS, an application of the CAST3M finite element code for PCI three-dimensional modelling, Proceedings of the International Seminar on Pellet-Clad Interaction in Water Reactor Fuels, Aix-en-Provence, France, March 9-11, 2004.

Bernard L.C., Jacoud J.L., Vesco P. (2002). An efficient model for the analysis of fission gas release, Journal of Nuclear Materials, vol. 302, pp. 125-134.

Blair P., Romano A., Hellwig Ch., Chawla R. (2006). Calculations on fission gas behaviour in the high burnup structure, Journal of Nuclear Materials, vol. 350, pp. 232-239.

Booth A.H. (1957). A Method of Calculating Gas Diffusion from UO_2 Fuel and its Application to the X-2-f Loop Test, AECL-496, Atomic Energy of Canada Ltd.

Calvin C., Nowak D. (2010). High performance computing in nuclear engineering, in: Cacuci D.G. (Ed.), Handbook of Nuclear Engineering, Springer, pp. 1449-1517.

Cheon J-S., Koo Y.-H., Lee B-H., Oh J-Y., Sohn D.-S. (2004). Modeling of a Pellet-Clad Mechanical Interaction in LWR Fuel by Considering Gaseous Swelling, Proceedings of the International Seminar on Pellet-Clad Interaction in Water Reactor Fuels, Aix-en-Provence, France, March 9-11, 2004.

Cornell R.M. (1971). An electron microscope examination of matrix fission-gas bubbles in irradiated uranium dioxide, Journal of Nuclear Materials, vol. 38, pp. 319-328.

Cornell R.M., Speight M.V., Masters B.C. (1969). The role of bubbles in fission gas release from uranium dioxide, Journal of Nuclear Materials, vol. 30, pp. 170-178.

Di Marcello V., Luzzi L. (2008). Modelling of Pellet Cladding Interaction during Power Ramps in PWR Rods by means of Transuranus Fuel Rod Analysis Code, Proceedings of the OECD/NEA-IAEA Workshop on Structural Materials for Innovative Nuclear Systems (SMINS), NEA No. 6260, pp. 417-428.

Djurle S. (1979). The Studsvik Inter-Ramp Project, Final Report STUDSVIK-STIR-53, Studsvik AB Atomenergi, Sweden.

Djurle S. (1984). The Super-Ramp Project, Final Report STUDSVIK-STSR-32, Studsvik Energiteknik AB, Nykoping, Sweden.

Elton P.T., Lassmann K. (1987). Calculational methods for diffusional gas release, Nuclear Engineering and Design, vol. 101, pp. 259-265.

Franklin D.G. , Roberts J.T.A., C.-Y. Li (1984). Low temperature swelling and densification properties of LWR fuels, Journal of Nuclear Materials, vol. 125, pp. 96-103.

Frost B.R.T. (Ed.) (1994). Materials Science and Technology: A Comprehensive Treatment - Nuclear Materials, voll. 10A-10B, VCH, Weinheim.

Garcia P., Struzik C., Agard M., Louche V. (2002). Mono-dimensional mechanical modelling of fuel rods under normal and off-normal operating conditions, Nuclear Engineering and Design, vol. 216, pp. 183-201.

Govers K., Lemehov S., Verwerft M. (2008). In-pile Xe diffusion coefficient in UO_2 determined from the modeling of intragranular bubble growth and destruction under irradiation, Journal of Nuclear Materials, vol. 374, pp. 461-472.

Grimes R.W., Catlow C.R.A (1991). The stability of fission products in uranium dioxide, Philosophical Transactions of the Royal Society A, vol. 335, pp. 609-634.

Gulden M.E. (1967). Migration of gas bubbles in irradiated uranium dioxide, Journal of Nuclear Materials, vol. 23, pp. 30-36.

Ham F.S. (1958). Theory of diffusion-limited precipitation, Journal of Physics and Chemistry of Solids, vol. 6, pp. 335-351.

IAEA (1998). Fuel modelling at extended burnup, Technical Report IAEA TECDOC 998.

IAEA (2011). Fuel Modelling at extended burnup (Fumex-II), Report of a coordinated research project, Technical Report IAEA TECDOC, http://infcis.iaea.org.

Jackson P.A., Turnbull J.A., White R.J. (1989). A description of the ENIGMA fuel performance code, Report IAEA-TECDOC-697, pp. 28-38.

Jiang Y., Cui Y., Huo Y, Ding S. (2011). Three-dimensional FE analysis of the thermal–mechanical behaviors in the nuclear fuel rods, Annals of Nuclear Energy, vol. 38, pp. 2581–2593.

Karahan A., Kazimi M.S. (2011). On the significance of modeling nuclear fuel behavior with the right representation of physical phenomena, Nuclear Engineering and Design, vol. 241, pp. 484-491.

Kashibe S., Une K. (1997). Effect of external restraint on bubble swelling in UO_2 fuels, Journal of Nuclear Materials, vol. 247, pp. 138-146.

Kashibe S., Une K., Nogita K. (1993). Formation and growth of intragranular fission gas bubbles in UO_2 fuels with burnup of 6-83 GWd/t, Journal of Nuclear Materials, vol. 206, pp. 22-34.

Killeen J., Turnbull J.A., Sartori E. (2007). Fuel Modelling at Extended Burnup: IAEA Coordinated Research Project FUMEX-II, Proceedings of International LWR Fuel Performance Meeting, American Nuclear Society, San Francisco, California, USA, September 30-October 3, 2007.

Killeen J., Sartori E., McGrath M. (2009). FUMEX-III: A new IAEA coordinated research project on fuel modelling at extended burnup, Proceedings of the International Conference on Water Reactor Fuel Performance, Paris, France, September 6-10, 2009, pp. 336-343.

Kim Y.-s. (2004). Theoretical analysis of two-stage fission gas release processes: grain lattice and grain boundary diffusion, Journal of Nuclear Materials, vol. 326, pp. 97-105.

Kogai T. (1997). Modelling of fission gas release and gaseous swelling of light water reactor fuels, Journal of Nuclear Materials, vol. 244, pp. 131-140.

Kogai T., Ito K., Iwano Y. (1988). The effect of cladding restraint on fission gas release behavior, Journal of Nuclear Materials, vol. 158, pp. 64-70.

Konings R.J.M., Wiss T., Guéneau C. (2010). Nuclear Fuels, in: Morss L.R., Fuger J., Edelstein N.M. (Eds.), The Chemistry of Actinides and Transactinide Elements, Springer, 4th Edition, Chap. 34, pp. 3665-3812.

Koo Y.-H., Lee B.-H., Sohn D.-S. (2000). Analysis of fission gas release and gaseous swelling in UO_2 fuel under the effect of external restraint, Journal of Nuclear Materials, vol. 280, pp. 86-98.

Lassmann K. (1980). The structure of fuel element codes, Nuclear Engineering and Design, vol. 57, pp. 17-39.

Lassmann K. (1987). A fast and simple iteration scheme for the temperature calculation in a fuel rod, Nuclear Engineering and Design, vol. 103, pp. 211-214.

Lassmann K. (1988). Modelling of fuel rod behaviour and recent advances of the TRANSURANUS code, Nuclear Engineering and Design, vol. 106, pp. 291-313.

Lassmann K (1992). TRANSURANUS: a fuel rod analysis code ready for use, Journal of Nuclear Materials, vol. 188, pp. 295-302.

Lassmann K (2001). The TRANSURANUS Code – Past, present and future (Review Article), ITU Activity Report 2001 - EUR 20252, ISBN 92-894-3639-5, pp. 16-22.

Lassmann K., Benk H. (2000). Numerical algorithms for intragranular fission gas release, Journal of Nuclear Materials, vol. 280, pp. 127-135.

Lassmann K., Hohlefeld F. (1987). The revised URGAP model to describe the gap conductance between fuel and cladding, Nuclear Engineering and Design, vol. 103, pp. 215-221.

Lassmann K., Van Uffelen P. (2004). The Structure of fuel rod codes, Publications Office, JRC Publications, Report EUR 21400 EN, European Commission.

Lassmann K., Schubert A., Van Uffelen P., Győri C., van de Laar J. (2011). TRANSURANUS Handbook, Copyright ©1975-2011, Institute for Transuranium Elements, Karlsruhe, Germany.

Lewis B.J. (1987). Fission product release from nuclear fuel by recoil and knockout, Journal of Nuclear Materials, vol. 148, pp. 28-42.

Lösönen P. (2000). On the behaviour of intragranular fission gas in UO_2 fuel, Journal of Nuclear Materials, vol. 280, pp. 56-72.

Lösönen P. (2002). Modelling intragranular fission gas release in irradiation of sintered LWR UO_2 fuel, Journal of Nuclear Materials, vol. 304, pp. 29-49.

Luzzi L. (2002). Validation of TRANSURANUS Code on the Basis of the Studsvik Super-Ramp PWR Database Files, Technical Report JRC-ITU-TN-2002/08, Institute for Transuranium Elements, Karlsruhe, Germany.

Luzzi L, Di Marcello V., Botazzoli P., Győri C., Schubert A., Spino J., van de Laar J., Van Uffelen P. (2008). Analysing Operational Transients by means of the TRANSURANUS Code, Proceedings of the Enlarged Halden Programme Group Meeting, Loen, Norway, May 18-23, 2008.

Manley A.J. (1968). Transmission electron microscopy of irradiated UO_2 fuel pellets, Journal of Nuclear Materials, vol. 27, pp. 216-224.

Marchal N., Campos C., Garnier C. (2009). Finite element simulation of Pellet-Cladding Interaction (PCI) in nuclear fuel rods, Computational Materials Science, vol. 45, pp. 821–826.

Massih A.R., Forsberg K. (2008). Calculation of grain boundary gaseous swelling in UO_2, , Journal of Nuclear Materials, vol. 377, pp. 406-408.

MATPRO (1979). Version 11 – A Handbook of Material Properties for Use in the Analysis of LWR Fuel Rod Behaviour, NUREG/CR-0497, TREE-1280.

Matthews J.R. (1978), Fast reactor fuel pin performance, Review of SMiRT 4, Nuclear Energy, vol. 17, pp. 211-216.

Matthews J.R., Wood M.H. (1979). Modelling the transient behaviour of fission gas, Journal of Nuclear Materials, vol. 84, pp. 125-136.

Matzke H. (1980). Gas release mechanisms in UO_2 – a critical review, Radiation Effects, vol. 53, p. 219-242.

Metcalf M., Reid J., Cohen M. (2004). Fortran 95/2003 explained, Oxford University Press.

Mogensen M., Bagger C., Walker C.T. (1993). An experimental study of the distribution of retained xenon in transient-tested UO_2 fuel, Journal of Nuclear Materials, vol. 199, pp. 85-101.

Mogensen M., Walker C.T., Ray I.L.F., Coquerelle M. (1985). Local fission gas release and swelling in water reactor fuel during slow power transients, Journal of Nuclear Materials, vol. 131, pp. 162-171.

Oguma M. (1983). Cracking and relocation behaviour of nuclear fuel pellets during rise to power, Nuclear Engineering and Design, vol. 76, pp. 35-45.

OECD/NEA (2004). Pellet-Clad Interaction in Water Reactor Fuels, Seminar Proceedings, Aix-en-Provence, France, March 9-11, 2004.

Olander D.R. (1976). Fundamental aspects of nuclear reactor fuel elements, Technical Information Center - Energy Research and Development Administration, University of California, Berkeley.

Olander D.R. (2001). Light water reactor fuel design and performance, in: Encyclopedia of materials: Science and Technology, Elsevier Science Ltd., ISBN: 0-08-0431526, pp. 4490-4504.

Olander D.R. (2009). Nuclear fuels – Present and future, Journal of Nuclear Materials, vol. 389, pp. 1-22.

Olander D.R., Van Uffelen P. (2001). On the role of grain boundary diffusion in fission gas release, Journal of Nuclear Materials, vol. 288, pp. 137-147.

Olander D.R., Wongsawaeng D. (2006). Re-solution of fission gas – A review: Part I. Intragranular bubbles. Journal of Nuclear Materials, vol. 354, pp. 94-109.

Pastore G., Botazzoli P., Di Marcello V., Luzzi L. (2009a). Simulation of Power Ramp Tested LWR Fuel Rods by means of the TRANSURANUS Code, Proceedings of the International Conference on Water Reactor Fuel Performance, Paris, France, September 6-10, 2009, pp. 223-232.

Pastore G., Botazzoli P., Di Marcello V., Luzzi L. (2009b). Assessment of the Prediction Capability of the TRANSURANUS Fuel Performance Code on the Basis of Power Ramp Tested LWR Fuel Rods, Proceedings of the 8th International Conference on WWER Fuel Performance, Modelling and Experimental Support, Bourgas, Bulgaria, September 26-October 4, 2009, pp. 300-308.

Rest J. (2003). The effect of irradiation-induced gas-atom re-solution on grain-boundary bubble growth, Journal of Nuclear Materials, vol. 321, pp. 305-312.

Reynolds G.L., Burton B. (1979). Grain-boundary diffusion in uranium dioxide: the correlation between sintering and creep and a reinterpretation of creep mechanism, Journal of Nuclear Materials, vol. 82, p. 22.

Roberts J.T.A. (1981). Structural Materials in Nuclear Power Systems, Plenum Press, New York.

Ross A.M., Stoute R.L. (1962). Heat transfer coefficient between UO_2 and Zircaloy-2, Technical Report AECL-1552, AECL.

Sartori E., Killeen J., Turnbull J.A. (2010). International Fuel Performance Experiments (IFPE) Database, OECD-NEA, http://www.oecd-nea.org/science/fuel/ifpelst.html.

Schubert A., Botazzoli P., Boneva S., Di Marcello V., Pastore G., van de Laar J., Van Uffelen P. (2011). Application of the extended TRANSURANUS code in the FUMEX-III Project, Proceedings of the 9th International Conference on WWER Fuel Performance, Modelling and Experimental Support, Bourgas, Bulgaria, September 17 – 24, 2011.

Speight M.V. (1969). A Calculation on the Migration of Fission Gas in Material Exhibiting Precipitation and Resolution of Gas Atoms Under Irradiation, Nuclear Science and Engineering, vol. 37, pp. 180-185.

Speight M.V., Beere W. (1975). Vacancy Potential and Void Growth on Grain Boundaries, Metal Science, vol. 9, pp. 190-191.

Spino J., Rest J., Goll W., Walker C.T. (2005). Matrix swelling rate and cavity volume balance of UO_2 fuels at high burn-up, Journal of Nuclear Materials, vol. 346, pp. 131-144.

Suk H.C., Wang W., Kim B.G., Kim K.S., Heo Y.H. (1992). In: Technical committee meeting on fission gas release and fuel chemistry related to extended burn-up, April 1992, Pembroke, Ontario, Canada.

Suzuki M. (2000). Light Water Reactor Fuel Analysis Code FEMAXI-V (Ver. 1), JAERI-Data/Code 2000-030.

Suzuki M., Uetsuka H., Saitou H. (2004). Analysis of mechanical load on cladding induced by fuel swelling during power ramp in high burn-up rod by fuel performance code FEMAXI-6, Nuclear Engineering and Design, vol. 229, pp. 1-14.

Tsederberg N.V., Popov V.N., Morozova N.A. (1971). Thermodyanmic and thermophysical properties of Helium, Israel Program for Scientific Translations, Jerusalem.

Tucker M.O., White R.J. (1979). The release of unstable fission products from UO_2 during irradiation, Journal of Nuclear Materials, vol. 87, pp. 1-10.

Turnbull J.A. (1971). The distribution of intragranular fission gas bubbles in UO_2 during irradiation, Journal of Nuclear Materials, vol. 38, pp. 203-212.

Turnbull J.A. (1974), The effect of grain size on the swelling and gas release properties of UO_2 during irradiation, Journal of Nuclear Materials, vol. 50, pp. 62-68.

Turnbull J.A., Friskney C.A., Findlay J.R., Johnson F.A., Walter A.J. (1982). The diffusion coefficients of gaseous and volatile species during the irradiation of uranium oxide, Journal of Nuclear Materials, vol. 107, pp. 168-184.

Turnbull J.A., Tucker M.O. (1974). Swelling in UO_2 under conditions of gas release, Philosophical Magazine, vol. 30, no. 1, pp. 47-63.

Turnbull J.A., White R.J., Wise C.A. (1988). The diffusion coefficient for fission gas atoms in uranium dioxide, Proceedings of Technical Committee Meeting on Water Reactor Fuel Element Computer Modelling in Steady State, Transient and Accidental Conditions, Preston, England, September 18-22, 1988.

Van Uffelen P. (2002). Contribution to the Modelling of Fission Gas Release in Light Water Reactor Fuel, Ph.D. thesis, University of Liege.

Van Uffelen P., Konings R.J.M., Vitanza C., Tulenko J. (2010). Analysis of reactor fuel rod behavior, in: Cacuci D.G. (Ed.), Handbook of Nuclear Engineering, Springer, pp. 1519-1627.

Van Uffelen P., Pastore G., Di Marcello V., Luzzi L. (2011). Multiscale modelling for the fission gas behaviour in the TRANSURANUS code, Nuclear Engineering and Technology, vol. 43, no. 6, pp. 477-488.

Van Uffelen P, Schubert A., van de Laar J., Győri C., Elenkov D., Boneva S., Georgieva M., Georgiev S., Hózer Z., Märtens D., Spykman G., Hellwig C., Nordstrøm Å., Luzzi L., Di Marcello V., Ott L. (2007). The Verification

of the TRANSURANUS Fuel Performance Code - an Overview, Proceedings of the 7th International Conference on WWER Fuel Performance, Modelling and Experimental Support, Albena, Bulgaria, September 17-21, 2007, pp. 305-320.

Van Uffelen P., Sheindlin M., Rondinella V., Ronchi C. (2004). On the relations between the fission gas behaviour and the pellet-cladding mechanical interaction in LWR fuel rods, Proceedings of the International Seminar on Pellet-Clad Interaction in Water Reactor Fuels, Aix-en-Provence, France, March 9-11, 2004.

Veshchunov M.S. (2008). Modelling of grain face bubbles coalescence in irradiated UO_2 fuel, Journal of Nuclear Materials, vol. 374, pp. 44-53.

Vitanza C., Graziani U., Fordestrommen N.T., Vilpponen K.O. (1978). Fission gas release from in-pile measurements, Technical Report HPR-221.10, OECD Halden Reactor Project.

Walker C.T., Knappik P., Mogensen M. (1988). Concerning the development of grain face bubbles and fission gas release in UO_2 fuel, Journal of Nuclear Materials, vol. 160, pp. 10-23.

White R.J. (1994). A new mechanistic model for the calculation of fission gas release, Proceedings of the International Topical Meeting on Light Water Reactor Fuel Performance, West Palm Beach, Florida, USA, April 17-21, 1994.

White R.J. (2004). The development of grain-face porosity in irradiated oxide fuel, Journal of Nuclear Materials, vol. 325, pp. 61-77.

White R.J., Corcoran R.C., Barnes J.P. (2006). A Summary of Swelling Data Obtained from the AGR/Halden Ramp Test Programme, Report R&T/NG/EXT/REP/0206/02, 2006.

White R.J., Tucker M.O. (1983). A new fission-gas release model, Journal of Nuclear Materials, vol. 118, pp. 1-38.

Wise C. (1985). Recoil release of fission products from nuclear fuel, Journal of Nuclear Materials, vol. 136, pp. 30-47.

Wood M.H., Matthews J.R. (1980). A simple operational gas release and swelling model. I: intragranular gas, Journal of Nuclear Materials, vol. 91, pp. 35-40.

Yagnik S.K. (1998). Overview of EPRI fuel performance code FALCON, Seminar Proceedings, Nuclear Science, Cadarache, France, March 3-6, 1998, pp. 267-272.

Zimmermann H. (1978). Investigations on swelling and fission gas behaviour in uranium dioxide, Journal of Nuclear Materials, vol. 75, pp. 154-161.

Appendix A

In this appendix, the semianalytical solution of the mechanical problem used in the TRANSURANUS code is derived. Some of the adopted symbol definitions differ from those used in the previous parts of the thesis.

The problem is formulated under the following assumptions:

- The axial strain is constant across the radius.
- The Young´s modulus, *E*, and Poisson's ratio, ν, of the material are isotropic and constant within the considered cylindrical ring.
- The small displacement theory is adopted.
- The constitutive equations are given by

$$\begin{aligned} \varepsilon_r &= \varepsilon_r^{el} + \varepsilon_r^{ex} \\ \varepsilon_\theta &= \varepsilon_\theta^{el} + \varepsilon_\theta^{ex} \\ \varepsilon_z &= \varepsilon_z^{el} + \varepsilon_z^{ex} \end{aligned} \tag{A1}$$

  where ε^{el} indicates the elastic strain, and ε^{ex} the sum of the non-elastic strains.

The compatibility equations are

$$\begin{aligned} \varepsilon_r(R) &= \frac{du(R)}{dR} \\ \varepsilon_\theta(R) &= \frac{u(R)}{R} \\ \varepsilon_z(R) &= C_3 \end{aligned} \tag{A2}$$

The equation of equilibrium is

$$\frac{d\sigma_r(R)}{dR} = \frac{\sigma_\theta(R) - \sigma_r(R)}{R} \tag{A3}$$

where $R = r + u$ is the radius of the deformed geometry and r the radius of the reference geometry. The equation above shows that the equilibrium is always taken at the deformed geometry.

Starting from Eqs. A1 written in the form

$$\varepsilon_r(R)=\frac{1}{E}\left[\sigma_r(R)-\nu\left(\sigma_\theta(R)+\sigma_z(R)\right)\right]+\varepsilon_r^{ex}(R)$$

$$\varepsilon_\theta(R)=\frac{1}{E}\left[\sigma_\theta(R)-\nu\left(\sigma_r(R)+\sigma_z(R)\right)\right]+\varepsilon_\theta^{ex}(R) \qquad \text{(A4)}$$

$$\varepsilon_z(R)=\frac{1}{E}\left[\sigma_z(R)-\nu\left(\sigma_r(R)+\sigma_\theta(R)\right)\right]+\varepsilon_z^{ex}(R)$$

one obtains for the stresses

$$\sigma_r(R)=\frac{E}{1+\nu}\left[\varepsilon_r(R)-\varepsilon_r^{ex}(R)\right]+\frac{\nu E}{(1+\nu)(1-2\nu)}\left[\varepsilon_r(R)+\varepsilon_\theta(R)+\varepsilon_z(R)-\varepsilon_{tot}^{ex}(R)\right]$$

$$\sigma_\theta(R)=\frac{E}{1+\nu}\left[\varepsilon_\theta(R)-\varepsilon_\theta^{ex}(R)\right]+\frac{\nu E}{(1+\nu)(1-2\nu)}\left[\varepsilon_r(R)+\varepsilon_\theta(R)+\varepsilon_z(R)-\varepsilon_{tot}^{ex}(R)\right] \qquad \text{(A5)}$$

$$\sigma_z(R)=\frac{E}{1+\nu}\left[\varepsilon_z(R)-\varepsilon_z^{ex}(R)\right]+\frac{\nu E}{(1+\nu)(1-2\nu)}\left[\varepsilon_r(R)+\varepsilon_\theta(R)+\varepsilon_z(R)-\varepsilon_{tot}^{ex}(R)\right]$$

where $\varepsilon_{tot}^{ex}=\varepsilon_r^{ex}+\varepsilon_\theta^{ex}+\varepsilon_z^{ex}$.

Introducing Eqs. A2 into the first two of Eqs. A5 leads to

$$\sigma_r(R)=\frac{E}{1+\nu}\left[\frac{du(R)}{dR}-\varepsilon_r^{ex}(R)\right]+\frac{\nu E}{(1+\nu)(1-2\nu)}\left[\frac{du(R)}{dR}+\frac{u(R)}{R}+C_3-\varepsilon_{tot}^{ex}(R)\right]$$

$$\sigma_\theta(R)=\frac{E}{1+\nu}\left[\frac{u(R)}{R}-\varepsilon_\theta^{ex}(R)\right]+\frac{\nu E}{(1+\nu)(1-2\nu)}\left[\frac{du(R)}{dR}+\frac{u(R)}{R}+C_3-\varepsilon_{tot}^{ex}(R)\right] \qquad \text{(A6)}$$

Substituting Eqs. A6 into Eq. A3, one obtains

$$\frac{d^2u(R)}{dR^2}+\frac{1}{R}\frac{du(R)}{dR}-\frac{1}{R^2}u(R)=\frac{1-2\nu}{1-\nu}\left[\frac{1}{R}\left(\varepsilon_r^{ex}(R)-\varepsilon_\theta^{ex}(R)\right)+\frac{d\varepsilon_r^{ex}(R)}{dR}\right]+\frac{\nu}{1-\nu}\frac{d\varepsilon_{tot}^{ex}(R)}{dR} \qquad \text{(A7)}$$

and multiplying by R^2

$$R^2\frac{d^2u(R)}{dR^2}+R\frac{du(R)}{dR}-u(R)=\frac{1-2\nu}{1-\nu}\left[R\left(\varepsilon_r^{ex}(R)-\varepsilon_\theta^{ex}(R)\right)+R^2\frac{d\varepsilon_r^{ex}(R)}{dR}\right]+\frac{\nu}{1-\nu}R^2\frac{d\varepsilon_{tot}^{ex}(R)}{dR} \qquad \text{(A8)}$$

To solve Eq. A8, the following substitutions are made:

$$R = e^x$$

$$u(e^x) = z(x)$$

$$\varepsilon_r^{ex}(e^x) = \phi_r^{ex}(x)$$

$$\varepsilon_t^{ex}(e^x) = \phi_t^{ex}(x)$$

$$\varepsilon_{tot}^{ex}(e^x) = \phi_{tot}^{ex}(x)$$

and therefore

$$dR = e^x dx$$

$$\frac{du(e^x)}{dx} = e^{-x}\frac{dz(x)}{dx}$$

$$\frac{d^2u(e^x)}{dx^2} = e^{-2x}\left(\frac{d^2z(x)}{dx^2} - \frac{dz(x)}{dx}\right)$$

$$\frac{d\varepsilon_r^{ex}(e^x)}{dx} = e^{-x}\frac{d\phi_r^{ex}(x)}{dx}$$

$$\frac{d\varepsilon_{tot}^{ex}(e^x)}{dx} = e^{-x}\frac{d\phi_{tot}^{ex}(x)}{dx}$$

Then, Eq. A8 becomes

$$\frac{d^2z(x)}{dx^2} - z(x) = \frac{1-2\nu}{1-\nu}e^x\left(\phi_r^{ex}(x) - \phi_\theta^{ex}(x) + \frac{d\phi_r^{ex}(x)}{dx}\right) + \frac{\nu}{1-\nu}e^x\frac{d\phi_{tot}^{ex}(x)}{dx} \qquad \text{(A9)}$$

For a theorem, the general solution of Eq. A9 is of the type

$$z(x) = z_H(x) + \bar{z}(x) \qquad \text{(A10)}$$

where $z_H(x)$ is the general solution of the associated homogeneous equation

$$\frac{d^2z(x)}{dx^2} - z(x) = 0 \qquad \text{(A11)}$$

and $\bar{z}(x)$ is a solution of the complete Eq. A9.

The general solution of the homogeneous Eq. A11 is

$$z_H(x) = D_1 e^{x} + D_2 e^{-x} \tag{A12}$$

For the superposition principle, any solution of the complete Eq. A9 can be written as

$$\bar{z}(x) = \bar{z}_1(x) + \bar{z}_2(x) \tag{A13}$$

where $\bar{z}_1(x)$ is a solution of the equation

$$\frac{d^2\bar{z}_1(x)}{dx^2} - \bar{z}_1(x) = \frac{1-2\nu}{1-\nu} e^{x}\left(\phi_r^{ex}(x) - \phi_\theta^{ex}(x) + \frac{d\phi_r^{ex}(x)}{dx}\right) \tag{A14}$$

and $\bar{z}_2(x)$ is a solution of the equation

$$\frac{d^2\bar{z}_2(x)}{dx^2} - \bar{z}_2(x) = \frac{\nu}{1-\nu} e^{x} \frac{d\phi_{tot}^{ex}(x)}{dx} \tag{A15}$$

A solution of Eq. A14 is[10]

$$\bar{z}_1(x) = \frac{1-2\nu}{1-\nu}\frac{1}{2}\int_{x_i}^{x}\left(e^{x}e^{-x'} - e^{-x}e^{x'}\right)e^{x'}\left(\phi_r^{ex}(x') - \phi_\theta^{ex}(x') + \frac{d\phi_r^{ex}(x')}{dx'}\right)dx' \tag{A16}$$

The integration is carried out between $x_i = lnR_i$ and $x = lnR$, where R_i is the inner radius of the considered cylindrical ring and R is the current radius. After some transformations, one obtains:

---

[10] For a theorem, given a second order linear differential equation

$$\frac{d^2y(x)}{dx^2} + a\frac{dy(x)}{dx} + by(x) = f(x),$$

if the solutions of the associated homogeneous equation can be written as linear combinations of two functions $y_1(x)$ and $y_2(x)$, then a solution of the complete equation is:

$$\bar{y}(x) = \int_{x_0}^{x} K(x,x')f(x')dx',$$

where

$$K(x,x') = \frac{\begin{vmatrix} y_1(x') & y_2(x') \\ y_1(x) & y_2(x) \end{vmatrix}}{\begin{vmatrix} y_1(x') & y_2(x') \\ \dfrac{dy_1(x')}{dx'} & \dfrac{dy_2(x')}{dx'} \end{vmatrix}}$$

$$\bar{z}_1(x)=\frac{1-2\nu}{2(1-\nu)}\left\{e^{-x}\int_{x_i}^{x}e^{2x'}\left(\phi_r^{ex}(x')+\phi_\theta^{ex}(x')\right)dx'+e^{x}\int_{x_i}^{x}\left(\phi_r^{ex}(x')-\phi_\theta^{ex}(x')\right)dx'\right\}+$$
$$+\frac{1-2\nu}{2(1-\nu)}\left(-e^{x}\phi_r^{ex}(x_i)+e^{-x}e^{2x_i}\phi_r^{ex}(x_i)\right) \tag{A17}$$

Similarly, a solution of Eq. A15 is

$$\bar{z}_2(x)=\frac{\nu}{2(1-\nu)}\int_{x_i}^{x}\left(e^{x}e^{-x'}-e^{-x}e^{x'}\right)e^{x'}\ \frac{d\phi_{tot}^{ex}(x')}{dx'}\,dx' \tag{A18}$$

After some transformations, one obtains

$$\bar{z}_2(x)=\frac{\nu}{1-\nu}e^{-x}\int_{x_i}^{x}e^{2x'}\phi_{tot}^{ex}(x')dx'+\frac{\nu}{2(1-\nu)}\left(-e^{x}\phi_{tot}^{ex}(x_i)+e^{-x}e^{2x_i}\phi_{tot}^{ex}(x_i)\right) \tag{A19}$$

Then, the general solution of Eq. A9 is (see Eqs. A10 and A13)

$$z(x)=\frac{1-2\nu}{2(1-\nu)}\left\{e^{-x}\int_{x_i}^{x}e^{2x'}\left(\phi_r^{ex}(x')+\phi_\theta^{ex}(x')\right)dx'+e^{x}\int_{x_i}^{x}\left(\phi_r^{ex}(x')-\phi_\theta^{ex}(x')\right)dx'\right\}+$$
$$+\frac{\nu}{1-\nu}e^{-x}\int_{x_i}^{x}e^{2x'}\phi_{tot}^{ex}(x')dx'+\frac{1-2\nu}{2(1-\nu)}\left(-e^{x}\phi_r^{ex}(x_i)+e^{-x}e^{2x_i}\phi_r^{ex}(x_i)\right)+ \tag{A20}$$
$$+\frac{\nu}{2(1-\nu)}\left(-e^{x}\phi_{tot}^{ex}(x_i)+e^{-x}e^{2x_i}\phi_{tot}^{ex}(x_i)\right)+D_1e^{x}+D_2e^{-x}$$

or equivalently

$$z(x)=\frac{1-2\nu}{2(1-\nu)}\left\{e^{-x}\int_{x_i}^{x}e^{2x'}\left(\phi_r^{ex}(x')+\phi_\theta^{ex}(x')\right)dx'+e^{x}\int_{x_i}^{x}\left(\phi_r^{ex}(x')-\phi_\theta^{ex}(x')\right)dx'\right\}+$$
$$+\frac{\nu}{1-\nu}e^{-x}\int_{x_i}^{x}e^{2x'}\phi_{tot}^{ex}(x')dx'+C_1e^{x}+C_2e^{-x} \tag{A21}$$

Substituting $R=e^{x}$ in Eq. A21, the general solution of Eq. A8 is obtained

$$u(R)=\frac{1-2\nu}{2(1-\nu)}\left\{\frac{1}{R}\int_{R_i}^{R}R'\left(\varepsilon_r^{ex}(R')+\varepsilon_\theta^{ex}(R')\right)dR'+R\int_{R_i}^{R}\frac{\left(\varepsilon_r^{ex}(R')-\varepsilon_\theta^{ex}(R')\right)}{R'}dR'\right\}+$$
$$+\frac{\nu}{1-\nu}\frac{1}{R}\int_{R_i}^{R}R'\varepsilon_{tot}^{ex}(R')dR'+C_1R+\frac{C_2}{R} \tag{A22}$$

which is the semianalytical expression for the radial displacement. Introducing Eqs. A.22 into Eqs. A2, it results for the strains

$$\varepsilon_r^j(R)=\frac{1-2\nu^j}{2\left(1-\nu^j\right)}\left\{I_2^j+2\varepsilon_r^{ex}-\frac{1}{R^2}I_1^j\right\}+\frac{\nu^j}{1-\nu^j}\left\{\varepsilon_{tot}^{ex}-\frac{1}{R^2}I_3^j\right\}+C_1^j-\frac{C_2^j}{R^2}$$

$$\varepsilon_\theta^j(R)=\frac{1-2\nu^j}{2\left(1-\nu^j\right)}\left\{\frac{1}{R^2}I_1^j+I_2^j\right\}+\frac{\nu^j}{\left(1-\nu^j\right)R^2}I_3^j+C_1^j+\frac{C_2^j}{R^2} \tag{A23}$$

$$\varepsilon_z^j(R)=C_j^3$$

and for the stresses

$$\sigma_r^j(R)=\frac{E^j}{1+\nu^j}\left\{\frac{C_1^j}{1-2\nu^j}-\frac{C_2^j}{R^2}+\frac{\nu^jC_3^j}{1-2\nu^j}\right\}+\frac{E^j}{2\left[1-\left(\nu^j\right)^2\right]}\frac{1}{R^2}\left\{-\left(1-2\nu^j\right)I_1^j+R^2I_2^j-2\nu^jI_3^j\right\}$$

$$\sigma_\theta^j(R)=\frac{E^j}{1+\nu^j}\left\{\frac{C_1^j}{1-2\nu^j}+\frac{C_2^j}{R^2}+\frac{\nu^jC_3^j}{1-2\nu^j}-\frac{\varepsilon_\theta^{ex}+\nu^j\varepsilon_z^{ex}}{1-\nu^j}\right\}+\frac{E^j}{2\left[1-\left(\nu^j\right)^2\right]}\frac{1}{R^2}\left\{\left(1-2\nu^j\right)I_1^j+R^2I_2^j+2\nu^jI_3^j\right\}$$

$$\sigma_z^j(R)=\frac{E^j}{1+\nu^j}\left\{\frac{2\nu^jC_1^j}{1-2\nu^j}+\frac{\left(1-\nu^j\right)C_3^j}{1-2\nu^j}-\frac{\nu^j\varepsilon_t^{ex}+\varepsilon_z^{ex}}{1-\nu^j}\right\}+\frac{E^j}{2\left[1-\left(\nu^j\right)^2\right]}\frac{1}{R^2}2\nu^jR^2I_2^j \tag{A24}$$

The superscript j indicates a cylindrical ring with the inner radius R_j and the outer radius R_0. The integrals I_1, I_2 and I_3 are defined by

$$I_1^j(R)=\int_{R_i}^{R}R\left(\varepsilon_r^{ex}+\varepsilon_\theta^{ex}\right)dR$$

$$I_2^j(R)=\int_{R_i}^{R}\frac{\varepsilon_r^{ex}-\varepsilon_\theta^{ex}}{R}dR \tag{A25}$$

$$I_3^j(R)=\int_{R_i}^{R}R\varepsilon_{tot}^{ex}dR$$

Appendix B

In this appendix, some on-going developments of the new model of fission gas swelling and release dealt with in the present work are discussed. In particular, an approach is proposed for modelling the intra-granular behaviour of the fission gases, which represents a modification of the preliminary treatment described in Section 3.2. Given that this modified model is at present not implemented in the TRANSURANUS code, it was not adopted for the calculations presented in this thesis. The work was published in *Nuclear Engineering and Technology* (Van Uffelen et al., 2011). The paper is reported in the next pages. Some of the adopted symbol definitions differ from those used in the previous parts of the thesis.

http://dx.doi.org/10.5516/NET.2011.43.6.477

MULTISCALE MODELLING FOR THE FISSION GAS BEHAVIOUR IN THE TRANSURANUS CODE

P. VAN UFFELEN[1,*], G. PASTORE[2], V. DI MARCELLO[1], and L. LUZZI[2]
[1] European Commission, Joint Research Centre,
Institute for Transuranium Elements, Germany
[2] Politecnico di Milano, Department of Energy,
Nuclear Engineering Division (CeSNEF), Italy
[*]Corresponding author. E-mail : paul.van-uffelen@ec.europa.eu

Received November 19, 2011

A formulation is proposed for modelling the process of intra-granular diffusion of fission gas during irradiation of UO_2 under both normal operating conditions and power transients. The concept represents a simple extension of the formulation of Speight, including an estimation of the contribution of bubble motion to fission gas diffusion. The resulting equation is formally identical to the diffusion equation adopted in most models that are based on the formulation of Speight, therefore retaining the advantages in terms of simplicity of the mathematical-numerical treatment and allowing application in integral fuel performance codes. The development of the new model proposed here relies on results obtained by means of molecular dynamics simulations as well as finite element computations. The formulation is proposed for incorporation in the TRANSURANUS fuel performance code.

KEYWORDS : Nuclear Fuel, Fuel Performance, Intra-granular Diffusion, Fission Gas Release

1. INTRODUCTION

In order to improve the fuel performance codes, calculations at lower scale can be applied to derive improved modelling of material properties. Several examples have been published recently. Molecular dynamics computations were applied for extracting the thermal expansion and thermal conductivity of un-irradiated UO_2 fuel and implementing the correlation in the FRAPCON code [1]. A similar molecular dynamics analysis was carried out to simulate the interaction of a He or Xe filled bubble with a fission fragment [2], or empirical potential simulations were applied in order to predict swelling due to soluble solid fission in a fuel performance code [3]. This has led to an improved assessment of the resolution process coefficient, which remains up until now a fitting parameter in several fission gas release models of fuel performance codes. First principles-based predictions of the migration energies for point defects in UN by means of the VASP DFT code were introduced in the thermal creep model of the TRANSURANUS fuel performance code [4]. In the current paper, a new model for the intra-granular fission gas behaviour is proposed that draws on both molecular dynamics calculations for resolution and finite element simulations for the simultaneous evolution of gas atoms and bubbles in the grains.

The fission gases xenon and krypton are unceasingly generated in irradiated nuclear fuel, which is a sintered compact of granular uranium dioxide in current commercial LWRs. As a consequence of their low solubility in UO_2, the fission gases tend either to precipitate into bubbles or to be released to the free volume in the rod. Gaseous bubble formation contributes to swelling, hence to a potential strong mechanical interaction with the metallic cladding tube. On the other hand, the released gas brings about a pressure rise and thermal conductivity degradation of the rod filling gas. Both fission gas swelling and release therefore affect the thermo-mechanical performance of the fuel rod and may eventually lead to cladding failure, especially at high burn-up and during power transients [5]. Hence, the description of fission gas behaviour is an essential aspect of fuel rod analysis.

The model describing the intra-granular behaviour of fission gases is an important component of any fuel performance code. All gas atoms are generated within the grains where gas bubbles are formed. At the same time, gas diffuses to the grain boundaries leading to the formation and growth of inter-granular bubbles and the related inter-granular swelling. Inter-granular bubbles eventually interlink and form paths for fission gas release (FGR).

Most of the gas remains in the bulk of the material under normal operating conditions in a LWR, and the model for intra-granular behaviour is called many times in a fuel performance code. Moreover, during transient conditions, when the tunnel network along the grain boundaries is assumed to remain open, the migration of the gas in the grains is rate-limiting for FGR. It is therefore essential to have a model that is simple enough to compute the fractional release from and gaseous swelling in the grains in an efficient manner to an accuracy that is better than or equivalent to the experimental scatter. The degree of simplicity of the model in a fuel performance code is largely justified by the uncertainties pertaining to some of the parameters like diffusion coefficients (at least a factor of 10) [5-7].

Diffusion models used in fuel rod analysis (e.g., [5, 8, 9]) make use of an effective gas atom diffusion coefficient that is generally based on the formulation of Speight [10]. This concept implies a level of simplicity of the mathematical-numerical treatment that allows application to integral fuel performance codes [8]. It is known that the application of the effective diffusion coefficient during high temperature and transient conditions leads to a systematic underestimation of the release fraction (e.g., [8, 11]). This has been overcome by introducing artificially thermal resolution of gas [7, 12], or by increasing the empirical diffusion coefficient during transients [13], or by adding an additional empirical release term from the grains [14, 15].

In this work, an extension of the formulation of Speight [10] is proposed, which includes an estimation of the contribution of bubble motion to fission gas diffusion, while retaining the advantages in terms of simplicity of the mathematical-numerical treatment, thus offering great advantages for implementation in fuel performance codes. Bubble movement can provide an explanation for the sudden increase of the effective diffusion coefficient during transients, although there is an alternative explanation [16] based on the intersection of growing bubbles with the grain boundaries, which is consistent with the sudden increase of the release fraction from the grains as proposed by Verwerft [17] and implemented in the COSMOS code [14, 15].

The structure of the paper is as follows. In the next section, the original model of Speight [10] is outlined, along with the necessary assumptions and the corresponding equations for the new model. The formulation for the irradiation induced resolution term is inferred from the recent molecular dynamics studies. The section also provides a preliminary assessment of the implications in diffusion calculations through an analytical study of the resulting effective diffusion coefficient. The subsequent section contains a validation and a sensitivity study of the model, considering both the effects of model simplifications as well as the effects of uncertainties on model parameters. For the validation of the new model, detailed finite element calculations have been carried out by means of the COMSOL Multiphysics software [18] (hereafter called COMSOL). The final section summarises the main findings of the multi-scale approach for the fission gas behaviour that will be applied in the TRANSURANUS fuel performance code.

2. A NEW MODEL FOR INTRA-GRANULAR BEHAVIOUR OF FISSION GAS

2.1 The Basic Model of Speight

The formulation of Speight [10] describes intra-granular diffusion of fission gas during irradiation of UO_2 assuming that (i) gas atoms diffuse through the UO_2 lattice with a single atom diffusion coefficient D_s, (ii) gas bubbles are immobile, (iii) gas atoms are absorbed into bubbles at a rate g (trapping parameter), (iv) gas atoms are knocked back from bubbles into the lattice at a rate b (irradiation-induced resolution parameter), and (v) bubbles are effectively saturated (quasi-stationary approach). The parameters g and b are taken to be spatially independent within the grain and slowly varying in time [10, 19]. Under the above assumptions, the intra-granular gas diffusion in presence of trapping and irradiation-induced resolution may be evaluated by solving a single diffusion equation, instead of a diffusion equation coupled with an equation for the gas balance in the bubbles. According to the formulation of Speight, the time evolution of the concentration of gas generated uniformly at a rate β within a spherical grain may be determined by the rate equation:

$$\frac{\partial C_t}{\partial t} = \frac{b}{b+g} D_s \nabla^2 C_t + \beta \qquad (1)$$

where C_t is the local total concentration of gas within the grain (single atoms + bubbles). The major advantage of Eq.(1) is that it is formally identical to the diffusion equation previously derived by Booth [20] for the case of diffusion of single gas atoms in absence of bubbles. In the formulation of Speight, trapping and irradiation-induced resolution are taken into account by replacing the single atom diffusion coefficient D_s by an effective single atom diffusion coefficient [10]:

$$D_{s,eff} = \frac{b}{b+g} D_s \qquad (2)$$

With respect to the Booth model, the *apparent* diffusion rate under irradiation is therefore described by a reduced (effective) single atom diffusion coefficient, since only a fraction b/(b+g) of the gas – namely, the fraction existing as single atoms – contributes to diffusion, while the remaining fraction g/(b+g) is trapped into immobile bubbles. However, the formulation of Speight has a tendency to under-predict FGR under high temperature and power transient conditions [8, 11].

The different symbols and notations used in this paper are summarised in Table 1.

2.2 Extending the Model of Speight

The effective diffusion coefficient of Speight is based on the assumption that the atoms are mobile only during the fraction of the time that they are available for diffusion in the lattice, which is given by the ratio of the rates of resolution and trapping as indicated in Eq.(2). As a logical extension of Speight's model, it is proposed here to consider the mobility of the gas while it is being kept in the bubbles, i.e. to consider the contribution of bubble mobility to the gas transfer to grain boundaries. The resulting effective

Table 1. Nomenclature

Symbol	Definition	Units	Typical/adopted value
b	Irradiation-induced resolution parameter for intra-granular bubbles	$[s^{-1}]$	$3 \cdot 10^{-4}$ [21-23]
C_b	Local concentration of gas residing in bubbles	$[(at.) \cdot m^{-3}]$	–
C_s	Local concentration of gas existing as single atoms	$[(at.) \cdot m^{-3}]$	–
C_t	Local concentration of gas ($C_t=C_s+C_b$)	$[(at.) \cdot m^{-3}]$	–
D_b	Bubble diffusion coefficient	$[m^2 \cdot s^{-1}]$	–
D_{eff}	Effective diffusion coefficient	$[m^2 \cdot s^{-1}]$	–
D_s	Single atom diffusion coefficient	$[m^2 \cdot s^{-1}]$	–
$D_{s,eff}$	Effective single atom diffusion coefficient	$[m^2 \cdot s^{-1}]$	–
D_v	Volume self-diffusion coefficient in UO_2	$[m^2 \cdot s^{-1}]$	–
F	Fission rate density	$[(fiss.) \cdot m^{-3} \cdot s^{-1}]$	10^{19}
g	Trapping parameter	$[s^{-1}]$	–
k	Boltzmann constant	$[eV \cdot K^{-1}]$	$8.62 \cdot 10^{-5}$
l_f	Length of a fission fragment track	[m]	$6 \cdot 10^{-6}$ [5]
m	Number of gas atoms per bubble	$[(at.) \cdot (bub.)^{-1}]$	–
N_b	Local concentration of bubbles	$[(bub.) \cdot m^{-3}]$	10^{23}-10^{24}
q'	Linear power	$[kW \cdot m^{-1}]$	–
$\overline{N}_b$	Mean concentration of bubbles within a grain	$[(bub.) \cdot m^{-3}]$	10^{23}-10^{24}
P	Gas pressure in the bubbles	[Pa]	–
Q_v	Migration energy of vacancies in UO_2	[eV]	3.03
$\overline{R}_b$	Mean radius of bubbles within a grain	[m]	$> 0.5 \cdot 10^{-9}$
R	Rod power	[W/g]	–
t	Time	[s]	–
T	Temperature	[K]	–
Z_0	Radius of influence of a fission fragment track	[m]	10^{-9} [5]
β	Fission gas generation rate	$[(at.) \cdot m^{-3} \cdot s^{-1}]$	$2.5 \cdot 10^{18}$
γ	Surface tension of bubbles	$[J/m^2]$	1
σ_h	Hydrostatic stress	[Pa]	–
ω	Van der Waals' volume of a gas atom	$[m^3]$	$8.5 \cdot 10^{-29}$
Ω_{fg}	Volume occupied by a gas atom inside a bubble	$[m^3]$	$3 \cdot 10^{-29}$ [21]

diffusion coefficient for the total gas in the grains becomes therefore the moderated sum of the single gas atoms diffusion coefficient and the bubble diffusion coefficient, whereby the moderation corresponds to the fraction of the time that the gas atom spends in the respective phase:

$$D_{eff} = \frac{b}{b+g} D_s + \frac{g}{b+g} D_b \tag{3}$$

where the trapping rate is based on the assumptions that it is diffusion controlled and that the trapping density is very dilute [5, 22]:

$$g = 4\pi D_s R_b N_b \tag{4}$$

where R_b and N_b denote the average radius and number density of the intra-granular bubbles. The resolution rate is originally based on the heterogeneous model for resolution:

$$b = 3.03 F \pi l_f \left(\bar{R}_b + Z_0\right)^2 \tag{5}$$

where F represents the local fission rate density and Z_0 is the radius of influence for bubble destruction around the fission fragment track. However, recent molecular dynamics simulations of resolution from a Xe filled bubble in a grain of UO_2 indicated that the process is almost independent from the intra-granular bubble size [16]. Eq.(5) is therefore reduced to [23]

$$b = 3 \cdot 10^{-23} \cdot F \tag{6}$$

2.2.1 Considering Bubble Motion in Stationary Conditions

Bubble motion has been experimentally observed [24-27] and is expected to play a relevant role in gas diffusion under high temperature [19, 28-30] and power transient conditions [28, 30], even though the bubble diffusion coefficient is subject to large uncertainties like the gas atoms diffusion coefficient. Assuming that the driving force of bubble diffusion is the bubble concentration gradient – hence, that bubbles move by Brownian motion (b.m.) [31-34] – the second Fick's law may be applied giving the following rate equation:

$$\left(\frac{\partial N_b(r,t)}{\partial t}\right)_{b.m.} = D_b \nabla^2 N_b(r,t) \tag{7}$$

where $N_b(r,t)$ is the local concentration of bubbles and D_b is the bubble diffusion coefficient. If the number of gas atoms per bubble is denoted by m, the local concentration of gas residing in bubbles, $C_b(r,t)$, is:

$$C_b(r,t) = \mathrm{m}(r,t) \cdot \mathrm{N_b}(r,t) \tag{8}$$

and the time variation of $C_b(r,t)$ may be expressed as:

$$\frac{\partial \mathrm{C_b}}{\partial \mathrm{t}} = \mathrm{m}\frac{\partial \mathrm{N_b}}{\partial \mathrm{t}} + \mathrm{N_b}\frac{\partial \mathrm{m}}{\partial \mathrm{t}}. \tag{9}$$

Following the quasi-stationary approach of Speight intra-granular bubbles are considered to be saturated, giving $\partial m/\partial t=0$, and Eqs. (7) and (9) may be rearranged to yield:

$$\left(\frac{\partial \mathrm{C_b}}{\partial \mathrm{t}}\right)_{\mathrm{b.m.}} = \mathrm{m D_b} \nabla^2 \mathrm{N_b}. \tag{10}$$

where

$$m = \frac{\left(\frac{4\pi}{3} R_b^3 - m \cdot \omega\right) P}{kT} \tag{11}$$

when we apply the modified equation of van der Waals as equation of state of the gas, with ω representing the van der Waals' volume of the gas atom, P the gas pressure, T the absolute temperature and k Boltzmann's constant. The gas pressure is in mechanical equilibrium with the surface tension (γ) and the surrounding hydrostatic stress (σ_h):

$$P = \frac{2\gamma}{R_b} + \sigma_h \approx \frac{2\gamma}{R_b} \tag{12}$$

Given the small size of the intra-granular bubbles, the hydrostatic stress is neglected in comparison with the surface tension force.

Assuming further that m is spatially independent within the grain, Eq.(7) may be written as:

$$\left(\frac{\partial \mathrm{C_b}}{\partial \mathrm{t}}\right)_{\mathrm{b.m.}} = \mathrm{D_b} \nabla^2 \mathrm{C_b}. \tag{13}$$

As a result, the time evolution of the gas concentrations may be described by the following partial differential equations:

$$\frac{\partial C_s(r,t)}{\partial t} = D_s \nabla^2 C_s(r,t) - g(r,t) C_s(r,t) + b(r,t) C_b(r,t) + \beta_s \tag{14}$$

$$\frac{\partial C_b(r,t)}{\partial t} = D_b \nabla^2 C_b(r,t) + g(r,t) C_s(r,t) - b(r,t) C_b(r,t) + \beta_b \tag{15}$$

where $C_s(r,t)$ is the local concentration of gas existing as single atoms dissolved dynamically in the lattice, and β_s and β_b are the source terms representing the effects – both resulting from the fission events – of gas atom generation and bubble nucleation, respectively. The source term of bubbles in Eq.(15) relies on the heterogeneous nucleation model [21].

So far it has been assumed that all intra-granular bubbles have one constant number of gas atoms m. Adding equations (14) and (15) yields:

$$\frac{\partial C_t(r,t)}{\partial t} = \nabla^2 \left[D_s C_s(r,t) + D_b C_b(r,t)\right] + \beta \tag{16}$$

where

$$\beta_s + \beta_b = \beta \tag{17}$$

We now introduce the quasi-stationary approximation of Speight for the intra-granular bubbles:

$$g \cdot C_s = b \cdot C_b \tag{18}$$

This assumption is consistent with our hypothesis that m is constant and uniform in the bubbles. This reduces the set of equations (14) and (15) to an equivalent set of equations (16) and (18). The quasi-stationary equation for bubbles leads to the following relations:

$$\begin{aligned} C_s(r,t) &= \frac{b(t)}{b(t)+g(r,t)} C_t(r,t) \\ C_b(r,t) &= \frac{g(r,t)}{b(t)+g(r,t)} C_t(r,t) \end{aligned} \tag{19}$$

Introducing these relations in Eq.(16), leads to

$$\begin{aligned} \frac{\partial C_t(r,t)}{\partial t} = \nabla^2 \left\{ \left[D_s \frac{b(t)}{b(t)+g(r,t)} \right.\right. \\ \left.\left. + D_b \frac{g(r,t)}{b(t)+g(r,t)} \right] C_t(r,t) \right\} + \beta \end{aligned} \tag{20}$$

This equation can be brought in a form identical to Eq.(1) when introducing the assumption of Speight et al., namely that the ratio g/b is uniform and equal to the average value in the grain, but with an effective diffusion coefficient given by Eq.(3):

$$\frac{\partial C_t}{\partial t} = \left(\frac{b}{b+g} D_s + \frac{g}{g+b} D_b \right) \nabla^2 C_t + \beta . \tag{21}$$

It should be underlined that the smearing out of the trapping probability across the spherical grains in solving the partial differential equations above is inconsistent with the idea of considering bubble diffusion towards the boundary where they are released as induced by a bubble concentration gradient. Nevertheless, this approximation has a negligible impact on the outcome when considering the uncertainties pertaining to other model parameters, not the least being the diffusion coefficient, which is subject to uncertainties about one order of magnitude, as shown in the next section. This negligible impact is outweighed by the major advantage that consist of offering a simple and powerful solution that enables to accounts for the mobility of gas while being trapped in bubbles.

In order to evaluate the effective diffusion coefficient, analytical descriptions are needed of the four parameters appearing in the right-hand side of Eq.(21). In this work, the three-term formulation for the single atom diffusion coefficient D_s proposed by Turnbull et al. [35, 36] and used by many authors (e.g., [5, 11, 22, 39]) is adopted:

$$D_s = D_1 + D_2 + D_3 \tag{22}$$

where D_1 represents high temperature intrinsic diffusion by means of thermally activated vacancies, and D_2 and D_3 represent the effect of irradiation enhancement. The first two terms are calculated as:

$$D_1 = 7.6 \cdot 10^{-10} \exp(-3.03/kT) \tag{23}$$

$$D_2 = 3.22 \cdot 10^{-16} \sqrt{R} \exp(-1.19/kT). \tag{24}$$

where R corresponds to the rod power (W/g). The purely rating dependent term D_3 is not taken into account, since it has no visible effect on the diffusion of stable gas atoms [7, 23].

Assuming that the bubble motion during irradiation is controlled by the volume diffusion mechanism [24, 33, 37, 38], the bubble diffusion coefficient takes the form:

$$D_b = \frac{3\Omega_{fg}}{4\pi \bar{R}_b^3} D_v . \tag{25}$$

To describe the volume self-diffusion coefficient, D_v, the following correlation proposed by Evans [39] and based on the bubble diffusivity results of Gulden [24] is adopted:

$$D_v = 3 \cdot 10^{-5} \exp(-4.5/kT). \tag{26}$$

2.2.2 Considering Non-stationary Precipitation in Bubbles

During power variations, the balance of gas in the intra-granular bubbles will evolve according to Eq.(15), affecting in turn the average trapping rate applied in the effective diffusion coefficient of Eq.(3). The radial average trapping rate is directly related to the radial average gas concentration in the bubbles, $\bar{C}_b(t)$. The variation of this average concentration is to a first approximation not affected by diffusion, which operates mostly at the outer surface of the grains, but rather by the following balance equation:

$$\begin{aligned} \frac{\partial \bar{C}_b(t)}{\partial t} &= g(t)\bar{C}_s(t) - b(t)\bar{C}_b(t) + \beta_b \\ &= g(t)\left[\bar{C}_t(t) - \bar{C}_b(t)\right] - b(t)\bar{C}_b(t) + \beta_b \end{aligned} \tag{27}$$

which is a non-homogeneous ordinary differential equation that is solved numerically by means of the Runge-Kutta method with adaptive step-size control and enables us to account for the effect of diffusion-limited precipitation and irradiation induced re-solution on the balance of gas in the intra-granular bubbles during the ramp. The model of Speight is therefore extended to include the effect of bubble motion during ramps in the effective diffusion coefficient of Eq.(3), and by accounting for the evolving concentration of trapped gas via Eq.(27). The coupled set of Eq.(14) and Eq.(15) is therefore replaced by Eq.(21) and Eq.(27).

3. ASSESSMENT AND DISCUSSION OF THE EXTENDED MODEL

The main objective of the new model is to predict the cumulative fraction of released fission gas from spherical grains for a fuel performance code. Its assessment therefore relies on analysing the effect of model assumptions and parameter changes on the predicted FGR in a sphere.

The first important test considers the consequence of introducing the assumption of Speight, i.e. a radial average value of g/b in Eq.(20), in order to obtain the simplified diffusion Eq.(21), with the effective diffusion coefficient. To this end, numerical solutions of Eqs.(14) and (15) have been derived by means of finite elements in COMSOL and compared against the approximation of Eqs.(21) and (27) under different conditions. The main irradiation conditions to be considered are the temperature and the corresponding fission rate density[a]. In order to cover the most representative conditions (while avoiding fuel restructuring), the temperatures T = 1300 K and 1900 K have been considered. The corresponding power density was taken to be 0.4 W/mm^3 and 1 W/mm^3. This test is similar to the first simplified test in the FUMEX-I benchmark exercise of the IAEA [40]. The results are summarised in Figure 1 and Figure 2 at 1300 K and 1900 K, respectively. In the same figures, the results have been plotted when taking into consideration the uncertainties pertaining to the diffusion coefficients by means of a multiplication by a factor 5.

First of all, the figures point out the obvious effect of the increasing irradiation temperature and the associated variations of the gas diffusion coefficient on the increased predicted fraction release values from a sphere. More importantly, however, the figures also reveal that the error on the predicted fraction of fission gas release by means of the extended Speight model, which assumes that g/b is uniform in the sphere, is much smaller than the effect caused by the accepted uncertainties on the diffusion coefficient. This justifies the simplification of the extended Speight model and its implementation in a fuel performance code.

In Figure 3 and Figure 4, the effect of various physical phenomena is analysed separately on the predicted release fraction from the sphere. More precisely, a comparison is made of the FGR fraction

a) when considering single gas atom diffusion alone (i.e., disregarding the presence of bubbles and the associated trapping),
b) when considering the model of Speight with saturated and stationary bubbles that uphold a fraction of the migrating gas,
c) when considering the extended model of Speight wherein saturated traps are allowed to move towards the boundary of the spherical grain,
d) and finally when solving the two equations of the extended model of Speight with uniformly nucleated bubbles that move towards the grain boundary.

At low temperature (Figure 3), when the diffusion

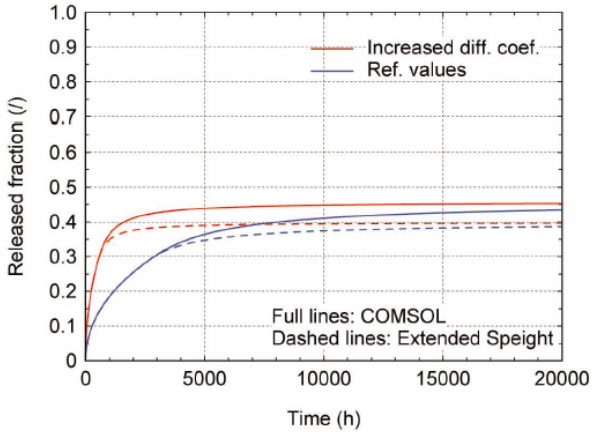

Fig. 1. Cumulative Fraction of Released Fission Gases from a Spherical Grain as a Function of Time (h), Computed by Means of the Set of Equations Governing the Gas Atoms and Bubbles in COMSOL (Full Lines) and by Means of the Extended Model of Speight (Dashed Lines), for Various Values of the Diffusion Coefficients at 1300 K. For D_b Equation (25) is Applied.

[a]The effect of the ratio of the nucleation rates β_s/β_b on the fractional release curves under the considered conditions was proven to be negligible.

coefficients as well as the trapping rate of bubbles are small, the FGR is similar for all models except for the one where only gas atoms diffusion is considered. In the latter model, larger amounts of gas atoms can diffuse towards the outer surface, and the single gas atom diffusion coefficient is far more larger in comparison with the bubble diffusion coefficient at 1300 K. At high temperatures (Figure 4), the mobility of bubbles plays a role and explains why the original Speight model, wherein bubbles are immobile, entails smaller FGR values when compared to the extended version that does consider bubble movement. It should be pointed out that the extended model of Speight presented in this paper does not consider the formation of intra-granular bubbles of several 100 nm, which could be caused for example by coalescence, and the associated reduction of the global trapping probability. However, the total bubble number density decrease is considered due to the total gas release, hence the reduction of the overall trapping reduction by bubbles during ramps is indirectly accounted for.

Figure 3 and Figure 4 also reveal a transition in the controlling mechanism for FGR: from gas atom diffusion at the beginning to bubble diffusion in the cases under consideration, especially at higher temperature (Figure 4). This transition is caused by the fact that the number of, hence the importance of the bubbles increases with

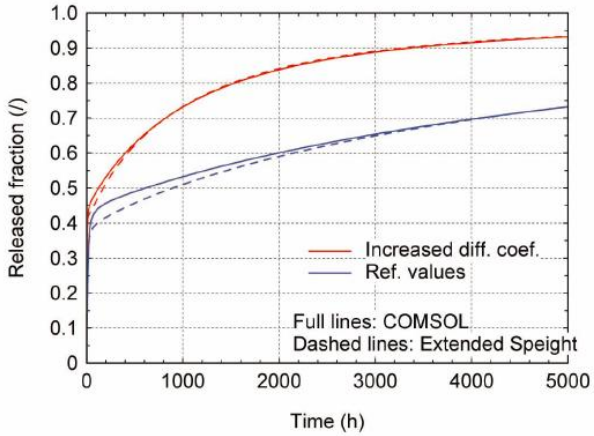

Fig. 2. Cumulative Fraction of Released Fission Gases from a Spherical Grain as a Function of Time (h), Computed by Means of the Set of Equations Governing the Gas Atoms and Bubbles in COMSOL (Full Lines) and by Means of the Extended Model of Speight (Dashed Lines) for Various Values of the Diffusion Coefficients at 1900 K. For D_b Equation (25) is Applied.

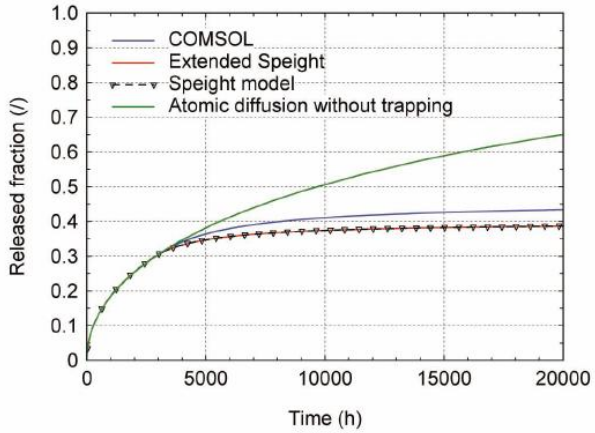

Fig. 3. Cumulative Fraction of Released Fission Gases at 1300 K as a Function of Time (h), Computed by Means of the Set of Two Partial Differential Equations Governing the Gas Atoms and Bubbles, the Extended Model of Speight, the Original Model of Speight, and a Model Considering Single Gas Atoms Diffusion without Bubbles ($g = 0$). For D_b Equation (25) is Applied.

irradiation time and therefore the fraction of time that gas atoms spent in the bubbles, which is given by the ratio g/(b+g).

It should be pointed out that diffusion can also be considered to represent the scenario [16, 17] according to which FGR is controlled by bubble intersection with the adjacent grain boundary. Subsequent to the intersection and associated venting of the gas to the grain boundaries, new bubbles can be generated in the neighbourhood of the grain face and/or existing ones will grow until they intersect again. Such a sudden contribution to release is consistent with the empirical bulk contribution proposed in the COSMOS code [14, 15] during power increases. They considered an instantaneous empirical additional release fraction from the bulk of the grains when certain local temperature and burn-up conditions were fulfilled. Nevertheless, the intersection process of the bubbles is difficult to model properly in a fuel performance code. It seems therefore reasonable to consider simulating this process by means of an equivalent diffusion of bubbles towards the grain face as presented above. Indeed, after the intersection of some bubbles occurred, time is required to reproduce and/or grow bubbles in the area adjacent to the grain boundaries. The bubble growth required to cause renewed intersection with the grain boundary is also (vacancy) diffusion controlled as accounted for via Eq.(27).

The second important test considered here consists of assessing the effect of a power ramp and power cycling. It is based on the AGR/Halden Ramp Test Programme from the IFPE database [41, 42], although one should bear in mind that only one equivalent spherical grain is considered in the model presented here. The test series involved the base-irradiation in a commercial reactor up to burn-ups of around 21 GWd/tU and a subsequent ramp test of Advanced Gas cooled Reactor (AGR) UO_2 fuel rods in the Halden Reactor. The ramp is schematically presented in Figure 5. In fact, three different types of ramps have been analysed: the parameters of a slow and a fast ramp are summarised in Table 2, whereas the parameters of a power cycling test are summarised in Table 3.

As shown in Figure 6 the extended Speight model underestimates the FGR during the ramp, when compared to the solution of Eqs.(14) and (15) by means of COMSOL. This is essentially because the strong bubble concentration near the grain face at high temperature is properly accounted for in the COMSOL model, whereas the extended Speight model only considers the total gas concentration gradient

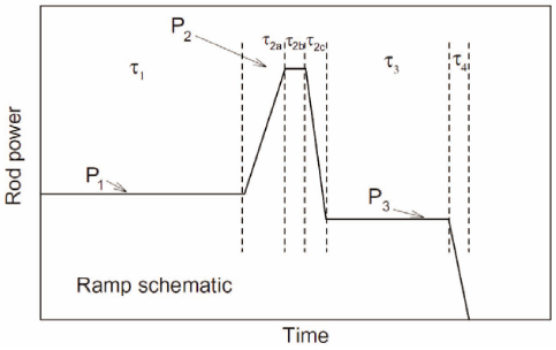

Fig. 5. Schematic of the Irradiation Tests of the AGR/Halden Ramp Test Programme [41, 42]

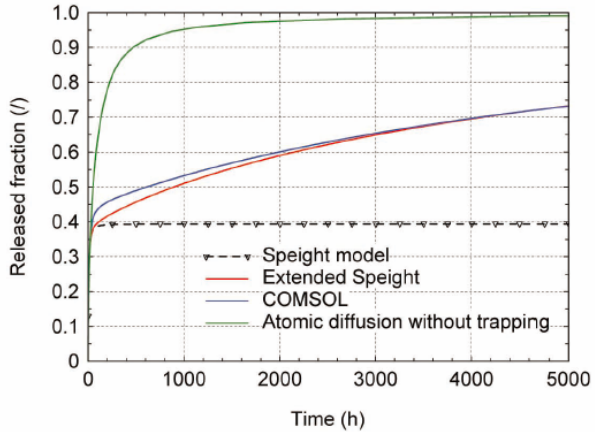

Fig. 4. Cumulative Fraction of Released Fission Gases at 1900 K as a Function of Time (h), Computed by Means of the Set of Two Partial Differential Equations Governing the Gas Atoms and Bubbles, the Extended Model of Speight, the Original Model of Speight, and a Model Considering Single Gas Atoms Diffusion without Bubbles (g = 0). For D_b Equation (25) is Applied.

and applies the radially averaged trapping rate. The total gas concentration gradient is therefore smaller than the gradient of the gas concentration in bubbles when the bubble diffusion coefficient is high. However, the results in Figure 6 also point out that even during the ramp under consideration, the error introduced in the predicted FGR fractions by the approximations in the extended Speight model is still smaller than the effects caused by the uncertainties pertaining to the diffusion coefficients.

The predicted FGR fractions during a power ramp of short duration in Figure 7 also reveal that the approximation of the extended model is justified for FGR predictions in a spherical grain. It can also be concluded that the release caused by diffusion of gas atoms and bubbles during the short ramp is very modest according to both models, even when multiplying the diffusion coefficient by a factor of 5.

Finally, the effect of power cycling on the predicted FGR fraction by means of the extended Speight model is shown in Figure 8, and confirms our findings. More precisely, it reveals that at operating temperatures below about 1900K, the approximations in the extended Speight model provide good predictions for FGR in a spherical grain, when taken into account uncertainties caused by the physical parameters such as the diffusion coefficients. Above this temperature, the smearing out of the trapping rate or bubble concentration in the grains causes errors on predicted FGR fractions during power variations that become of the same order of magnitude as those caused by

Table 2. Details of Single Power Ramps from the AGR/Halden Ramp Test Programme Considered

Rod identifier	Power 1 [kW/m]	τ_1	τ_{2a} [min]	Power 2 [kW/m]	τ_{2b} [min]	τ_{2c} [s]	Power 3 [kW/m]	τ_3 [min]	τ_4
4000	14.0	12d	1.52	40.0	30.0	100	14.0	99.0	SCRAM
4064	20.0	15wk	47.0	43.0	0.0	–	SCRAM	–	–

Table 3. Details of the Power Cycle from the AGR/HAlden Ramp Test Programme Considered

Rod identifier	Power 1 [kW/m]	Time 1	Ramp up	Power up [kW/m]	Ramp down	Power down [kW/m]
4159	18.0	7d	30min	26.0 for 1h	30min	18.0 for 2h
			115 – 4h cycles			

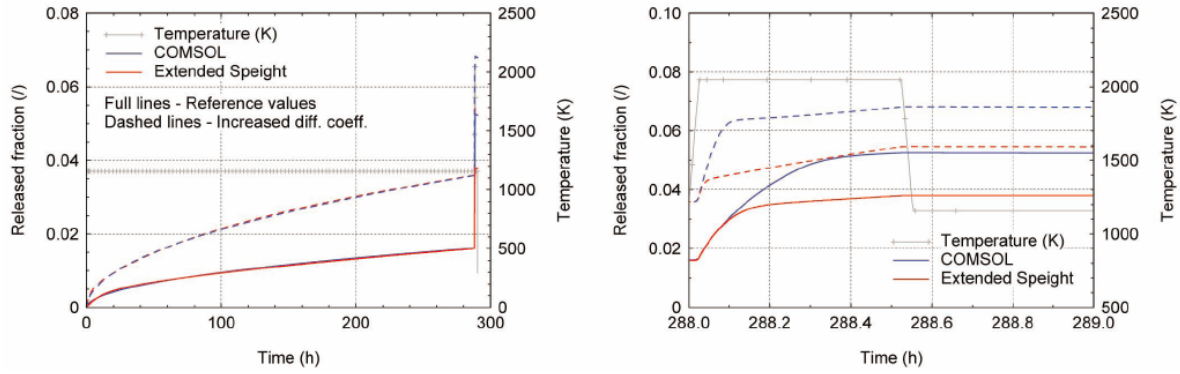

Fig. 6. Predicted FGR in a Single Grain Submitted to the Ramp Test Corresponding to Rod nr. 4000 of the AGR/Halden Ramp Test Programme [41, 42], by Means of COMSOL (Blue Color) and the Extended Speight model (Red Color), Applying References values of the Diffusion Coefficients (Full Lines), as well as Diffusion Coefficients Multiplied by a Factor 5 (Broken Lines). The Figure on the Left-Hand Side shows the Entire Irradiation Time, whereas the Right-hand Side Zooms in on the Ramp.

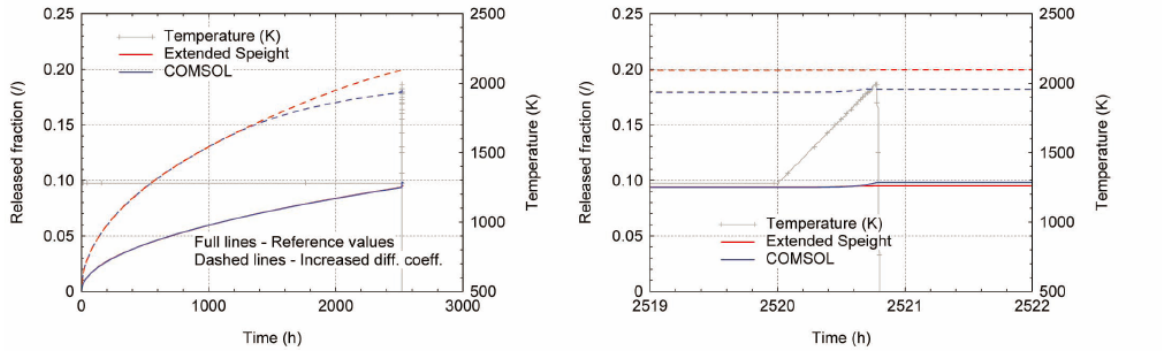

Fig. 7. Predicted FGR in a Single Grain Submitted to the Ramp Test Corresponding to Rod nr. 4064 of the AGR/Halden Ramp Test Programme [41, 42], by Means of COMSOL (Blue Color) and the Extended Speight model (Red Color), Applying References Values of the Diffusion Coefficients (Full Lines), as well as Diffusion Coefficients Multiplied by a Factor 5 (Broken Lines). The Figure on the Left-Hand Side shows the Entire Irradiation Time, whereas the Right-hand Side Zooms in on the Ramp.

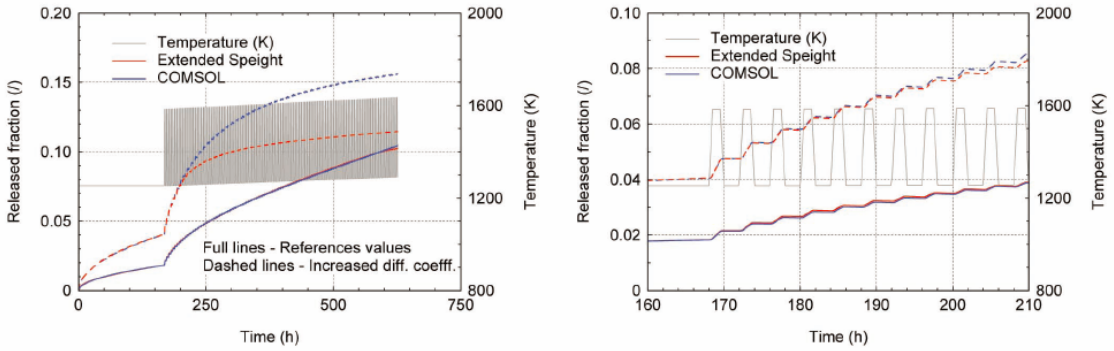

Fig. 8. Predicted FGR in a Single Grain Submitted to the First Ten Cycles of the Power Cycling Test Corresponding to Rod nr. 4059 of the AGR/Halden Ramp Test Programme Programme [41, 42], by Means of COMSOL (Blue Color) and the Extended Speight Model (Red Color), Applying References Values of the Diffusion Coefficients (Full Lines), as well as Diffusion Coefficients Multiplied by a Factor 5 (Broken Lines). The Figure on the Left-hand Side shows the Entire Irradiation Time, whereas the Right-hand Side Zooms in on the First Cycles.

uncertainties on the physical parameters. Nevertheless, it should be pointed out that at those temperature levels other physical phenomena must be taken in account, such as grain growth, which is prone to very large uncertainties as well. Furthermore, when applying the extended Speight model in a fuel performance code, it must be born in mind that also the behaviour of the fission gas at the grain boundaries is subject to uncertainties during power ramps, for example when grain boundary cracking occurs [14, 43].

4. CONCLUSIONS AND PERSPECTIVES

Multi-scale modelling becomes more and more important and supports the conventional fuel performance codes and experiments by improving material properties and models. Also the TRANSURANUS code benefits from such an approach. The radial redistribution of actinides in mixed oxide fuels [44] and the solid fission product swelling model [3] have been published recently. In the current paper, a new mesco-scopic model for the intra-granular fission gas behaviour in UO_2 is proposed that constitutes an extension of the formulation of Speight. It draws on both molecular dynamics calculations for resolution and finite element simulations for the simultaneous evolution of gas atoms and bubbles in the grains. The proposed concept allows taking into account in an approximate manner the contribution of bubble motion to the apparent gas diffusion and the precipitation kinetics of gas in bubbles during ramps, while retaining the advantages of the formulation of Speight in terms of simplicity of the mathematical-numerical treatment. An

analytical study of the resulting effective diffusion coefficient indicates that the contribution of bubble motion is negligible during normal LWR operation conditions, hence there is also no need to introduce an empirical threshold to trigger the additional release contribution like in other empirical approaches for ramp release. The proposed formulation could lead to improvements in the simulation of fission gas behaviour during high temperature conditions, at least when the temperatures do not exceed those where grain growth becomes important. The formulation is therefore proposed for incorporation in the TRANSURANUS fuel performance code [45] and verification against experimental data, e.g. from the IFPE (International Fuel Performance Experiments) [42] database and in the frame of the FUMEX-III benchmark organised by the IAEA.

Current multi-scale developments for the TRANSURANUS code mainly focus on fast reactor fuels, being considered in the frame of the Generation IV type of reactors. First principle and finite element calculations are underway to assess for example mechanical (e.g., elastic constants) as well as heat transport properties (e.g., heat capacity), or in order to assess the solid fission product swelling contribution in nitride fuels.

ACKNOWLEDGEMENTS

This study was partly supported by the F-BRIDGE project (Contract No. 211690) from the European Union FP7 program, the PhD grant for G. Pastore from Politecnico di Milano, and the support for training from ITU. The authors also acknowledge the critical comments from and fruitful discussions with Dr. M. Veschchunov (IBRAE, Russia) in the course of this work.

REFERENCES

[1] Watanabe, T., et al., *Thermal Transport in Off-Stoichiometric Uranium Dioxide by Atomic Level Simulation*. J. Am. Ceram. Soc., 2009. **92**(4): p. 850-856.

[2] Parfitt, D.C. and R.W. Grimes, *Predicting the probability for fission gas resolution into uranium dioxide*. Journal of Nuclear Materials. **In Press, Corrected Proof**.

[3] Middleburgh, S.C., et al., *Swelling due to fission products and additives contained within the uranium dioxide lattice*. Journal of Nuclear Materials, 2011. **submitted for publication**.

[4] Kotomin, E.A., et al., *Implementing first principles calculations of defect migration in a fuel performance code for UN simulations*. Journal of Nuclear Materials, 2009. **393**: p. 292-299.

[5] White, R.J. and M.O. Tucker, *A new fission gas release model*. Journal of Nuclear Materials, 1983. **118**: p. 1-38.

[6] Matzke, H., *Gas release mechanisms in UO_2 - a critical overview*. Radiation Effects, 1980. **53**: p. 219-242.

[7] White, R.J. and M.O. Tucker. *A new mechanistic model for the calculation of fission gas release*. in *International Topical Meeting on LWR Fuel Performance*. 1994. West Palm Beach, Florida.

[8] Lassmann, K. and H. Benk, *Numerical algorithms for intragranular fission gas release*. Journal of Nuclear Materials, 2000. **280**(2): p. 127-135.

[9] Lassmann, K., et al., *TRANSURANUS Handbook*. 2005.

[10] Speight, M.V., *A calculation on the migration of fission gas in material exhibiting precipitation and re-solution of gas atoms under irradiation*. Nuclear Science and Engineering, 1969. **37**: p. 180-185.

[11] Lösönen, P., *On the behaviour of intragranular fission gas in UO_2 fuel*. Journal of Nuclear Materials, 2000. **280**: p. 56-72.

[12] Veshchunov, M.S., *On the theory of fission gas bubble evolution in irradiated UO_2*. Journal of Nuclear Materials 2000. **277** p. 67-81.

[13] Hoppe, N., et al., *COMETHE version 4D release 021 (4.4-021), Vol. 1, General Description*. April 1995, Belgonucleaire Report BN-9409844/220 A.

[14] Koo, Y.H., B.H. Lee, and D.S. Sohn, *COSMOS: A computer code to analyze LWR UO_2 and MOX fuel to high burn-up*. Annals of Nuclear Energy, 1999. **26**: p. 47-67.

[15] Koo, Y.H., B.H. Lee, and D.S. Sohn, *Analysis of fission gas release and gaseous swelling in UO_2 fuel under the effect of external restraint*. Journal of Nuclear Materials, 2000. **280**: p. 86-98.

[16] Govers, K., et al., *Molecular dynamics study of Xe bubble re-solution in UO_2*. Journal of Nuclear Materials 2012. **420** p. 282-290.

[17] Verwerft, M., *Multiple voltage electron probe microanalysis of fission gas bubbles in irradiated nuclear fuel*. Journal of Nuclear Materials, 2000. **282**: p. 97-111.

[18] *COMSOL Multiphysics Modeling Guide, Version 3.5a*. 2008, COMSOL Inc.

[19] Wood, M.H. and J.R. Matthews, *A simple operational gas release and swelling model. Part I: Intragranualar gas*. Journal of Nuclear Materials, 1980. **91**: p. 35-40.

[20] Booth, A.H., *A method of calculating fission gas diffusion from UO_2 fuel and its application to the x-2-f loop test*. 1957.

[21] Olander, D.R. and D. Wongsawaeng, *Re-solution of fission gas – A review: Part I. Intragranular bubbles*. Journal of Nuclear Materials, 2006. **354**: p. 94-109.

[22] Ham, F.S., *Theory of diffusion-limited precipitation*. Journal of Physical Chemistry in Solids, 1958. **6**: p. 335-351.

[23] Lösönen, P., *Modelling intragranular fission gas release in irradiation of sintered LWR UO_2 fuel*. Journal of Nuclear Materials, 2002. **304**: p. 29-49.

[24] Gulden, M.E., *Migration of gas bubbles in irradiated uranium dioxide*. Journal of Nuclear Materials, 1967. **23**: p. 30-36.

[25] Cornell, R.M. and G.H. Bannister, Proc. British Ceramic Society, 1967. **7**: p. 355.

[26] Baker, C., *The fission gas bubble distribtion in uranium dioxide from high temperature irradiated SGHWR fuel pins*. Journal of Nuclear Materials, 1977. **66**: p. 283-291.

[27] Baker, C., *The migration of intragrnular fisson gas bubbles in irradiated uranium dioxide*. 1977. **71**: p. 117-123.

[28] Matthews, J.R. and M.H. Wood, *Modelling the transient behaviour of fission gas*. Journal of Nuclear Materials, 1979. **84**: p. 125-136.

[29] Wood, M.H. and J.R. Matthews, *A model of fission gas release at high temperatures*. Journal of Nuclear Materials, 1981. **102**: p. 223-225.

[30] Evans, J.H., *The role of directed bubble diffusion to grain*

boundaries in post-irradiation fission gas release from UO_2: a quantitative assessment. Journal of Nuclear Materials, 1996. **238**: p. 175-182.

[31] Cornell, R.M., M.V. Speight, and B.C. Masters, *The role of bubbles in fission gas release from uranium dioxide*. Journal of Nuclear Materials, 1969. **30**: p. 170-178.

[32] Cornell, R.M., *An electron microscope examination of matrix fission-gas bubbles in irradiated uranium dioxide*. Journal of Nuclear Materials, 1971. **38**: p. 319-328.

[33] Turnbull, J.A., *The mobility of intragranular bubbles in uranium dioxide during irradiation*. Journal of Nuclear Materials, 1976. **62**: p. 325-328.

[34] Chkuaseli, V.F. and H. Matzke, *Fission gas bubble behaviour in uranium dioxide*. Journal of Nuclear Materials, 1993. **201**: p. 92-96.

[35] Turnbull, J.A., et al., *The diffusion coefficients of gaseous and volatile species during the irradiation of uranium oxide*. Journal of Nuclear Materials, 1982. **107**: p. 168-184.

[36] Turnbull, J.A., R.J. White, and C.A. Wise. *The diffusion coefficient for fission gas atoms in uranium dioxide*. in *Technical Committee Meeting on Water Reactor Fuel Element Computer Modelling in Steady State, Transient and Accidental Conditions*. 1988. Preston, England: International Atomic Energy Agency.

[37] Nichols, F.A., *Kinetics of diffusional motion of pores in solids. A review*. Journal of Nuclear Materials, 1969. **30**: p. 143-165.

[38] Veshchunov, M.S. and V.E. Shestak, *An advanced model for intragranular bubble diffusivity in irradiated UO_2 fuel*. Journal of Nuclear Materials, 2008. **376**: p. 174-180.

[39] Evans, J.H., *Bubble diffusion to grain boundaries in UO_2, and metals during annealing: a new approach*. Journal of Nuclear Materials, 1994. **210**: p. 21-29.

[40] *Report of the Co-ordinated Research Project on Fuel modelling at extended burnup - FUMEX*. Vol. IAEA-TECDOC-998. 1998: IAEA.

[41] White, R.J., R.C. Corcoran, and J.P. Barnes, *A Summary of Swelling Data Obtained from the AGR/Halden Ramp Test Programme*. 2006.

[42] Sartori, E., J. Killeen, and J.A.T. Turnbull, *International Fuel Performance Experiments (IFPE) Database*. 2010, OECD-NEA.

[43] Van Uffelen, P., et al. *Development of a transient fission gas release model for TRANSURANUS. in Water Reactor Fuel Performance Meeting*. 2008. Seoul, Korea.

[44] Di Marcello, V., et al., *Extension of the TRANSURANUS plutonium redistribution model for fast reactor performance analysis*. Nuclear Engineering and Design, 2011. **submitted for publication**.

[45] Lassmann, K., *TRANSURANUS: a fuel rod analysis code ready for use*. Journal of Nuclear Materials, 1992. **188**: p. 295-302.

Appendix C

In this appendix, an input file of the TRANSURANUS code (version v1m1j11), used for the fuel rod analyses presented in Chapter 5, is reproduced. Specifically, reference is made to the analysis of the PK1-1 rod from the Super-Ramp Project. The file is commented for allowing interpretation of the selected options. Details on the meaning of the different variables and settings can be found in (Lassmann et al., 2011). According to the modified version of the TRANSURANUS code set up and used in this work, the new model of fission gas swelling and release is selected by ModFuel(4) = 43, as in the input file reported hereinafter.

```
*******************************************************************************
*
* TRANSURANUS Standard Input Format
*
*          Corresponds to Version  v1m1j11
*
*******************************************************************************
*
* KANF(=IDEN)     Identification for beginning of data set
* INTRUP          Restart Option
*
*--++----------------------------------------------------------------------------
IDEN0
*--++----------------------------------------------------------------------------
* format: A4,I1
*
*******************************************************************************
*
* NKOMM           Number of input text records incl. specification of output files
* PINCHA (1)      Reactor
* PINCHA (2)      Flux
* PINCHA (3)      Fuel Material
* PINCHA (4)      Clad Material
*
* nkomm   pincha(1) pincha(2) pincha(3) pincha(4)
*+-------+--+------+--+------+--+------+--+------+----------------------------------
 9       LWR       THE       OXI       ZIR
*+-------+--+------+--+------+--+------+--+------+----------------------------------
* format:I2,8X,4(A3,7X)
*
*******************************************************************************
*
* Input text records the last 5 of which contain specification of output files
*
* ITEXTK(NKOMM-4)  Statistic File
* ITEXTK(NKOMM-3)  Plot Information File
* ITEXTK(NKOMM-2)  Micro Step File
* ITEXTK(NKOMM-1)  Macro Step File
* ITEXTK(NKOMM)    Restart File
*
*-------------------------------------------------------------------------+------
Simulation of PK1-1 in Experiment Super-Ramp
===========================================

PK1-1.sta
PK1-1.pli
PK1-1.mic
PK1-1.mac
PK1-1.res
*-------------------------------------------------------------------------+------
* format: A80
*
*******************************************************************************
*
*  m3     fgrmod    ixmode   ModProp    istati    ibmech    izenka    ioxire
*     itheoc    ikuehl    iDifSolv   ModAx     idensi    ialpha    insta     kplot
*---+----+----+----+----+----+----+----+----+----+----+----+----+----+----+------
   3   1  10   1    0    6    4    0    0    2    0    2    0    0    0    1
*---+----+----+----+----+----+----+----+----+----+----+----+----+----+----+------
```

```
* format:16I5
*
***************************************************************************************************
*
* ihgap    istruk    ikueka    ibloc    ireloc    iria     ihbs    icrkpi
*     intaxl    irand     itemte    ModStr    nfront    igd      ifba     kokoko
*---+----+----+----+----+----+----+----+----+----+----+----+----+----+----+----+------
    0    1    0    0    0    0    0    0    8    0    0    0    1    0    1    0
*---+----+----+----+----+----+----+----+----+----+----+----+----+----+----+----+------
* format:16I5
*
***************************************************************************************************
*
* islice    ipure    isurfb    istzne   iplnum    igrbdm    iTLog
*     ihydd     ipoint    igrnsz    icorro    inoise    iHe     iClFail
*---+----+----+----+----+----+----+----+----+----+----+----+----+----+----+----+------
    1    0    0    0    0    1    0   11    0    0    0    0    0    0
*---+----+----+----+----+----+----+----+----+----+----+----+----+----+----+----+------
* format:11I5
*
***************************************************************************************************
*
* iPhaseZr  iOxide
*     iLOCA
*---+----+----+----+----+----+----+----+----+----+----+----+----+----+----+----+------
    0    0    0
*---+----+----+----+----+----+----+----+----+----+----+----+----+----+----+----+------
* format:11I5
*
***************************************************************************************************
*
* Options for general material properties
*
*MPgen_cool
* MPgen_clad
*   MPgen_fuel(l)
*+-+-+-+-+-+-+-+-+-+-+-+-+------------------------------------------------------------
 120202020
*+-+-+-+-+-+-+-+-+-+-+-+-+------------------------------------------------------------
* format:40I2
*
***************************************************************************************************
*
* Options for specific material properties (cladding)
*
* ModClad(1:20)
*-+--+--+--+--+--+--+--+--+--+--+--+--+--+--+--+--+--+--+--+------------------------
  0  0  0  0  0  0  0  0  0  0  0  0  0  0  0  0  0  0  0  0
*-+--+--+--+--+--+--+--+--+--+--+--+--+--+--+--+--+--+--+--+------------------------
* format:20I3
*
***************************************************************************************************
*
* Options for specific material properties (fuel)
*
* ModFuel(1:20)
*-+--+--+--+--+--+--+--+--+--+--+--+--+--+--+--+--+--+--+--+------------------------
  0  0  0 43  0 21  0  0  0  0  0  0  0  0  0  0  0  0  0  0
*-+--+--+--+--+--+--+--+--+--+--+--+--+--+--+--+--+--+--+--+------------------------
```

```
* format:20I3
*
*******************************************************************************************
*******************************************************************************************
*
* BETA   Axial anisotropy factor for densification
*
*--------+----------------------------------------------------------------------------
  0.
*--------+----------------------------------------------------------------------------
* format:F10.5
*
*******************************************************************************************
*
* TTRANS  Time at which transient starts [h]
* DTMAX   Maximum time step length [h]
* DT000   Length of the first time step as prescribed by the user
* DBLIND  Blind variable
*
* ttrans           dtmax             dt000             dblind
*------------------+------------------+------------------+------------------+------
1.0d+20             1000.              0.1               1.
*------------------+------------------+------------------+------------------+------
* format:4D20.3
*
*******************************************************************************************
*
* ETACRP  Maximum creep rate (standard value) [1/h]
* nCracks Number of cracks in fuel
* Gas_gb  Saturation limit for grain boundary gas [mikromol/mm^2]
*
*  ETACRP   nCracks    Gas_gb
*--------+---------+---------+-------------------------------------------------------
   0.1e-04    6.e+00   -1.e-04
*--------+---------+---------+-------------------------------------------------------
* format:3E10.3
*
*******************************************************************************************
*
* Auxiliary variables used for model development
*
* iiii(1:5) rrrr(1)   rrrr(2)   rrrr(3)   rrrr(4)   rrrr(5)
*+-+-+-+-+---------+---------+---------+---------+---------+-------------------------
 0 0 0 0 0 +1.00e+20   0.0       0.0       0.0       0.0
*+-+-+-+-+---------+---------+---------+---------+---------+-------------------------
* format:5I2,5E10.3
*
*******************************************************************************************
*
* FMUEH   Friction coefficient between fuel and cladding: static friction
* FMUEF   Friction coefficient between fuel and cladding: sliding friction
* RSNTR0  Maximum density change determined by a resintering test of 24 h
* TSINT0  Input sintering temperature of the fuel [C]
* COLDWO  Cold work (fraction of cross-sectional area reduction)
*         Texture factors for cladding irradiation growth:
* FTXRAD  Radial
* FTXTAN  Circumferential
* FTXAXI  Axial
*
```

```
* fmueh   fmuef    rsntr0    tsint0    coldwo    FtxRad    FtxTan    FtxAxi
*--------+---------+---------+---------+---------+---------+---------+---------+------
0.8       0.8       0.019033  1700.     0.        -999.     -999.     -999.
*--------+---------+---------+---------+---------+---------+---------+---------+------
* format:8F10.5
*
*******************************************************************************************
*
* T23INP  Temperature boundary between the columnar and equiaxed-grain zone [C]
* T34INP  Temperature boundary between the equiaxedand unrestructured-grain zone [C]
* G23INP  Grain Size defining the boundary between columnar and equiaxed zones  [mm]
* G34INP  Grain Size defining the boundary between equiaxed
*                                    and unstructured zones       [mm]
* P23INP  Pore migration length for the boundary between columnar
*                                    and equiaxed zones           [mm]
* P34INP  Pore migration length for the boundary between equiaxed
*                                    and unstructured zones       [mm]
*
*t23inp   t34inp    g23inp    g34inp    p23inp    p34inp
*--------+---------+---------+---------+---------+---------+---------+---------+------
0.        0.        0.        0.        0.        0.
*--------+---------+---------+---------+---------+---------+---------+---------+------
* format:8F10.5
*
*******************************************************************************************
*
* FASTLF  Fast leakage factor only relevant for the RADAR model (iform = 2)
* RESESC  Resonance escape probability only relevant for the RADAR model (iform = 2)
*
*fastlf   resesc
*--------+---------+-----------------------------------------------------------------
0.975     0.65
*--------+---------+-----------------------------------------------------------------
* format:2F10.5
*
*******************************************************************************************
*
* CANF(I) Initial fill gas concentrations ( / )
*
* canf(1:10)
*He     Ar      Kr      Xe      N2      H2      O2      CO      CO2     H20
*------+-------+-------+-------+-------+-------+-------+-------+-------+-------+------
1.0     0.      0.      0.      0.      0.      0.      0.      0.      0.
*------+-------+-------+-------+-------+-------+-------+-------+-------+-------+------
* format:10F8.5
*
*******************************************************************************************
*
* HHREF(L) Reference heights of axial slices [mm]
*
* hhref(l), l=1,m31
*--------+---------+---------+---------+---------+---------+---------+---------+------
104.      80.       128.      32.
*--------+---------+---------+---------+---------+---------+---------+---------+------
* format:8F10.5
*
*******************************************************************************************
*
*
```

```
* AEAX1   Input mode for radial discretization
*
*---+----------------------------------------------------------------------------
   0
*---+----------------------------------------------------------------------------
* format:I5
*
*******************************************************************************
*
* AEGROB  Mode for radial discretisation of coarse zones
* AEFEIN  Mode for radial discretisation of fine zones
* M1      Number of coarse zones in (fuel + cladding)
* M1H     Number of coarse zones in cladding
*
*  aegrob    m1
*     aefein    m1h
*---+----+----+----+-------------------------------------------------------------
   0    0   15    1
*---+----+----+----+-------------------------------------------------------------
* format:4I5
*
*******************************************************************************
*
* IFALLL(L)=3  Analysis of a fuel rod; fuel and cladding are not
*                                in contact (standard case)
*
* ifalll(l)
*---+----------------------------------------------------------------------------
   3
*---+----------------------------------------------------------------------------
* format:I5
*
*******************************************************************************
*
* M2(IGROB)    Number of mesh points per coarse zone
*
*---+----+----+----+----+----+----+----+-----------------------------------------
  15   15   15   15   15   15   15   15   15   15   15   15   15   15   15   15
*---+----+----+----+----+----+----+----+-----------------------------------------
* format:16I5
*
*******************************************************************************
*
* RIB     Inner fuel radius      [mm]
* RAB     Outer fuel radius      [mm]
* RIH     Inner cladding radius  [mm]
* RAH     Outer cladding radius  [mm]
* Raubl   Surface roughness fuel [mm]
* Rauhl   Surface roughness clad [mm]
*
* rib     rab       rih       rah       raubl     rauhl
*--------+---------+---------+---------+---------+-------------------------
0.       4.555     4.655     5.3815    0.002     0.0005
*--------+---------+---------+---------+---------+-------------------------
* format:8F10.5
*
*******************************************************************************
*******************************************************************************
*
```

```
* AEAX6   Input mode for grain size in axial dimension
* IKORN   Input mode for grain size in radial dimension
*
* aeax6
*      ikorn
*---+----+-------------------------------------------------------------------------
   0    0
*-------------------------------------------------------------------------------
* format:2I5
*
*********************************************************************************
*
* KORNGR  Grain diameter (mm)
*
* korngr(igrob,i)
*--------+---------+---------+---------+---------+---------+---------+---------+------
0.0060
*--------+---------+---------+---------+---------+---------+---------+---------+------
* format:8F10.5
*
*********************************************************************************
*
* DKORN   Averaged grain diameter (mm) for specific creep correlations
*
*--------+----------------------------------------------------------------------
0.0060
*--------+----------------------------------------------------------------------
* format:F10.5
*
*********************************************************************************
*
* AEAX3   Input mode for initial porosity in axial dimension
* IPORO   Input mode for initial porosity in radial dimension
*
* aeax3
*      iporo
*---+----+-------------------------------------------------------------------------
   0    0
*---+----+-------------------------------------------------------------------------
* format:2I5
*
*********************************************************************************
*
* PRODIS  Fraction of dish volume ( / )
* OpenPor Open Porosity           ( / )
*
* prodis
*         openpor
*--------+---------+---------+---------+---------+---------+---------+---------+------
0.022     0.027
*--------+---------+---------+---------+---------+---------+---------+---------+------
* format:8F10.5
*
*********************************************************************************
*
* POR000  Total fabrication porosity (average)
*
*--------+----------------------------------------------------------------------
0.05474
```

```
*--------+---------------------------------------------------------------------
* format:F10.5
*
*****************************************************************************************
*
* DENPOR  Porosity at the end of sintering
* DENBUP  Burn-up at which sintering has stopped
*
* denpor
*        denbup
*--------+---------+---------------------------------------------------------------
0.0344     10000.
*--------+---------+---------------------------------------------------------------
* format:2F10.5
*
*****************************************************************************************
*
* AEAX7   Input mode for fuel enrichment
*
*---+-----------------------------------------------------------------------------
   0
*---+-----------------------------------------------------------------------------
* format:I5
*
*****************************************************************************************
*
* ENRI35    atoms of  U-235  / number of heavy metal atoms
* ENRI39    atoms of  Pu-239 / number of heavy metal atoms
* ENRI40    atoms of  Pu-240 / number of heavy metal atoms
* ENRI41    atoms of  Pu-241 / number of heavy metal atoms
* ENRI42    atoms of  Pu-242 / number of heavy metal atoms
*
* enri35(I)         enri40(I)          enri42(I)
*         enri39(I)          enri41(I)
*--------+---------+---------+---------+---------+----------------------------------
0.032     0.0       0.        0.        0.
*--------+---------+---------+---------+---------+----------------------------------
* format:8F10.5
*
*****************************************************************************************
*
* AEAX2  Input mode for flux depression factor
* IFORM  Input mode for power density form factor
*
* aeax2
*      iform
*---+----+------------------------------------------------------------------------
   0    5
*---+----+------------------------------------------------------------------------
* format:2I5
*
*****************************************************************************************
*
* FLUXFA(L)  Flux thermal (0.) or fast (1.)
*
*--------+---------+---------+---------+---------+---------+---------+---------+------
0.
*--------+---------+---------+---------+---------+---------+---------+---------+------
* format:8F10.5
```

```
*
*******************************************************************************
*
* AEAX4  Input mode for stoichiometry data in axial dimension
* IOZUM  Input mode for stoichiometry data in radial dimension
*
* aeax4
*      iozum
*---+----+----------------------------------------------------------------------
   0    0
*---+----+----------------------------------------------------------------------
* format:2I5
*
*******************************************************************************
*
* OZUM0  Average O/M ratio (stoichiometry)
*
*--------+-------------------------------------------------------------------
2.00
*--------+-------------------------------------------------------------------
* format:F10.5
*
*******************************************************************************
*
* AEAX5  Input mode for Pu concentration in axial dimension
* ICNPU  Input mode for Pu concentration in radial dimension
*
* aeax5
*      icnpu
*---+----+----------------------------------------------------------------------
   0    0
*---+----+----------------------------------------------------------------------
* format:2I5
*
*******************************************************************************
*
* CNPU0    Average Pu concentration in section or slice
* IBRUT(L) Variable defining fissile or fertile material
*
* cnpu0
*         ibrut(l)
*--------+----+----------------------------------------------------------------
0.        0
*--------+----+----------------------------------------------------------------
* format:F10.5,I5
*
*******************************************************************************
*
* IVAR1   Calculation mode for inner pin pressure
*
*---+----------------------------------------------------------------------
   2
*---+----------------------------------------------------------------------
* format:I5
*
*******************************************************************************
*
* PI0EIN  Fillgas pressure  [MPa]
* TI0EIN  Fillgas temperature [C]
```

```
* UPLVG   Lower plenum volume (maximum) [mm**3]
* AUPL    Volume fraction factor in lower plenum
* AOPL    Volume fraction factor in upper plenum
* ASP     Volume fraction factor in gap
* AZK     Volume fraction factor in central void
*
* pi0ein  ti0ein    uplvg     aupl      aopl      asp       azk
*--------+---------+---------+---------+---------+---------+---------+---------+------
2.25      20.000    1406.     0.        0.7000    1.00      1.00
*--------+---------+---------+---------+---------+---------+---------+---------+------
* format:8F10.5
*
*********************************************************************************
*################################################################################
#####
* Macrostep Part - Label IMAK followed by 4 dummy lines
*################################################################################
#####
*
IMAK
1
2
3
4
*********************************************************************************
*         ---------
*         Time Step
*         0 h
*         ---------
*-------------------------------------------------------------------------------
*   iwert
*       iaxvar
*         zeit              wert              dwert
*-------------------------------------------------------------------------------
*
*
*   1: print-out the results at time a (hours)
*---+----+------------------+------------------+---------+-------------------------
    1    0 0.0000000000000D+00
*---+----+------------------+------------------+---------+-------------------------
*   2: linear rod power (kW/m)
*---+----+------------------+------------------+---------+-------------------------
    2    1 0.0000000000000D+00 0.0000000000000D+00
*---+----+------------------+------------------+---------+-------------------------
* format:2I5,2D20.13,D10.3
*
*-------------------------------------------------------------------------------
*       iaxvar=1 -->  axial profile read in:
*                     axvar2(1:mend)
*--------+---------+---------+---------+---------+---------+---------+---------+------
  1.00000   1.00000   1.00000
*--------+---------+---------+---------+---------+---------+---------+---------+------
* format:8F10.5
*
*-------------------------------------------------------------------------------
*
*
*   3: flux (1/(cm**2 s))
*---+----+------------------+------------------+---------+-------------------------
```

```
   3    0 0.0000000000000D+00 0.0000000000000D+00
*---+----+------------------+------------------+---------+-------------------------
* format:2I5,2D20.13,D10.3
*
*-----------------------------------------------------------------------------------
*
*
*   9: coolant temperature (C)
*---+----+------------------+------------------+---------+-------------------------
   9    1 0.0000000000000D+00 0.2000000000000D+02
*---+----+------------------+------------------+---------+-------------------------
* format:2I5,2D20.13,D10.3
*
*-----------------------------------------------------------------------------------
*       iaxvar=1 -->  axial profile read in:
*                     axvar2(1:mend)
*--------+---------+---------+---------+---------+---------+---------+---------+------
  1.00000   1.00000   1.00000
*--------+---------+---------+---------+---------+---------+---------+---------+------
* format:8F10.5
*
*-----------------------------------------------------------------------------------
*
*
*  10: coolant pressure (MPa)
*---+----+------------------+------------------+---------+-------------------------
  10    0 0.0000000000000D+00 0.1000000000000D+00
*---+----+------------------+------------------+---------+-------------------------
* format:2I5,2D20.13,D10.3
*
  25    0 0.0000000000000D+00 1.0000000000000D+01
*-----------------------------------------------------------------------------------
*       iaxvar=0 --> no axial profile
*
*  30:  print out of the radial profile at time "ZEIT"
*---+----+------------------+------------------+---------+-------------------------
  30    0 0.0000000000000D+00
*---+----+------------------+------------------+---------+-------------------------
***********************************************************************************
*         ----------------------------
*         Further Macro Time Steps
*         ----------------------------
*
*-----------------------------------------------------------------------------------
*
* data point #001 begin
*
*
** BASE-IRRADIATION
*
   2    1 0.4333333333333D+00 0.2600000000000D+01
  1.00000   1.00000   1.00000
   3    0 0.4333333333333D+00 0.7500000000000D+14
   9    1 0.4333333333333D+00 0.2953000000000D+03
  1.00000   1.00000   1.00000
  10    0 0.4333333333333D+00 0.1450000000000D+02
*
*
*
```

```
   2    1 0.1066666666667D+01 0.2600000000000D+01
  1.00000   1.00000   1.00000
   9    1 0.1066666666667D+01 0.2953000000000D+03
  1.00000   1.00000   1.00000
*
*
*
   2    1 0.1933333333333D+01 0.7800000000000D+01
  1.00000   1.00000   1.00000
   9    1 0.1933333333333D+01 0.2998800000000D+03
  1.00000   1.00000   1.00000
*
*
*
   2    1 0.2350000000000D+01 0.7800000000000D+01
  1.00000   1.00000   1.00000
   9    1 0.2350000000000D+01 0.2998800000000D+03
  1.00000   1.00000   1.00000
*
*
*
   2    1 0.3650000000000D+01 0.1560000000000D+02
  1.00000   1.00000   1.00000
   9    1 0.3650000000000D+01 0.3066800000000D+03
  1.00000   1.00000   1.00000
*
*
*
   2    1 0.5401666666667D+01 0.1560000000000D+02
  1.00000   1.00000   1.00000
   9    1 0.5401666666667D+01 0.3066800000000D+03
  1.00000   1.00000   1.00000
*
*
*
   2    1 0.6598333333333D+01 0.2278000000000D+02
  1.00000   1.00000   1.00000
   9    1 0.6598333333333D+01 0.3128500000000D+03
  1.00000   1.00000   1.00000
*
*
*
   2    1 0.5967358333333D+03 0.2278000000000D+02
  1.00000   1.00000   1.00000
   9    1 0.5967358333333D+03 0.3128500000000D+03
  1.00000   1.00000   1.00000
*
*
*
   2    1 0.5972641666667D+03 0.2595000000000D+02
  1.00000   1.00000   1.00000
   9    1 0.5972641666667D+03 0.3155500000000D+03
  1.00000   1.00000   1.00000
*
*
*
... (OMITTED TIME STEPS)
...
...
```

```
...
...
**         RE-IRRADIATION
*
   1    0 0.2102999833333D+05
   2    1 0.2102999833333D+05 0.0000000000000D+00
  1.00000   1.00000   1.00000
   9    1 0.2102999833333D+05 0.2000000000000D+02
  1.00000   1.00000   1.00000
  30    0 0.2102999833333D+05
*
*
*
   2    1 0.2103000166667D+05 0.0000000000000D+00
  1.00000   1.00000   1.00000
   9    1 0.2103000166667D+05 0.3140000000000D+03
  1.00000   1.00000   1.00000
  10    0 0.2103000166667D+05 0.1450000000000D+02
*
*
*
   2    1 0.2103495833333D+05 0.0000000000000D+00
  1.00000   1.00000   1.00000
   9    1 0.2103495833333D+05 0.3140000000000D+03
  1.00000   1.00000   1.00000
*
*
*
   2    1 0.2103704166667D+05 0.1137333333333D+02
  0.98916   1.09906   0.91178
   3    0 0.2103704166667D+05 0.8000000000000D+14
   9    1 0.2103704166667D+05 0.3189000000000D+03
  0.99984   1.00151   0.99865
*
*
*
   2    1 0.2104095833333D+05 0.1137333333333D+02
  0.98916   1.09906   0.91178
   9    1 0.2104095833333D+05 0.3189000000000D+03
  0.99984   1.00151   0.99865
*
*
** RAMP TEST
*
   1    0 0.2104304166667D+05
   2    1 0.2104304166667D+05 0.2275333333333D+02
  0.98931   1.09874   0.91195
   9    1 0.2104304166667D+05 0.3237400000000D+03
  0.99966   1.00297   0.99737
  30    0 0.2104304166667D+05
*
*
*
   1    0 0.2106704166667D+05
   2    1 0.2106704166667D+05 0.2275333333333D+02
  0.98931   1.09874   0.91195
   9    1 0.2106704166667D+05 0.3237400000000D+03
  0.99966   1.00297   0.99737
  30    0 0.2106704166667D+05
```

```
*
*
*
   1    0 0.2106707222226D+05
   2    1 0.2106707222226D+05 0.3776333333333D+02
  0.98905   1.09895   0.91200
   9    1 0.2106707222226D+05 0.3300066666667D+03
  0.99949   1.00468   0.99583
  30    0 0.2106707222226D+05
*
*
*
   1    0 0.2107907222226D+05
   2    1 0.2107907222226D+05 0.3776333333333D+02
  0.98905   1.09895   0.91200
   9    1 0.2107907222226D+05 0.3300066666667D+03
  0.99949   1.00468   0.99583
  30    0 0.2107907222226D+05
*
*
*
   2    1 0.2108207222226D+05 0.1888000000000D+02
  0.98888   1.09905   0.91208
   9    1 0.2108207222226D+05 0.3296966666667D+03
  0.99949   1.00459   0.99592
*
*
*
   2    1 0.2108457222226D+05 0.1888000000000D+02
  0.98888   1.09905   0.91208
   9    1 0.2108457222226D+05 0.3296966666667D+03
  0.99949   1.00459   0.99592
*
*
*
   2    1 0.2108757222226D+05 0.0000000000000D+00
  1.00000   1.00000   1.00000
   3    0 0.2108757222226D+05 0.0000000000000D+00
   9    1 0.2108757222226D+05 0.3140000000000D+03
  1.00000   1.00000   1.00000
*
*
*
   2    1 0.2108857222226D+05 0.0000000000000D+00
  1.00000   1.00000   1.00000
   9    1 0.2108857222226D+05 0.3140000000000D+03
  1.00000   1.00000   1.00000
*
*
*
****************************** END OF IRRADIATION ***********************************
*        ----------------
*        cold point final
*        ----------------
*        Time Step
*        21089 h
*        ----------------
*
*
```

```
*-------------------------------------------------------------------------------
*   iwert
*       iaxvar
*         zeit                wert                dwert
*-------------------------------------------------------------------------------
*
*
*   1: printout of the result at time "ZEIT"
*---+----+------------------+------------------+---------+-------------------------
    1    0 0.2108900000000D+05
*---+----+------------------+------------------+---------+-------------------------
*
*
*   2: linear rod power (kW/m)
*---+----+------------------+------------------+---------+-------------------------
    2    1 0.2108900000000D+05 0.0000000000000D+00
*---+----+------------------+------------------+---------+-------------------------
*       iaxvar=1 -->  axial profile read in:
*                     axvar2(1:mend)
*--------+---------+---------+---------+---------+---------+---------+---------+------
  1.00000   1.00000   1.00000
*--------+---------+---------+---------+---------+---------+---------+---------+------
*
*
*   9: coolant temperature (C)
*---+----+------------------+------------------+---------+-------------------------
    9    1 0.2108900000000D+05 0.2000000000000D+02
*---+----+------------------+------------------+---------+-------------------------
*       iaxvar=1 -->  axial profile read in:
*                     axvar2(1:mend)
*--------+---------+---------+---------+---------+---------+---------+---------+------
  1.00000   1.00000   1.00000
*--------+---------+---------+---------+---------+---------+---------+---------+------
*
*
*  10: coolant pressure (MPa)
*---+----+------------------+------------------+---------+-------------------------
   10    0 0.2108900000000D+05 0.1000000000000D+00
*---+----+------------------+------------------+---------+-------------------------
*       iaxvar=0 --> no axial profile
*-------------------------------------------------------------------------------
*
*
*  30:  print out of the radial profile at time "ZEIT"
*---+----+------------------+------------------+---------+-------------------------
   30    0 0.2108900000000D+05
*---+----+------------------+------------------+---------+-------------------------
*
*
*  00:  last line of data set
*---+----+------------------+------------------+---------+-------------------------
00000    0 0.2108900000000D+05
*---+----+------------------+------------------+---------+-------------------------
```